

# HIGH RESOLUTION MEDIUM ENERGY ION BEAM ANALYSIS AND PROCESSING OF ULTRA-THIN FILMS

FINAL REPORT

ROBERT A. WELLER

SEPTEMBER 15, 1999

U. S. ARMY RESEARCH OFFICE

DAAH 04-95-1-0565

VANDERBILT UNIVERSITY

NASHVILLE, TENNESSEE

APPROVED FOR PUBLIC RELEASE;  
DISTRIBUTION UNLIMITED.

THE VIEWS, OPINIONS, AND FINDINGS CONTAINED IN THIS REPORT ARE THOSE OF THE  
AUTHOR AND SHOULD NOT BE CONSTRUED AS AN OFFICIAL DEPARTMENT OF THE ARMY PO-  
SITION, POLICY, OR DECISION, UNLESS SO DESIGNATED BY OTHER DOCUMENTATION.

DTIC QUALITY INSPECTED 4

19991102 089

REPORT DOCUMENTATION PAGE			Form Approved OMB NO. 0704-0188	
<small>Public reporting burden for this collection of information is estimated to average 1 hour per response, including the time for reviewing instructions, searching existing data sources, gathering and maintaining the data needed, and completing and reviewing the collection of information. Send comments regarding this burden estimate or any other aspect of this collection of information, including suggestions for reducing this burden, to Washington Headquarters Services, Directorate for Information Operations and Reports, 1215 Jefferson Davis Highway, Suite 1204, Arlington, VA 22202-4302, and to the Office of Management and Budget, Paperwork Reduction Project (0704-0188), Washington, DC 20503.</small>				
1. AGENCY USE ONLY (Leave blank)		2. REPORT DATE September 15, 1999		3. REPORT TYPE AND DATES COVERED Final
4. TITLE AND SUBTITLE High Resolution Medium Energy Ion Beam Analysis and Processing of Ultra-thin Films			5. FUNDING NUMBERS DA AHO4-95-1-0565	
6. AUTHOR(S) Robert A. Weller				
7. PERFORMING ORGANIZATION NAME(S) AND ADDRESS(ES) Vanderbilt University Nashville, TN 37235			8. PERFORMING ORGANIZATION REPORT NUMBER	
9. SPONSORING / MONITORING AGENCY NAME(S) AND ADDRESS(ES) U. S. Army Research Office P.O. Box 112211 Research Triangle Park, NC 27709-2211			10. SPONSORING / MONITORING AGENCY REPORT NUMBER ARO 34480.17-MS	
11. SUPPLEMENTARY NOTES The views, opinions and/or findings contained in this report are those of the author(s) and should not be construed as an official Department of the Army position, policy or decision, unless so designated by other documentation.				
12a. DISTRIBUTION / AVAILABILITY STATEMENT Approved for public release; distribution unlimited.			12 b. DISTRIBUTION CODE	
13. ABSTRACT (Maximum 200 words) Medium energy time-of-flight spectrometry has been optimized for high resolution depth profiling of ultra-thin films. This report reviews the technical accomplishments of the project and discusses applications of the analytical technique to problems in semiconductor processing, trace element analysis, and organic thin film research.				
14. SUBJECT TERMS ion beam analysis, thin film analysis, Rutherford backscattering, medium energy backscattering, depth profiling, trace element analysis, time of flight			15. NUMBER OF PAGES 118	
			16. PRICE CODE	
17. SECURITY CLASSIFICATION OF REPORT UNCLASSIFIED	18. SECURITY CLASSIFICATION OF THIS PAGE UNCLASSIFIED	19. SECURITY CLASSIFICATION OF ABSTRACT UNCLASSIFIED	20. LIMITATION OF ABSTRACT UL	

## FOREWORD

The project to develop time-of-flight medium energy backscattering spectrometry (MEBS) as a complement to conventional MeV Rutherford backscattering spectrometry (RBS) began at Vanderbilt approximately ten years ago. Support from the U.S. Army Research Office, in the form of this grant, and a predecessor program has been crucial in completing the work. Throughout the effort, the goals have been to understand the time-of-flight spectrometer, to optimize its design until its performance is limited by fundamental physical constraints, and to apply the technique to novel problems that are difficult or impossible to address using earlier methods. The submission of this report occasions the completion of this project. The central issues, to establish the efficiency and resolution of the spectrometer, have been resolved, and analytical tools have been developed to optimize spectrometer design and to facilitate the analysis of MEBS data. In order to document the full project in one place, we are including a collection of publications as an appendix to this report that form the core of the effort spanning its full duration. The papers chosen for inclusion document spectrometer physics and the mathematical tools that have been developed to support the method. Also included are a few reports of applications chosen to emphasize the strength of this method relative to alternatives. These, along with a tutorial article to appear in a forthcoming reference work on analytical methods in materials research, which is cited in the bibliography below, can be viewed as the definitive description of the work of the project.

## TABLE OF CONTENTS

Foreword.....	2
Table of Contents.....	3
Statement of the problem .....	4
Summary of Results.....	5
Time-of-flight Spectrometer Resolution.....	5
Analytical tools.....	6
Alternative Methods.....	7
Applications .....	8
Publications (References).....	10
Inventions .....	12
Participating Scientific Personnel .....	13
Appendix .....	14



## STATEMENT OF THE PROBLEM

The title of this project was "High resolution medium energy ion beam analysis and processing of ultra-thin films." Building upon the results of an earlier ARO sponsored program,<sup>1</sup> it sought to accomplish several objectives needed to complete the development of time-of-flight medium energy ion beam analysis, and thereby to make it generally useful for thin-film materials science. The stated objectives of the program were as follows:

- To enhance time-of-flight spectrometer timing resolution through a combination of measures in order to achieve near surface depth resolution of approximately 1 nm, and to apply this to the analysis of oxide and nitride films on semiconductors.
- To develop analytical methods and corresponding computer tools to obtain the maximum information available from high-resolution backscattering data.
- To explore the relative merits of alternate strategies, including pulsed-beam approaches, for high-resolution ion beam analysis.
- To use medium energy ion beam analysis to investigate selected organic and inorganic thin films, and in the course of this work to optimize analytical strategies for them.

The goal of this program was to establish a body of literature sufficient in scope and detail that a thin film materials scientist familiar with ion beam analysis could implement a time-of-flight system suitable for the problem at hand, could apply this system with confidence, and could interpret the data in order to draw useful conclusions.

---

<sup>1</sup> The Analysis of Hydrogen in Materials Using Low Energy Ion Beams, U. S. Army Research Office, DAAL 03-92-G-0037, Robert A. Weller.

## SUMMARY OF RESULTS

Although the scope of this program was limited after the first year as a result of fiscal constraints, all the objectives set forth in the original program were nevertheless accomplished. In the following sections, which are keyed to the bullet list above, the basic findings are summarized briefly.

### TIME-OF-FLIGHT SPECTROMETER RESOLUTION

Understanding the factors that control spectrometer resolution proved to be the most difficult and time-consuming question in the whole of the medium energy backscattering project. The issue concerned identifying the reason that carbon-foil-based time of flight spectrometers failed to achieve the resolution expected theoretically based upon reasonable physical assumptions about their behavior. As described in our paper, reference 2 below, others had attributed this discrepancy to unidentified path length uncertainty over and above that which would be expected from an analysis of the spectrometer geometry. We showed in reference 2 that, in fact, it is due to unexpected roughness in the carbon foils that are used in spectrometers of this type. On an atomic scale, the path lengths of ion passing through these foils are much more variable than foil manufacturers' specifications imply. We demonstrated this both by ion beam analysis of a foil and by atomic force microscopy.

When the measured foil roughness parameters are folded into our spectrometer model, we achieved excellent agreement between predicted and measured system resolution. With the long-standing discrepancy between these values finally resolved, we were able to predict the system resolution and to identify the optimum design for spectrometers

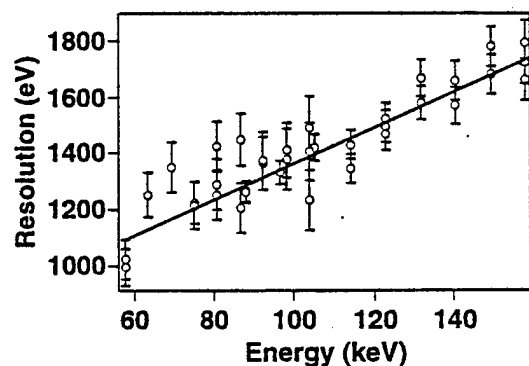


Fig. 1. Energy resolution of the time-of-flight spectrometer as a function of particle energy. From McDonald, Weller, and Liechtenstein 1999, cited below.

of this type. The optimum design varies from our current configuration only in having a different start-foil geometry, one in which the plane of the foil is normal to the spectrometer axis. However, the difference is small. With available carbon foils, we achieve an energy resolution for detection of oxygen in thin oxides of about 1.3 keV (see fig. 1), which translates to a depth resolution of about 13 Å for oxygen on silicon with a beam-surface angle of 45° (<110> direction in the silicon crystal). See

fig. 2. Near surface resolution is actually  $< 10 \text{ \AA}$  at  $55^\circ$ , a reasonable and widely used angle for backscattering. Thus, we have achieved the goal,  $10 \text{ \AA}$  at the surface of  $\text{SiO}_2$ , set forth originally.

If the technology for making ultra-uniform carbon foils can be developed (and recent work at NIST on foils for x-ray work suggests that it can), then the time-of-flight approach to medium energy backscattering spectrometry will be fully competitive with the electro-

static analyzer (ESA) method. As of this writing, the ESA approach gives marginally better resolution but enough so to make it preferred (if it is available) for the very highest resolution studies of ultra-thin dielectrics. This having been said, in general applications requiring high depth resolution for thin film analysis, MEBS is probably the best technique now available, especially for relatively fragile films such as organic layers.

## ANALYTICAL TOOLS

Experimental advances in medium energy ion beam analysis generated parallel requirements for computational tools with which to analyze data. The general-purpose, spectrum analysis tools developed over the years for conventional Rutherford backscattering spectrometry were never intended to handle situations where projectile energies necessitate the use of screened cross sections. Moreover, they were computer hardware dependent and not easily adaptable, at least by other than their original authors, to medium energy work. As a result, we undertook over several years to develop a comprehensive, self-consistent set of computational tools for ion beam work using the computer mathematics system *Mathematica*<sup>2</sup>. These are computer-hardware independent, modular, and much more flexible than earlier systems. As a result, they

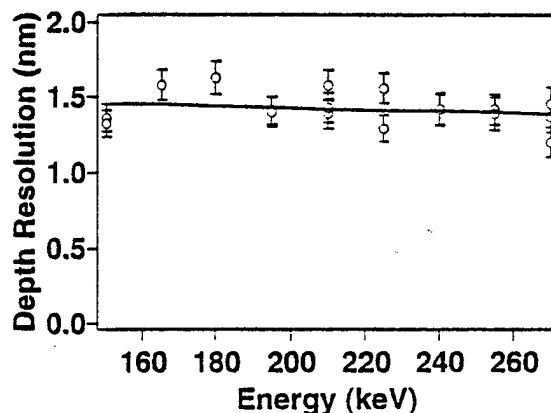


Fig. 2. ToF spectrometer depth resolution for oxygen in  $\text{SiO}_2$  at a target angle of  $45^\circ$  as a function of  $\text{He}^+$  ion beam energy. From McDonald, Weller, and Liechtenstein 1999, cited below.

<sup>2</sup> Wolfram, S., *The Mathematica Book*, 3<sup>rd</sup> ed, Cambridge: Cambridge University Press, 1996. *Mathematica*<sup>®</sup>, the programming environment for technical computing, is a product of Wolfram Research, Inc. <http://www.wri.com>.

are especially useful for one-of-a-kind computations. The system is documented in reference 8 in the publication list below. This paper also appears in full in the appendix.

Because it has been implemented in *Mathematica*, this tool set offers the user access to extremely powerful general-purpose mathematical functions both in support of the ion beam routines and for combining results in novel and interesting ways. Of particular note is the availability of symbolic computation. This innovation makes it possible to differentiate, integrate and otherwise manipulate quantities for which closed-form expressions exist. Wherever possible, this tool set returns closed form symbolic expressions.

The philosophy of the calculations generally follows that of the underlying program *Mathematica*. Computational accuracy, embodied in the selection of algorithms, takes precedence over execution speed. As a result, some functions in the tool set are slow when compared with implementations in a compiled language such as C or Fortran. In a case where greater speed is needed, it is often possible to take advantage of *Mathematica's* own tools, such as those for function approximation, to achieve it. Overall, it has been our experience through several years of development and use that the efficiency of getting final answers to complex problems using this tool set is higher than with any other computational strategy that we have employed.

During the course of this work we also briefly explored alternative data analysis approaches characterized by the work described in ref. 7 below. While intriguing, the demands made by these methods for sheer numbers of computer cycles were incompatible with the decision described above to concentrate on accuracy rather than efficiency. As a result, we have left these methods as the subject for further work as computer speeds advance. Nevertheless, as demonstrated in ref. 2, the system described in ref. 8, more than exceeds our objectives as outlined in the bullet list above.

## ALTERNATIVE METHODS

Preliminary computations undertaken prior to this project suggested that pulsed-beam time-of-flight spectrometry might be competitive with the carbon foil method that we were developing. However, early in the project we concluded after more careful analysis that the disadvantages of the pulsed-beam technique were sufficient to make it unlikely that it could compete in either resolution or sensitivity.

Basically, there were two problems with the pulsed beam approach. First, the finite size of the beam spot produced path length variations as a function the location of ion im-

pacts on the target that resulted in unacceptably large timing uncertainty. These variations are not present in the start-foil system and as a result, start foils yield better resolution. The second problem with pulsed beam systems was duty factor. In order to obtain short pulses, it is necessary to either reduce the duty factor or modulate the beam energy or both. An attractive optimization of these quantities could not be convincingly established, even though discussions with an accelerator vendor, National Electrostatics, Corporation, suggested that sufficiently short beam pulses could indeed be produced with beam drift lengths downstream of a pulser and buncher which were consistent with space available in our laboratory.

It is our conclusion that for a resolution optimized system, only electrostatic spectrometers (and possibly magnetic spectrometers) are competitive with time-of-flight. The trade-offs among these systems are discussed in reference 1.

## APPLICATIONS

In selecting applications we sought problems which were not easily accessible by other techniques. Here we mention three, depth profiling of dielectric films on silicon, quantification of surface hydrogen, and the analysis of organic layers. The profiling of dielectrics was done in collaboration with colleagues at Texas Instruments, Inc., and is documented in ref. 12, which also appears in full in the appendix.

One of the early motivations for this work was to establish an additional method for quantifying surface and near surface hydrogen. Hydrogen is important in determining properties of materials, yet it is surprisingly difficult to measure, particularly when it is present in low concentrations. One of the conclusions of this work is that, while medium energy hydrogen measurements are possible, the optimum energy for forward recoil hydrogen measurement is probably in the range of 1-5 MeV, at least when using projectiles such as oxygen, neon, or argon. Reference 10 below provides further details on this conclusion.

The most surprising result to be obtained in the course of this work comes from one of the applications, the analysis of aluminum in an organic light emitting diode structure (Ref. 4). In this experiment, medium energy backscattering was used to show that aluminum from one of the metallic electrodes migrated into the organic film and influenced the photoluminescence. Aluminum oxide was found to suppress this migration. The interesting thing for the purpose of this report is the extreme detail obtained by medium energy backscattering. Not only was aluminum identified in the organic ma-

trix in excess of its normal concentration, but a surface layer was identified and correlated with excess oxygen, revealing the layer to be in all probability  $\text{Al}_2\text{O}_3$ . These data were particularly gratifying since strenuous efforts had been made previously without success to analyze these samples using conventional Rutherford backscattering.

Finally, it is important to note our measurement of trace element sputtering. One of the spin-offs from Vanderbilt's medium energy ion scattering program was a collaboration with Sandia National Laboratories to build a time-of-flight backscattering system optimized for ultra-high sensitivity trace element analysis of semiconductors using heavy ions such as carbon and nitrogen. This system, known as the HIBS system for heavy-ion backscattering spectrometry, has been used by our Sandia colleagues to obtain the highest sensitivity backscattering measurements ever made. Reference 11 describes measurements at Vanderbilt undertaken to establish the rate of sputtering of trace constituents of a surface, and thereby to assess the best sensitivity which is physically possible to achieve by backscattering.

## PUBLICATIONS (REFERENCES)

1. R. A. Weller, "Introduction to Medium Energy Ion Beam Analysis," in "Methods in Materials Research," Unit 13C, John Wiley & Sons, 1999, in press.
2. K. McDonald, R. A. Weller, and V. K. Liechtenstein, "Quantitative evaluation of the determinants of resolution in time-of-flight spectrometers for medium energy ion beam analysis," *Nuclear Instruments & Methods in Physics Research, Section B (Beam Interactions with Materials and Atoms)*, vol. 152, pp. 171-81, 1999.
3. Y. Wu, C. H. M. Marée, R. F. Haglund, Jr, J. D. Hamilton, M. A. Morales Paliza, M. B. Huang, L. C. Feldman, and R. A. Weller, "Resistivity and oxygen content of indium tin oxide films deposited at room temperature by pulsed-laser ablation," *Journal of Applied Physics*, vol. 86, pp. 991-4, 1999.
4. M. B. Huang, K. McDonald, J. C. Keay, Y. Q. Wang, S. J. Rosenthal, R. A. Weller, and L. C. Feldman, "Suppression of penetration of aluminum into 8-hydroxyquinoline aluminum via a thin oxide barrier," *Applied Physics Letters*, vol. 73, pp. 2914-16, 1998.
5. R. H. Magruder, III, R. A. Weeks, R. A. Weller, R. A. Zuhr, and D. K. Hensley, "Formation and photosensitivity of defects in Se implanted silica," *Journal of Non-Crystalline Solids*, vol. 239, pp. 78-83, 1998.
6. C. H. M. Marée, R. A. Weller, L. C. Feldman, K. Pakbaz, and H. W. H. Lee, "Accurate thickness/density measurements of organic light-emitting diodes," *Journal of Applied Physics*, vol. 84, pp. 4013-16, 1998.
7. V. M. Prozesky, J. Padayachee, R. Fischer, W. Von der Linden, V. Dose, and R. A. Weller, "Bayesian techniques and the principle of maximum entropy in ion-beam analysis applications," *Nuclear Instruments & Methods in Physics Research, Section B (Beam Interactions with Materials and Atoms)*, vol. 136-138, pp. 1146-51, 1998.
8. R. A. Weller, "General purpose computational tools for simulation and analysis of medium-energy backscattering spectra," presented at Applications of Accelerators in Research and Industry, The University of North Texas, Denton, Texas, 1998.
9. Y. F. Zhao, R. D. Schrimpf, A. R. Patwary, M. A. Neifeld, A. W. Al-Johani, R. A. Weller, and K. F. Galloway, "Annealing effects on multi-quantum well laser diodes

after proton irradiation," IEEE Transactions on Nuclear Science, vol. 45, pp. 2826-32, 1998.

10. J. H. Arps and R. A. Weller, "Determination of the hydrogen sensitivity and depth resolution of medium-energy, time-of-flight, forward-recoil spectrometry," Nuclear Instruments & Methods in Physics Research, Section B (Beam Interactions with Materials and Atoms), vol. 119, pp. 527-32, 1996.
11. D. Pedersen, R. A. Weller, M. R. Weller, V. J. Montemayor, J. C. Banks, and J. A. Knapp, "Sputtering and migration of trace quantities of transition metal atoms on silicon," Nuclear Instruments & Methods in Physics Research, Section B (Beam Interactions with Materials and Atoms), vol. 117, pp. 170-4, 1996.
12. R. A. Weller, K. McDonald, D. Pedersen, and J. A. Keenan, "Analysis of a thin, silicon-oxide, silicon-nitride multilayer target by time-of-flight medium energy back-scattering," Nuclear Instruments & Methods in Physics Research, Section B (Beam Interactions with Materials and Atoms), vol. 118, pp. 556-9, 1996.



## INVENTIONS

The time-of-flight spectrometer that was the focal point of much of this work was developed and patented at Vanderbilt University. While significant improvements were made to this device in the course of this project, none of these were separately disclosed or patented. Rather, they were put into the public domain through the publications reported above.

## PARTICIPATING SCIENTIFIC PERSONNEL

Here we list those persons who participated at a substantial level in this work. Additional collaborators may be noted in the author lists of the publications above.

1. Robert A. Weller, Vanderbilt University. Principal investigator.
2. Kyle McDonald, Vanderbilt University. Ph.D candidate. Degree expected, May 2000.
3. Hui Fang, Vanderbilt University. Ph.D. candidate.
4. Diane Pedersen, Vanderbilt University. Ph.D. candidate.
5. M. B. Huang, Vanderbilt University. Research Associate.
6. John Coleman, Vanderbilt University. Undergraduate research assistant.
7. Michael Moshier, Vanderbilt University. Undergraduate research assistant.
8. Joseph A. Keenan, Texas Instruments, Inc., Dallas, Texas.
9. James C. Banks, Sandia National Laboratories, Albuquerque, New Mexico.
10. James A. Knapp, Sandia National Laboratories.
11. Vitaly Kh. Liechtenstein, RRC Kurchatov Institute, Moscow, Russia.

## APPENDIX

The papers that are reproduced below form the core documentation of the time-of-flight medium energy ion scattering project. Here we list the papers in order and provide a sentence or two describing their content or significance.

1. R. A. Weller, "General purpose computational tools for simulation and analysis of medium-energy backscattering spectra," presented at Applications of Accelerators in Research and Industry, The University of North Texas, Denton, Texas, 1998. An extensive body of analytical tools for analysis of medium energy data was written over the years in the *Mathematica*<sup>®</sup> computer language. These tools are documented in this paper.
2. K. McDonald, R. A. Weller, and V. K. Liechtenstein, "Quantitative evaluation of the determinants of resolution in time-of-flight spectrometers for medium energy ion beam analysis," *Nuclear Instruments & Methods in Physics Research, Section B (Beam Interactions with Materials and Atoms)*, vol. 152, pp. 171-81, 1999. This paper identifies the non-uniformity of the carbon start foil as the most important factor in determining spectrometer resolution, and thus solves the last major outstanding problem in understand spectrometer performance.
3. M. B. Huang, K. McDonald, J. C. Keay, Y. Q. Wang, S. J. Rosenthal, R. A. Weller, and L. C. Feldman, "Suppression of penetration of aluminum into 8-hydroxyquinoline aluminum via a thin oxide barrier," *Applied Physics Letters*, vol. 73, pp. 2914-16, 1998. In this application, aluminum was observed to migrate into organic thin films and to change their optical properties. Rutherford backscattering was unable to see the effect. Here it is observed and quantified.
4. J. H. Arps and R. A. Weller, "Determination of the hydrogen sensitivity and depth resolution of medium-energy, time-of-flight, forward-recoil spectrometry," *Nuclear Instruments & Methods in Physics Research, Section B (Beam Interactions with Materials and Atoms)*, vol. 119, pp. 527-32, 1996. This paper establishes the quantitative parameters for hydrogen measurement by medium energy forward recoil spectrometry.
5. D. Pedersen, R. A. Weller, M. R. Weller, V. J. Montemayor, J. C. Banks, and J. A. Knapp, "Sputtering and migration of trace quantities of transition metal atoms on silicon," *Nuclear Instruments & Methods in Physics Research, Section B (Beam Interactions with Materials and Atoms)*, vol. 117, pp. 170-4, 1996. One of the spin-offs from

this project was the heavy ion backscattering (HIBS) project at Sandia National Laboratories in which a time-of-flight medium energy backscattering system was optimized for ultra-high sensitivity trace element analysis using heavy projectiles. Sputtering is one factor limiting the ultimate sensitivity. This is, we believe, the first paper to deal with the sputter removal of trace elements.

6. R. A. Weller, K. McDonald, D. Pedersen, and J. A. Keenan, "Analysis of a thin, silicon-oxide, silicon-nitride multilayer target by time-of-flight medium energy backscattering," *Nuclear Instruments & Methods in Physics Research, Section B (Beam Interactions with Materials and Atoms)*, vol. 118, pp. 556-9, 1996. One of the original reasons for developing MEBS was to analyze ultra-thin dielectrics on semiconductors. This paper describes the measurement of such a target and is representative of semiconductor applications.
7. J. H. Arps and R. A. Weller, "Time-of-flight elastic recoil analysis of ion beam modified nitrocellulose thin films," *Nuclear Instruments & Methods in Physics Research, Section B (Beam Interactions with Materials and Atoms)*, vol. B100, pp. 331-5, 1995. One of the significant strengths of MEBS is its ability to analyze fragile organic thin films. This paper describes such an analysis and is particularly noteworthy in that it is an example of the use of ion backscattering to observe a chemical process, the radiation induced remove of NO<sub>2</sub> groups from the target material.
8. R. A. Weller, "The impact of spectrometer efficiency on the trace-element sensitivity of time-of-flight medium energy backscattering," *Nuclear Instruments & Methods in Physics Research, Section B (Beam Interactions with Materials and Atoms)*, vol. B99, pp. 491-4, 1995, and (erratum) B111, p. 190, 1996. This paper establishes the relationship between spectrometer parameters and trace element sensitivity and thereby provides a means to predict the performance of MEBS (or HIBS) in this application.
9. J. H. Arps, M. E. Miklis, and R. A. Weller, "Adaptation of particle-telescope technology for medium energy ion beam analysis," *Review of Scientific Instruments*, vol. 65, pp. 1575-9, 1994. This proof-of-concept paper describes a spectrometer that uses a surface barrier detector for stop signals, and demonstrates the value of the energy information in discriminating useable signal in the presence of background.
10. R. A. Weller, J. H. Arps, D. Pedersen, and M. H. Mendenhall, "A model of the intrinsic efficiency of a time-of-flight spectrometer for keV ions," *Nuclear Instruments*

*& Methods in Physics Research, Section A (Accelerators, Spectrometers, Detectors and Associated Equipment)*, vol. 353, pp. 579-82, 1994. This paper describes a mathematical model of the time-of-flight spectrometer quantum efficiency and represents the culmination of the research into this aspect of spectrometer behavior.

11. M. H. Mendenhall and R. A. Weller, "An algorithm for ab initio computation of small-angle-multiple scattering angular distributions," *Nuclear Instruments & Methods in Physics Research, Section B (Beam Interactions with Materials and Atoms)*, vol. B93, pp. 5-10, 1994. In this paper, we revisit the well-known problem of small-angle multiple scattering and present new algorithms based upon the fast Fourier transform algorithm, for obtaining multiple scattering angular distributions. These are needed for computing spectrometer efficiency.
12. J. H. Arps and R. A. Weller, "Measurement of time-of-flight spectrometer efficiency for light ions at medium energies," *Nuclear Instruments & Methods in Physics Research, Section B (Beam Interactions with Materials and Atoms)*, vol. B90, pp. 547-51, 1994. Numerous factors affect time-of-flight spectrometer efficiency. This paper presents measurements of the efficiency for detecting light ions of interest for backscattering spectrometry.
13. R. A. Weller, "Instrumental effects on time-of-flight spectra," *Nuclear Instruments & Methods in Physics Research, Section B (Beam Interactions with Materials and Atoms)*, vol. B79, pp. 817-20, 1993. This paper establishes the criterion for trace element sensitivity and presents the mathematical relationship between observed time-of-flight spectra and corresponding energy spectra as a function of count rate. The model is useful for predicting the effects of count rate and establishes the theoretical basis for converting time-of-flight spectra to energy spectra.
14. J. H. Arps and R. A. Weller, "Medium energy elastic recoil analysis of surface hydrogen," *Nuclear Instruments & Methods in Physics Research, Section B (Beam Interactions with Materials and Atoms)*, vol. B79, pp. 539-44, 1993. This paper introduces medium energy forward recoil spectrometry as a method for measuring surface hydrogen and other low atomic mass surface constituents.
15. M. H. Mendenhall and R. A. Weller, "High-resolution medium-energy backscattering spectrometry," *Nuclear Instruments & Methods in Physics Research, Section B (Beam Interactions with Materials and Atoms)*, vol. B59-B60, pp. 120-3, 1991. This paper discusses the relative merits of medium energy ion beam analysis with ions

such as  $\text{Li}^+$ , and presents examples including the ion beam erosion of  $\text{CaF}_2$ .

16. M. H. Mendenhall and R. A. Weller, "Algorithms for the rapid computation of classical cross sections for screened Coulomb collisions," *Nuclear Instruments & Methods in Physics Research, Section B (Beam Interactions with Materials and Atoms)*, vol. B58, pp. 11-17, 1991. Previous papers dealing with the computation of the classical scattering cross section for realistic potentials had used brute force with high-order quadratures. In this paper, we present algorithms for computing classical cross sections that are both accurate and efficient. This work forms the basis for computing all screened Coulomb cross sections used in this project. See 1 above.
17. M. H. Mendenhall and R. A. Weller, "Destruction of a  $\text{MgF}_2$  optical coating by 250 keV alpha particle irradiation," *Applied Physics Letters*, vol. 57, pp. 1712-14, 1990. This was one of the first significant applications of MEBS. In this paper, using the high depth resolution of the technique, we showed that radiation effects data on bulk  $\text{MgF}_2$  were not sufficient to predict the effects of  $\alpha$  particle radiation on thin films, and thereby identified a potential problem for optical coatings in the radiation environment of space.
18. M. H. Mendenhall and R. A. Weller, "Performance of a time-of-flight spectrometer for thin film analysis by medium energy ion scattering," *Nuclear Instruments & Methods in Physics Research, Section B (Beam Interactions with Materials and Atoms)*, vol. B47, pp. 193-201, 1990. This paper presented the first experimental results of our time-of-flight medium energy ion beam analysis program.
19. M. H. Mendenhall and R. A. Weller, "A time-of-flight spectrometer for medium energy ion scattering," *Nuclear Instruments & Methods in Physics Research, Section B (Beam Interactions with Materials and Atoms)*, vol. B40-41, pp. 1239-43, 1989. This paper, written during the building of our first spectrometer, outlined its theory of operation and offered predictions as to the performance that would be achieved. (We underestimated the quality of data that would result.)

# General Purpose Computational Tools for Simulation and Analysis of Medium-Energy Backscattering Spectra

Robert A. Weller\*

Vanderbilt University, Nashville, Tennessee 37235

This paper describes a suite of computational tools for general-purpose ion-solid calculations, which has been implemented in the platform-independent computational environment *Mathematica*<sup>®</sup>. Although originally developed for medium energy work (beam energies < 300 keV), they are suitable for general, classical, non-relativistic calculations. Routines are available for stopping power, Rutherford and Lenz-Jensen (screened) cross sections, sputtering yields, small-angle multiple scattering, and backscattering-spectrum simulation and analysis. Also included are a full range of supporting functions, as well as easily accessible atomic mass and other data on all the stable isotopes in the periodic table. The functions use common calling protocols, recognize elements and isotopes by symbolic names and, wherever possible, return symbolic results for symbolic inputs, thereby facilitating further computation. A new paradigm for the representation of backscattering spectra is introduced.

## INTRODUCTION

In spite of the great advances in the processing power of computers over the last few years most practitioners in the ion-solid interactions community still find it necessary to rely on a collection of books, tables, special-purpose commercial or freeware programs, and locally written software, when doing calculations. Although excellent and very widely used programs such as RUMP<sup>1</sup> exist for special purpose calculations, their output is often cumbersome to combine and use in other environments.<sup>2</sup>

This paper describes a consistent set of computational tools for ion-solid work that has been constructed in order to facilitate prototyping and one-of-a-kind computations. Because it has been implemented in *Mathematica*,<sup>3</sup> this tool set is platform independent and offers the user access to extremely powerful general-purpose mathematical functions both in support of these routines and for combining their results in novel and interesting ways. Of particular note is the availability of symbolic computation. This innovation makes it possible to differentiate, integrate and otherwise manipulate quantities for which closed-form expressions exist. Wherever possible, this tool set returns these closed form symbolic expressions.

The philosophy of the calculations generally follows that of the underlying program *Mathematica* in which computational accuracy, embodied in the selection of algorithms, takes precedence over execution speed. As a result, some functions in the tool set are slow when compared with implementations in a compiled language such as C or Fortran. In a case where greater speed is needed, it is often possible to take advantage of *Mathematica's* own tools, such as those for function approximation, to achieve it. Overall, it has been our experience through several years of

development and use that the efficiency of getting final answers to complex problems using this tool set is higher than with any other computational strategy that we have employed.

## FUNCTION DESCRIPTIONS

Almost all of the functions defined in the tool set, or the algorithms from which they derive, have been previously documented in the literature. In general, every tool is a function that returns an object as its value. In the case of a simple function like stopping power, the object is an approximate real number. In other cases, several different return values are possible. For example, the backscattering kinematic factor KScatter will return an approximate real number for a backscattering collision when explicit colliding species and an angle are given. However, if these arguments are symbolic, the return value is itself symbolic. In the more unusual forward-scattering case where the kinematic factor is double valued,<sup>4</sup> the return value is a list of approximate real numbers corresponding to the two possibilities. When KScatter is used as a component of other calculations, the user must anticipate the possible inputs and be prepared to deal with the corresponding outputs.

When an element or chemical compound is appropriate as an argument it may be entered symbolically. For example, the element silicon can be represented as "Silicon." without the quotation marks, of course. Specific isotopes are represented as, e.g., Silicon[28]. All the naturally occurring isotopes of the elements in the periodic table are cataloged along with their masses and abundances<sup>5</sup> and several functions are provided for extracting this information. For example, the function IsotopeExpand when applied to a chemical formula returns that formula expanded to include properly weighted isotopes.

Chemical formulae are represented using the *Mathematica* concept of lists. Thus, "SiO<sub>2</sub>" becomes "{Sili-

\* Electronic mail: Robert.A.Weller@Vanderbilt.Edu

con,1},{Oxygen,2}}" again without quotations. Multi-layer planar targets are also represented by lists. In this case, each element of the list is itself a list describing a single layer. The list describing a layer has three elements, the chemical formula, the molecular density in molecules/cm<sup>3</sup> and the thickness in cm. The formula for a pure element is, e.g. for elemental silicon, "{Silicon,1}." Of course, with fully expanded isotopes, the form for a pure element is identical to that for a compound. A function MolecularDensity is provided for obtaining the number of molecules/cm<sup>3</sup> given a chemical formula and a mass density in g/cm<sup>3</sup>.

In order to deal with the common case of a trace element with sub-monolayer coverage, the concept of a zero-thickness layer has been introduced. When the thickness of a layer is given as 0 cm, the density is assumed to be areal density in units of molecules/cm<sup>2</sup>. No *a priori* restrictions are placed on the complexity of multi-layer targets or the chemical compounds of which they are composed. Of course, very complex targets, especially with expanded isotopes, may take a long time to process depending upon the operation.

## SPECTRUM SIMULATION

Chu, Mayer and Nicolet described the basic physics of backscattering-spectrum simulation,<sup>6</sup> with additional considerations discussed by Doolittle.<sup>1</sup> Doolittle's implementation of the algorithms in the computer program called RUMP is one of the most widely used software tools in the ion-solid community. Our implementation shares many similarities with RUMP but differs in other important details. The most significant of these is the way in which we have chosen to represent spectra.

So far as we know, all previous backscattering simulation implementations, including RUMP, have viewed the backscattering spectrum and the representation of the spectrum as a list of discrete values at equally spaced energies as identical. In other words, the spectrum and the multi-channel analyzer picture of the spectrum have been viewed as synonymous. In our implementation, computation of the spectrum and evaluation of the spectrum are distinct operations.

The computation of a backscattering spectrum is handled by the function SimulateRBS (Fig.1). SimulateRBS requires as arguments (in order) a projectile, e.g. Helium[4], a multi-layer planar target defined as described above, a beam energy in eV, and directions of the beam and the target outward normal specified as {polar, azimuthal} angles in degrees expressed in a consistent spherical coordinate system. SimulateRBS returns a complex object called a ScatteringSpectrum, which is a deterministic rule for obtaining the numerical value of the backscattering spectrum given a numerical value of energy. In other words, SimulateRBS returns a function. You can subsequently evaluate this function at equally spaced channels and obtain the conventional multichannel-an-

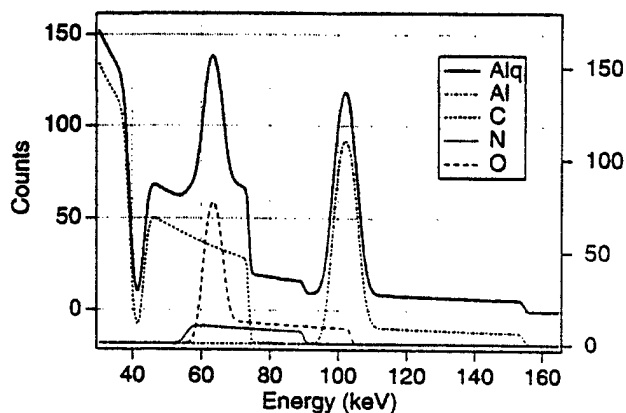


Figure 1. 270 keV He<sup>+</sup> backscattering spectrum (normal incidence, 150° scattering angle) of 120 nm of the organic light emitting diode constituent 8-hydroxyquinoline aluminum (Al<sub>3</sub>C<sub>27</sub>H<sub>18</sub>N<sub>3</sub>O<sub>3</sub>) on 11 nm Al<sub>2</sub>O<sub>3</sub> on a C substrate. Individual elemental constituents are shown as dotted lines offset downward for clarity.

alyzer representation of the spectrum. More likely, however, you will use *Mathematica*'s Plot function to adaptively select points to provide a high quality graphical representation of the full spectrum or any portion thereof with minimal computation.

Like RUMP, SimulateRBS produces a "brick," for every distinct constituent of every layer of the target. At any given energy, the full spectrum is the sum of the contribution of all the bricks. However, following the general philosophy of *Mathematica* we do not make numerical approximations. Whenever a value for stopping power or cross section is needed, a call to the appropriate defining function is made. Stopping powers use the procedures originally described of Ziegler, et al.<sup>7</sup> and return numerical values identical to those tabulated by Rauhala,<sup>8</sup> while straggling is computed using the method described by Yang, et al.<sup>9</sup> Lenz-Jensen cross sections are used and computed by a variant on the method described by Mendenhall and Weller.<sup>10</sup> All integrations are handled by *Mathematica*'s built in numerical integrator.

By not optimizing the simulation algorithms to fit the capability of current computing, we are, of course, paying a hefty price in execution speed. However, the impact of the penalty continues to drop with time. When the first version of SimulateRBS was written in 1992, it was limited in practicality to simulating at most two or three layer targets without isotope expansion. Presently, it can be used in a closed-loop, non-linear, least-squares fitting procedure for similar targets of typical semiconductor complexity will all isotopes included explicitly, and can return best-fit values in a reasonable time. This functionality has derived from the generality of the design, in spite of the fact that it was never originally intended for closed loop or automated use. Another collateral benefit of this design is that if a user wishes to refine functions such as those for cross sections or stopping power the changes will be automatically reflected in other functions, such as simulation, which use the values.



SimulateRBS represents a brick in a manner chosen by the routine itself. For bricks that are sufficiently narrow, a quadratic polynomial in energy  $E$  is used. For thicker bricks, additional basis functions,  $E^{-1}$  and  $E^{-2}$  are added for a total of five parameters. (This is to be contrasted with RUMP, which uses polynomials.) The use of the inverse powers makes it possible to describe very wide regions of the spectrum without having to manually divide the target into narrow layers. Our experience with medium energy backscattering (at 270 keV primarily) has been that it is never necessary to manually subdivide even the substrate. The choice of which basis to use to represent a brick is made using the concept of singular-value decomposition.<sup>11</sup> If using the full basis set leads to singular values in the solution for the coefficients, the polynomial basis is used.

The most vexing detail of the algorithm used by SimulateRBS was how to deal with the situation that arises if the target is thicker than the range of the projectile, or at least thick enough that some backscattered particles are not energetic enough to emerge from the target. A related issue is how to truncate bricks at the low end of the energy spectrum. This is solved by creating two callable functions in real time. The first gives the energy of the incident particle as a function of depth in the target. The second gives the energy that a backscattered particle must have in order to emerge from a specified depth with a given energy, the minimum energy in the spectrum, taken by default to be 10 keV. These functions make it possible to analyze each brick individually and to truncate it as necessary so that the minimum energy is the preset value. As a result, no special consideration must be given to the thickness of the substrate, although it is desirable from the standpoint of efficiency not to make it unnecessarily thick.

Evaluation of a backscattering spectrum at a specific energy is carried out by rules associated with the term ScatteringSpectrum. These rules assemble the functions describing the individual bricks, evaluate, and sum them. At this stage, the effects of straggling and instrumental resolution are also included. Straggling is intrinsic and is computed by SimulateRBS and included in the ScatteringSpectrum object. Instrumental resolution, which is usually a function of energy for medium energy backscattering spectra, is incorporated when a spectrum is evaluated. Thus, one can explore the effects of various detection strategies (time-of-flight, surface-barrier detectors, etc.) without the time-consuming process of recomputing the intrinsic spectrum itself.

Straggling is handled by convolution assuming that the kernel is a Gaussian with an energy-dependent width. It is assumed that the variance increases linearly from the high-energy to low-energy side of the brick. This energy dependence of the convolution kernel was the most significant mathematical problem encountered in this work. After examining very many approaches to this problem, using built-in *Mathematica* functions, various analytic expansions, and numerical approximations, we concluded that simple Gaussian quadrature used in conjunction with a

range-reduction strategy offered the best compromise between generality and efficiency. By dynamically adjusting the integration range for each brick as each point is evaluated, it has been possible to use a fixed-order Gaussian quadrature (order 42) to achieve numerical accuracy exceeding the physical accuracy of the model in a more-or-less definitive way. Surprisingly, this simple procedure is faster than an earlier implementation that used a simple but robust recursive, adaptive quadrature.

The representation of a spectrum by a function instead of by an array of numbers makes it possible to implement functional operators. A functional operator is a mathematical operator that operates on functions to produce other functions. We have, thus far, implemented four such operators, for addition of spectra, multiplication of spectra by a numerical constant, extraction from spectra of individual contributions by location in the target, by element (Fig. 1), or by isotope, and a functional operator which mimics the effects of channeling in the substrate of a target. The first two of these operations occur in response to the use of the ordinary numerical operators for addition and multiplication when the operations involve ScatteringSpectrum objects. Functional operators called ExtractLayer and ExtractElement operate on ScatteringSpectrum objects to produce new ScatteringSpectrum objects that meet the specified criteria. Channeling is approximated by a functional operator called ChannelSubstrate (Fig. 2).

The ordinary arithmetic operators can be used to implement effects that are not easily simulated in an environment that is inherently structured on the concept of uniform layers. For example, in ref. (12) these operators are used to simulate the effect of a non-uniform carbon layer by constructing a Gaussian convolution involving fifty

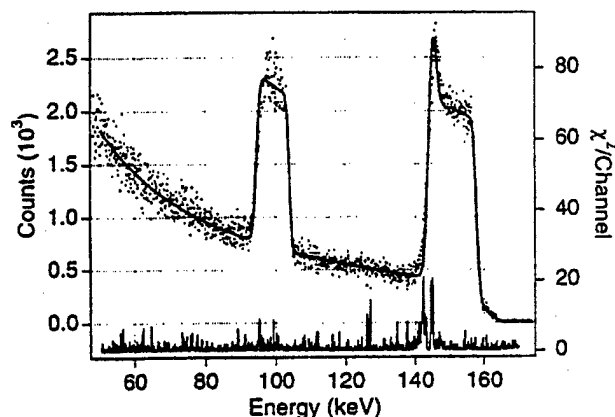


Figure 2. A non-linear least squares fit (solid line) to 270 keV  $\text{He}^+$  backscattering data (dots) for an  $\text{SiO}_2$  thin film on Si using the function ChannelSubstrate to approximate the effects of channeling in the  $\langle 110 \rangle$  direction. The film was found to be 9.7 nm thick and to have a surface peak about 50% larger than the theoretical expectation. The channeling  $\chi_{\text{min}}$  was 9%. The overall  $\chi^2$  for the fit was about 1.3 per degree of freedom. The curve at the bottom of the figure shows the  $\chi^2$  per channel and indicates that the model fits least well in the vicinity of the Si surface peak.

properly weighted individual simulated spectra in which the carbon layer takes on various thicknesses.

Simulating channeled spectra using correct physics is very complex because it involves both a detailed knowledge of the target crystallinity and the use of more advanced potentials.<sup>13</sup> Nevertheless, it is commonplace in the analysis of backscattering data to encounter spectra in which channeling has occurred. Frequently, the channeling is intentional in order to reduce the substrate background beneath spectral features of interest. The backscattering yield from a crystalline target is often described with respect to the yield of a random target of the same substance through a quantity called  $\chi$  which is the ratio of counts in the channeled spectrum to the number in the random spectrum at the same energy.<sup>13</sup> For well-channeled ions the minimum  $\chi$  called  $\chi_{\min}$  is often no larger than 5%.

The functional operator ChannelSubstrate approximates the effects of channeling using three user-supplied  $\chi$  values corresponding to the counts ratio at the left, center and right edges of the bricks representing the substrate constituents. The resulting ScatteringSpectrum is an approximation to the actually observed spectrum that agrees at three points. Because the substrate contribution is ordinarily quite smoothly varying, the overall approximation is quite good. The  $\chi$  parameters can, of course, be taken to be variables in a fitting operation using SpectrumFit and in this way replace *ad hoc* background subtraction for fits such as SiO<sub>2</sub> on Si. In a case such as this, the physical substrate is best described as two layers one, typically of zero thickness and areal density chosen by theoretical considerations,<sup>13</sup> and the true bulk described in the usual way. By doing this, the simulation accurately captures the surface peak that is observed experimentally (Fig. 2).

The function SpectrumFit is included in the tool kit primarily for experimental prototyping. It uses Marquardt's method<sup>14</sup> with numerical differentiation to perform non-linear, least-squares fits. Any parameter that is adjustable in the simulation or evaluation of a spectrum can, in principle, be fit using this routine. Thus, one may find best-fit values to layer widths, densities, or compositions, or to detector resolution, channeling  $\chi$  values, etc. Note, however, that as of this writing, such fits can be slow, and may not practical for repetitive use when dedicated tools such as RUMP offer the same functionality.

## CONCLUSION

A set of general-purpose computational tools for the simulation and analysis of medium energy backscattering spectra has been implemented in *Mathematica*. Implementations of published algorithms are included for stopping power,<sup>7,8</sup> straggling,<sup>9</sup> cross sections,<sup>10</sup> multiple scattering,<sup>15</sup> and sputtering yield,<sup>16</sup> as well as a comprehensive database of properties of elements.<sup>5,17</sup> The complete tool set is available on-line<sup>18</sup> and is accompanied by a descriptive document<sup>19</sup> which gives examples of the use of each tool.

## ACKNOWLEDGMENTS

Thanks to Kyle McDonald for the data in Fig. 2 and to Kyle McDonald and Martha R. Weller for critical comments on this manuscript. Portions of this work were supported by the U. S. Army Research Office under contract number DAAH-04-95-1-0565.

## REFERENCES

1. Doolittle, L. R., *Nucl. Instr. and Meth.* **B9**, 344-251, 1985.
2. Doolittle, L. R., *Nucl. Instr. and Meth.*, **B15**, 227-231, 1986.
3. See Leavitt, J. A., McIntyre, L. C., and Weller, M. R., *Handbook of Modern Ion Beam Analysis*, Pittsburgh: Materials Research Society, 1995, ch. 4, pp. 37-81, and references therein, for a comprehensive compilation of backscattering simulation programs.
4. Wolfram, S., *The Mathematica Book*, 3<sup>rd</sup> ed, Cambridge: Cambridge University Press, 1996. *Mathematica*®, the programming environment for technical computing, is a product of Wolfram Research, Inc. <http://www.wri.com>.
5. Weller, R. A., *Handbook of Modern Ion Beam Analysis*, Pittsburgh: Materials Research Society, 1995, Appendix 4, pp. 411-416.
6. Audi, G. and Wapstra, A.H., *Nuclear Physics*, **A595**, 409-480, 1995. Data obtained from "The 1995 update to the atomic mass evaluation," National Nuclear Data Center, Brookhaven National Laboratory, [http://www.nndc.bnl.gov/nndcscr/masses/RCT1\\_RMD.MAS95](http://www.nndc.bnl.gov/nndcscr/masses/RCT1_RMD.MAS95).
7. Chu, W.-K., Mayer, J. W., and Nicolet, M.-A., *Backscattering Spectrometry*, New York: Academic Press, 1978, ch. 4, pp. 89-122.
8. Ziegler, J. F., Biersack, J. P. and Littmark, U., *The Stopping and Ranges of Ions in Matter*, New York: Pergamon, 1985, pp. 218-222.
9. Rauhalä, E., *Handbook of Modern Ion Beam Analysis*, Pittsburgh: Materials Research Society, 1995, ch. 2, pp. 3-19 and pp. 385-410.
10. Yang, Q., O'Connor, D. J., and Wang, Z., *Nucl. Instr. and Meth.* **B61**, 149-155, 1991.
11. Mendenhall, M. H., and Weller, R. A., *Nucl. Instr. and Meth.* **B58**, 11-17, 1991.
12. Press, W. H., Teukolsky, S. A., Vetterling, W. T., and Flannery, B. P., *Numerical Recipes in C*, Cambridge: Cambridge University Press, 1992, ch. 2, pp. 59-65.
13. McDonald, K. and Weller, R. A., *Nucl. Instr. and Meth. B*, submitted, 1998.
14. Feldman, L. C., Mayer, J. W., and Picraux, S. T., *Materials Analysis by Ion Channeling*, New York: Academic Press, 1982, pp. 20-26, and pp. 160-166.
15. Press, W. H., Teukolsky, S. A., Vetterling, W. T., and Flannery, B. P., *Numerical Recipes in C*, Cambridge: Cambridge University Press, 1992, ch. 15, pp. 681-688.
16. Mendenhall, M. H., and Weller, R. A., *Nucl. Instr. and Meth.* **B93**, 5-10, 1994.
17. Yamamura, Y., and Tawara, H., *Atomic Data and Nuclear Data Tables* **62**, 149-253, 1996.
18. Emsley, J., *The Elements*, New York: Oxford University Press, 1989.
19. <http://particlesolid.vuse.vanderbilt.edu>
20. Weller, R. A., *Particle-Solid Tools*, <http://particlesolid.vuse.vanderbilt.edu>



ELSEVIER

Nuclear Instruments and Methods in Physics Research B 152 (1999) 171–181

---

---

**NIM B**  
Beam Interactions  
with Materials & Atoms

---

---

## Quantitative evaluation of the determinants of resolution in time-of-flight spectrometers for medium energy ion beam analysis

Kyle McDonald <sup>a</sup>, Robert A. Weller <sup>a,\*</sup>, V.Kh. Liechtenstein <sup>b</sup>

<sup>a</sup> *Vanderbilt University, Nashville TN 37235, USA*

<sup>b</sup> *RRC "Kurchatov Institute", 123182 Moscow, Russian Federation*

Received 1 September 1998; received in revised form 8 December 1998

---

### Abstract

The determinants of resolution of a time-of-flight spectrometer for medium energy ion beam analysis have been identified and analyzed. The primary determinants are uncertainty of ion path length, kinematic dispersion from the finite detector solid angle, straggling in the start foil and variability of the start foil thickness. The first three of these have been considered in previous studies of time-of-flight spectrometer resolution, but foil non-uniformity has not been examined in detail. Using backscattering analysis and atomic force microscopy, we have measured the thickness and roughness of carbon start foils and found them to be larger than suggested by their nominal specifications. As a result, energy uncertainty introduced by foil non-uniformity has been found to be a critical factor in determining resolution. Using measured values of foil parameters and known geometric characteristics of our spectrometer, Monte Carlo simulations of backscattering spectra of SiO<sub>2</sub> thin films on Si substrates have been computed and found to reproduce well the experimentally observed system resolution of 1350 eV for 104 keV He. Additional simulations show that spectrometer design changes could reduce this value to about 1 keV at which point it is, for all practical purposes, optimum. © 1999 Elsevier Science B.V. All rights reserved.

PACS: 07.81.+a; 68.55.-a; 68.35.Bs; 61.18.Bn

Keywords: Time-of-flight spectrometer; Resolution; Thin films; Carbon foils; Roughness; Backscattering spectrometry

---

### 1. Introduction

Backscattering spectrometry is a mature technique widely used for the quantitative analysis of thin films and interfaces. In conventional backscattering analysis a silicon surface barrier detector

is used for energy spectrometry. Although surface barrier detectors are extremely well suited to this application, their resolution typically exceeds 10 keV so that beam energies in the MeV range are required to achieve adequate differentiation of important spectral features. Surface barrier detectors also degrade quickly when used to detect heavy ions. As a result, surface barrier detectors are not well suited to experiments involving heavy ions or reduced ion-beam energies, which

---

\* Corresponding author. Tel.: 615-343-6027; fax: 615-343-6614; e-mail: robert.a.weller@vanderbilt.edu

fundamental considerations of the collision cross section suggest would lead to superior surface analytical results.

A number of considerations, including similar stopping power, larger scattering cross section, and less radiation damage, point to the 100–300 keV energy range as especially useful for ion beam analysis, particularly of ultra-thin films. However, alternatives to surface barrier detectors must be implemented for particle spectrometry. Most commonly, electrostatic and time-of-flight spectrometers have been used. Medium energy ion scattering using a toroidal electrostatic spectrometer has been shown to provide exceptional resolution,  $\Delta E/E \sim 10^{-3}$ , corresponding to a depth resolution  $< 1$  nm [1,2]. As a result, this technique has been singularly effective for analyzing ultra thin films ( $\sim 1$ –10 nm) [3–5]. However, an electrostatic analyzer is sensitive to the charge state of the backscattered particle and only limited energy ranges can be measured at one time.

Time-of-flight spectrometry is an attractive alternative to electrostatic spectrometry for a number of reasons. Originally developed for use in nuclear physics to measure heavy ion reactions, its first application in materials analysis was for heavy-ion backscattering [6–9]. Time-of-flight spectrometers are insensitive to the charge state of the backscattered particle and can measure all energies simultaneously, characteristics which closely parallel those of surface barrier detectors. Moreover, time-of-flight spectrometers can be optimized for specific applications such as heavy

ion backscattering, where they deliver high sensitivity, mass and depth resolution [10].

The first application of time-of-flight spectrometry to surface analysis by medium energy backscattering is now almost a decade old [11,12]. The original spectrometer designs proposed by Mendenhall and Weller stressed simplicity and were intended to yield medium energy backscattering spectra with information content similar to that which is obtainable with a surface barrier detector at conventional energies. However, it has become apparent that with a properly designed system the ultimate resolution of the technique can be very high, and that the information obtained, especially about films  $< 10$  nm in thickness, cannot be duplicated by conventional MeV backscattering. It is thus natural to ask what factors control the resolution of a time-of-flight spectrometer and in what relative measure, so that a system can be optimized for the best possible performance in the depth profiling of ultra-thin films.

## 2. Background

The time-of-flight spectrometer system is shown in Fig. 1. A signal is produced by the impact on the start detector of secondary electrons created by the passage of a backscattered particle through the carbon start foil. A second signal is produced by the particle's subsequent impact on the stop detector. The time difference between the two signals is measured to produce a time spectrum that is

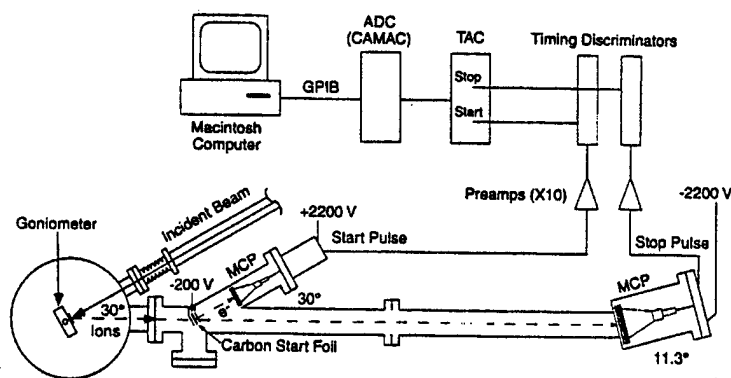


Fig. 1. Schematic of the time-of-flight spectrometer system. The drift length is 112 cm, and the angles of the start foil and stop microchannel plate (MCP) to the spectrometer axis are  $30^\circ$  and  $11.3^\circ$ , respectively.

then mathematically converted to an energy spectrum for analysis.

The primary determinants of the resolution for a time-of-flight spectrometer are straggling in the start foil, start foil thickness variability, ion path length uncertainty, and kinematic dispersion from the finite spectrometer acceptance angle. Charge exchange in the start foil (which is biased at about  $-200$  V with respect to ground), the intrinsic secondary electron energy spectrum, the instrumental timing uncertainty, beam energy stability, straggling in the target, multiple scattering in the start foil, target bias, and other processes affect the measured resolution to a lesser extent. By optimizing the spectrometer design, the effects of these processes can be substantially reduced, and the spectrometer's resolution can approach fundamental physical limits.

Because the backscattered ion beam approximates a point source originating from the target, there is a distribution of scattering angles for particles entering the spectrometer. This angular spread leads to a distribution of flight paths between the start foil and stop detector and a distribution of velocities associated with the kinematic factor. By adjusting the angle between the start foil and the stop detector, the effects of path length differences and kinematic dispersion can be reduced [13]. In the current spectrometer configuration (Fig. 1), the scattering angle is  $150^\circ$ , the start foil is oriented  $30^\circ$  to the spectrometer axis, and the stop detector angle is  $11.3^\circ$ . The stop detector angle was calculated to minimize the path length difference and kinematic dispersion for helium scattering from silicon at  $150^\circ$  with a start foil angle of  $30^\circ$ . Slight flight time differences ( $\leq 1$  ns) still exist for other target species because of kinematic dispersion. Because the effects of path length difference and kinematic dispersion are so closely correlated, henceforth in this paper they will be combined as a single effect, path length differences.

Because of the random nature of the deposition of the carbon foils, large errors ( $\sim 25\%$ ) in the thickness are common [14,15]. Also, even though pure graphite is used to manufacture the foils, oxygen, hydrogen, and other impurities are easily adsorbed from the deposition process and the release agent [16–18]. Furthermore, because the re-

lease agent is itself an evaporated thin film its surface morphology will strongly influence that of the carbon foil. As a result of these inherent characteristics, the foils are expected to be thicker and less uniform than their nominal values. If the foil were uniform and only thicker than nominal, the expected energy loss and straggling in the foil would increase. The resolution would be adversely affected due to the increase in straggling, but the extra width would simply add in quadrature to the nominal resolution. If the foil is non-uniform, however, the variation in thickness leads to a trajectory-dependent variation in the energy loss, straggling, and multiple scattering that broadens spectral features in a manner dependent on the thickness distribution. If the magnitude of the non-uniformity and its effect on resolution are small, these questions could probably be ignored and small corrections to calculations with the nominal thickness could be used. We have discovered, however, that not only can foil non-uniformity not be ignored, but that it is a very large determinant of resolution.

In early work, we used a carbon start foil with a quoted areal density of  $1.7 \pm 5\% \mu\text{g}/\text{cm}^2$ . The measured resolution using this foil was  $2.7$  keV for  $104$  keV helium ions. Monte Carlo simulations, however, predicted a resolution of  $1.1$  keV, and so a large constituent of the resolution was unexplained. Published analyses of spectrometer resolution associated all unexplained extra width with path length uncertainty [8,19]. However, backscattering analysis of the foil showed that the thickness was  $2.6 \mu\text{g}/\text{cm}^2$  and highly non-uniform. Atomic force microscopy (see Fig. 2(a)) confirmed this result by showing that the foils, measured to be  $13$  nm thick, had a root-mean-square (rms) roughness of  $10$  nm [20]. These observations suggested strongly that the carbon foil morphology was influencing spectrometer resolution more strongly than had previously been appreciated.

This paper presents the results of a program to identify and quantify all the significant elements of resolution for the tilted-start-foil spectrometer design first proposed in Ref. [11] (Fig. 1). The spectrometer resolution was determined by backscattering analysis of high-quality  $\text{SiO}_2$  thin films on Si. We introduce a method to parameterize

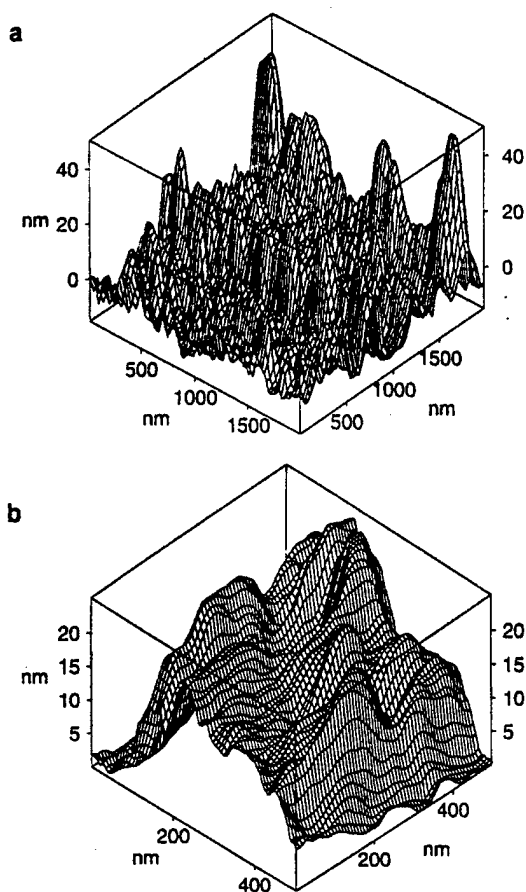


Fig. 2. (a) Atomic force microscope image of a C foil measured to be  $2.6 \mu\text{g}/\text{cm}^2$  ( $13 \text{ nm}$ ) thick exhibiting an rms roughness of  $10 \text{ nm}$ . (b) Atomic force microscope image of a diamond-like carbon foil measured to be  $1.2 \mu\text{g}/\text{cm}^2$  ( $6 \text{ nm}$ ) thick with an rms roughness of  $6 \text{ nm}$ .

the foil non-uniformity that is distinct from simple rms surface roughness and measure the relevant parameters experimentally. These parameters are then combined with known geometrical factors to produce Monte Carlo simulations of the  $\text{SiO}_2$  backscattering spectra that are in excellent agreement with experimental observations. By extending these simulations to other geometries, we suggest the optimum spectrometer configuration and predict its resolution for both real and ideal start foils.

### 3. Procedure

In order to minimize the contribution of straggling to resolution and to reduce the effects of

multiple scattering in the start foil, diamond-like carbon foils with a nominal diameter of  $1.27 \text{ cm}$  and thickness of  $0.6 \mu\text{g}/\text{cm}^2$  were produced and mounted on gridded apertures [21,22]. These are approximately as thin as it is possible to make a self-supporting foil even over a gridded opening. The foils are deposited by sputtering pure graphite in a low-density krypton plasma and are considered hydrogen free [23]. Atomic force microscopy was used to evaluate surface morphology of the foil and measure the rms roughness.

To measure the energy resolution of the spectrometer, ion backscattering spectra were taken of a set of high-quality  $\text{SiO}_2/\text{Si}$  samples with oxide thicknesses from  $2$  to  $12 \text{ nm}$ . The samples were analyzed using a  $270 \text{ keV}$  He beam with a scattering angle of  $150^\circ$ . The beam currents were  $30$ – $100 \text{ nA}$  with a total dose of  $10^{15}$  He ions, and the beam spot size was  $5 \text{ mm}^2$ . The samples were tilted  $45^\circ$  to the incident ion beam ( $75^\circ$  to the spectrometer) with an exit angle of  $15^\circ$  to the sample plane. This angle was used to orient the silicon substrate in the  $\langle 110 \rangle$  channeling direction to reduce the silicon background in the region of the spectrum containing the oxygen peak. This orientation also has a depth resolution  $\approx 3$  times greater than normal incidence. To determine if there is an energy that optimizes the depth resolution for backscattering from oxygen at  $45^\circ$ , additional spectra were taken at beam energies from  $150$  to  $270 \text{ keV}$  in  $15 \text{ keV}$  increments.

The oxygen peaks were fit with the following semi-empirical function

$$f(E) = c_0 + c_1 E + H \left[ \frac{m}{\sqrt{2\pi}} \left( \sigma_2 \text{Exp} \left( \frac{-(E - E_2)^2}{2\sigma_2^2} \right) - \sigma_1 \text{Exp} \left( \frac{-(E - E_1)^2}{2\sigma_1^2} \right) \right) \right] + H \left[ \frac{1}{2} \left( 1 + m \left( E - \left( \frac{E_1 + E_2}{2} \right) \right) \right) \right] \times \left( \text{Erf} \left( \frac{E - E_2}{\sqrt{2}\sigma_2} \right) - \text{Erf} \left( \frac{E - E_1}{\sqrt{2}\sigma_1} \right) \right) \quad (1)$$

which is derived from the convolution of a negatively sloped line segment extending from  $E_2$  to  $E_1$ ,

representing the oxygen peak, and a Gaussian weight function of constant width, which represents straggling and the system resolution. Since the system resolution and straggling are actually functions of energy and not constant, a correction is made to the convolution by having different widths for the front and back edges. This function is superimposed on a linear background from the silicon in the spectrum.  $E_1$  and  $E_2$  are the energies of the front (surface) and back (buried interface) edges of the peak, respectively, and  $\sigma_1$  and  $\sigma_2$  are the front and back edge widths expressed as standard deviations.  $H$  is the height of the center of the peak,  $m$  the slope parameter of the top of the peak determined by the scattering cross section, and  $c_0$  and  $c_1$  are the intercept and slope of the linear background. The adjustable parameters of the equation are  $E_1$ ,  $E_2$ ,  $\sigma_1$ ,  $\sigma_2$ ,  $H$ ,  $c_0$ , and  $c_1$ . The slope parameter,  $m$ , was determined from spectrum simulations and held constant during the fit. Resolution as used in this paper is defined as the full width at half maximum of an isolated Gaussian peak, or equivalently, the width of the edge of an error function from 12% to 88% of the edge height. This value is 2.35 times the corresponding standard deviation. The resolution of the spectrometer was assumed to be equal to the front edge width of the oxygen peak.

Backscattering analysis was also used to determine the diamond-like carbon foil thickness and non-uniformity. Spectra were taken of a bare tantalum sample and of a diamond-like carbon foil nominally  $0.8 \mu\text{g}/\text{cm}^2$  thick mounted on a nickel mesh placed in front of the tantalum sample. The displacement of the tantalum edge and the increase of its width are measures of the carbon foil thickness and uniformity, respectively.

Monte Carlo simulations of the backscattering spectra were computed in order to assist in the interpretation of experimental data. Processes included in the calculations were (1) finite beam size, (2) angles of the target, foil, and stop detector with respect to beam, (3) ion scattering angle, scatter depth, and solid angle weighted by the scattering cross section, (4) start foil uniformity, (5) energy loss and straggling in target and start foil, and (6) multiple scattering in the start foil. Random scattering depth and scattering angle were determined

from distributions derived from the Lenz–Jensen cross section. Multiple scattering was determined from distributions computed using the methods in Ref. [24]. For each simulated spectrum,  $10^5$  trajectories were computed. Charge exchange in the foil, intrinsic instrumental timing resolution, and secondary electron timing uncertainties were not included in the calculations since they are small, independent effects.

#### 4. Results and discussion

Fig. 2(b) shows an atomic force microscope image of the surface of a  $0.6 \mu\text{g}/\text{cm}^2$  diamond-like carbon foil. Clearly, with a rms roughness of 6 nm the diamond-like carbon is smoother than the conventional foil shown in Fig. 2(a) whose rms roughness is 10 nm. However, it still is substantially rough when viewed in comparison with its nominal thickness, which is of order 3 nm.

Fig. 3(a) shows a typical backscattering spectrum of an  $\text{SiO}_2$  film with nominal thickness of 10 nm on a Si substrate. The original time-of-flight spectrum has been mathematically rendered as an energy spectrum. The beam is incident along the  $\langle 110 \rangle$  channeling direction in order to minimize background in the region of the oxygen peak and to enhance depth resolution. Fig. 3(b) shows an expanded view of the oxygen peak along with a non-linear least squares fit to the data using the function given in Eq. (1). The system resolution is taken to be the width of the leading edge at approximately 104 keV. The resolution, obtained as an average over an ensemble of backscattering spectra like those of Fig. 3, is  $1350 \pm 40$  eV for 104 keV helium particles. This corresponds to a depth resolution of 1.3 nm for oxygen in  $\text{SiO}_2$  at a beam incident at  $45^\circ$  with respect to the surface normal and 0.5 nm at a  $55^\circ$  incident angle, or an improvement of approximately a factor of 2 when compared with the results obtained with the foil in Fig. 2(a).

The energy dependence of the spectrometer resolution is shown in Fig. 4(a). It is well characterized by a linear relationship  $(728 \pm 44 \text{ eV}) + ((6.4 \pm 0.4) \times 10^{-3}) E$ , where  $E$  is the energy of the particle entering the spectrometer in eV. The

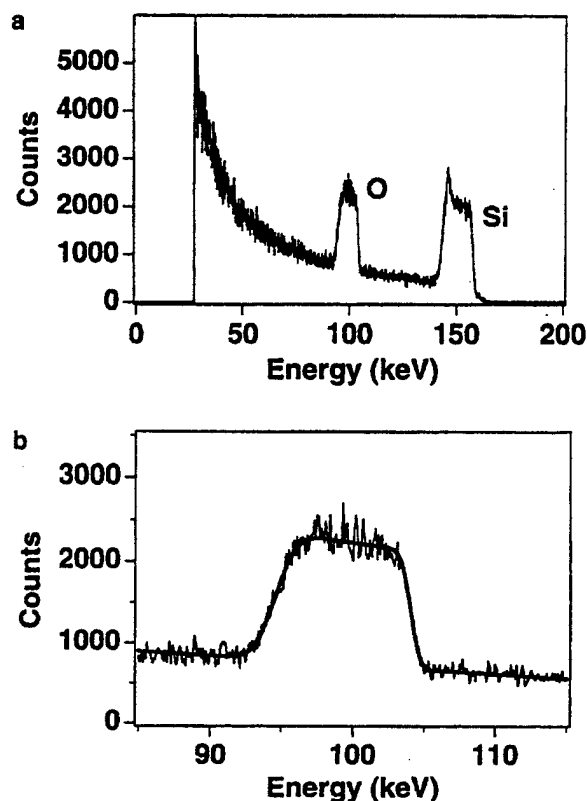


Fig. 3. (a) Backscattering spectrum of 10 nm SiO<sub>2</sub>/Si at 45° using a 270 keV He<sup>+</sup> beam. (b) Close-up of the O peak in the spectrum of (a). The bold line is a fit to the peak using Eq. (1).

backscattering depth resolution for oxygen corresponding to this energy resolution is shown in Fig. 4(b). The abscissa is the incident beam energy. Theoretically, there should be a minimum in the curve in Fig. 4(b) at an incident energy of 260 keV for helium scattering from oxygen at 45°, assuming the above linear relationship. However, our range of initial energies was not adequate to reveal this minimum, although a general decrease up to our maximum of 270 keV is apparent.

Fig. 5 shows the tantalum edge from backscattering spectra of the tantalum specimen with and without the 0.8 μg/cm<sup>2</sup> carbon foil placed in front of it. Notice that the carbon foil both shifts and widens the edge. The shift is due to energy loss as He ions pass through the carbon foil before and after scattering. The widening is due to a combination of straggling in the foil and non-uniformity in the foil thickness (or density). We have observed

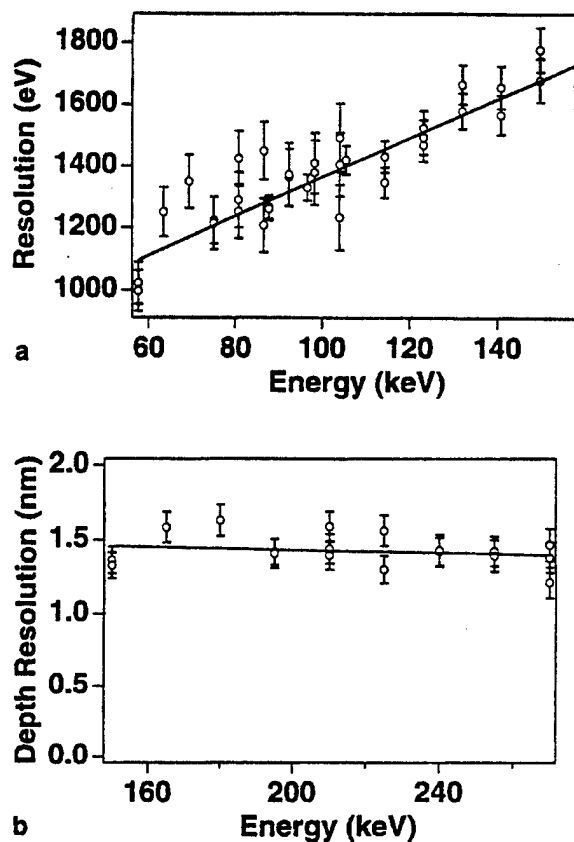


Fig. 4. (a) Measured energy resolution versus particle kinetic energy for He<sup>+</sup> backscattering from SiO<sub>2</sub> at beam energies from 150 to 270 keV. The slope of the line is 728 eV + 0.006 \*  $E$ , where  $E$  is the energy of the particle entering the spectrometer in eV. (b) The equivalent depth resolution for O in SiO<sub>2</sub> at 45° versus incident particle energy.

empirically that the widening of the tantalum edge in this figure is well described by the convolution of the bare tantalum edge with a Gaussian weight function. The required width of the Gaussian function may, therefore, be used to parameterize the non-uniformity. The procedure used is as follows.

It is assumed that the spectrum with carbon in place can be obtained from the bare tantalum spectrum by three operations, a simple translation in energy, a scaling of the overall normalization, and a convolution characterized by a width. Eq. (2) shows conceptually how a model function containing three parameters, the energy shift of the tantalum edge ( $\delta E$ ), the normalization ( $A$ ), and the



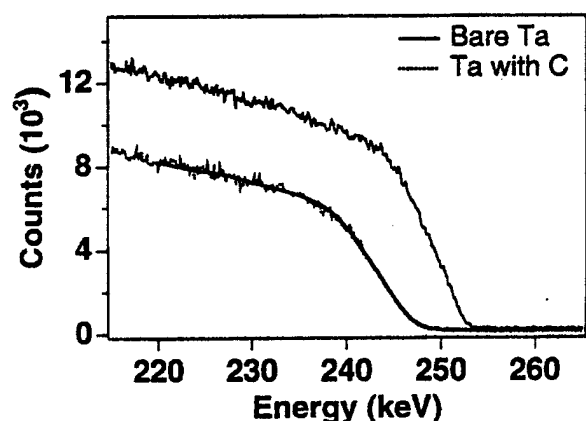


Fig. 5. Ta edge in the backscattering spectra of bare Ta and Ta with a  $1.6 \mu\text{g}/\text{cm}^2$  diamond-like carbon foil placed in front. The bold line is the fit to the Ta edge with the foil in front using the bare Ta edge as a basis.

width of the Gaussian function ( $\sigma$ ), was constructed.

$$S_{\text{Ta+C}}(E) = A \int_{-\infty}^{\infty} S_{\text{Ta}}(\varepsilon) W(\sigma; E + \delta E - \varepsilon) d\varepsilon, \quad (2)$$

where  $S_{\text{Ta+C}}(E)$  is the tantalum spectrum with the carbon in place,  $S_{\text{Ta}}(E)$  is the bare tantalum spectrum, and

$$W(\sigma; E) = \frac{1}{\sqrt{2\pi\sigma^2}} \text{Exp} \left[ \frac{-E^2}{2\sigma^2} \right] \quad (3)$$

is the Gaussian weight function with  $\sigma$  as its rms. In practice, the convolution (Eq. (2)) is performed by using fast Fourier transforms of the bare tantalum spectrum and Gaussian function followed by shifting and scaling.

This model function was used in a fully non-linear fitting procedure [25] in order to obtain the best values of the three parameters and a covariance matrix. The advantage of this method is that the contribution to the edge width attributable to the tantalum surface roughness and instrumental resolution are separated from the edge width which is added by the foil without the need for extra parameters. In addition, error estimates for all the parameters are immediately available from the covariance matrix.

The nominal thickness of the foil was determined from the energy shift of the tantalum edge

using stopping power calculations. Although the exact amount of hydrogen, oxygen, and other contaminants adsorbed on the carbon is unknown, it should only be a few atomic percent [16–18]. Therefore, the foil was assumed to be pure carbon for energy loss and straggling calculations, and with this assumption, an areal density of  $1.6 \mu\text{g}/\text{cm}^2$  was obtained.

In order to associate the effective foil thickness distribution with the observed increase in tantalum edge width, it was necessary to compute simulated backscattering spectra for targets with a non-uniform layer. This was accomplished by computing the convolution of a simulated tantalum spectrum covered with various thicknesses of carbon layers using Gaussian quadrature to manually evaluate the convolution integral [26]. Two foil thickness distributions were considered, a Gaussian (see Eq. (3)) terminated at  $\pm 3\sigma$  because the foil had finite thickness, and a finite step function given by Eq. (4),

$$W(\sigma; x) = \frac{1}{2\sqrt{3}\sigma}, \quad |x| \leq \sqrt{3}\sigma, \quad (4)$$

$$W(\sigma; x) = 0, \quad |x| > \sqrt{3}\sigma,$$

where  $\sigma$  is the rms of the step distribution. Fifty terms were used in the quadrature sum, and the result was a simulated spectrum with the thickness and fractional rms roughness of the carbon foil as parameters. Spectra were simulated for a  $1.6 \mu\text{g}/\text{cm}^2$  carbon foil, with fractional roughness values from 0 to 0.3 for the Gaussian and 0 to 0.55 for the step function.

Using the same procedure as was used to reduce the experimental data, the tantalum edges in these simulated spectra were fit to obtain the additional edge width and edge displacement produced by carbon coverage. The results of these calculations are shown in Fig. 6 as points, with the interpolating functions shown as smooth curves. Note that the difference between the extra edge widths generated by the two distributions is small. This implies that the critical parameter affecting the resolution is the rms roughness, not the detailed shape of the distribution.

Using Fig. 6, the additional edge width from the experimental data was then converted to an

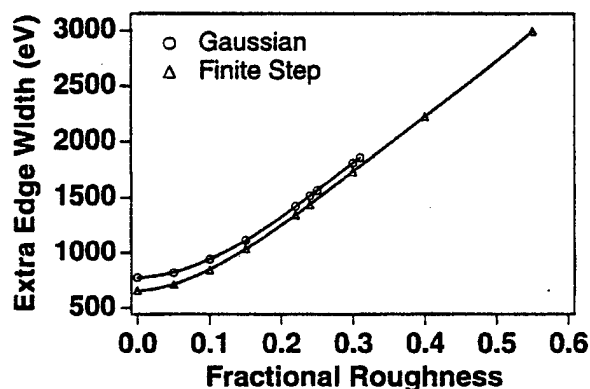


Fig. 6. Incremental edge width versus foil roughness as determined by the fitting of simulated spectra of C covered Ta using a simulated spectrum of bare Ta in conjunction with the Gaussian and finite step convolution models discussed in the text. The points are the extra edge widths determined by the fits and the solid lines are the interpolation functions.

equivalent foil roughness. The extra edge width added to the tantalum by the  $1.6 \mu\text{g}/\text{cm}^2$  foil used in the experiment (Fig. 5) was 1530 eV, which corresponds to a fractional non-uniformity of foil thickness of 0.24 for the Gaussian distribution and 0.26 for the finite step distribution. We assume the fractional non-uniformity is approximately constant in this thickness range and so also attribute the same fractional non-uniformity to foils used in the spectrometer. It is important to note, however, that the roughness being measured here is not the same as that measured by atomic force microscopy. Correlations in roughness on the two sides of the foil as well as possible micro-voids, density fluctuations, and the total size of the measured region must be considered.

Note by way of comparison that the rms roughness obtained by atomic force microscopy on one side of these foils was 6 nm (Fig. 2(a)). For a  $1.2 \mu\text{g}/\text{cm}^2$  foil (the value obtained by scaling the nominal  $0.6 \mu\text{g}/\text{cm}^2$  by the same factor as was observed for the  $0.8 \mu\text{g}/\text{cm}^2$  specimen), the 0.24 non-uniformity corresponds to a rms length of about 1.4 nm. The discrepancy between this value and the atomic force microscopy result indicates strong correlation between the topography on the two sides of the foil, probably as a result of the

morphology of the underlying surface or release agent.

Monte Carlo simulations of the spectrometer were performed using the foil parameters determined by the procedure described above. The target was assumed to be 10 nm of  $\text{SiO}_2$ , and the incident He energies ranged from 150 to 270 keV. We assumed that the foil thickness scaling determined from the  $0.8 \mu\text{g}/\text{cm}^2$  foil also applies to the  $0.6 \mu\text{g}/\text{cm}^2$  foil mounted in the spectrometer. We also used a Gaussian foil thickness distribution (the same results are achieved with a step distribution) and so assumed a carbon start foil with a thickness of  $1.2 \pm 24\% \mu\text{g}/\text{cm}^2$ . The simulated spectra were fit in exactly the same way as the experimental data (Eq. (1)) and the resolution was identified with the leading edge of the peaks. The energy dependence of the resolution obtained from these simulations is shown in Fig. 7. The simulation omits intrinsic timing, secondary electron timing, and charge exchange in the foil. These terms are estimated to add  $\approx 250$  eV to the resolution, in quadrature. For an energy of 104 keV, the simulation yields a resolution of  $1350 \pm 30$  eV, which becomes  $1370 \pm 30$  eV when the instrumental effects are added. This value compares favorably with the experimentally measured resolution of  $1350 \pm 40$  eV. The agreement between the simulated and experimental resolutions is, in fact, excellent for all energies.

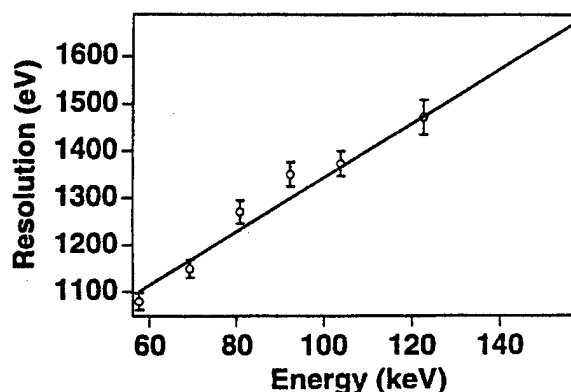


Fig. 7. Energy resolution versus particle kinetic energy for Monte Carlo simulations of  $\text{He}^+$  backscattering from  $\text{SiO}_2$  at beam energies from 150 to 270 keV. The slope of the line is  $768 \text{ eV} + 0.006 \cdot E$ , with  $E$  in eV.

It is a common practice to model the total spectrometer resolution by the addition in quadrature of various contributions such as those from straggling, instrumental effects, path length differences, and foil uniformity [8,27]. However, because foil uniformity is coupled to variations in the total energy loss, straggling, and multiple scattering, it is clear that many of these terms are not statistically independent. To determine the magnitudes of the relative contributions of these processes to the total observed resolution we have performed additional Monte Carlo simulations of the oxygen peak assuming both rough and uniform start foils. The results of simulations for different foil configurations are shown in Table 1.

Simulation of a uniform  $1.2 \mu\text{g}/\text{cm}^2$  carbon foil yields a resolution of 1070 eV. In this case, the resolution is determined only by straggling and path length differences, which are not strongly correlated. Straggling alone for a uniform  $1.2 \mu\text{g}/\text{cm}^2$  carbon foil is  $\approx 800$  eV, and its subtraction in quadrature from the total resolution gives an estimate of  $\approx 700$  eV for the contribution from path length differences. By subtracting in quadrature the resolution obtained for a hypothetical uniform foil from that of a  $1.2 \pm 24\% \mu\text{g}/\text{cm}^2$  foil, the magnitude of the effect of foil non-uniformity is estimated to be  $\approx 800$  eV. Although these values are only estimates, the large effect foil non-uniformity has on the resolution can clearly be seen.

The resolution obtained by simulating a uniform foil, 1070 eV at 104 keV, is an estimate of the best resolution achievable for a spectrometer in the geometric configuration shown in Fig. 1. If the

$1.2 \pm 24\% \mu\text{g}/\text{cm}^2$  start foil is oriented normal to the spectrometer axis [19] and the stop detector is aligned at angle of  $5.4^\circ$ , which removes path length differences for oxygen, the simulated resolution is 1090 eV. Using the same estimation method as above, the straggling is  $\approx 800$  eV, path length differences add  $\approx 200$  eV, and foil roughness adds  $\approx 700$  eV. Simulation of a uniform foil in this spectrometer configuration yields a resolution of 800 eV. This value represents the absolute physical limit for the best achievable resolution of the spectrometer with a  $1.2 \mu\text{g}/\text{cm}^2$  start foil.

From these results, we conclude that the optimum design is to orient the start foil and detector normal to the spectrometer axis and to provide the flexibility to adjust the angle of the stop detector to minimize path length differences for the spectral feature of greatest interest. Several start foil configurations using electrostatic mirrors or magnets have been designed for heavy ions or high-energy particles that meet these criteria and appear to be the best systems for creating start pulses [19,28–30]. Extra caution should be used when using these designs for medium energy ions, however. For example, all fields should be properly terminated to eliminate stray fields and thereby reduce the deviation of the exiting ions and the corresponding path length perturbations.

## 5. Conclusions

The determinants of resolution of a time-of-flight spectrometer for medium energy backscat-

Table 1

Results of Monte Carlo simulations of backscattering from a 10 nm  $\text{SiO}_2$  film. The measured thickness and non-uniformity of the nominally  $0.6 \mu\text{g}/\text{cm}^2$  diamond-like carbon film were  $1.2 \mu\text{g}/\text{cm}^2$  and 24%. The experimentally observed resolution including all contributions was  $1350 \pm 40$  eV

Thickness ( $\mu\text{g}/\text{cm}^2$ )	Non-uniformity (%)	Start detector angle	Stop detector angle	Instrumental resolution (eV)	Resolution for oxygen (eV)
1.2	24	$30^\circ$	$11.3^\circ$	250	$1370 \pm 30$
1.2	24	$30^\circ$	$11.3^\circ$	0	$1350 \pm 30$
1.2	0	$30^\circ$	$11.3^\circ$	0	$1070 \pm 20$
1.2	24	$0^\circ$	$5.4^\circ$	0	$1090 \pm 20$
1.2	0	$0^\circ$	$5.4^\circ$	0	$800 \pm 20$

tering have been quantitatively evaluated. Of greatest importance are straggling in the start foil, start foil thickness variability, path length differences, and kinematic dispersion from the finite spectrometer acceptance angle. In our spectrometer, the resolution has been greatly improved by using a diamond-like carbon start foil, which is smoother and thinner than the conventional arc-deposited carbon foils used previously. The apparent thickness of foils nominally under  $1 \mu\text{g}/\text{cm}^2$  is approximately a factor of two greater, probably due to the nature of the deposition process or the accumulation of contaminants in handling. A resolution of  $1350 \pm 40 \text{ keV}$  is obtained for helium at an energy of  $104 \text{ keV}$ . This corresponds to a depth resolution of  $1.3 \text{ nm}$  for oxygen in  $\text{SiO}_2$  at a  $45^\circ$  sample angle and  $0.5 \text{ nm}$  at a  $55^\circ$  sample angle. Monte Carlo simulations indicate that it is possible to achieve a resolution of  $\approx 1 \text{ keV}$  by geometric refinements, at which point the thickness and uniformity of the start foil are the only degrees of freedom available for additional improvements. The correlation between the surface topography on the two sides of the foil implied by the data presented here suggests that with improved fabrication techniques, possibly involving improved surface morphology of the release agent, such improvements may be possible.

### Acknowledgements

The authors thank M. L. Green, Lucent Technologies, for providing the  $\text{SiO}_2/\text{Si}$  films and J. Hamilton and J. Taylor, Vanderbilt University, for the atomic force microscopy measurements. This work was supported by the US Army Research Office under contract DAAH 04-95-1-0565 and by a grant from Texas Instruments.

### References

- [1] R.G. Smeenk, R.M. Tromp, H.H. Kersten, A.J.H. Boerboom, F.W. Saris, Nucl. Instr. and Meth. 195 (1982) 581.
- [2] J.F. van der Veen, Surf. Sci. Rep 5 (1985) 199.
- [3] J.C. Lee, C.S. Chung, H.J. Kang, Y.P. Kim, H.K. Kim, D.W. Moon, J. Vac. Sci. Technol. A 13 (1995) 1325.
- [4] D. Hüttner, O. Meyer, J. Reiner, G. Linker, Nucl. Instr. and Meth. B 118 (1996) 578.
- [5] E.P. Gusev, H.C. Lu, T. Gustafsson, E. Garfunkel, Appl. Surf. Sci. 104/105 (1996) 329.
- [6] A. Chevarier, N. Chevarier, S. Chiodelli, Nucl. Instr. and Meth. 189 (1981) 525.
- [7] A. Chevarier, N. Chevarier, Nucl. Instr. and Meth. 218 (1983) 1.
- [8] M. Döbeli, P.C. Haubert, R.P. Livi, S.J. Spicklemire, D.L. Weathers, T.A. Tombrello, Nucl. Instr. and Meth. B 47 (1990) 148.
- [9] T.M. Stanescu, J.D. Meyer, H. Baumann, K. Bethge, Nucl. Instr. and Meth. B 50 (1990) 167.
- [10] J.A. Knapp, J.C. Banks, Nucl. Instr. and Meth. B 79 (1993) 457.
- [11] M.H. Mendenhall, R.A. Weller, Nucl. Instr. and Meth. B 40/41 (1989) 1239.
- [12] M.H. Mendenhall, R.A. Weller, Nucl. Instr. and Meth. B 47 (1990) 193.
- [13] R.A. Weller, K. McDonald, D. Pedersen, J.A. Keenan, Nucl. Instr. and Meth. B 118 (1996) 556.
- [14] M. Rubel, B. Emmoth, H. Bergsaker, M.A. Gruntman, V.K. Liechtenstein, Nucl. Instr. and Meth. B 47 (1990) 202.
- [15] G. Both, E.P. Kanter, Z. Vager, B.J. Zabransky, D. Zajfman, Rev. Sci. Instrum. 58 (1987) 424.
- [16] D. Balzer, G. Bonani, Nucl. Instr. and Meth. 167 (1979) 129.
- [17] D.L. Weathers, J.L. Duggan, R.B. Escue, F.D. McDaniel, Nucl. Instr. and Meth. A 303 (1991) 69.
- [18] A. Veeck, K.X. Jing, Q. Sui, L.G. Moretto, G.J. Wozniak, Nucl. Instr. and Meth. B 108 (1996) 159.
- [19] M. Döbeli, R.M. Ender, V. Liechtenstein, D. Vetterli, Nucl. Instr. and Meth. B 142 (1998) 417.
- [20] R. A. Weller, "Depth resolution of time-of-flight medium energy backscattering for the analysis of thin silicon oxide and oxynitride films," Fourteenth International Conference on the Application of Accelerators in Research and Industry, Denton, Texas Nov. 6-9, 1996.
- [21] T.M. Ivkova, V.K. Liechtenstein, E.D. Olshanski, Nucl. Instr. and Meth. A 362 (1995) 77.
- [22] V.Kh. Liechtenstein, T.M. Ivkova, E.D. Olshanski, I. Feigenbaum, R. DiNardo, M. Döbeli, Nucl. Instr. and Meth. A 397 (1997) 140.
- [23] J.C. Angus, C.C. Hayman, Science 241 (1988) 913.
- [24] M.H. Mendenhall, R.A. Weller, Nucl. Instr. and Meth. B 93 (1994) 5.
- [25] W.H. Press, B.P. Flannery, S.A. Teukolsky, W.T. Vetterling, Numerical Recipes in C, Cambridge U. Press, Cambridge, 1988, p. 540.
- [26] R.A. Weller, "Evaluation of medium energy backscattering spectra with Mathematica," Fifteenth International Conference on the Application of Accelerators in Research and Industry, Denton, Texas, Nov. 4-7, 1998.

- [27] J.K. Kim, Y.S. Kim, G.D. Kim, H.W. Choi, H.J. Woo, S.Y. Cho, C.N. Whang, *Nucl. Instr. and Meth. B* 140 (1998) 380.
- [28] A.M. Zebelman, W.G. Meyer, K. Halbach, A.M. Poskanzer, R.G. Sextro, G. Gabor, D.A. Landis, *Nucl. Instr. and Meth.* 141 (1977) 439.
- [29] F. Busch, W. Pfeffer, B. Kohlmeyer, D. Schüll, F. Pühlhoffer, *Nucl. Instr. and Meth.* 171 (1980) 71.
- [30] Z. Fang, D.J. O'Connor, *Rev. Sci. Instrum.* 68 (1997) 4027.

## Suppression of penetration of aluminum into 8-hydroxyquinoline aluminum via a thin oxide barrier

M. B. Huang, K. McDonald, and J. C. Keay

*Department of Physics and Astronomy, Vanderbilt University, Nashville, Tennessee 37235*

Y. Q. Wang and S. J. Rosenthal

*Department of Chemistry, Vanderbilt University, Nashville, Tennessee 37235*

R. A. Weller

*Department of Electrical and Computer Engineering and Department of Physics and Astronomy, Vanderbilt University, Nashville, Tennessee 37235*

L. C. Feldman

*Department of Physics and Astronomy, Vanderbilt University, Nashville, Tennessee 37235*

(Received 17 August 1998; accepted for publication 15 September 1998)

We report a direct observation of Al penetration into an organic film of 8-hydroxyquinoline aluminum (Alq) in a Alq/Al bilayer, a common interface occurring in many organic light-emitting diode structures. The Al penetration has a strong correlation with Alq photoluminescence quenching. We also demonstrate that the penetration and luminescence quenching can be effectively suppressed by  $\sim 20$  Å of an intervening layer of  $\text{Al}_2\text{O}_3$  at the Alq/Al interface. © 1998 American Institute of Physics. [S0003-6951(98)02346-8]

Organic light-emitting diodes (OLEDs) using 8-hydroxyquinoline aluminum (Alq) as emitters have attracted much attention since the first report of efficient electroluminescence (EL) from Alq-based heterostructures.<sup>1</sup> Recent studies showed that in addition to the work function of electrodes, the interface between the electrode and the organic layer plays an important role in determining EL efficiency of OLEDs.<sup>2-4</sup> In particular, a thin insulator film inserted at the Alq/Al interface can substantially enhance OLED performance.<sup>2-4</sup> It was suggested that the role of an insulator layer at the metal/organic interface is to remove the gap states responsible for luminescence quenching.<sup>5</sup>

In this letter, we use time-of-flight medium-energy backscattering (MEBS) to show that Al atoms can penetrate into Alq films and accumulate in the surface region. A thin  $\text{Al}_2\text{O}_3$  layer inserted at the Alq/Al interface is found to serve as a barrier to metallic Al diffusion into the Alq film. Photoluminescence (PL) measurements as a function of inserted  $\text{Al}_2\text{O}_3$  layer thickness are also reported, demonstrating the correlation of PL quenching with Al diffusion.

Metal diffusion into organic films has been recognized as one of the factors limiting OLED performance.<sup>6-10</sup> Diffusion of Ga and Ca into Alq has recently been reported.<sup>9</sup> Despite its relatively high work function, Al is widely used as a cathode material due to its high resistance to corrosion and its compatibility with Si integration technology.<sup>2</sup> However, there has been no study of Al diffusion in Alq films.

Evaporation of Al and Alq films was carried out in a vacuum chamber with a base pressure  $\sim 5 \times 10^{-6}$  Torr. An Al film of 10–60 Å in thickness was first evaporated on either graphite (for the MEBS experiment) or glass (for the PL measurement) substrates. For growth of  $\text{Al}_2\text{O}_3$  layers, we followed a layer-by-layer procedure<sup>3,4</sup> in which thick  $\text{Al}_2\text{O}_3$  layers were obtained by room-temperature oxidation of a 10-Å-thick Al film, repeatedly. Oxidation was achieved by exposing the evaporated thin Al film to air.<sup>11</sup> Finally, Alq films were deposited at a rate of 2–4 Å/s on the top of Al or  $\text{Al}_2\text{O}_3$

layers. The film thickness was determined with a quartz crystal monitor calibrated by Rutherford backscattering (RBS). MEBS experiments were performed in an ultrahigh vacuum chamber ( $\sim 10^{-8}$  Torr) with 270 keV He ion beams at normal incidence. Scattered ions were collected at  $150^\circ$  using a time-of-flight spectrometer with a resolution of  $\sim 1.8$  keV for surface Al.<sup>12</sup> PL measurements were made using excitation light of 400 nm from a Xe-arc lamp.

Figure 1 shows the MEBS spectra for the Alq/graphite and Alq/Al/graphite samples.<sup>13</sup> The spectrum for the Alq/graphite sample (open circles) shows a characteristic ion scattering energy distribution, displaying Al (leading edge at 155 keV), O (leading edge at 106 keV), N (leading edge at 90 keV), and C (leading edge at 75 keV) all from the pure Alq film, and in good agreement with the ion scattering simulation. The spectrum for the Alq/Al/graphite sample (full circles) clearly shows the appearance of an excess Al surface peak in the surface region of the Alq film, indicating Al penetration from the underlying metal layer into Alq and segregation in the near-surface region. The MEBS spectrum for the Alq/graphite sample is well described by standard simulation codes, while the MEBS spectrum of the Alq/Al/graphite sample does not agree with the calculated spectrum for the expected structure. The excess Al atoms in the surface region (155 keV) is estimated to be  $\sim 1.6 \times 10^{15}/\text{cm}^2$ , about 6.8% of the total deposited Al film (or  $\sim 2.5$  Å of Al). Correspondingly, an excess surface O peak (103 keV) also appears in the spectrum of the Alq/Al/graphite sample, indicating oxidation of the excess surface Al. The excess Al atoms in the surface region was found to be a constant for a wide range of incident He beam charges, indicating that the effects of the analyzing ion beam is not a factor giving rise to the Al diffusion. The ion scattering yield in the energy range of 80–90 keV is also higher for the Alq/Al/graphite sample than the Alq/graphite sample, which is due to partial oxidation of the underlying Al film during the thermal deposition process. When Alq films were deposited on fully oxidized Al

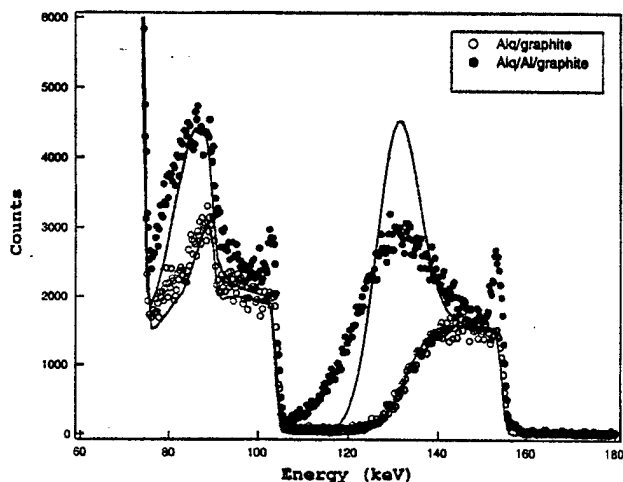


FIG. 1. MEBS spectra for (a) Alq/graphite (open circle) and (b) Alq/Al/graphite (full circle). The thickness for Alq and Al is 850 and 30 Å, respectively. The solid lines represent the calculated spectra, assuming no Al penetration.

layers (i.e.,  $\text{Al}_2\text{O}_3$ ),<sup>11</sup> both the additional surface peaks for Al and O are not present (Fig. 2). Unlike the Alq/Al/graphite sample, the MEBS spectrum for the Alq/ $\text{Al}_2\text{O}_3$ /graphite sample can be well simulated without assuming extraneous Al diffusion. The absence of the excess Al surface peak in the Alq/ $\text{Al}_2\text{O}_3$ /graphite sample allows us to further rule out the possibility of sample contamination or beam effects as the source of the anomalous Al surface accumulation.

MEBS spectra for the Alq/ $\text{Al}_2\text{O}_3$ /Al/graphite samples were collected as a function of intervening oxide thickness. The number of excess Al atoms in the Alq surface region decreases with increasing thickness ( $t_{\text{oxide}}$ ) of the inserted  $\text{Al}_2\text{O}_3$  layer. For  $t_{\text{oxide}} = 28$  Å, Al migration to the surface is not detectable, indicating that a 28-Å  $\text{Al}_2\text{O}_3$  layer at the Alq/Al interface can totally suppress Al penetration into the Alq surface region.

PL measurements were also conducted to examine the effects of inserted  $\text{Al}_2\text{O}_3$  layers on Alq luminescence. For the PL experiment all films were deposited on glass substrates

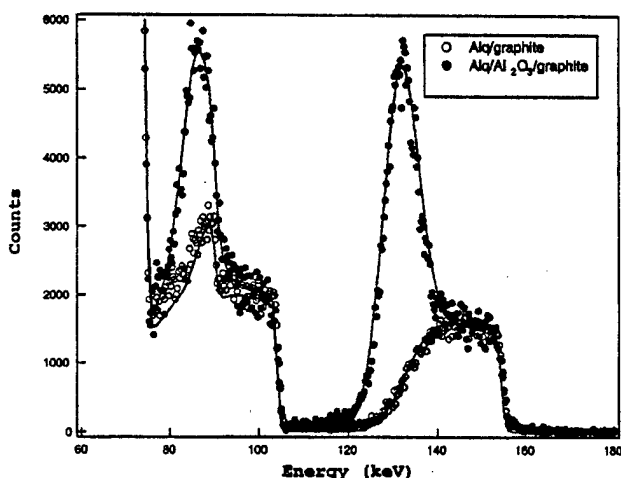


FIG. 2. MEBS spectra for (a) Alq/graphite (open circle) and (b) Alq/ $\text{Al}_2\text{O}_3$ /graphite (full circle) samples. The thickness for Alq and  $\text{Al}_2\text{O}_3$  is 850 and 40 Å, respectively. The solid lines represent the calculated spectra, assuming an unmodified, "as-grown" structure.

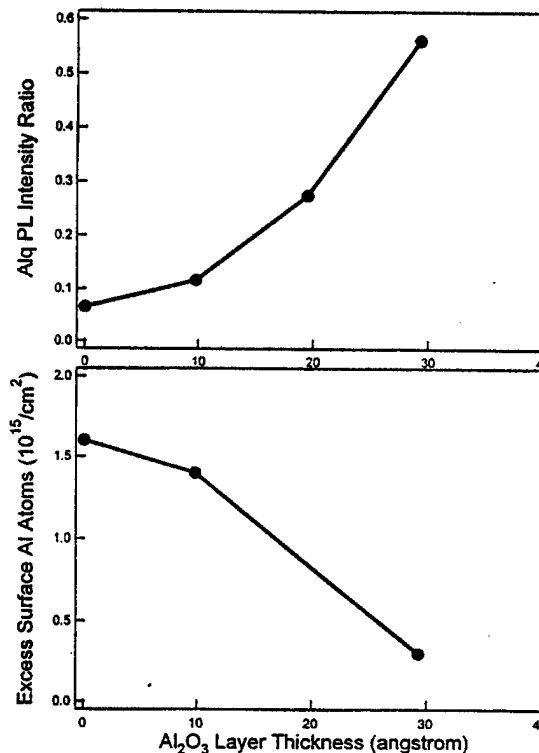


FIG. 3. (a) The ratio of PL intensity at 530 nm as a function of  $\text{Al}_2\text{O}_3$  layer thickness in the Alq/ $\text{Al}_2\text{O}_3$ /Al/glass samples. The thickness of the Alq and Al films is 100 and 30 Å, respectively; (b) the number of excess Al atoms in the surface of the Alq film (850 Å in thickness) at different  $\text{Al}_2\text{O}_3$  layer thickness for the Alq/ $\text{Al}_2\text{O}_3$ /Al/graphite samples.

whose fluorescence background can be ignored in the spectral range of interest. The thickness of the Alq film for the PL experiments is 100 Å, shorter than the exciton diffusion length,<sup>14</sup> so that the luminescence quenching effects induced by the Al atoms present at the surface and interface can be detected. The PL spectrum of Alq consists of a broad peak centered at a 530-nm wavelength. The ratio of PL intensities at the 530-nm wavelength,  $I/I_0$ , is presented in Fig. 3(a), where  $I$  is the PL intensity for the Alq/ $\text{Al}_2\text{O}_3$ /Al samples, and  $I_0$  the PL intensity for a control sample obtained by directly depositing the 100-Å-thick Alq film on the glass substrate. For the Alq/Al sample (i.e.,  $t_{\text{oxide}} = 0$ ), almost 95% of the generated excitons are quenched. The PL intensity of the Alq/ $\text{Al}_2\text{O}_3$ /Al samples increases with the thickness of the inserted  $\text{Al}_2\text{O}_3$  layer, while the aluminum in the surface region of the Alq film decreases with the thickness of  $\text{Al}_2\text{O}_3$  layers added at the interface [Fig. 3(b)].

Metal diffusion in polymer and organic materials has been reported by many groups and is shown to be strongly related to the reactivity of metals with the polymer and organic materials.<sup>6-10</sup> It is generally observed that less reactive metals diffuse much faster in polymer and organic materials. Recently, Probst and Haight found that diffusion of Ga into Alq films can occur at room temperature, whereas Ca, a more reactive metal, only forms interface states and shows no diffusion into Alq.<sup>9</sup> Since Al and Ga are chemically similar, diffusion of Al into Alq may also be expected. Our study suggests that the Al diffusion coefficient in Alq at room temperature is  $\sim 10^{-18}$  cm<sup>2</sup>/s, which is on the same order of magnitude as the Ga diffusivity in Alq, estimated from the

data published by Probst and Haight. Ion repulsion due to metal ionization has been suggested as the mechanism for indium diffusion into perylenetetracarboxylic dianhydride (PTCTA) films.<sup>7,8</sup> Such a mechanism may also be operative in diffusion of Al into Alq films, since the ionization energy of Al (5.99 eV) is only slightly higher than that of In (5.79 eV).<sup>7</sup> The crystalline structure, especially the grain boundaries in Alq films, may aid in Al diffusion and segregation. It is well known that metal segregation in inorganic semiconductors occurs as a result of an amorphous/crystalline (a/c) phase transition.<sup>15</sup> This mechanism may also play a role in the observed surface segregation of Al in Alq, since crystallization of polymer and organic films can take place at room temperature via molecular self-assembly.<sup>16</sup> The morphology of the structure must also be considered for the effects observed here. For example, pinholes in Alq could serve as fast diffusion pipes and lead to the surface accumulation of free Al through the surface diffusion process. Scanning electron microscopy (SEM) shows no evidence of such pipes.

Metal-induced luminescence quenching of organic films<sup>17</sup> is a serious problem for OLED devices. Various mechanisms have been proposed, including metallic clustering, band bending at the metal/organic interface, and metal diffusion into organic films. Clustering of Al on the Alq/Al interface can be easily excluded as the cause for luminescence quenching of Alq, since formation of metal clusters prohibits metal diffusion in organic films,<sup>7,8,10</sup> contrary to our observation. Band bending at the metal/organic interface<sup>17</sup> may be one of the mechanisms for luminescence quenching, if a sharp interface between the Al and Alq layers can be still defined. The strong correlation between the retardation of Al penetration and the recovery of Alq PL intensity suggests that diffusion of Al into Alq may be a major mechanism for Al-induced luminescence quenching of Alq. The incorporation of excess Al atoms (via diffusion) could induce lattice deformation in Alq films and, therefore, lead to the formation of gap states which serve as exciton quenching sites.<sup>5</sup> The Alq PL intensity can be recovered substantially by adding an intervening oxide layer as a diffusion barrier to metallic Al (the Al diffusivity<sup>18</sup> at room temperature is estimated as  $\sim 10^{-85}$  cm<sup>2</sup>/s, however, the actual diffusivity in such ultrathin films may be strongly modified). It is well known that when exposed to air at room temperature, Al metal forms a protective oxide layer ( $\sim 20$ – $30$  Å) on its surface which inhibits the oxidation of the underlying Al.<sup>19</sup> Therefore, an interface oxide layer of 20–30 Å in thickness should be able to completely suppress the Al diffusion and fully recover the PL intensity. However, at  $t_{\text{oxide}} \approx 30$  Å, the PL intensity ratio is only  $\sim 0.6$ . The mechanical imperfection (e.g., pinholes) in the oxide, or the chemical reaction between the Alq and the hydrated outer layer<sup>11</sup> of the oxide, may be the reason for the incomplete recovery of PL.

From our study we see significant potential for further improving the performance of Alq-based OLEDs by adding

a more effective diffusion barrier than Al<sub>2</sub>O<sub>3</sub> at the Alq/Al interface. This diffusion barrier should be thick enough to stop Al diffusion into Alq and if insulating, thin enough for direct electron tunneling from Al into Alq. The optimal thickness of the Al<sub>2</sub>O<sub>3</sub> layer for maximum EL efficiency in Alq-based OLEDs was recently reported to be  $\sim 12$  Å.<sup>3</sup> Clearly, this is a compromise between suppression of Al penetration and efficient electron tunneling. Our data show that at  $t_{\text{oxide}} \approx 10$  Å, the number of excess Al atoms diffusing into the Alq surface region does not decrease significantly, and the PL intensity for this sample is only  $\sim 12\%$  of that for the Alq control sample. This suggests that the optimum EL efficiency of Alq-based OLEDs may be further enhanced by depositing an appropriate thin film ( $\sim 10$  Å), which is more efficient than Al<sub>2</sub>O<sub>3</sub> in retarding Al diffusion.

In summary, we present direct evidence for Al penetration into Alq films. The role of a thin Al<sub>2</sub>O<sub>3</sub> layer inserted at the Alq/Al interface is, in fact, a barrier to Al diffusion. The recovery of luminescence intensity due to the interface Al<sub>2</sub>O<sub>3</sub> layer is correlated with the reduction of Al diffusion, suggesting that optical quenching of Alq may be caused by indiffusion of Al.

The authors acknowledge the assistance of C. T. Maree, M. Morales, J. Desper, and H. Lee (Livermore) to this work.

<sup>1</sup>C. W. Tang and S. A. VanSlyke, Appl. Phys. Lett. **51**, 913 (1987).

<sup>2</sup>L. S. Hung, C. W. Tang, and M. G. Mason, Appl. Phys. Lett. **70**, 152 (1997).

<sup>3</sup>F. Li, H. Tang, J. Anderegg, and J. Shinar, Appl. Phys. Lett. **70**, 1233 (1997).

<sup>4</sup>H. Tang, F. Li, and J. Shinar, Appl. Phys. Lett. **71**, 2560 (1997).

<sup>5</sup>Y. Park, V.-E. Choong, B. R. Hsieh, C. W. Tang, and Y. Gao, Phys. Rev. Lett. **78**, 3955 (1997).

<sup>6</sup>A. R. Schlatmann, D. Wilms Floet, A. Hilberer, F. Garten, P. J. Smulders, T. M. Klapwijk, and G. Hadzioannou, Appl. Phys. Lett. **69**, 1764 (1996).

<sup>7</sup>Y. Hirose, A. Kahn, V. Aristov, P. Soukiasian, V. Bulovic, and S. R. Forrest, Phys. Rev. B **54**, 13748 (1996).

<sup>8</sup>Y. Hirose, A. Kahn, V. Aristov, and P. Soukiasian, Appl. Phys. Lett. **68**, 217 (1996).

<sup>9</sup>M. Probst and R. Haight, Appl. Phys. Lett. **70**, 1420 (1997).

<sup>10</sup>F. Faupel, R. Willecke, and A. Thran, Mater. Sci. Eng., R **22**, 1 (1998).

<sup>11</sup>A. C. Miller, F. P. McCluskey, and J. Ashley Taylor, J. Vac. Sci. Technol. A **9**, 1461 (1991), and references therein. These authors note that air passivated Al layers consist of a hydrated outer and nonhydrated interface layer of Al<sub>2</sub>O<sub>3</sub>.

<sup>12</sup>M. H. Mendenhall and R. A. Weller, Nucl. Instrum. Methods Phys. Res. B **47**, 193 (1993).

<sup>13</sup>Graphite is used as a "low Z" substrate to enable an accurate ion scattering analysis of the deposited thin films.

<sup>14</sup>J. Kalinowski, G. Giro, P. Di Marco, N. Camaioni, and V. Fattori, Chem. Phys. Lett. **265**, 607 (1997).

<sup>15</sup>J. S. Custer, A. Polman, and H. M. van Pinxteren, J. Appl. Phys. **75**, 2809 (1994).

<sup>16</sup>G. Reiter and J. U. Sommer, Phys. Rev. Lett. **80**, 3771 (1998).

<sup>17</sup>V. Choong, Y. Park, Y. Gao, T. Wehrmeister, K. Müllen, B. R. Hsieh, and C. W. Tang, Appl. Phys. Lett. **69**, 1492 (1996).

<sup>18</sup>B. J. Wuensch, in *Mass Transport in Solids*, edited by F. Bénére and C. R. A. Catlow (Plenum, New York, 1983).

<sup>19</sup>O. Kubaschewski and B. E. Hopkins, *Oxidation of Metals and Alloys* (Academic, New York, 1953).





ELSEVIER

# Determination of the hydrogen sensitivity and depth resolution of medium-energy, time-of-flight, forward-recoil spectrometry

James H. Arps<sup>1</sup>, Robert A. Weller<sup>\*</sup>*Vanderbilt University, Box 1687, Station B, Nashville, TN 37235, USA*

Received 19 February 1996; revised form received 5 July 1996

## Abstract

Medium energy time-of-flight forward recoil spectrometry has been developed recently as a complement to conventional ion beam analysis methods such as nuclear reaction analysis and elastic recoil detection. Here we report measurements of the minimum detectable surface concentration and near surface depth resolution for hydrogen by forward recoil spectrometry using a number of beam species and energies. The primary physical limitations encountered in these measurements are identified and discussed. Using an 810 keV  $\text{Ar}^{3+}$  beam, H on a carbon substrate can, in principle, be detected at areal densities as low as  $1 \times 10^{13}$  H/cm<sup>2</sup>. A 540 keV  $\text{O}^{2+}$  beam has been found to be a suitable choice for depth profiling of H in Si achieving a resolution of approximately 6 nm near the surface. Examples are given which demonstrate the utility of the technique for hydrogen profiling.

## 1. Introduction

Elastic recoil detection (ERD) and nuclear reaction analysis (NRA) are two methods widely used for the measurement of hydrogen in materials [1,2]. Detection sensitivity and depth resolution are the primary attributes usually considered in assessing the capabilities of these ion beam analytical techniques and are often used as benchmarks for comparison. Szilagy et al. [3], have reported an optimized depth resolution of 2 nm for ERD using a 2.5 MeV C beam. Nagai and coworkers [4] claim a detection limit of  $2 \times 10^{12}$  H/cm<sup>2</sup> based on the measurement of a single recoil atom. In NRA, a near-surface depth resolution of 5 nm and a bulk sensitivity of less than 10 ppm can be achieved for hydrogen using the  $^1\text{H} (^{15}\text{N}, \alpha\gamma)^{12}\text{C}$  reaction [5,6]. Medium energy (0.1–1 MeV) time-of-flight forward recoil spectrometry has also been demonstrated to be a suitable method for determining the light element composition at or near the surface of a material [7]. A number of advantages may be realized over the methods noted above. A smaller, less expensive accelerator is needed, while good depth resolution near the surface is achieved due to the favorable timing properties of the time-of-flight spectrometer. Because the technique is sensitive to the velocity, rather than the energy of the recoil and scattered particles,

separation and simultaneous identification of a number of light elements near the surface are possible without the use of an absorber foil. By using lower energy beams, sensitivity to light elements is increased due to the larger scattering cross sections and the total energy deposited in the sample is reduced. Recently, the first essentially nondestructive ion beam evaluations of radiation sensitive nitrocellulose and Langmuir–Blodgett organic thin films have been carried out using this technique [8].

This paper describes experiments designed to establish values for hydrogen sensitivity and depth resolution using medium energy time-of-flight (TOF) forward recoil spectrometry. A number of incident beam species and energies are considered in order to identify the optimal analysis conditions. Brief descriptions of the physical processes which affect sensitivity and depth resolution are given in order to identify the limiting factors associated with time-of-flight measurements. Lastly, the technique is applied in the measurement of buried H at C/Si interfaces and 500 eV  $\text{H}^+$  implanted along random and channeled directions in Si.

## 2. Theoretical considerations

Hydrogen sensitivity refers to the minimum surface or bulk H content that may be detected in a material at a prescribed confidence level. Ultimately, this requires the accumulation of a statistically significant number of counts associated with recoil H in the time-of-flight spectrum.

<sup>\*</sup> Corresponding author. Fax: +1-615-343-7263; email: [weller@vuse.vanderbilt.edu](mailto:weller@vuse.vanderbilt.edu).

<sup>1</sup> Present address: Southwest Research Institute, San Antonio, TX.

The number of real counts  $Y_R$  attributable to the feature of interest and the associated error  $\sigma_R$  determined by Poisson statistics are given by

$$Y_R = Y_T - Y_B, \quad (1a)$$

$$\sigma_R = \sqrt{\sigma_T^2 + \sigma_B^2} = \sqrt{Y_R + 2Y_B}, \quad (1b)$$

where the subscripts T and B refer to the total and background counts and errors, respectively. In order for the measurement to be statistically significant, the number of real counts must be a factor  $\alpha$  greater than the error in the measurement  $\sigma_R$ , where  $\alpha = 1, 2$ , or 3 at a 66, 95, or 99% confidence level, respectively. Solving for  $Y_R$  in terms of the number of background counts gives

$$Y_R = \frac{\alpha^2}{2} \left[ 1 + \left( 1 + \frac{8Y_B}{\alpha^2} \right)^{1/2} \right] \quad (2)$$

for the minimum detectable yield.

Background in a time-of-flight spectrometer is produced by random coincidences. These events occur when different particles initiate otherwise valid start and stop pulses. Hence, random coincidence background depends on the probability for generating valid start and stop events as well as the rate at which particles enter the spectrometer. The composition of the substrate is one factor contributing to this background because the flux of scattered particles depends on the mass of the substrate and, ultimately, the scattering cross section. The distribution of random counts is approximately uniform in time and increases linearly with current for a given total number of incident particles, since the rate of scattered particles scales directly with the rate of incident particles. Background subtraction, however, is particularly simple by using the kinematically inaccessible region of the spectrum as a baseline.

The solid angle and detection efficiency are fixed by the choice of geometry and spectrometer configuration (flight path, foil thickness, etc.), directly affecting the number of detected recoils. Two competing factors complicate the choice of beam species and energy for optimal sensitivity in analysis. While recoil H cross sections favor the use of high-Z analysis beams, the time-of-flight spectrometer's efficiency decreases with decreasing energy of the recoil H. Sputtering of hydrogen by the incident beam is a further limitation on sensitivity and will be of the most concern in the use of a high-mass analysis beam. A formula has been proposed which considers sputtering along with a detailed treatment of the random coincidence background to arrive at a limit for sensitivity [9]. However, the magnitude of the sputtering contribution in the case of hydrogen is difficult to quantify since the rate of removal will likely be influenced by the host material. A reasonable order-of-magnitude estimate of the minimum detection limit imposed by sputtering might be an areal density of surface hydrogen equal to the ion dose used in the analy-

sis. In most analyses by forward recoil spectrometry, it is likely that random coincidence background will be the dominant term affecting sensitivity.

The ability of a technique to resolve two distinct, same-element features separated by a certain thickness of material is characterized by the depth resolution of the system

$$\Delta x = \frac{\Delta E}{\epsilon(E)}, \quad (3)$$

$$\epsilon(E) = \frac{1}{\cos \theta_1} K' S_i(E) + \frac{1}{\cos \theta_2} S_r(K'E), \quad (4)$$

where  $\Delta E$  is the energy resolution,  $\epsilon(E)$  is the stopping cross section factor, and  $\theta_1$  and  $\theta_2$  are, respectively, the incident and exit angles measured from the surface normal [10].  $S_i(E)$  and  $S_r(K'E)$  represent stopping cross sections for the incident and recoil particles at the incident and recoil energies respectively. The energy resolution for a particular element may be inferred from the fwhm of a scattering peak corresponding to a monolayer or submonolayer coverage. Of course, for a thicker scattering feature,  $\Delta E$  may be determined from the leading and trailing edge widths of the distribution.

Timing resolution, energy straggling, geometric broadening, and multiple scattering all contribute to the measured energy resolution. An electronic timing resolution of 1 ns will have a variable effect depending on the species mass and energy. For example, the contribution of spectrometer timing to the energy spread of a 50 keV H recoil is approximately 1 keV. In general, the spread will increase for particles with higher energy and mass.

A geometric contribution to the energy resolution arises from the angular spread of scattered particles originating from a beam spot of finite size and sampled by a spectrometer with a finite aperture width. Particles detected at slightly different scattering angles will have different recoil energies. Paszti et al. [11] discuss the optimization of an ERD system for depth resolution, and derive an expression for the geometrical effect. A further approximation applies for scattering events in the near surface region.

$$\Delta E_g = 2K'E_0 \Delta \gamma \tan \phi, \quad (5)$$

where

$$\Delta \gamma = \frac{1}{D} \sqrt{w^2 + \frac{d^2 \cos^2 \theta_2}{\cos^2 \theta_1}}. \quad (6)$$

In the forward recoil configuration used in our laboratory,  $\theta_1 = \theta_2 = 69^\circ$ , and the forward recoil angle  $\phi = 42^\circ$ . The detector-target distance  $D$  is 30.5 cm, with an aperture width  $w = 0.42$  cm and a typical beam width,  $d$ , of 0.5 cm measured in the scattering plane. The resultant broadening is equal to  $\sim 4\%$  of the surface recoil energy, or 2 keV for 50 keV recoil H.

The ability to sense spatial variations in the elemental distribution depends not only on the intrinsic resolution and acceptance angle of the spectrometer but also on the energy straggling experienced by the ions in penetrating the target. The effect of energy straggling on the detector resolution is expected to be the dominant term, particularly for heavy ions, away from the near-surface region of the material. For numerical estimates of straggling at energies below 1 MeV the empirical formulae of Yang, O'Connor and Wang [12] may be used.

Multiple scattering gives rise to an uncertainty in energy as particles experience a gradual angular and lateral divergence in penetrating a material. The effect tends to dominate in situations where the incident or scattering angles with respect to the surface are very small (i.e. large  $\theta_1$ ,  $\theta_2$  and small  $\phi$ ) and the penetration depth is large. Empirical estimates of the angular and lateral dispersion have been made in hydrogen ERD and RBS analyses aimed at optimized depth profiling [13]. These effects are minimal for the forward recoil geometry used in our laboratory because of the relatively large forward scattering angle. For instance, the angular spread experienced by 810 keV Ar traveling through 10 nm of Si contributes only 2 keV to the energy resolution, much less than the energy straggling for this thickness.

Multiple scattering also occurs when the incident or recoil species experiences more than one large-angle elastic collision. Such collisions, which add up to a net deflection of  $42^\circ$ , tend to produce particles with larger final energies than single scattering events. In a forward recoil time-of-flight spectrum, a small background tail is often seen to extend in front of the leading edge of a thick target recoil or scattering feature.

### 3. Experiment and results

#### 3.1. H sensitivity measurements

Detection limits for surface H on C and Si substrates were determined using 270 keV He<sup>+</sup>, C<sup>+</sup>, and Ar<sup>+</sup>, 540 keV O<sup>2+</sup> and Ne<sup>2+</sup>, and 810 keV Ar<sup>3+</sup> ion beams. Clean

samples of silicon and graphite were analyzed in a bakable, hydrocarbon-free, stainless steel vacuum chamber at a pressure of approximately  $2 \times 10^{-8}$  Torr. Beam currents in the range 0.25–0.50 nA (with the exception of 2.5 nA for He) were used in order to minimize the random coincidence background in the measurements. The typical collection time for each spectrum was 30 min. Small, well separated peaks attributable to surface H were observed in each spectrum. The minimum H yield was determined using Eq. (2) at 99% confidence ( $\alpha = 3$ ). From each spectrum, the number of background counts in the surface peak  $Y_B$  was computed by multiplying the measured peak width in channels by the average number of background counts per channel in a nearby but kinematically inaccessible region. Finally, the areal density of surface H was computed using the appropriate recoil cross section, spectrometer efficiency  $\eta$ , and solid angle.

The results for measuring H on carbon with various beams are compared in Table 1. The lower mass C substrate limits the flux of scattered beam particles and substrate recoils by more than a factor of three compared with the Si substrates. In some cases, such as the scattering of Ar from C, an angle of  $42^\circ$  is larger than the kinematic maximum for binary collisions. The large recoil cross section and reasonable H detection efficiency favor 810 keV Ar<sup>3+</sup> for the sensitive measurement of surface H. It is important to note that by acquiring a spectrum over the span of approximately 5 h, an order of magnitude additional charge could be applied at the same current. Such a measurement would lower the detection limit by more than a factor of three. The implied sensitivity of  $\sim 1 \times 10^{13}$  H/cm<sup>2</sup> is equal to or better than the best values reported using conventional ERD when differences in the definition of sensitivity used by various authors are considered.

#### 3.2. H depth resolution measurements

The depth resolution for near surface H may be calculated from the same spectra used for the H sensitivity measurements. After transformation of the spectrum from the time to energy domain, the hydrogen surface peak was fit to a Gaussian, with  $\Delta E$  equal to the fwhm separation.

Table 1

Comparison of H minimum detection limits ( $N_H$ ) for various analysis beams incident on a C substrate. The background counts in the surface peak ( $Y_B$ ), minimum detectable yield ( $Y_R$ ), deposited charge ( $Q$ ), recoil cross section ( $\sigma_H$ ), and effective solid angle ( $\eta \cdot \Omega_H$ ) used in each computation are also provided.

Beam	Energy (keV)	$Y_B$ (counts)	$Y_R$ (counts)	$Q$ ( $10^{12}$ ions)	$\sigma_H$ ( $10^{-22}$ cm <sup>2</sup> /sr)	$\eta \Omega_H$ ( $10^{-5}$ sr)	$N_H$ ( $10^{13}$ /cm <sup>2</sup> )
He	270	37	31	31	0.173	3.0	69
C	270	9.5	18	3.1	10.2	2.1	9.8
O	540	4.4	14	3.1	7.77	2.6	8.0
Ne	540	7.5	17	1.6	18.2	2.4	8.8
Ar	270	140	55	1.3	675	0.5	4.4
Ar	810	7.3	17	1.0	92.1	2.1	3.0

Table 2

Effect of analysis beam on near-surface energy resolution ( $\Delta E$ ) and depth resolution ( $\Delta x$ ) for H on a C substrate

Beam/energy (keV)	$\Delta E$ (keV)	$\epsilon(E)$ (eV/ $10^{15}/\text{cm}^2$ )	$\Delta x$ $10^{15}/\text{cm}^2$	nm
He/270	5.5	26.1	75.5	6.7
C/270	3.5	23.2	54.1	4.8
C/540	5.0	27.7	64.7	5.7
O/540	4.5	25.6	63.0	5.6
Ne/540	4.0	22.6	63.4	5.6
Ar/270	2.5	16.0	56.0	5.0
Ar/810	3.5	20.3	61.8	5.5

Stopping powers computed as in Ref. [14] were used to calculate the stopping cross section factor  $\epsilon(E)$  and the depth resolution  $\Delta x$  was then determined. The resulting values are compiled in Table 2. The measured energy widths are generally consistent with the estimated contributions due to timing resolution and geometric broadening. No substantial improvement in the resolution is observed as a function of the analysis beam mass and energy. A possible explanation is that while the stopping cross section increases at higher energies the energy resolution of the spectrometer decreases. With increasing recoil H energy, the effects of spectrometer timing resolution and scattering geometry become more significant. The estimated 6 nm H depth resolution compares favorably with the results typically achieved by conventional ERD and NRA [3,5,6].

Since variation of the beam species and energy offers no clear advantage in depth resolution near the surface, issues of sensitivity and analyzable depth will play a defining role in choosing a beam for H profiling. The analyzable depth for light element profiling is reduced by heavier recoils or scattered beam ions from the surface having the same velocity (and flight time) as the recoils from deeper within the target. Fig. 1 plots the analyzable depth as a function of beam energy for H in Si with the minimum energy before scattering determined by the point of interference from the next nearest scattering feature (either the scattered beam, for He, C, and O incident ions,

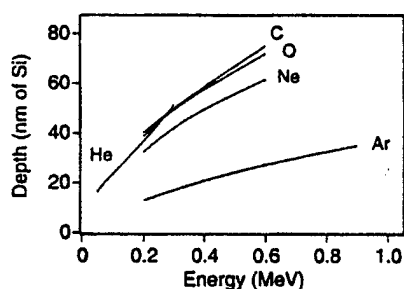


Fig. 1. Analyzable depth for H in Si as a function of beam species.

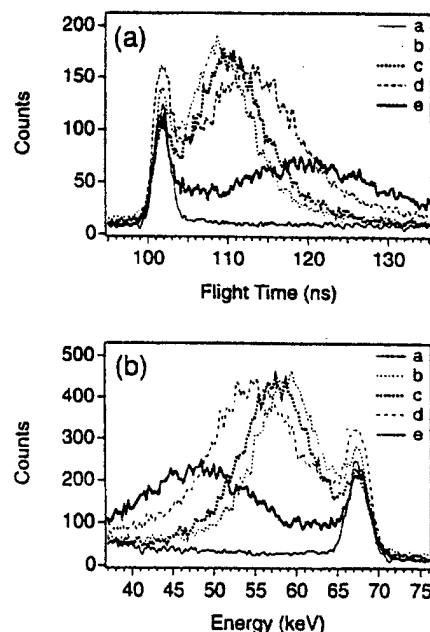


Fig. 2. (a) Time-of-flight and (b) energy spectra of recoil H from Si surfaces covered by C layers of varying thicknesses: (a) bare Si, (b)  $1.8 \mu\text{g}/\text{cm}^2$ , (c)  $2.3 \mu\text{g}/\text{cm}^2$ , (d)  $3.0 \mu\text{g}/\text{cm}^2$ , (e)  $5.0 \mu\text{g}/\text{cm}^2$ . The ion beam was 540 keV  $\text{O}^{2+}$ .

or recoil C for Ne and Ar ions). Given that C and O produced generally similar results, a 540 keV  $\text{O}^{2+}$  beam was chosen for the sensitive depth profiling of H because it is easier to generate in our ion source. Note, however, that with values typically less than 100 nm in a material such as Si, maximum analyzable depth is a clear limitation of medium energy forward recoil spectrometry when compared with conventional ERD or NRA, which can be used at depths of a  $\mu\text{m}$  or more [1,2].

An important test of any hydrogen depth profiling technique is the ability to resolve surface from buried hydrogen. To study this by medium-energy, time-of-flight spectrometry, five Si samples were cleaved from a 8 inch Si wafer, dipped in HF for  $\sim 2$  min, then rinsed in deionized water. Carbon foils of varying thickness ( $\rho = 2 \text{ g}/\text{cm}^3$ ) were floated onto the surface of a water bath and drawn onto the Si samples. The carbon thicknesses stated by the manufacturer (ACF metals) were 1.8, 2.3, 3.0, and  $5.0 \mu\text{g}/\text{cm}^2$  with uncertainties of at least  $\pm 0.5 \mu\text{g}/\text{cm}^2$ . Fig. 2 shows the time-of-flight and corresponding energy spectra from analysis of these samples by 540 keV  $\text{O}^{2+}$  at a deposited charge of  $5 \mu\text{C}$ . A significant concentration of H at the C/Si interface is observed ( $\approx 1 \times 10^{16}/\text{cm}^2$ ), due perhaps to either trapped water or hydrocarbon contaminants introduced during preparation. The surface and buried H distributions are clearly resolved with the latter broadened and shifted lower in energy as the thickness of the C overlayer is increased.

Table 3

Measured and calculated energy shifts,  $\delta E_{\text{exp}}$  and  $\delta E_{\text{calc}}$  for H at four C/Si interfaces. See corresponding spectra in Fig. 2

Sample	C thickness ( $10^{17}$ atoms/cm $^2$ )	$\delta E_{\text{exp}}$ (keV)	$\delta E_{\text{calc}}$ (keV)
b	1.0	8.5	7.1
c	1.1	9.8	7.8
d	1.8	12.3	12.8
e	2.3	18.7	16.3

The measured positions of the buried H peaks were compared with calculations based on the standard energy loss equation

$$\delta E = K'E_0 - E_c = \frac{d}{\cos \theta_1} K'S_i(E_{\text{in}}) + \frac{d}{\cos \theta_2} S_r(E_{\text{out}}), \quad (7)$$

where  $d$  is the carbon thickness and  $E_c$  is the position of the centroid. Values for the carbon layer thicknesses were determined by 810 keV  $\text{Ar}^{3+}$  forward recoil and 270 keV  $\text{He}^+$  backscattering measurements. The experimental and calculated energy shifts and the measured foil thicknesses used in the calculations are given in Table 3. Agreement to  $\pm 15\%$  is consistent with the uncertainties for the computed carbon foil thicknesses and energy losses, providing strong evidence that the hydrogen is confined to the interface. Based on estimates of the spectrometer timing uncertainty, multiple scattering, geometric broadening, and energy straggling, the energy widths of the buried H distribu-

tions are consistent with a thin hydrocarbon layer trapped at the C/Si interface.

A final demonstration of the application of forward recoil spectrometry to hydrogen profiling is the measurement of low energy proton implant distributions. For light ions with energies in the range 0.5–5 keV, the structure of a solid is known to strongly affect the mean projected range [15]. Experiments by Bourque et al. [16] have determined the ranges and straggling of 1 keV deuterons in amorphous, polycrystalline, random and channeled Si. Such measurements are particularly useful for comparison with TRIM [14] or other Monte Carlo simulations of low energy ion trajectories. Fig. 3 compares time-of-flight and energy spectra for 0.5 keV  $\text{H}^+$  implanted in randomly oriented ( $22.5^\circ$  tilt) and channeled  $\langle 110 \rangle$  Si. The two samples, prepared at the University of Quebec, have estimated peak H atomic concentrations of 10%. A control sample was also analyzed to identify the surface H contribution. As anticipated, the implanted range increases along the channeling direction. A mean projected range of 10 nm was estimated for the randomly oriented sample using TRIM and is consistent with the depth profile deduced from the energy spectrum [17].

#### 4. Conclusions

A number of buried and implanted hydrogen distributions have been measured by medium energy time-of-flight forward recoil spectrometry. Results show that this technique compares favorably with conventional ion beam analytical techniques in sensitivity and resolution for near surface H. Minimum coverages of  $1 \times 10^{13}$  H/cm $^2$  can, in principle, be measured using an 810 keV  $\text{Ar}^{3+}$  analysis beam while a near-surface depth resolution of approximately 6 nm has been achieved with 540 keV  $\text{O}^{2+}$  ions. Further optimizations of the time-of-flight spectrometer and the scattering geometry should result in substantial improvement over these quoted values.

#### Acknowledgements

The authors are very grateful to Gilles Bourque and Bernard Terreault of the University of Quebec for their preparation of the H-implanted Si. This work was supported in part by the U.S. Army Research Office under contracts DAAL 03-92-G-0037 and DAAH 04-95-1-0565.

#### References

- [1] J.C. Barbour and B.L. Doyle, in: Handbook of Modern Ion Beam Analysis, eds. J.R. Tesmer and M. Nastasi (Materials Research Society, Pittsburgh, 1995) p. 83.

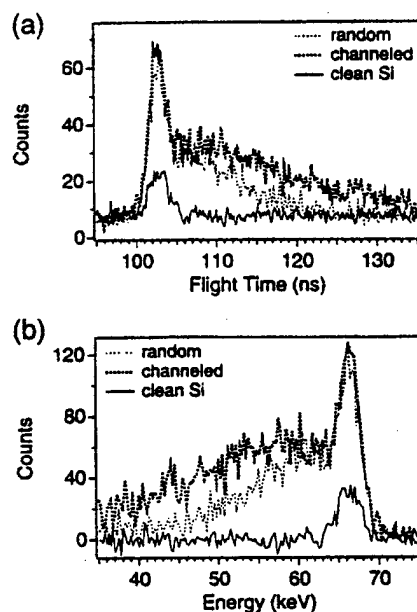


Fig. 3. (a) Time-of-flight and (b) energy spectra of recoil H from Si surfaces implanted with 500 eV  $\text{H}^+$  along the  $[110]$  direction and in a pseudo-random direction. The beam was 540 keV  $\text{O}^{2+}$ .

- [2] W.A. Landford, in: Handbook of Modern Ion Beam Analysis, eds. J.R. Tesmer and M. Nastasi (Materials Research Society, Pittsburgh, 1995) p. 193.
- [3] E. Szilagy, F. Paszti, V. Quillet and F. Abel, Nucl. Instr. and Meth. B 85 (1994) 63.
- [4] H. Nagai et al., Nucl. Instr. and Meth. B 28 (1987) 59.
- [5] B. Maurel and G. Amsel, Nucl. Instr. and Meth. 218 (1983) 159.
- [6] D. Endisch, H. Sturm and F. Rauch, Nucl. Instr. and Meth. B 84 (1994) 380.
- [7] J.H. Arps and R.A. Weller, Nucl. Instr. and Meth. B 79 (1993) 539.
- [8] J.H. Arps and R.A. Weller, Nucl. Instr. and Meth. B 99 (1995) 623.
- [9] R.A. Weller, Nucl. Instr. and Meth. B 79 (1993) 817.
- [10] W.K. Chu, J.W. Mayer and M.A. Nicolet, Backscattering Spectrometry (Academic Press, New York, 1978) p. 74.
- [11] F. Paszti, E. Szilagy and E. Kotai, Nucl. Instr. and Meth. B 54 (1991) 507.
- [12] Q. Yang, D. J. O'Connor and Z. Wang, Nucl. Instr. and Meth. B 61 (1991) 149.
- [13] J.S. Williams and W. Moller, Nucl. Instr. and Meth. 157 (1978) 213.
- [14] J. F. Ziegler, J. P. Biersack and U. Littmark, The Stopping and Range of Ions in Solids (Pergamon Press, London, 1985) p. 218.
- [15] M. Hou and M.T. Robinson, Nucl. Instr. and Meth. 132 (1976) 641.
- [16] G. Bourque, B. Terreault, G.G. Ross and D. Theriault, Nucl. Instr. and Meth. B 90 (1994) 175.
- [17] J.H. Arps, The measurement of low mass surface constituents by medium energy time-of-flight forward recoil spectrometry, Ph.D. Thesis (Vanderbilt University, 1995) p. 122.



ELSEVIER

## Sputtering and migration of trace quantities of transition metal atoms on silicon

Diane Pedersen<sup>a</sup>, Robert A. Weller<sup>a,\*</sup>, Martha Riherd Weller<sup>b</sup>, Victor J. Montemayor<sup>b</sup>,  
J.C. Banks<sup>c</sup>, J.A. Knapp<sup>c</sup>

<sup>a</sup> *Vanderbilt University, Nashville, TN 37235, USA*

<sup>b</sup> *Middle Tennessee State University, Murfreesboro, TN 37132, USA*

<sup>c</sup> *Sandia National Laboratories, Albuquerque, NM 87185, USA*

Received 10 November 1995; revised form received 26 February 1996

### Abstract

We have investigated the behavior of low levels of transition metal atoms on silicon surfaces subject to nitrogen bombardment. Submonolayer coverages of gold, iron, copper, molybdenum and tungsten were deposited on  $\langle 100 \rangle$  silicon surfaces. Samples were analyzed using 270 keV  $\text{He}^+$  time-of-flight backscattering before and after irradiation with 6 mC of 270 keV  $\text{N}^+$  at current levels in the hundreds of nanoamps. The yield of sputtered metallic atoms ranged from  $1.0 \times 10^{-3}$  per incident nitrogen ion to  $3.3 \times 10^{-3}$  per incident ion. Lower yields were correlated with migration of the metallic species into the silicon. The implications for ultra-high sensitivity measurement of contamination on silicon wafers by time-of-flight heavy-ion backscattering spectrometry are discussed.

### 1. Introduction

Improving the sensitivity of surface analytical techniques to metallic contaminants is of vital importance to the semiconductor industry. Heavy-metal contamination present in materials and arising from processing and cleaning operations is detrimental to devices because it results in defects which limit wafer yields and compromise circuit operation. In the near future, new generations of semiconductor devices will require increasing efforts at detecting and eliminating such contamination. Areal densities of surface metallic impurities as low as  $10^8$  at/cm<sup>2</sup> may hinder circuitry performance [1,2], and the detection of levels below  $1 \times 10^9$  at/cm<sup>2</sup> will probably be necessary by the year 2000 [3].

Extensive efforts have been made to develop or modify surface analytical techniques to enhance sensitivity to trace species. Researchers have been able to attain sensitivities of about  $5 \times 10^9$  at/cm<sup>2</sup> for Fe using total reflection X-ray fluorescence spectrometry without using chemical techniques to concentrate the material to a small spot [3,4]. Also impressive are the improvements in sensitivity resulting from optimization of time-of-flight backscattering spectrometry [1]. To optimize sensitivity, the yield of real

counts must be increased while background counts are reduced. The use of heavy ions at energies lower than those used in conventional Rutherford backscattering increases the yield since the scattering cross section is increased. Medium energy (a few hundred keV) time-of-flight backscattering with heavy ions can provide a sensitivity to trace elements which is improved by a factor of  $10^3$  relative to that which is possible with conventional Rutherford backscattering [1].

As the sensitivity of surface analytical techniques is improved, other factors which limit sensitivity to surface species come into play. For techniques which rely on backscattering of incident ions, the ultimate limit to sensitivity may be imposed by the sputter removal of the material of interest [3,5,6]. The same physical processes that enhance sensitivity for medium energy backscattering also govern sputtering yields. In particular, the increase in scattering cross section which occurs at low incident beam energies and for higher  $Z$  incident ions yields more backscattered particles, but also results in greater damage to the target near the surface and larger sputtering yields.

Many expressions and definitions for detection limits in experiments involving Poisson counting statistics have been proposed [7]. We prefer to estimate the optimum sensitivity in the presence of sputtering by requiring that the fractional statistical uncertainty,  $\epsilon$ , of the measurement be equal to the fraction of surface material that is sputtered

\* Corresponding author.

away [6]. We can write the fractional statistical uncertainty as

$$\varepsilon \equiv \frac{\sqrt{C+2B}}{C} = \frac{\Delta\rho}{\rho}, \quad (1)$$

where  $\rho$  is the areal density of the surface species,  $C$  is the yield of backscattered particles, and  $B$  is the background in the region of interest. The yield of backscattered particles is given by

$$C = N\sigma\rho\Omega\eta, \quad (2)$$

where  $N$  is the number of incident projectiles,  $\sigma$  is the differential scattering cross section,  $\Omega$  is the solid angle of detection, and  $\eta$  is the efficiency of the detector. The number of sputtered surface atoms within the area  $A$  irradiated by the beam is  $NP(\rho)$ , where  $P(\rho)$  is the number of sputtered atoms per incident ion as a function of surface coverage. Applying the requirement that  $\varepsilon$  must equal the fraction of surface material which is sputtered away, we have

$$\varepsilon = \frac{NP(\rho)}{\rho A}. \quad (3)$$

The resulting equation for the minimum concentration,  $\rho_{\min}$ , detectable in a backscattering measurement is

$$\rho_{\min}^2 = \frac{1 + \sqrt{1 + 8\varepsilon^2 B}}{2\varepsilon^3} \cdot \frac{P(\rho_{\min})}{A\sigma\Omega\eta}. \quad (4)$$

The function  $P(\rho)$  is not known a priori. The simplest assumption for  $P(\rho)$ , where  $\rho$  is substantially less than a monolayer, is that it varies linearly with coverage, where

$$P(\rho) = k\rho \quad (5)$$

defines the constant of proportionality. We can estimate  $k$  by making the further assumption that trace atoms are removed randomly via collision cascades dominated by substrate atoms, and that the number of trace atoms removed is proportional to their percentage representation in the affected volume of material [6]. This gives

$$P_{\text{stoch}}(\rho) \approx \frac{Y_s}{\rho_s} \rho, \quad (6)$$

where  $Y_s$  is the sputtering yield of the substrate, and  $\rho_s$  is the areal density of substrate atoms in the region from which sputtered atoms originate (typically the top 3 atomic layers).

In this experiment, we observed the behavior of dispersed metallic atoms on silicon substrates under bombardment by heavy ions with energies typical of those used for time-of-flight heavy ion backscattering spectrometry. By studying the behavior of several species of metallic atoms and determining experimental values for  $P$ , where

$$P_{\text{exp}} = P(\rho_{\text{exp}}) = \frac{A(\Delta\rho)_{\text{exp}}}{N}, \quad (7)$$

limitations to detection sensitivity arising from the sputter removal of the measured species can be estimated for a variety of trace elements.

## 2. Experimental procedure

Two sets of samples were used in the measurements. One set was prepared by sputter deposition of submonolayer amounts of gold, copper, iron, molybdenum or tungsten onto the entire surface of device grade, 1 inch, (100) silicon wafers. Prior to deposition, the wafers were ultrasonically cleaned first with acetone, then methanol, and finally rinsed with DI water. A 270 keV Ar<sup>+</sup> beam at 10  $\mu$ A was used to sputter from thin metal foils onto the targets. The resulting metallic atom coverages ranged from  $2.3 \times 10^{14}$  at/cm<sup>2</sup> for Au to  $6.9 \times 10^{14}$  at/cm<sup>2</sup> for Mo. To check for uniformity of coverage, three spots on each sample were analyzed by backscattering with 270 keV He<sup>+</sup> normally incident on the target, at a scattering angle of 150° and with a beam spot size of 0.03 cm<sup>2</sup>. A total deposited charge of 20  $\mu$ C was used in the analysis of the gold, molybdenum and tungsten deposits, and 54  $\mu$ C was used in the analysis of the iron and copper deposits. Measured variations in initial coverage were less than 10% from spot to spot on an individual sample. The samples were then scanned with 6 mC of 270 keV N<sup>+</sup> at currents ranging from 100 nA to 800 nA over an area encompassing approximately 0.4 cm<sup>2</sup>. Thus, the number of incident N<sup>+</sup> ions was  $(1 \pm 0.1) \times 10^{17}$  ions/cm<sup>2</sup>. (The uncertainty in this value is due primarily to uncertainties in determining the area of the scanned spot.) The purpose of scanning the nitrogen was to insure uniform irradiation and to minimize edge effects when reanalyzing the irradiated area. Following scanning, the samples were reanalyzed with He<sup>+</sup> in the same three locations that had been analyzed previously. In all cases, at least one of the analyzed spots was outside the scanned region and served as a control for the measurements.

The other set of samples was prepared by evaporating the same five metals onto 150 Å films of silicon which had previously been evaporated onto a graphite substrate. This sample structure was designed to allow us to measure the rate of sputter removal for both the silicon and the metal atoms. Areal densities for the metallic species ranged from  $6.7 \times 10^{14}$  at/cm<sup>2</sup> for gold to  $2.3 \times 10^{15}$  at/cm<sup>2</sup> for iron and tungsten. The samples were analyzed for uniformity by backscattering with a total analysis charge of 20  $\mu$ C of 270 keV He<sup>+</sup>. The samples were then scanned with 200  $\mu$ C of 270 keV He<sup>+</sup> in an effort to prevent blistering of the silicon film by subsequent N<sup>+</sup> irradiation. The three spots were reanalyzed to verify that this scan did not erode the sample. Next the samples were scanned with 6 mC of 270 keV N<sup>+</sup>. Beam currents and scan areas were both comparable to those used for the first set of samples.



Finally, these samples were reanalyzed with  $\text{He}^+$  after the  $\text{N}^+$  irradiation.

For all backscattering analyses and for the nitrogen irradiation, the ambient pressure in the target chamber was in the high  $10^{-8}$  Torr range and was due primarily to helium from the ion source and helium desorption from the ion pumps. Ambient pressure during the sputter deposition of samples was in the  $10^{-9}$  Torr range. To prevent cross-contamination of samples due to sputtering or overlaying of the metallic species with sputtered silicon, samples were analyzed individually with only one sample in the vacuum chamber at a time.

Aside from a slightly discolored region corresponding to the area scanned by the nitrogen beam, there was little visible difference in the sputter-deposited samples before and after irradiation and analysis. Damage to the samples, again in the area scanned by the nitrogen beam, was much more obvious on the evaporated samples. Scanning electron micrographs of these samples showed that the silicon film had blistered or flaked away in some areas. Thus, we were able to obtain only qualitative results from the evaporated Si film samples. Nevertheless, backscattering analyses from these samples support more quantitative results obtained from the sputter-deposited samples.

### 3. Results and discussion

Figs. 1, 2 and 3 show the trace element features in the backscattering energy spectra for the sputter deposited samples before and after nitrogen irradiation. Areal densities of the materials before and after irradiation are given

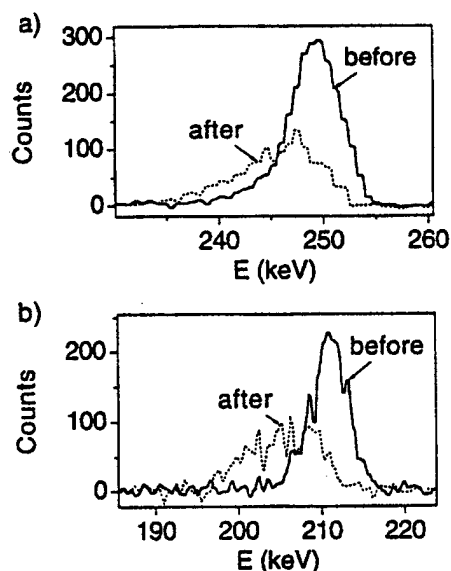


Fig. 1. Au (a) and Cu (b), before and after irradiation with 6 mC of  $\text{N}^+$ . Charge used for the analysis (270 keV  $\text{He}^+$  backscattering) was 20  $\mu\text{C}$  for the Au and 54  $\mu\text{C}$  for the Cu.

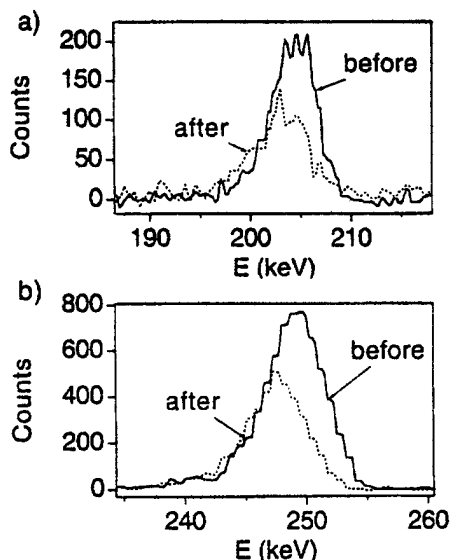


Fig. 2. Fe (a) and W (b), before and after irradiation with 6 mC of  $\text{N}^+$ . Charge used for the analysis (270 keV  $\text{He}^+$ ) was 54  $\mu\text{C}$  for the Fe and 20  $\mu\text{C}$  for the W.

for each species in Table 1. The table also contains  $P_{\text{exp}}$  which is the experimentally determined value for the number of metal ions lost per incoming nitrogen ion,  $P_{\text{stoch}}(\rho_{\text{exp}})$  which is the corresponding calculated quantity obtained from Eq. (6) and, for comparison purposes,  $Y_{\text{bulk}}$  which is the sputtering yield for the corresponding bulk metallic target subject to 270 keV  $\text{N}^+$  irradiation.  $P_{\text{exp}}$  is obtained using Eq. (7). To obtain  $P_{\text{stoch}}(\rho_{\text{exp}})$ , we have used  $2 \times 10^{15}$  at/cm<sup>2</sup> as  $\rho_s$  for silicon, based upon an areal density of  $0.68 \times 10^{15}$  at/cm<sup>2</sup> for a Si (100) surface.  $Y_{\text{bulk}}$  is calculated using the expression of Matsunami et al. [8]. Estimated uncertainties in the table reflect statistical uncertainties in the data. Uncertainties due to current integration are much smaller than the statistical uncertainties while uncertainties in solid angle and detector efficiency have not been considered because they cancel in the calculation of  $P_{\text{exp}}$ .

There are several features of note in the figures. In all cases, there is a significant decrease in peak height for the

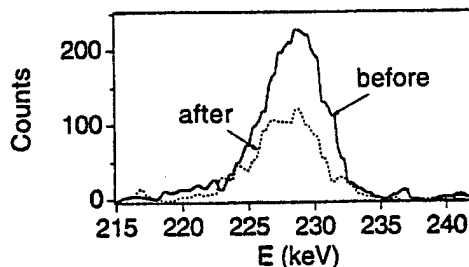


Fig. 3. Mo before and after irradiation with 6 mC of  $\text{N}^+$ . This spectrum was taken with 20  $\mu\text{C}$  of 270 keV  $\text{He}^+$ .

metallic species after irradiation compared with the corresponding height before irradiation. With the exception of the Mo data (Fig. 3), there is also a noticeable shift of the peak centroid towards lower energies, consistent with migration of metallic atoms into the silicon. This shift is particularly noticeable for Cu, where it corresponds to approximately 90 Å in the substrate, and for Au, where it represents about 50 Å (see Fig. 1). Significant peak broadening is also evident for Cu and Au. The centroid shifts for W and Fe are both equivalent to about 20 Å. The statistical error in determining these centroid shifts is insignificant. However, from an analysis of the unirradiated control spots we conclude that the uncertainties in these values are approximately 10 Å. Similar centroid movements were observed in the corresponding spectra obtained from the evaporated Si film samples.

Examining the data presented in the table, we note that values for  $P_{\text{exp}}$  seem to fall into three groups. Au and Cu have the lowest values while Mo has the highest value for  $P_{\text{exp}}$ . Values for Fe and W are intermediate. Considering this trend in light of the spectra in Fig. 1–3, we note that smaller values of  $P_{\text{exp}}$  seem to be correlated with the extent to which the deposited material has migrated away from the surface. Molybdenum shows the greatest loss due to sputtering and is the only element which has remained on the surface (Fig. 3). In contrast, Au and Cu have the smallest losses due to sputtering and the most significant migration into the silicon. In cases where we were able to estimate a sputter-removal rate for the evaporated Si film samples, we observed a similar correlation between migration and sputter removal.

An analysis of the data shows that the probability of removing an ion,  $P_{\text{exp}}$ , was lower than suggested by the stochastic argument of Eq. (6). However, for both sets of samples the relative ordering of the elements by amount of material lost was the same.  $P_{\text{exp}}$  was smaller than  $P_{\text{stoch}}(\rho_{\text{exp}})$  by factors ranging from 0.08 to 0.14.

One potential ambiguity in our determination of  $P_{\text{exp}}$  arises from the fact that it depends upon the rate of diffusion of metallic atoms into the bulk during irradiation. The total number of nitrogen atoms incident on the target

during an irradiation ( $\approx 10^{17}$  ions/cm<sup>2</sup>) is much larger than the number necessary for heavy-ion backscattering analysis of samples of this type. It is possible that most of the erosion occurs almost immediately, before significant diffusion occurs. If so, there would not be a simple correlation between deposited charge and erosion rates. Actual initial sputter yields for those materials which exhibit diffusion into the bulk would be higher than our results indicate. If this is the case, our estimates for sensitivity would be optimistic.

There are also several factors not included in the approximation for  $P_{\text{stoch}}(\rho_{\text{exp}})$  which are expected to influence the yield of removed particles [5]. One is the mass difference between the surface materials and the substrate. Sputtering occurs when a collision cascade, generated by energy deposited in the solid through nuclear collisions, intersects the surface and provides surface atoms with enough energy to escape. Energy transfer is most efficient in collisions between atoms of like mass, and therefore we may expect large mass differences between atoms of the substrate and those of the trace constituent to reduce the rate of sputter removal of the latter. Ion beam mixing of the surface and near surface layers of material will also reduce the rate of sputter removal by reducing the concentration of the trace species on the surface. Thus, the estimate of  $P_{\text{stoch}}(\rho_{\text{exp}})$  from Eq. (6) is expected to be conservative. Surface binding energies also influence the rate of sputter removal. Depending on the binding energies of the trace species relative to the binding energies of Si atoms at the substrate surface, the rate of sputter removal could be either increased or decreased.

Using our results for  $P_{\text{exp}}$ , we can make some predictions about detection limits. We assume that Eq. (5) is applicable so that  $P(\rho_{\text{min}}) = P_{\text{exp}}(\rho_{\text{min}}/\rho_{\text{exp}})$ . The minimum detectable areal density for copper on silicon has been estimated previously [5] to be about  $10^{12}$  atoms/cm<sup>2</sup> for nitrogen backscattering under conditions similar to those we have used. Our data suggest that, in the absence of background, sensitivities of about  $1.5 \times 10^{11}$  at/cm<sup>2</sup> should be attainable using a spectrometer with a solid angle of 0.8 msr and a beam spot size of 0.03 cm<sup>2</sup>. This is

Table 1

Areal densities of surface metallics before and after irradiation with 6 mC of 270 keV N<sup>+</sup>, experimental and stochastic (calculated from Eq. (6)) values of  $P$ , and bulk sputtering yields. Errors are statistical and do not include other sources of error, such as solid angle, current integration and detection efficiency

Metal species	$\rho_{\text{exp}}$ (before) ( $10^{14}$ cm <sup>-2</sup> )	$\rho_{\text{exp}}$ (after) ( $10^{14}$ cm <sup>-2</sup> )	$P_{\text{exp}}$	$P_{\text{stoch}}(\rho_{\text{exp}})$	$Y_{\text{bulk}}$
Au	$2.3 \pm 0.1$	$1.3 \pm 0.1$	$0.0010 \pm 0.0003$	0.0079	0.5
Cu	$4.9 \pm 0.2$	$3.6 \pm 0.2$	$0.0013 \pm 0.0005$	0.0169	0.33
Fe	$5.7 \pm 0.2$	$3.3 \pm 0.2$	$0.0024 \pm 0.0006$	0.0200	0.18
W	$6.0 \pm 0.1$	$3.6 \pm 0.1$	$0.0024 \pm 0.0004$	0.0207	0.11
Mo	$6.9 \pm 0.2$	$3.6 \pm 0.2$	$0.0033 \pm 0.0007$	0.0238	0.092

with a detector efficiency of only about 4% for 270 keV  $N^+$  backscattered from Cu. Eq. (4) indicates some modifications which can be made to improve upon this sensitivity. For example, the prototype HIBS machine at Sandia National Laboratories has a solid angle of 34 msr and an aperture defining a 1 mm diameter beam spot size. Under these conditions, our data suggest a sensitivity for Cu on Si of about  $3.4 \times 10^9$  at/cm<sup>2</sup>. A newer machine, developed by Sandia and Sematech, has 3 detectors, each with a solid angle of about 30 msr, and a beam spot size of 0.09 cm<sup>2</sup>. Using this instrument, Knapp et al. [9] have recently reported sensitivities for Fe of  $6 \times 10^9$  at/cm<sup>2</sup> for Fe on Si and  $3 \times 10^8$  at/cm<sup>2</sup> for Au on Si, based on statistics which included background counts. Based on Vanderbilt detector efficiencies and assuming the optimum situation of no background, our data suggest that sensitivities would be limited by sputtering to  $1 \times 10^9$  at/cm<sup>2</sup> for Fe and to  $6 \times 10^7$  at/cm<sup>2</sup> for Au for the Sandia/SEMATECH instrument.

#### 4. Conclusion

Measurements of the rate of sputter removal of several trace-elements on Si wafers have been conducted and yields have been found to be only about 12% as large as estimates based upon a simple stochastic estimate. At the observed levels, sputter removal of the trace elements under investigation is not a serious limitation to the sensitivity of time-of-flight backscattering spectrometry. Measurements indicate that beam-induced or enhanced diffusion plays a significant role in suppressing removal rates. Diffusion of trace atoms away from the surface, although very modest in extent, is nevertheless sufficient to move a large fraction of atoms out of the zone from which they may be sputtered.

With target sputtering now demonstrated not to be a significant limitation to the sensitivity of heavy ion

backscattering, background produced by higher order scattering processes should be regarded as the determining factor limiting the ultimate trace-element sensitivity of the technique. Furthermore, theoretical models of trace-element sputtering must carefully take into account the location of the trace element atoms as well as their migration induced by exposure to radiation.

#### Acknowledgements

The authors wish to thank Marcus H. Mendenhall, James H. Arps and Kyle McDonald for assistance in the laboratory. This research was supported under a Department of Energy Contract DE-AC04-94AL85000 through Sandia National Laboratories and a Cooperative Research and Development Agreement (CRADA) with SEMATECH. Additional support was provided by the U.S. Army Research Office under contract DAAL 03-92-G-0037.

#### References

- [1] J.A. Knapp and J.C. Banks, Nucl. Instr. and Meth. B 79 (1993) 457.
- [2] D. Deal, *Precis. Cleaning*, Vol. II, No. 6 (1994) 24.
- [3] J.A. Knapp, J.C. Banks and B.L. Doyle, Time-of-Flight Detector for Heavy Ion Backscattering Spectrometry, Sandia report SAND94-0391 UC-404, Sandia National Laboratories.
- [4] U. Weisbrod, R. Gutschke, J. Knoth and H. Schwenke, Appl. Phys. A 53 (1991) 449.
- [5] R.A. Weller, Nucl. Instr. and Meth. B 99 (1995) 491.
- [6] R.A. Weller, Nucl. Instr. and Meth. B 79 (1993) 817.
- [7] L.A. Currie, Anal. Chem. 40 (1968) 586.
- [8] N. Matsunami, Y. Yamamura, Y. Itikawa, N. Itoh, Y. Kazumata, S. Miyagawa, K. Morita, R. Shimizu and H. Tawara, Atomic Data and Nucl. Data Tabl. 31 (1984) 1.
- [9] J.A. Knapp, D.K. Brice and J.C. Banks, Presented at 12th Int. Conf. on Ion Beam Analysis, Tempe, Arizona (1995).

## Analysis of a thin, silicon-oxide, silicon-nitride multilayer target by time-of-flight medium energy backscattering

Robert A. Weller <sup>a,\*</sup>, Kyle McDonald <sup>a</sup>, Diane Pedersen <sup>a</sup>, Joseph A. Keenan <sup>b</sup>

<sup>a</sup> *Vanderbilt University, Nashville, TN 37235, USA*

<sup>b</sup> *Texas Instruments, Inc., Dallas, TX 75265, USA*

### Abstract

Initial results of a program to optimize the resolution of a time-of-flight medium energy backscattering system for analyses of thin oxide and oxynitride films on silicon are reported. Through a redesign of the time-of-flight spectrometer, it has been possible not only to reduce the timing uncertainty attributable to differing path lengths but also, by deliberately introducing small path length differences correlated with scattering angle, to significantly reduce the kinematic dispersion resulting from the finite solid angle of the instrument. Straggling and the energy distribution of the secondary electrons which generate the start signal remain as the primary contributors to system timing uncertainty. Initial measurements of SiO<sub>2</sub> and Si<sub>3</sub>N<sub>4</sub> multilayer films in the 10 nm thickness range have been made using channeling in the  $\langle 110 \rangle$  direction of the Si substrate to suppress background. The depth resolution of the measurements appears to be  $\approx 2$  nm.

### 1. Introduction

Time-of-flight spectrometers designed to analyze ions in the energy range from a few tens to a few hundreds of keV have opened a new window for backscattering and elastic recoil analyses of surfaces. The resulting spectrometry achieves its full potential when applied to films with thicknesses up to a few tens of nanometers. Most recent work has focused upon establishing the efficiency of spectrometers for use in quantitative thin film analysis [1] and upon optimizing their performance for ultra-high sensitivity trace element analysis [2]. In this paper, we revisit the issue of spectrometer resolution with the objective of optimizing a system for the measurement of SiO<sub>2</sub>, TiN, Si<sub>3</sub>N<sub>4</sub>, and similar films which have applications in modern field-effect transistors. The thickness range of interest is from the threshold of detectability up to perhaps 30–40 nm.

The system which we shall consider uses a spectrometer which derives a start signal from secondary electrons emitted by the passage of a backscattered particle through a carbon foil (nominally 1.7  $\mu\text{g}/\text{cm}^2$ ) and a stop signal from the particle's subsequent impact on a microchannel plate. The basic elements which contribute to the finite timing resolution of such a spectrometer have been outlined in Ref. [3]. They include kinematic dispersion from the finite acceptance solid angle, ion path length uncertain-

ties, electronic timing resolution, straggling in the start foil, non-uniformity in the start foil thickness, and the intrinsic energy spectrum of secondary electrons. Charge exchange in the start foil, which is biased at  $-400$  V, also produces a broadening of spectral features. In addition, backscattering spectra are subject to uncertainties produced by instability of the primary beam, straggling in the target, and several other processes [4]. The objective of this work has been to improve the system resolution until it approaches the limits established by the fundamental physical processes, such as straggling and secondary electron emission, which occur within the spectrometer.

### 2. Experimental procedure

The basic configuration of the time-of-flight spectrometer is shown in Fig. 1. In our original design, the stop microchannel plate was mounted normal to the spectrometer axis. Although it was clearly recognized that this introduced path-length variability, the degree of this variability was judged to be acceptable. In the present context, however, estimates indicated that this less than optimum configuration was the largest single source of instrumental uncertainty in measurements. Of course, for particles entering the spectrometer parallel to the axis, the tilt angles of the foil and stop detector should be the same. However, for particles radiating from a point source, such as the one approximated by the beam spot on the target, there is a distribution of scattering angles and a corresponding distri-

\* Corresponding author.

bution of flight paths between the planes of the start foil and the stop detector. A simple geometric construction shows that the width of this distribution of flight paths can be minimized by properly selecting the angle of rotation of the stop detector about an axis which is perpendicular to the plane formed by the incident beam and the axis of the spectrometer. Furthermore, since the velocity of backscattered particles is correlated with scattering angle through the kinematic factor, it is possible to minimize the width of the distribution of flight times by systematically lengthening the flight paths of particles with smaller scattering angles. This optimization is accomplished by a small additional adjustment to the stop-detector angle.

In the system shown in Fig. 1, where the tilt of the start foil is  $30^\circ$ , the distance from the target to the foil is 38 cm, and the flight path is 56 cm, the geometric argument implies that the angle of the stop detector should be  $12.2^\circ$ . For  $\alpha$  particles backscattered from Si, the optimum value of the tilt of the stop detector has been found to be  $15.5^\circ$ . The angle, as shown in Fig. 1, was chosen to be  $15^\circ$  for ease of manufacturability.

In order to assess the distribution of flight times, as well as to compare various alternative designs, we wrote a Monte Carlo code to simulate the effects of 1) beam spot size on the target; 2) all relevant apertures; 3) energy loss, straggling, and multiple scattering in the carbon start foil; and 4) the angles of the start foil and stop detector. Fig. 2 shows the results of the simulation of a time-of-flight spectrum of 270 keV  $\alpha$  particles backscattered from a single layer of Si atoms. The three curves on the left are for stop detector angles of  $0^\circ$ ,  $12.2^\circ$ , and  $15^\circ$  and omit the effects of energy loss and straggling in the carbon start foil. The curves on the right include stopping and straggling and are for detector angles of  $0^\circ$ ,  $15^\circ$  and  $30^\circ$ . It is clear from an examination of these curves that, with the  $15^\circ$  tilt, the geometrical effects are greatly reduced and that straggling and foil uniformity dominate uncertainty. The suppression of the kinematic dispersion is also seen to be quite significant. It is interesting to note that orienting the stop detector and carbon foil parallel to each other leads to results as poor as those obtained when no attempt is made

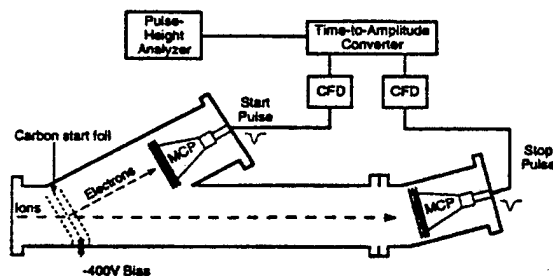


Fig. 1. Schematic of the time-of-flight spectrometer and associated electronics. The drift length is 56 cm. The angles of the carbon start foil and the plane of the stop detector with respect to the spectrometer axis are  $30^\circ$  and  $15^\circ$  respectively.

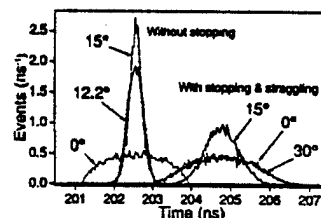


Fig. 2. Monte Carlo simulation of spectrometer resolution including effects of finite beam spot size, target angle, spectrometer apertures, and stop detector angle. The carbon foil angle is  $30^\circ$ . The curves centered near 202.5 ns are for detector angles of  $0^\circ$  (normal to the axis),  $12.2^\circ$  and  $15^\circ$  and include only geometrical factors, including the backscattering kinematic factor. The curves centered near 204.8 ns, for stop detector angles of  $0^\circ$ ,  $15^\circ$ , and  $30^\circ$ , also include straggling and energy loss in the start foil and a foil non-uniformity of 10%.

to optimize the geometry. The  $15^\circ$  curve on the right is well fit by a Gaussian with standard deviation  $\sigma \approx 0.43$  ns. This will be taken to be the contribution to timing uncertainty from geometric factors, straggling, and foil non-uniformity for  $\alpha$  particles backscattering from surface Si. Similar curves have been computed for scattering from other species.

To estimate the magnitude of the effects of electronic timing uncertainty and the secondary electron energy spread, which were not included in the simulation, we measured a thin Au layer on Si by proton backscattering at 270 keV. The observed peak was Gaussian in shape with a standard deviation  $\sigma \approx 0.45$  ns. Since the standard deviation of the Monte Carlo simulation of this peak was 0.08 ns, we can infer that an upper limit to the combined effects of electron-flight-time dispersion and electronic-timing uncertainty is  $\approx 1.04$  ns, fwhm. Here and subsequently we will define "resolution" to be the full width at half maximum of an equivalent isolated peak assuming normally distributed data. The fwhm value is  $2.35\sigma$  for a peak and equal to the 12–88% transition for an edge, which assumes the mathematical form of an error function.

The samples used in this work consisted of three dielectric layers,  $\text{SiO}_2$ ,  $\text{Si}_3\text{N}_4$  and  $\text{SiO}_x$  on crystalline Si. The buried oxide layer, whose stoichiometry was not known precisely, was nominally 1.5 nm thick. The  $\text{SiO}_2$  layer at the surface was nominally 2.0 nm. The nominal thickness of the nitride layers was 7–8 nm.

In order to increase energy loss and thereby to improve depth resolution, the target normal was oriented at  $45^\circ$  with respect to the beam (and  $75^\circ$  with respect to the spectrometer). Together with a scattering angle of  $150^\circ$ , this resulted in an exit angle for backscattered  $\alpha$  particles of  $15^\circ$  above the plane of the target. At  $45^\circ$  it was also (usually) possible by carefully mounting the target to adjust it so that a significant amount of the beam entering the Si substrate was captured in the  $\langle 110 \rangle$  channel. This greatly reduced the background in the region of the spectrum containing

the oxygen and nitrogen features. In all cases, the incident  $\alpha$  particle beam was 270 keV so that the critical angle for channeling was approximately  $1^\circ$ . Beam currents were typically 30–40 nA, while beam spot sizes were approximately  $5 \text{ mm}^2$ . Total beam exposures of approximately  $1\text{--}1.5 \times 10^{15}$   $\alpha$  particles were used in order to avoid producing significant radiation damage to the targets.

Auger depth profiles were measured for comparison with the backscattering data. The Auger data were acquired by sequential accumulation of spectra and sputtering by a 3 kV  $\text{Ar}^+$  ion gun. The double-pass cylindrical mirror analyzer was operated in pulse counting mode. The sample was sputtered for a measured ion dose rather than for a constant time. This is particularly important since the system is automated and runs unattended for long periods during which Ar pressure may vary. The resulting profile of Auger strengths versus accumulated  $\text{Ar}^+$  charge were normalized to the same total thickness as observed in the backscattering data.

### 3. Results and discussion

The solid curve in Fig. 3 is typical of the spectra which were measured under optimum channeling conditions at a target angle of  $45^\circ$ . The sample has a  $\text{Si}_3\text{N}_4$  layer which is nominally 7 nm thick. Also shown in Fig. 3 is a spectrum obtained from the same target at a target angle of  $49^\circ$ , but with half as much total beam. The data have been mathematically rebinned from time-of-flight to energy spectra, but have not been corrected for spectrometer efficiency or otherwise manipulated. Fig. 4a shows the oxygen-nitrogen region of the spectrum in Fig. 3 with background subtracted using a cubic polynomial. Fig. 4b was obtained similarly from another target with nominal nitride thickness of 8 nm. It is clear from comparing these spectra that significant structural information is present. However, to assess the quality of this information we must estimate the instrumental resolution in this energy range. This is an especially difficult task because of the difficulty of obtaining a target and verifying that a target is truly thin. Normally useful candidates such as evaporated Au on Si,

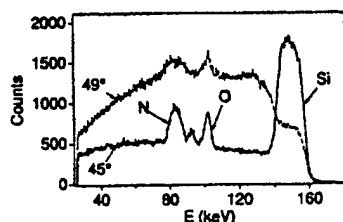


Fig. 3. Backscattering energy spectra of 270 keV  $\alpha$  particles incident on a target with nominal composition of  $\text{SiO}_2$ , 2 nm;  $\text{Si}_3\text{N}_4$ , 7 nm;  $\text{SiO}_x$ , 1.5 nm; Si (crystalline). At an orientation of  $45^\circ$ , the beam channels in the Si substrate. The  $45^\circ$  spectrum used 0.24 mC of charge while the  $49^\circ$  spectrum used 0.12 mC.

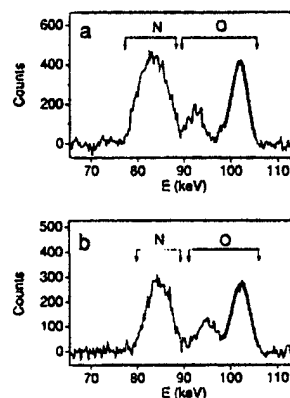


Fig. 4. (a) An expanded view of the region of Fig. 3 containing the oxygen and nitrogen features. Background has been subtracted using a cubic polynomial. The heavy solid line on the surface oxygen feature near 104 keV is the result of a fit of the data to the difference of two error functions. (b) The nitrogen-oxygen region of a second sample showing what appears to be a narrower  $\text{Si}_3\text{N}_4$  layer. This measurement used only  $3/4$  the charge of the one shown in part (a). The fit to the surface oxygen peak is shown by a heavy solid line.

which are adequate for proton backscattering, are not useful for  $\alpha$  backscattering because of the non-uniformity, both laterally and in depth, of the Au. (In fact, for this particular case, Au can be observed migrating in the substrate under prolonged irradiation.)

Using the standard deviation of the time of flight for  $\alpha$  particles backscattered from Si obtained from the simulation described above, along with an estimate of the timing and secondary electron contributions to uncertainty of 0.44 ns obtained from the proton scattering data, and expressing this as an energy uncertainty, we conclude that the instrumental resolution in the region of the Si edge is  $\approx 2.3$  keV. This is substantially smaller than the 4 keV observed by fitting the data of Fig. 3 to a difference of error functions, but this comparison is inappropriate because of the complicated structure of this target. Other samples of device-grade Si have yielded edges as sharp as  $2.8 \pm 0.7$  keV suggesting that the model is in reasonable agreement with the data.

For oxygen, the proton data indicate a timing resolution of 0.9 ns. Together with the standard deviation from the simulation this predicts an energy resolution of 1.7 keV. This estimate suggests that the oxygen peaks in Fig. 4 are wide enough to contain structural information. The broad smooth curves superimposed on the oxygen feature near 100 keV in Figs. 4a and 4b represent a fit to the difference of two error functions. The energy spread in the transition from 12 to 88% of peak height indicates  $2.8 \pm 0.7$  keV resolution. Less complex samples lead to values as small as  $1.8 \pm 0.3$  keV. Therefore, we adopt the modeled resolution of 1.7 keV to estimate the system's optimum resolution for oxygen in the  $\text{SiO}_2$  layer. This energy resolution

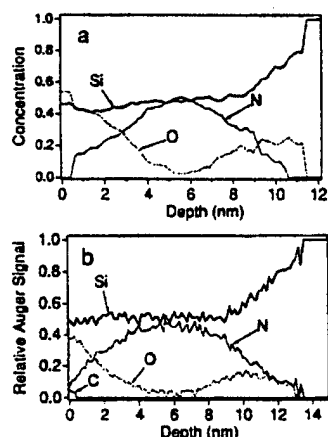


Fig. 5. (a) Depth profile obtained from the data shown in Fig. 3. (b) Auger depth profile of the same sample. Curves are relative and not normalized to concentrations. The depth scale is normalized using the backscattering data.

translates to a depth resolution for oxygen in  $\text{SiO}_2$  of 1.7 nm at the incident and scattering angles used in this experiment. Therefore, we conclude that Figs. 4a and 4b do indeed have information about the target structure near the surface.

The degradation in resolution with depth has been examined in detail by Williams and Möller [4]. Our resolution is approximately comparable to that which they obtained using a magnetic spectrometer. Although their work suggests that it should be possible to reach this level of resolution near the surface using conventional backscattering with a surface barrier detector, to do so would require a very steep target angle at which the advantage of background suppression afforded by the  $\langle 110 \rangle$  channel would not be present.

Fig. 5a shows a depth profile derived from the data of Fig. 3 using the same procedure which we have used successfully for a number of years to profile thicker semiconductor device structures from conventional backscattering data [5]. It is, of course, necessary to make some assumptions about target density in order to return a true depth profile. We assume that the bulk density of  $\text{SiO}_2$ ,  $2.22 \text{ g/cm}^3$ , applies when the oxygen concentration exceeds that of nitrogen and, conversely, that the bulk  $\text{Si}_3\text{N}_4$  density,  $3.44 \text{ g/cm}^3$ , applies when nitrogen exceeds oxygen. In light of the resolution inferred above, we conclude that the boundaries of the layers of this target are not

abrupt, but that there are measurable transition regions of intermediate composition. This conclusion is supported by the Auger depth profile shown in Fig. 5b. Note especially that the nitrogen signal begins to rise almost immediately after the erosion of the surface has begun. This is accompanied by a similarly rapid decrease in the oxygen signal. The similarity of the profiles in Figs. 5a and 5b is striking given the difference in the techniques used to produce them. These data suggest that depth resolutions of  $\approx 2 \text{ nm}$  can be achieved in targets such as these. Differences between the spectra of Figs. 5a and 5b such as the relative concentrations at depths greater than  $\approx 9 \text{ nm}$  will be the subject of future research.

#### 4. Conclusion

An improved time-of-flight spectrometer design has significantly reduced the contribution to measurement uncertainty from path length variability and kinematic dispersion. By using favorable target orientation to maximize ion path lengths and suppress background, depth profiles of silicon-oxide/silicon-nitride multilayers with approximately 2 nm depth resolution have been measured. The technique appears to be well suited for studying both the structure and composition of gate oxides and diffusion barriers as thin as 10 nm or even less.

#### Acknowledgements

This work was supported by a grant from Texas Instruments, Inc., by the U.S. Army Research Office under contract DAAL 03-92-G-0037 and by Sandia National Laboratories under contract AH-3292.

#### References

- [1] R.A. Weller, J.H. Arps, D. Pedersen and M.H. Mendenhall, Nucl. Instr. and Meth. A 353 (1994) 579.
- [2] J.A. Knapp and J.C. Banks, Nucl. Instr. and Meth. B 79 (1993) 457.
- [3] M.H. Mendenhall and R.A. Weller, Nucl. Instr. and Meth. B 40/41 (1989) 1239.
- [4] J.S. Williams and W. Möller, Nucl. Instr. and Meth. 157 (1978) 213.
- [5] J.A. Keenan, unpublished.

# Time-of-flight elastic recoil analysis of ion beam modified nitrocellulose thin films

James H. Arps, Robert A. Weller \*

*Vanderbilt University, Nashville, Tennessee 37235-1807, USA*

## Abstract

The erosion properties of nitrocellulose ( $C_6H_7N_3O_{11}$ ) thin films on Si have been studied under exposure to 270 keV H, He, C, and Ar ions. Time-of-flight elastic recoil spectrometry has been applied to determine the atomic composition of the films as a function of deposited charge. All exposed films exhibit an initial removal of N and O consistent with RO–NO<sub>2</sub> bond breaking, proceeding at a rate that appears to depend on the density of electronic excitation. A non-volatile, carbon-rich residue remains after prolonged exposure to H, He, and C ions, while the film is effectively removed under Ar irradiation. Experimental evidence supports the proposition that binary collisions are an important mechanism affecting desorption of the H and C components. The results are consistent with a suggestion that complete volatilization of the film is determined by the nuclear stopping power of the incident ion.

## 1. Introduction

The response of nitrocellulose to energetic ions is quite unusual. The material volatilizes completely under certain irradiation conditions, otherwise forming a radiation-hard residue. This property, frequently referred to as “self-development”, can be practically applied in lithography as a positive resist, or as a negative resist using the residue, to produce structures with lateral dimensions less than 100 nm [1]. Previous workers have attempted to identify the parameters affecting the nitrocellulose etch rate and the conditions under which a residue is formed. Kaneko et al., have reported that both the ion mass and energy play a role in the observed erosion behavior, suggesting a mechanism dependent on the electronic and nuclear energy losses of the ion in the material [2,3]. Mühle and Götz observed an initial etch rate independent of ion mass and found no correlation between the removed thickness and the total deposited ion energy [4]. Moliton et al., report etch rates dependent on the total energy loss with no effects tied to the individual nuclear and electronic losses [5].

A common method for measuring nitrocellulose film evolution has been surface profilometry. Unfortunately, the technique is insensitive to any changes in chemical composition during exposure. The use of a profilometer may also restrict the minimum thickness of films that may be stud-

ied. Perhaps because of this, many previous experiments have used films with an initial thickness greater than the projected range of the irradiating ions. Attempts to identify the individual contributions due to electronic or nuclear energy loss are complicated by significant variation in these values along the ion trajectory. Infrared spectroscopy has also been applied to study the evolution of the nitrocellulose chemical structure, and a number of reaction pathways have been suggested [6]. However, it may not be possible to identify the dominant reactions without quantitative information on the film stoichiometry.

In an attempt to further understand the erosion behavior of nitrocellulose, we have applied medium energy time-of-flight elastic recoil detection to the analysis of 270 keV H, He, C, and Ar ion irradiated thin films on silicon. This technique can simultaneously measure in situ the evolution of the individual atomic components in the film as a function of the accumulated dose. Thicknesses less than 20 nm were studied to minimize the variation in the nuclear and electronic energy loss as ions penetrate the film. The initial loss of nitrogen and oxygen for all exposures is generally compatible with desorption of NO<sub>2</sub>. Further, the change in N and O content appears to scale with the total deposited electronic energy density. These results provide at least circumstantial evidence that RO–NO<sub>2</sub> bond breaking is one of the dominant processes. For the cases of H, He and C exposure, a carbonaceous layer persists after prolonged exposure. The complete removal of the film by Ar irradiation suggests that binary collisions associated with nuclear energy loss are an important factor in determining the onset of volatilization.

\* Corresponding author. Tel. +1 615 343 7225, fax +1 615 343 7263, e-mail [weller@vuse.vanderbilt.edu](mailto:weller@vuse.vanderbilt.edu).



## 2. Experiment

A stock solution of nitrocellulose ( $C_6H_7N_3O_{11}$ )<sub>n</sub> in amyl acetate was diluted to a concentration of 1.5%. Using a syringe and a #18 needle, a single drop of liquid was cast on the surface of a deionized water bath. After allowing the solvent to partially evaporate, the film was drawn onto a clean 1-inch silicon wafer (Virginia Semiconductor). Each sample was dried in air for 30 minutes, then heated in a  $N_2$  ambient at 80°C for another 30 minutes to remove any remaining solvent. A thickness of 17 nm was estimated based on the weight of a drop of solution, the area of the cast film, and a density of 1.2 g/cm<sup>3</sup> for nitrocellulose.

The samples were placed in a vacuum chamber with a nominal base pressure of  $10^{-8}$  Torr.  $H^+$ ,  $He^+$ ,  $C^+$  and  $Ar^+$  ions were accelerated to 270 keV and directed at normal incidence to the samples. During each irradiation, the ions were rastered over a  $0.6 \pm 0.1$  cm<sup>2</sup> area with a current density of approximately 0.02  $\mu A/cm^2$ . At predetermined intervals, the exposures were interrupted and time-of-flight elastic recoil detection was used to measure the atomic composition of the film.

Complete descriptions of the time-of-flight detection scheme and its application to the detection of light elements are given elsewhere [7,8]. Briefly, a beam of 810 keV  $Ar^{3+}$  ions is directed at an angle of 21° to the sample surface. Light element recoils from the film, Si atoms from the substrate, and the scattered beam are detected at a 42° forward scattering angle relative to the initial beam direction. The particles pass through a thin carbon foil and generate one or more secondary electrons that, when detected by a microchannel plate, trigger a start pulse. The particles themselves generate a stop signal at a second microchannel plate after traversing a 37 cm flight path. Although the recoil energies determined by collision kinematics are usually larger for high-mass recoils, light atom recoils have the greater velocity and are well separated from Si and Ar events in the time-of-flight spectrum. The total number of ions needed to obtain each measurement was  $1 \times 10^{11}$ . By working at beam energies lower than for conventional elastic recoil detection, the total energy deposited in the sample is reduced and sensitivity to light elements is enhanced, due to the larger recoil cross sections. Hence, the damage to radiation sensitive material is minimized during analysis.

## 3. Results and discussion

A representative time-of-flight spectrum for a pristine nitrocellulose film is shown in Fig. 1a. Recoil H is easily identified, while overlap of the recoil C, N, and O features is observed due to straggling and energy loss in the film from both the incident Ar and recoil species. In short, the film is of sufficient thickness to cause a light element

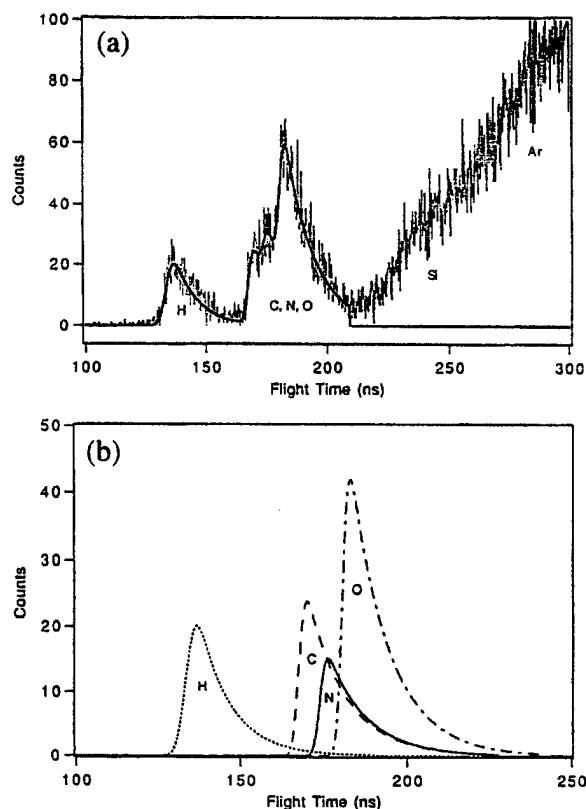


Fig. 1. (a) 810 keV  $Ar^{3+}$  time-of-flight spectrum and least-squares fit for a nitrocellulose thin film on Si.  $1 \times 10^{11}$  ions were deposited in the analysis. (b) Individual contributions of recoil H, C, N and O from the fit in (a).

recoil emerging from some depth within the film to have the same velocity as a heavier recoil near the surface. Though the profiling of much thinner layers could have reduced or eliminated this overlap, the erosion of the film then progresses too rapidly for a detailed series of measurements to be made. In order to extract the atomic concentrations of H, C, N, and O for each analysis, a peak fitting algorithm was employed. The time-of-flight distribution  $f(z)$  of a particular recoil species from a thin uniform layer, modified by energy loss and straggling, can be described empirically by a function that is the convolution of a Gaussian with a decaying exponential.

$$f(z) = \frac{Ak}{2} \exp \left[ \frac{k(k\sigma^2 - 2(z - z_0))}{2} \right] \times \left( 1 - \operatorname{erf} \left[ \frac{\sigma}{\sqrt{2}} \left( k - \frac{z - z_0}{\sigma^2} \right) \right] \right), \quad (1)$$

where  $f(z)$  has been normalized so that  $A$  gives the total yield,  $k$  is the decay constant,  $\sigma$  the Gaussian standard deviation, and  $z_0$  is the calculated flight time corresponding to recoils from the surface. The complete fitting function is the sum of the contributions in the form given in

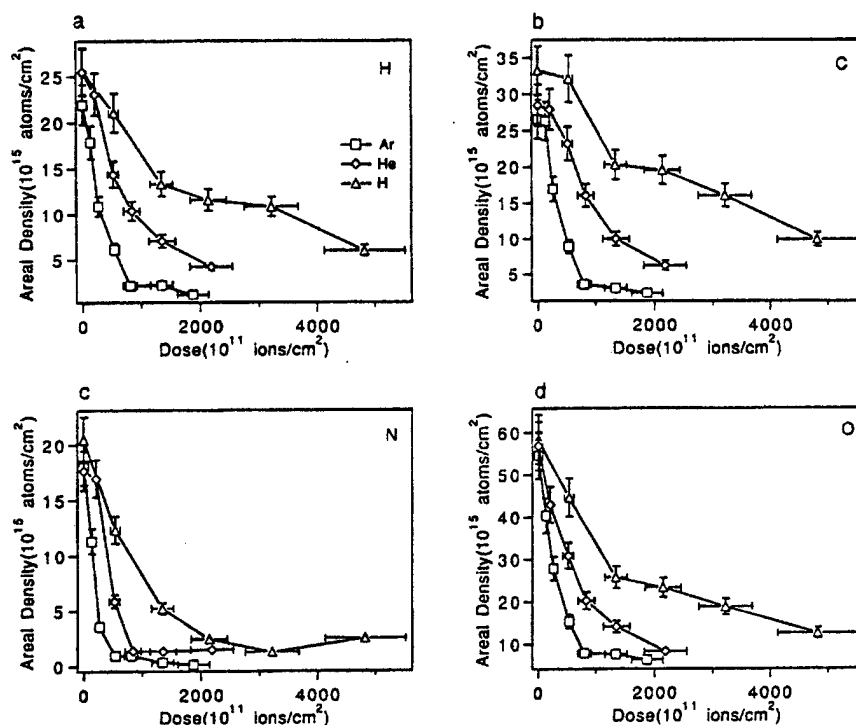


Fig. 2. (a)–(d) Change in the components H, C, N and O as a function of dose for Ar ( $\square$ ), He ( $\diamond$ ), and H ( $\triangle$ ) irradiation. The points are connected to aid the eye.

Eq. (1) for each component of the film. A total of eight parameters were used, including a yield for each of the four elements and a decay constant and width for H. A

single decay constant and width were assumed in describing C, N, and O, since the recoil velocities and energy loss characteristics are similar. The result of this general, non-

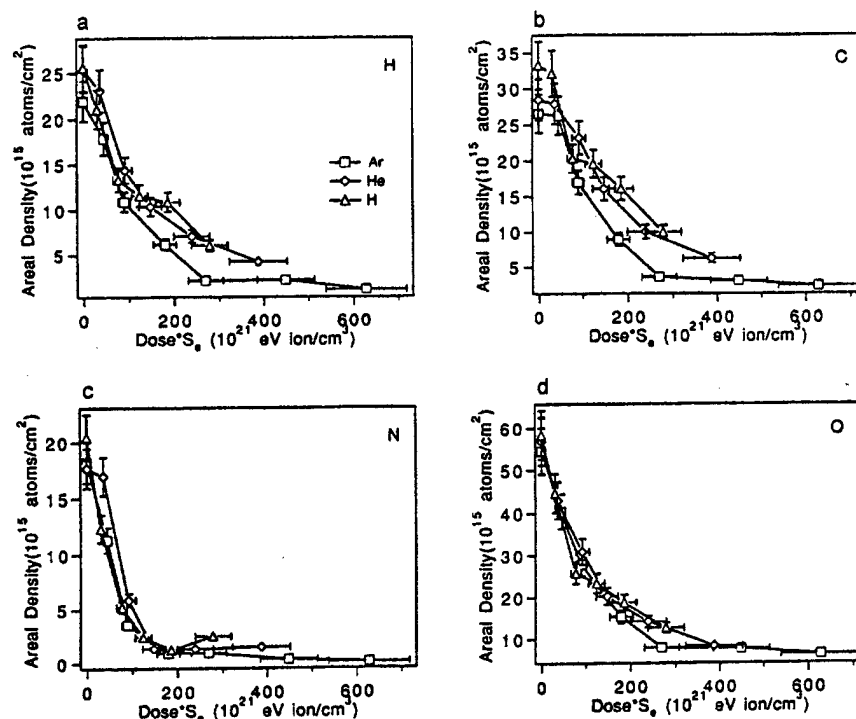


Fig. 3. (a)–(d) Change in the components H, C, N and O with the electronic energy density for Ar ( $\square$ ), He ( $\diamond$ ), and H ( $\triangle$ ) irradiation.

linear least squares fit to the data, with uncertainties determined by counting statistics, is also shown in Fig. 1a. The observed value of  $\chi^2$  for this fit, 376.2 for 368 degrees of freedom, was typical of the results obtained for all analyses. Fig. 1b shows the individual contributions of each species to the time-of-flight spectrum in Fig. 1a. For each computed yield, the areal density was calculated based on measured values for the detector efficiency, the Lenz–Jensen recoil cross section, and the number of incident ions. The initial stoichiometry and thickness generally agree with predicted values to within the  $\pm 10\%$  estimated uncertainty.

The evolution of the atomic components of the nitrocellulose film, subject to H, He, and Ar irradiation, is shown in Fig. 2 as a function of the dose. The data for C exhibits a rate of removal between those for He and Ar but are omitted from the graphs in order to simplify presentation and because of a smaller initial sample thickness. Not unexpectedly, the removal rate increases with the mass of the incident ion. It is important to note that the ions used in erosion differ greatly in both their relative and absolute values of the electronic and nuclear energy loss,  $S_e$  and  $S_n$ . Using an implementation of the TRIM algorithm [9], the electronic stopping power in nitrocellulose has been calculated to be 57.9, 177, 305, and 335 eV/nm for 270 keV H, He, C, and Ar ions while the nuclear stopping is 0.055, 0.735, 13.7 and 198 eV/nm, respectively. Studies of the ion beam modification of polymers other than nitrocellulose have suggested that electronic excitations alter the chemical structure creating ionized molecules, collective excitations, and highly excited species [10]. Fig 3 shows the variation of H, C, N, and O with the product of dose and electronic energy loss. While a scaling with the total deposited energy may not be ruled out completely, the overlap of the N and O curves suggests that the density of electronic energy deposition is a key parameter influencing the desorption of these components. From the basic structure of the nitrocellulose repeat unit, shown in Fig. 4, a

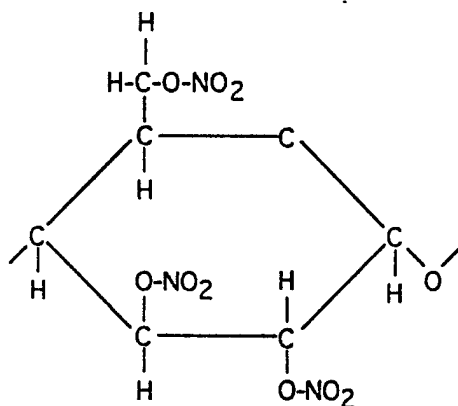


Fig. 4. Chemical structural formula of the nitrocellulose.

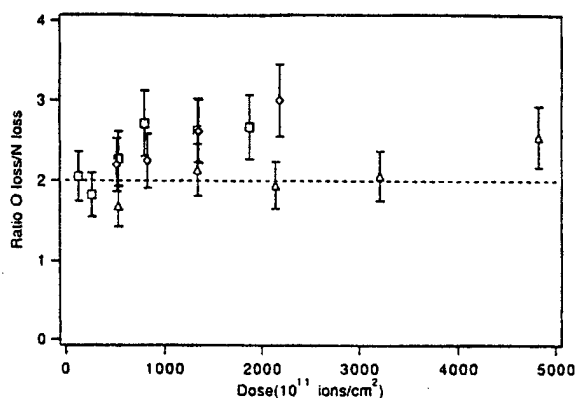


Fig. 5. Ratio of oxygen to nitrogen loss as a function of dose for Ar ( $\square$ ), He ( $\diamond$ ), and H ( $\triangle$ ) irradiation. The dashed line indicates the ratio consistent with the stoichiometry of  $\text{NO}_2$ .

likely path for the removal of N and O is the breaking of radical  $\text{O}-\text{NO}_2$  bonds. It has been previously suggested that under thermal annealing,  $\text{RO}-\text{NO}_2$  bond breaking acts as a trigger for the total decomposition of the molecule [11]. Additional evidence for this mechanism can be seen in the stoichiometry of the removal of N and O. The ratio of removed oxygen to removed nitrogen is plotted as a function of the accumulated dose in Fig. 5. For each of the incident ions, the initial ratio is consistent with the selective excision of  $\text{NO}_2$  fragments. For H irradiation, this ratio is effectively maintained throughout the exposure and may indicate the formation of a residue.

Examination of the erosion curves in Figs. 2a and 2b shows essentially complete removal of H and C under Ar irradiation. The remaining coverage of light elements is approximately the same as that found on a clean Si wafer. This result is not inconsistent with an earlier suggestion of a threshold based on a total energy loss of 350 eV/nm for volatilization of the residue [4]. For H, He and C irradiation, a carbon-rich, oxygen-depleted layer remains, suggesting that highly cross-linked, carbon networks could be formed by the reaction between adjacent radicals. The remaining residue is nearly twice as thick after H exposure compared with similar data for He while no statistically significant difference in stoichiometry is noted. For H and He irradiation, the overlap of the plots of removed H and C in Figs. 3a and 3b may point to a common bond breaking mechanism also based on electronic excitation. The H and C curves for Ar irradiation appear to overlap initially but decrease quickly as the film is removed. An additional mechanism is needed to explain the removal of the residue by Ar. As evidenced by the large difference in nuclear stopping between Ar and H or He, binary collisions could likely play a key role. Using the empirical formula of Matsunami et al. [12], comparative estimates of sputtering yields for carbon by 270 keV Ar, He, and H are 0.72, 0.002, and  $9.7 \times 10^{-5}$  atoms/ion, respectively.

Given that roughly  $5 \times 10^{15}$  atoms/cm<sup>2</sup> of carbon remain after He erosion, an exposure equal to the accumulated Ar dose,  $\sim 2 \times 10^{14}$  ions/cm<sup>2</sup>, could not remove this residue. Hence, simple differences in physical sputtering appear inadequate to explain complete removal of the film by Ar given the residue left by He. It appears more likely that a desorption mechanism incorporating collisional sputtering would proceed in conjunction with the bond breaking generated by electronic excitations rather than after the formation of a residue.

#### 4. Conclusion

Medium energy time-of-flight elastic recoil detection has been applied in the study of the real-time evolution of the atomic composition of nitrocellulose under H, He, C, and Ar ion irradiation. The technique has been shown to be a useful tool for the study of these radiation sensitive materials. The initial stoichiometry of desorbed N and O is consistent with a reaction involving the breakage of RO-NO<sub>2</sub> bonds. Good correlation is obtained between the removal of N and O and the electronic energy loss under all irradiation conditions. Removal of H and C show a similar scaling for H and He ions but differs for Ar because of the complete removal of the residue. The larger number of binary collisions experienced by Ar ions, as indicated by the higher nuclear stopping power and sputtering yield, is probably responsible for this observed behavior.

#### Acknowledgments

This work was supported in part by the U.S. Army Research Office under contract DAAL 03-92-G-0037.

#### References

- [1] M.W. Geis, J.N. Randall, T.F. Deutsch, N.N. Efremow, J.P. Donnelly and J.D. Woodhouse, *J. Vac. Sci. Technol.* B 3 (1985) 343.
- [2] H. Kaneko, Y. Yasuoka, K. Gamo and S. Namba, *Jpn. J. Appl. Phys.* 28 (1989) 716.
- [3] H. Kaneko, Y. Yasuoka, K. Gamo and S. Namba, *Jpn. J. Appl. Phys.* 28 (1989) 1113.
- [4] R. Mühle and G. Götz, *Nucl. Instr. and Meth. B* 46 (1990) 347.
- [5] J.P. Moliton, T. Triguad and A. Moliton, *Nucl. Instr. and Meth. B* 65 (1992) 428.
- [6] L. Merhari, J.P. Moliton, and C. Belorgeot, *J. Appl. Phys.* 68 (1990) 4837.
- [7] M.H. Mendenhall and R.A. Weller, *Nucl. Instr. and Meth. B* 40/41 (1989) 1239.
- [8] J.H. Arps and R.A. Weller, *Nucl. Instr. and Meth. B* 79 (1993) 539.
- [9] J.P. Biersack and L.G. Haggmark, *Nucl. Instr. and Meth.* 147 (1980) 257.
- [10] G. Marletta, *Nucl. Instr. and Meth. B* 46 (1990) 295.
- [11] H. Kaneko, Y. Yasuoka, K. Gamo and S. Namba, *J. Vac. Sci. Technol. B* 1 (1989) 1778.
- [12] N. Matsunami et al., *Atom. Data Nucl. Data Tables* 31 (1984) 1.



ELSEVIER

# The impact of spectrometer efficiency on the trace-element sensitivity of time-of-flight medium energy backscattering

Robert A. Weller \*

*Vanderbilt University, Nashville, Tennessee 37235, USA*

## Abstract

The intrinsic efficiency of a time-of-flight spectrometer which derives timing information from the passage of an ion through a carbon foil is governed primarily by secondary electron emission and multiple scattering in the foil and by the intrinsic responses of the detectors which generate the time markers. For all ions except hydrogen, the efficiency is a monotonically increasing function of energy in the range up to a few hundred keV used for medium energy backscattering. Combining expressions for spectrometer efficiency and trace element sensitivity obtained previously, we show that for a given ion the product of scattering cross section and spectrometer efficiency determines an optimum energy for trace element analysis by backscattering. The optimum choice of ion is a function of the mass of the trace element under investigation. If the limit of sensitivity is determined by sputtering, then light elements such as He appear to be unconditionally superior to heavy projectiles such as C or N. However, the numerical value of the limiting sensitivity for a given trace element is strongly influenced by the details of the sputtering and the degree of beam induced mixing at the surface. For elements in the region of Fe to Cu reasonable assumptions about sputtering lead to the conclusion that sensitivities of about  $3 \times 10^{10} \text{ cm}^{-2}$  are achievable using 100 keV  $\text{He}^+$  projectiles and a spectrometer which subtends a solid angle of 1 msr.

## 1. Introduction

One of the most promising applications of medium energy backscattering is in the detection of trace elements particularly on silicon where minute amounts of transition metal contaminants can cause device failure. The general trend of the scattering cross section, typified by the Rutherford case where  $\sigma \propto z_1^2/E^2$ , where  $z_1$  is the atomic number of the projectile and  $E$  its energy, seems to indicate that heavy ions at low energies should provide the greatest sensitivity for trace element detection [1]. However, this assumes that the detector of backscattered particles is equally sensitive to ions of all masses and energies. When a surface barrier detector is being used, this is a reasonably accurate assumption, provided the energies are high enough. For time-of-flight spectrometers, however, there is a species and velocity dependent efficiency which cannot be ignored.

In this paper, we will consider the behavior of time-of-flight spectrometers which derive their timing information from the interval between the detection of secondary electrons emitted as a particle passes through a thin carbon foil, and the particle's subsequent impact on a microchan-

nel plate [2]. The efficiency of such a spectrometer is determined primarily by secondary electron emission and multiple scattering in the foil and by the intrinsic efficiencies of microchannel plates for detecting electrons and heavy particles [3]. In the expression for the yield of backscattered particles, the spectrometer's efficiency and scattering cross section may be grouped together to form a single, energy dependent effective cross section which, for most ions which are candidates to use in backscattering, has a maximum in the range of a few hundred keV.

In this publication, we will explore the behavior of the effective cross section and its implications for the minimum measurable areal densities of various elements. Before presenting the results of these computations, we will briefly describe the spectrometer efficiency model and sputtering-limited sensitivity model which have been used to obtain them.

## 2. Computational method

The backscattering yield  $Y$  from a dispersed layer of atoms with areal density  $\rho$  is given in terms of the differential scattering cross section  $\sigma$ , and number  $N$  of incident particles by

$$Y = N\rho\sigma\Omega\eta, \quad (1)$$

\* Tel. +1 615 343 7225, fax +1 615 343 7263, e-mail [weller@vuse.vanderbilt.edu](mailto:weller@vuse.vanderbilt.edu).

where  $\Omega$  is the solid angle subtended by the detector and  $\eta$  is the intrinsic efficiency for detecting a backscattered particle. Since for a time-of-flight spectrometer both  $\sigma$  and  $\eta$  are dependent upon energy, it is reasonable to group them together into a single effective cross section  $\sigma(E)\eta(KE)$ , where  $E$  is the beam energy and  $K$  the kinematic factor associated with the collision. The quantity  $\sigma\eta$  is a figure of merit for trace element sensitivity since, when it is large, a relatively lower density  $\rho$  of target atoms will produce a statistically significant backscattering yield.

The intrinsic efficiency of time-of-flight spectrometers has recently been the subject of both experiments and mathematical modeling in our laboratory [3,4]. We have found good agreement with measurements using the following expression:

$$\eta = ATf(1 - e^{-\lambda \Delta S_c})(1 - e^{-\gamma(1 - e^{-\gamma_s(1 - e^{-\gamma_d(\dots)})})}), \quad (2)$$

where  $\gamma$  is the secondary electron yield of ions striking the stop detector,  $\gamma_s$  is the mean secondary electron yield of electrons in the channels of the stop detector, and  $g$  is defined by:

$$\gamma(1 - e^{-\gamma_s(\dots)}) \equiv g \Lambda_n S_{MCP}. \quad (3)$$

Here  $A$  is the open area of a microchannel plate;  $T$  is the transmission of all meshes along the trajectory of an ion in the spectrometer;  $f$  is the energy dependent fraction of particles which fall within the active area of the stop detector after being multiply scattered by the carbon start foil [5];  $\Delta S_c$  is the secondary electron yield of the start foil;  $\lambda$  is the probability that a secondary electron will trigger the start detector; and finally,  $g \Lambda_n \cdot S_{MCP}$  is a term representing the response of the stop detector to ions. Each of the terms  $S_c$ ,  $S_{MCP}$ , and  $f$ , representing (respectively) the stopping power of the ion in the start foil, the stopping power in the stop microchannel plate surface, and multiple scattering in the start foil, are strongly energy dependent for ions in the range up to a few hundred keV. As a result, the efficiency is small for low energy ions and, at a given energy, decreases with increasing atomic number because of the dominant effect of the multiple scattering term. In the curves presented below,  $\eta$  has been computed with parameter values described in Ref. [3], with the only exception being that a value of  $A$  was used for heavy ions which matches most closely the observed performance of our backscattering spectrometer rather than a compromise between our backscattering and forward scattering spectrometers.

In order to estimate the minimum measurable areal density of a surface layer, it is necessary to place some limits on the experimental conditions. From a practical point of view, time must certainly play a role as do other considerations such as background in the region of interest, multiple scattering in the target and the sputter removal of the layer by the beam being used to analyze it. In Ref. [2]

we established an expression for the minimum areal density which can be measured with fractional uncertainty  $\varepsilon$  in the presence of background  $B$  from all sources including multiple scattering in the substrate and random coincidences associated with count rate. The criterion used was that the fractional statistical uncertainty of the measurement equals the fraction of material removed by sputtering. The resulting expression is:

$$\rho = \frac{1 + \sqrt{1 + 4\varepsilon^2 B}}{2\varepsilon^3} \frac{Y_s}{\rho_s A_s \Omega(\sigma\eta)}. \quad (4)$$

Here  $A_s$  is the area of the target which is irradiated by the beam. This expression is based upon the assumption that the probability  $P$  that a beam ion removes a target atom is related to the sputtering yield of the substrate  $Y_s$  through the relation,

$$P \approx Y_s \frac{\rho}{\rho_s}, \quad (5)$$

where  $\rho_s$  is interpreted as the areal density of substrate atoms in the region from which sputtered particles are drawn. Eq. (5) expresses the assumption that trace elements are sputtered randomly from the surface with a probability equal to their fractional representation in the volume from which sputtered particles can emerge. As described below, this assumption is probably too conservative.

Expression (4) describes a more general limit than simple detectability which without specific definition is not a precise concept. In the computations presented below, a minimally detectable  $\rho_{\min}$  will be taken to be one for which  $\varepsilon = 0.3$ , which may be viewed as a non-zero signal with a confidence level of approximately three standard deviations. It is also assumed that  $B = 0$ . The result for  $B \neq 0$  (or a different  $\varepsilon$ ) can be obtained by scaling the graphs below by the leading factor in Eq. (4).

### 3. Results

Figs. 1 and 2 show, as a function of energy, the effective cross section for a number of ions incident on Cu

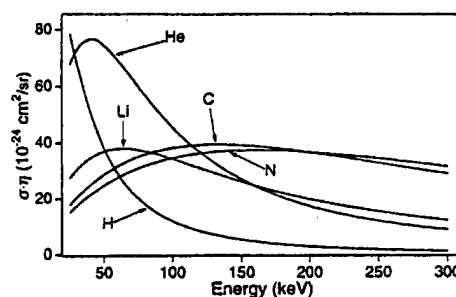


Fig. 1. The effective cross section for various ions scattering from Cu as a function of incident projectile energy. The scattering angle is 150°.

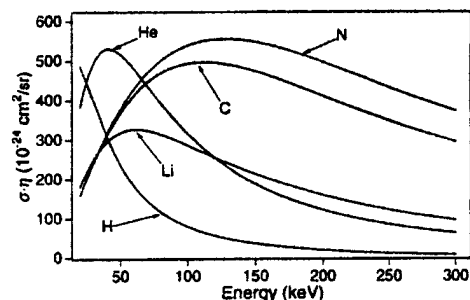


Fig. 2. The effective cross section for various ions scattering from Au as a function of incident projectile energy. The scattering angle is 150°.

and Au. The cross section  $\sigma$  is taken to be the Lenz-Jensen [6] screened cross section and is computed without approximation using methods similar to those described in Ref. [7]. The efficiency  $\eta$  is computed as described above. For all ions except H, the combination of screening and spectrometer efficiency is adequate to produce a maximum in the effective cross section. Perhaps most surprisingly, for detecting Cu, helium achieves greater sensitivity than heavy ions up to an energy somewhat larger than 100 keV. It is important to note that this is on a projectile-for-projectile basis and does not yet take account of the greater sputtering of the heavy ions. For Au, on the other hand, a nitrogen beam in the range of 125 keV would be preferred according to Fig. 2. These figures indicate that lithium offers no particular advantage in either case, at least so far as effective cross section is concerned.

Fig. 3 shows the energy at which  $\sigma\eta$  is maximum for He and N beams as a function of the atomic number  $z_2$  of the target element. For He this energy is remarkably constant and near 40 keV for most elements in the periodic table. For N it varies more strongly at lower masses where the backscattered energy (and therefore the efficiency) is low but remains near 130 keV for a wide range of elements.

Taken together, Figs. 1–3 offer a surprising insight. Picking a convenient energy of, say, 100 keV we see that effective cross section is simply not a very important

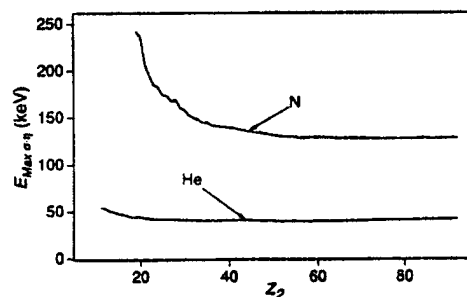


Fig. 3. The energy at which the effective cross section is maximum for He and N projectiles scattering at 150° as a function of the atomic number of the target particle.

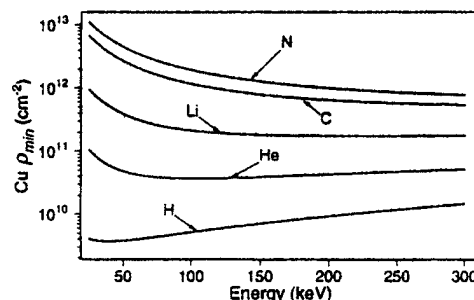


Fig. 4. The sputtering-limited minimum detectable areal density  $\rho_{\min}$  of Cu on Si as a function of beam energy for various projectiles. The geometric solid angle subtended by the spectrometer is assumed to be 0.8 msr.

criterion to use in selecting a beam for maximum sensitivity trace element analysis by time-of-flight backscattering. For beams from He through N, the effective cross section varies by only about 50% throughout the periodic table. Thus, we must look to other effects such as desired mass resolution or the limitations imposed by sputtering when selecting a beam.

In Fig. 4 we add the effects of sputtering and show  $\rho_{\min}$  from Eq. (4) for Cu on Si as a function of beam energy for various beams from H to N. The estimate is based upon the solid angle subtended by our spectrometer, 0.8 msr, and assumes a beam area on target of 0.03 cm². The sputtering yield of Si was computed using the expression of Matsunami et al. [8] and  $\rho_s$  was taken to be  $4 \times 10^{15}$  cm⁻², corresponding to about 3 atomic layers of Si. When sputtering is taken as the limiting process, light ions are seen to have dramatically greater potential for high sensitivity than heavy ions. However, the choice may not be as straightforward as Fig. 4 would seem to imply. Two issues must be considered, run time and the appropriateness of the sputtering model described by eq. (5). Of the former, one predicts that it should take approximately an order of magnitude (about  $10^{16}$  versus about  $10^{15}$ ) more He than N ions to make the measurement. Since it is not possible to compensate by running larger currents without incurring much increased background [2], the measurement with He must be assumed to take ten times longer. The issue of the correctness of the sputtering model is much more subtle.

Initially, if the trace element layer is dispersed and truly surface correlated, then the assumption described above is reasonable, except possibly in cases where a large mismatch in atomic mass between the substrate and trace constituents leads to poor transfer of energy between the two. However, as the analysis proceeds, the target atoms are not only sputtered but also mixed relatively deeply into the substrate where a significant number may be effectively eliminated as candidates to sputter but not to backscatter. Since heavy ions are expected to mix the surface more efficiently than lighter ones, the apparent

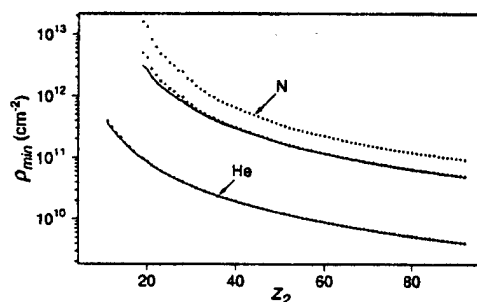


Fig. 5. Minimum detectable areal densities of trace elements using He and N beams as a function of the atomic number of the trace constituent. Solid curves represent measurement with the best beam energy. Dotted curves are for fixed beam energies of 100 keV (upper dotted curve) and 300 keV (lower dotted curve) for N, and 100 keV for He. The spectrometer solid angle is 0.8 msr.

advantage of light atoms derived by their lower sputtering rate may be diminished, at least for runs of constant duration. However, as the effective cross section graph shows, at least for the case of 100 keV He and N being used to measure Cu, it is never completely eliminated on an atom-for-atom basis. We conclude that, because of these considerations, the estimates given here should be regarded as conservative and that lower values of  $\rho_{\min}$  may be achieved if sputtering of the trace layer proceeds (for any reason) more slowly than estimated by Eq. (5).

Fig. 5 summarizes  $\rho_{\min}$  as a function of the atomic number of the target for analyses using N (upper group of curves) and He (lower curve) projectiles. The solid curves are obtained by using the best energy for each ion–target system, determined to be that energy for which the absolute minimum  $\rho_{\min}$  is obtained. For the analysis of copper, these correspond to the minima of the curves in Fig. 4. Also shown are three dotted curves. The upper dotted curve is for analysis with N at a fixed beam energy of 100 keV. Fixed-energy analysis is almost indistinguishable from best-energy analysis for He and N at 100 keV and 300 keV, respectively, as shown by the remaining dotted curves.

#### 4. Conclusion

Using a newly derived expression for time-of-flight spectrometer efficiency which has been shown to be in good agreement with experimental observations, we have revisited the problem of estimating the ultimate sensitivity of trace element analysis by medium energy backscattering with the objective of gaining insights which might be

useful in selecting effective experimental conditions. We find that the apparent advantage of heavy ions at low energies is less dramatic or even absent when screening of collisions and spectrometer efficiency are considered, and that the dominant roles of sputtering and spectral background, such as that caused by multiple scattering in the target, are clearly evident. For general trace element analysis, beams of 100 keV He or of 300 keV N are close to optimum with He being preferred for greatest sensitivity for elements near Cu in the periodic table. Using a spectrometer with characteristics similar to ours, one would expect, in the absence of background, to achieve a  $\rho_{\min}$  for Cu on Si of about  $3 \times 10^{10} \text{ cm}^{-2}$  with 1 msr of geometric solid angle. With large-solid-angle detectors, values of  $\rho_{\min}$  of  $< 10^9 \text{ cm}^{-2}$  appear possible under optimum conditions. Lower  $\rho_{\min}$  values for heavy ions than those computed here may result from the use of a sputtering model which properly incorporates the effects of ion beam mixing. Ultimately, the per-incident-ion rate of removal of trace elements on a surface must be settled by experiment. Only then can the sputtering-limited  $\rho_{\min}$  be established with confidence. In all likelihood, however, below areal densities of  $10^9 \text{ cm}^{-2}$ , considerations of background will dominate.

#### Acknowledgements

This work was supported in part by the U.S. Army Research Office under contract DAAL 03-92-G-0037 and by Sandia National Laboratories under contract AH-3292.

#### References

- [1] J.A. Knapp and J.C. Banks, Nucl. Instr. and Meth. B 79 (1993) 457.
- [2] R.A. Weller, Nucl. Instr. and Meth. B 79 (1993) 817.
- [3] R.A. Weller, J.H. Arps, D. Pedersen and M.H. Mendenhall, Nucl. Instr. and Meth. A 353 (1994) 579.
- [4] J.H. Arps and R.A. Weller, Nucl. Instr. and Meth. B 90 (1994) 547.
- [5] M.H. Mendenhall and R.A. Weller, Nucl. Instr. and Meth. B 93 (1994) 5.
- [6] P. Loftager, F. Besenbacher, O.S. Jensen and V.S. Sorensen, Phys. Rev. A 20 (1979) 1443.
- [7] M.H. Mendenhall and R.A. Weller, Nucl. Instr. and Meth. B 58 (1991) 11.
- [8] N. Matsunami, Y. Yamamura, Y. Itikawa, N. Itoh, Y. Kazumata, S. Miyagawa, K. Morita, R. Shimizu and H. Tawara, Atom. Data Nucl. Data Tables 31 (1984) 1.



Erratum

Erratum to: "The impact of spectrometer efficiency on the trace-element sensitivity of time-of-flight medium energy backscattering" [Nucl. Instr. and Meth. B 99 (1995) 491] <sup>\*</sup>

Robert A. Weller <sup>\*</sup>

*Vanderbilt University, Nashville, TN 37235, USA*

Received 18 October 1995

Eq. (4) of the cited article contains a typographical error due to the author. A numeral set as "4" should have been an "8". The correct equation is:

$$\rho = \frac{1 + \sqrt{1 + 8\varepsilon^2 B}}{2\varepsilon^3} \frac{Y_s}{\rho_s A_s \Omega(\sigma\eta)}.$$

The expression first appeared as Eq. (6) of Nucl. Instr. and Meth. B 79 (1993) 817, where it was set correctly.

---

<sup>\*</sup> SSDI of original article: 0168-583X(94)00578-8.

<sup>\*</sup> Corresponding author. Tel. +1 615 343-7225, fax +1 615 343-7263, e-mail [weller@vuse.vanderbilt.edu](mailto:weller@vuse.vanderbilt.edu).

# Adaptation of particle-telescope technology for medium energy ion beam analysis

James H. Arps, Mark E. Miklis, and Robert A. Weller  
*Vanderbilt University, Nashville, Tennessee 37235-1807*

(Received 10 November 1993; accepted for publication 31 January 1994)

Medium energy (100–300 keV) time-of-flight spectrometry for surface analysis uses the correlated detection of an energetic ion and the secondary electrons emitted as it passes through a carbon foil. When microchannel plates are employed in this detection scheme, a typical mean efficiency of detection of less than 30% is achieved. When instead a surface barrier detector is used to detect the ion, providing simultaneous acquisition of velocity and energy information, certain advantages are realized over the two microchannel plate configuration in the characterization of low level constituents of surfaces. Specifically, energy-discriminated gating of the start pulse was observed to nearly eliminate count rate dependent background in a time-of-flight spectrum. Further reduction in background was obtained by the selective elimination of forward recoil species or backscatters from the substrate. Replacement of the stop microchannel plate by a surface barrier detector has resulted in improved detection efficiency for He, as well as provided a means for further study of the processes which affect time-of-flight spectrometer response, including multiple scattering and secondary electron emission in the start foil. In this publication, we describe the application of this particle telescope to the backscattering analysis of gold on silicon and the forward scattering measurement of hydrogen in a self-supporting carbon film.

## I. INTRODUCTION

The term “particle telescope” is generally applied to any detection scheme which records information at two points along the linear trajectory of a particle. Typical measurements include energy loss, total energy, and time-correlated position, from which the particle velocity may be calculated. With knowledge of any two of these parameters, the mass of the particle may be extracted. The first applications of this technology were in nuclear physics, where it was used to characterize recoil nuclei produced by energetic heavy ion reactions.<sup>1</sup> More recently, particle telescopes have been used in the measurement of low Z elements in materials by elastic recoil detection analysis. Organic layers,<sup>2</sup> oxide layers,<sup>3</sup> and implanted materials<sup>4</sup> have been profiled using ion beams with typical atomic numbers from 2 to 20 at energies from 2 to 50 MeV.

In the analysis of the atomic composition of materials using ion beams, it is often sufficient to measure a single quantity such as scattered particle energy or velocity. Our group has applied time-of-flight (TOF) spectrometry using He ions from 100 to 300 keV in the backscattering measurement of thin optical coatings<sup>5</sup> and, recently, to submonolayer coverages of metals on silicon. Control of surface contamination due to iron and nickel is of particular interest to the semiconductor industry in efforts to fabricate defect-free structures. Measurements of heavy metal contaminants on silicon surfaces at levels of the order  $10^{11}$  Pb atoms/cm<sup>2</sup> have been reported using medium energy TOF backscattering with heavy ions.<sup>6</sup> We have also used this method in the analysis of hydrocarbon films by elastic recoil detection.<sup>7</sup> From this experiment, we inferred a sensitivity to hydrogen of order  $10^{13}$  atoms/cm<sup>2</sup>.

Two factors which may hinder further improvement in the sensitivity of ion scattering to either light or heavy ele-

ments are TOF spectrometer efficiency and intrinsic random coincidence background. Recent experiments have shown that the quantum efficiency of a two microchannel plate TOF spectrometer is less than 30% for low Z ions in the energy range 100–300 keV.<sup>8</sup> Multiple scattering and secondary electron emission from the start foil were identified as primary contributors to detector efficiency. A theoretical investigation of the effect of count rate on TOF spectra showed that a uniform rate dependent background is generated by random start and stop pulses produced by different particles.<sup>9</sup> In the analysis of low level surface constituents where large beam currents may be needed to obtain a statistically significant measurement, this random coincidence background will greatly limit the detectable amount of trace elements.

In this paper, we report a modification to our existing TOF spectrometer design which shows potential for enhancing the sensitivity of ion scattering measurements to low level surface constituents and provides further insight to the processes governing TOF spectrometer efficiency. A passivated, implanted, planar silicon (PIPS) detector has been substituted for the stop microchannel plate to produce a medium energy particle telescope capable of providing TOF and energy information on the detected particles. Improved detection efficiency is realized due to the unit quantum response of the PIPS detector compared to the 50% estimated active area of the microchannel plate. Windows in energy were chosen for the acquisition of gated TOF spectra. When the contribution of PIPS detector noise to the stop count rate is eliminated by setting a minimum energy threshold, random coincidence background is diminished. Elimination of events from the substrate or other scattering features by gating further reduces background. In order to demonstrate some of the capabilities of this technique, two representative samples were considered; a monolayer of gold on silicon and a thin self-supporting carbon film contaminated with residual

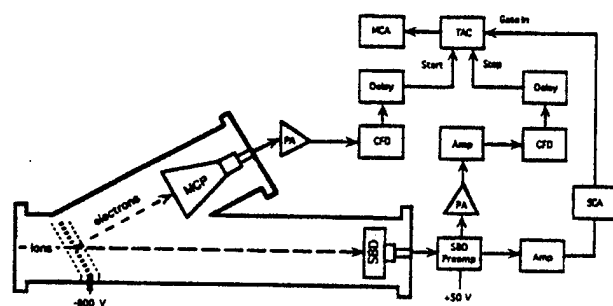


FIG. 1. Schematic of the spectrometer and associated detector electronics.

hydrogen. Some additional ideas for spectrometer design improvements are discussed as are the difficulties associated with using PIPS detectors for medium energy ions.

## II. EXPERIMENTAL

A schematic of the apparatus is shown in Fig. 1. Scattered ions or neutrals enter the spectrometer through an aperture and pass through a  $3 \mu\text{g}/\text{cm}^2$  carbon foil mounted on a 90% transmission nickel mesh which has been biased at  $-800 \text{ V}$  with respect to ground. Grounded meshes positioned  $0.5 \text{ cm}$  in front and back of the foil define the shape and extent of the electric field. Secondary electrons generated as the ion exits the foil are accelerated toward a microchannel plate assembly with the cathode grounded and the anode biased at  $+2200 \text{ V}$ . The ions drift through the spectrometer and strike a passivated, implanted, planar silicon detector (Ortec Ultra-series) with a  $50 \text{ mm}^2$  active area and a depletion depth of  $100 \mu\text{m}$ . The flight path from the start foil to the stop detector is approximately  $35 \text{ cm}$ . The aperture at the entrance to the spectrometer restricts the flux of scatters while a geometric solid angle of  $0.1 \text{ msr}$  is defined by the active area of the PIPS detector.

A schematic of the electronics used to acquire energy-gated TOF spectra is included in the same figure. Start event markers are generated from the amplified pulses of the microchannel plate by a constant fraction discriminator. The stop event markers from the timing output of the PIPS detector preamp were typically much less than  $5 \text{ mV}$  in amplitude for medium energy ions, requiring two stages of amplification. Discriminator thresholds in the start and stop channels were optimized to reduce the background count rate while continuing to pass real events. Energy pulses from the stop detector were amplified ( $0.5 \mu\text{s}$  shaping) and passed to a single channel analyzer, which produced  $500 \text{ ns}$  pulses used to gate the time-to-amplitude converter (TAC). A  $\sim 3.5 \mu\text{s}$  delay was added to each timing signal, in order to synchronize them with the gate pulse. A multichannel analyzer sorted the valid TAC events into a  $0.25 \text{ ns}/\text{channel}$  spectrum. The contribution of the external electronics to the detector timing resolution was measured with both detectors uncoupled from the system using a fast pulser ( $\sim 1 \text{ ns}$  rise time) to serve as a source of start pulses. These triggered a tail pulse generator which provided stop pulses for the PIPS preamp. The timing resolution measured by this method was  $1.5 \pm 0.3 \text{ ns}$ .

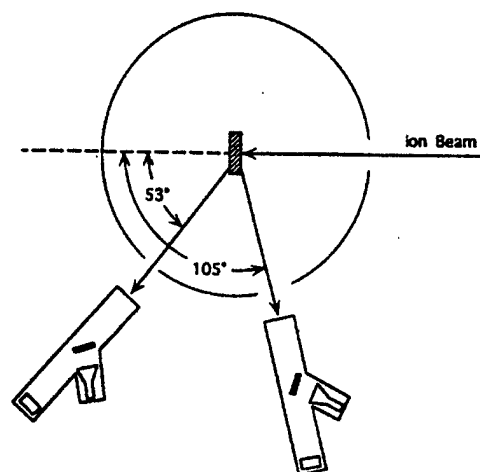


FIG. 2. Layout of forward and backscattering geometries.

The scattering geometry is shown in Fig. 2. Helium ions at  $275 \text{ keV}$  were directed at normal incidence and backscattered at  $\theta = 105^\circ$  from a silicon sample having a nominal coverage of gold, verified using our conventional TOF backscattering setup, of  $(1.0 \pm 0.1) \times 10^{15} \text{ atoms}/\text{cm}^2$ . In the forward scattering experiment, a self-supporting carbon foil was mounted on a stainless steel support with a  $0.5\text{-cm}$ -diam hole. A nominal thickness of  $(2.7 \pm 0.3) \times 10^{17} \text{ atoms}/\text{cm}^2$  was quoted by the manufacturer. H ions at  $105$  and  $275 \text{ keV}$  were forward scattered from the foil and detected at  $\theta = 53^\circ$  and an angle  $14^\circ$  above the horizontal plane. The integrated charge, collected with the beam incident on the foil, was adjusted by the ratio of the current deposited on a solid target to current through the foil in order to approximate the true value.

## III. RESULTS AND DISCUSSION

Energy spectra obtained from the PIPS detector are shown in Fig. 3 for  $275 \text{ keV}$  H and He ions scattered from the carbon film and the gold on silicon. An energy scale was established by measuring thick target edge positions on a number of samples. The estimated energy resolution for H and He from the carbon and gold peaks is approximately  $11$  and  $16 \text{ keV FWHM}$  in each case. The fraction of ions detected by the PIPS detector was derived for H and He by taking the ratio of computed to geometric solid angle. The calculation was based on the known values for the number of gold or carbon scattering centers/ $\text{cm}^2$ , the Lenz-Jensen scattering or recoil cross section, the number of incident ions, and the measured number of counts in the forward and backscattering peaks. The He backscattering and H forward scattering fractions measured by the PIPS detector were  $45\% \pm 5\%$  and  $20\% \pm 2\%$ , respectively. There are two important processes which give rise to the departure of these values from unit quantum efficiency. First, multiple scattering of the ions as they pass through the carbon start foil can cause them to be deflected out of the acceptance half-angle of the detector. In order to estimate the number of projectiles which are lost, we have made *ab initio* calculations of the multiple scattering distribution functions for H and He ions passing through the start foil using Bethe's equations.<sup>10</sup> Distribution

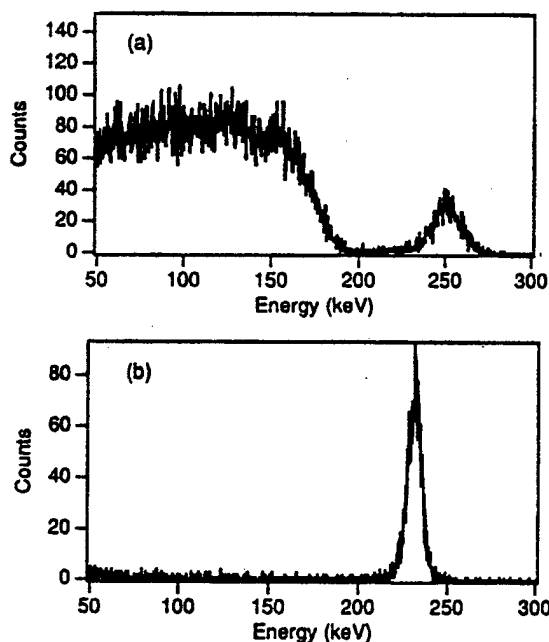


FIG. 3. PIPS detector energy spectra for (a) 275 keV  $\text{He}^+$  backscattered from a monolayer of gold on silicon and (b) 275 keV  $\text{H}^+$  forward scattered from a  $5.4 \mu\text{g}/\text{cm}^2$  carbon foil. The charge deposited during each analysis was  $12 \mu\text{C}$ .

functions were computed at 250 keV (the approximate scattered energy of the ions) using the Lenz-Jensen scattering cross section. The angular distributions were numerically integrated over the solid angle subtended by a  $0.5^\circ$  cone to give the fraction of multiply scattered ions falling within the acceptance half-angle of the stop detector. According to these theoretical estimates, 65% of the He and almost 90% of the H should reach the detector. We attribute the remaining discrepancy to misalignments of the detector and start foil with the point where the beam strikes the target. The H efficiency, as measured in the forward scattering geometry, is particularly sensitive to any such misalignment.

The gated TOF backscattering spectrum for 275 keV He on gold-covered silicon is shown in Fig. 4(a). A logarithmic display is chosen to better demonstrate the subsequent effects of gating on the background. Spectral features attributable to gold, the silicon substrate, and oxygen, presumably from the native silicon oxide layer, are identified. The estimated detection efficiency in TOF mode, again based on measurement of the gold coverage, is  $36\% \pm 4\%$ . This is an improvement in efficiency nearly twice that of our conventional TOF setup used under comparable conditions. The probability that a start event will be generated by secondary electrons from the foil largely accounts for the reduction in TOF spectrometer efficiency compared with that of the PIPS detector. The probability  $p$  that a pulse is recorded when one or more secondary electrons are emitted is simply  $p = 1 - e^{-\lambda n}$ , where  $n$  is the number of electrons and  $\lambda$  is the probability that a single electron will trigger an event. A value of  $\lambda = 0.3$ , based upon the work of Fraser,<sup>11</sup> reflects the limitations of microchannel plate active area and quantum efficiency for electrons. The yield of secondary electrons is

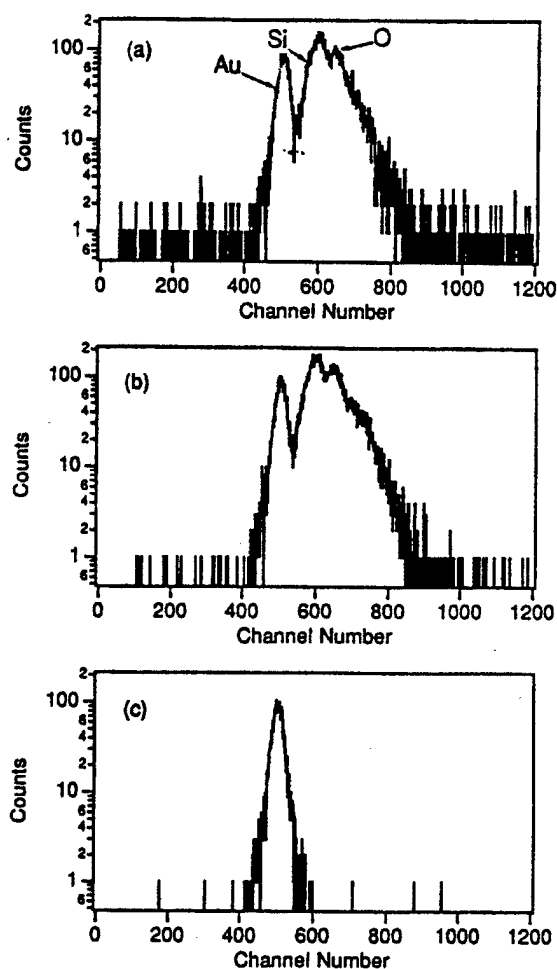


FIG. 4. TOF spectra for 275 keV  $\text{He}^+$  on a monolayer of gold on silicon subject to (a) no energy gating, (b) 20 keV, and (c) 215 keV upper level energy thresholds. The charge deposited during each analysis was  $18 \mu\text{C}$ .

proportional to the electronic stopping cross section of the ion in carbon. A proportionality constant of  $0.175 \text{ eV}/10^{15} \text{ atom}/\text{cm}^2$  was derived from recent experimental data published by Rothard and co-workers.<sup>12</sup> Based on this estimate, the probability that a 250 keV He ion will generate a start pulse is approximately 80%.

The effects of two different levels of energy gating on the TOF spectra are shown in Figs. 4(b) and 4(c). In the first case, a minimum energy threshold of 20 keV was set to eliminate pulses which could be attributable to low energy scattered ions or detector noise. For the later case, an upper threshold consistent with an ion energy of 215 keV was set to reject all scatters from the substrate. The random coincidence background in each spectrum was integrated over the entire time range excluding the region containing real events. The total measured background was 516, 41, and 4 counts for the cases of no gating, 20 keV gating, and 215 keV gating, respectively. The total number of counts in the gold peak was unaffected by the gating to within the uncertainty set by counting statistics. The significant reduction in background with increased gate threshold implies improved sensitivity to low levels of metal contaminants. We define a minimally

detectable feature as one whose integrated yield must be three standard deviations above the estimated error in the measurement. A minimum gold coverage of approximately  $2 \times 10^{12}$  atoms/cm<sup>2</sup> should be measurable by the present system, based on the background for the case of 215 keV gating. This lower level could be substantially improved by taking measures to increase the detector solid angle, such as moving the spectrometer closer to the target and using a PIPS detector of larger active area. The later modification would also reduce losses due to multiple scattering.

TOF spectra for protons scattered from the self-supporting carbon foil are shown in Fig. 5. A gating threshold of 20 keV, as in Fig. 5(b) again results in a significant reduction in background over the ungated spectrum 5(a). The ratio of TOF to PIPS detector efficiencies for the forward scattered H off C at 250 keV is  $47\% \pm 5\%$ . While smaller than the value for He, it is also consistent with estimates based on secondary electron emission and should be insensitive to detector alignment. This is quantitatively understood as the number of secondary electrons emitted by the passage of a H ion will be, in general, less than are generated by a He ion due to the smaller electronic stopping cross section. In Fig. 5(c) upper and lower thresholds were set to pass only ions with an energy below 125 keV, effectively eliminating all proton scatters from the carbon, while continuing to reject low energy events. An additional peak, resolved after collecting with a larger deposited charge, was tentatively identified as representing protons scatters from hydrogen in the foil with a recoil (or scatter) energy of approximately 100 keV. The correct location of the peak was confirmed by scattering a 105 keV H beam off the carbon foil to give ions of the same energy, as shown in Fig. 5(d). The estimated hydrogen concentration in the foil is  $(2.0 \pm 0.2) \times 10^{16}$  atoms/cm<sup>2</sup>.

The full width at half-maximum timing resolution, measured for the H and He scattering from carbon and gold, was  $4.5 \pm 0.3$  and  $6.5 \pm 0.3$  ns, respectively, and includes the contribution from the external electronics. In comparison, the nominal timing resolution for our two microchannel plate TOF detector is less than 1.0 ns. With the PIPS detector connected, significant time jitter occurs at the output of the detector preamplifier, causing a degradation in resolution. Radio frequency pickup by the detector from the accelerator high voltage source may have been a contributing factor and was due in part to insufficient ground isolation. This reduction in resolution could be compensated for by increasing the total flight distance. Such an improvement in timing resolution would probably be needed if identification of lower mass species by backscattering were attempted using the current setup.

We have demonstrated the application of particle telescope technology to the medium energy backscattering measurement of a gold monolayer on silicon and the forward scattering measurement of hydrogen in thin films. Comparisons of TOF to PIPS detector efficiency for H and He agree with theoretical estimates of the probability for generating a start event based on microchannel plate efficiency and secondary electron emission. Because of limitations in timing, the telescope is not particularly well suited for measurements requiring good depth resolution, such as the determination of

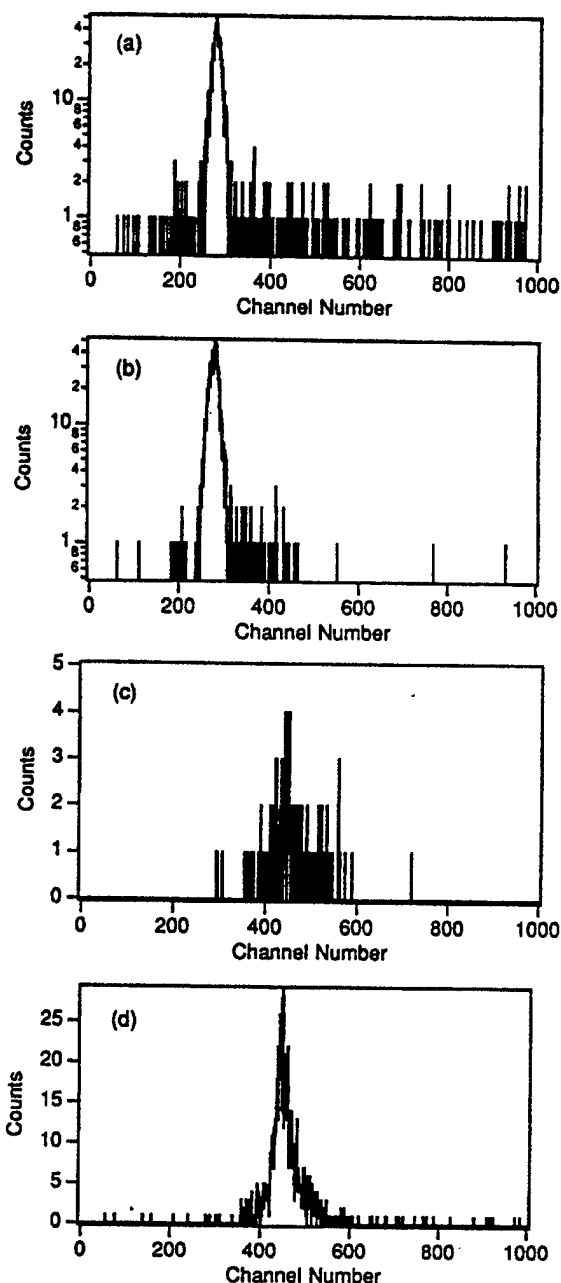


FIG. 5. TOF spectra for 275 keV H<sup>+</sup> on the self-supporting carbon foil subject to (a) no energy gating, (b) 20 keV upper level, and (c) 125 keV lower level energy thresholds. In (d) a 105 keV H<sup>+</sup> was used to produce scatters with the same energy as the ions in (c). The charge deposited was 6  $\mu$ C for (a) and (b), 48  $\mu$ C for (c), and 2  $\mu$ C for (d).

film thickness. The advantage of this technique over TOF or energy measurements alone is in the sensitive detection of low levels of surface contaminants. Selective screening of TOF events by particle energy reduces random coincidence background by roughly two orders of magnitude compared with a two microchannel plate setup, while eliminating contributions from low energy noise and pulse pileup from the surface barrier detector. Further optimization of geometric solid angle, flight path, and PIPS detector active area will be

necessary to produce a design capable of competing with the current state of the art in trace element detection.

#### ACKNOWLEDGMENT

This work was supported by the U.S. Army Research Office under Contract No. DAAL 03-92-G-0037.

<sup>1</sup>F. S. Landolt and B. G. Harvey, *Annu. Rev. Nucl. Sci.* **25**, 167 (1975).

<sup>2</sup>J. Sokolov, M. H. Rafailovich, R. A. L. Jones, and E. J. Kramer, *Appl. Phys. Lett.* **54**, 590 (1989).

<sup>3</sup>H. J. Whitlow, A. B. Andersson, and C. S. Petersson, *Nucl. Instrum. Methods B* **36**, 53 (1989).

<sup>4</sup>R. Groleau, S. C. Gujrathi, and J. P. Martin, *Nucl. Instrum. Methods* **218**, 11 (1983).

<sup>5</sup>M. H. Mendenhall and R. A. Weller, *Appl. Phys. Lett.* **57**, 1712 (1991).

<sup>6</sup>J. A. Knapp and J. C. Banks, *Nucl. Instrum. Methods B* **79**, 457 (1993).

<sup>7</sup>J. H. Arps and R. A. Weller, *Nucl. Instrum. Methods B* **79**, 539 (1993).

<sup>8</sup>J. H. Arps and R. A. Weller, *Nucl. Instrum. Methods B* (in press).

<sup>9</sup>R. A. Weller, *Nucl. Instrum. Methods B* **79**, 817 (1993).

<sup>10</sup>H. A. Bethe, *Phys. Rev.* **89**, 1256 (1953).

<sup>11</sup>G. W. Fraser, *Nucl. Instrum. Methods* **206**, 445 (1983).

<sup>12</sup>H. Rothard *et al.*, *Phys. Rev. A* **41**, 2521 (1990).

# A model of the intrinsic efficiency of a time-of-flight spectrometer for keV ions

Robert A. Weller \*, James H. Arps, Diane Pedersen, Marcus H. Mendenhall

*Vanderbilt University, Nashville, Tennessee 37235, USA*

## Abstract

We have constructed a first-order model of the intrinsic efficiency of a time-of-flight spectrometer for medium energy ions. The spectrometer uses secondary electrons from a thin carbon foil to generate a start signal and ion impact on a microchannel plate to generate the stop signal. The model includes the effects of the secondary electron yield, multiple scattering in the foil, and the response of the individual microchannel plates which comprise the instrument. We describe the model and the variation of the predicted efficiency with model parameters. Comparisons with measured efficiencies for several ions and energies ranging from 40 keV H to 500 keV O indicate that the model's predictive power is satisfactory for interpreting the results of routine surface analyses.

## 1. Introduction

Time-of-flight spectrometers are important tools for ion beam analysis of surfaces because they share many of the features, such as wide dynamic range and an insensitivity to a particle's charge state, which have made silicon surface barrier detectors uniquely effective for charged-particle spectrometry at tandem accelerator energies. At particle energies of tens to hundreds of keV, where surface barrier detectors are less useful, especially for heavy ions, time-of-flight spectrometers are the tools of choice for routine thin film analysis [1,2]. However, unlike surface barrier detectors which are usually assumed to have unit intrinsic efficiency, time-of-flight spectrometers have an energy-dependent efficiency which is typically considerably less than one.

In a previous publication, we examined the implications of the efficiency of a spectrometer for the shape of measured spectra and the amount of random coincidence background which these spectra contain [3]. We also suggested that the principal physical processes which limit a spectrometer's efficiency are secondary electron emission and multiple scattering in the start-foil assembly. In a subsequent publication, we presented measurements of the intrinsic efficiency of two similar time-of-flight spectrometers and compared the data with preliminary calculations based on the effects of these processes [4]. In this publica-

tion, we present a further elaboration of the efficiency model which includes a component describing the stop detector. While, in principle, this model has no adjustable parameters, in most cases the actual values of the variables are not known precisely. Thus, we explore the variation of the predicted efficiency with changes in these parameters. As we shall see, it is possible to obtain quite reasonable agreement with the results of experiments for a set of values of the parameters all of which are plausible, if not necessarily equal to a priori estimates. Indeed, our earlier speculation that it may be possible to obtain adequate estimates of efficiencies for various ions and energies using only one parameter to characterize a spectrometer continues to be a useful approximation. In its present form, this model is a useful tool both for summarizing and extrapolating the results of experimental calibrations and for evaluating the performance of hypothetical spectrometer designs.

## 2. The efficiency model

Fig. 1 shows a schematic of the spectrometer configuration to which the following considerations apply. Start pulses are produced when secondary electrons emitted from an electrically biased carbon foil mounted on the middle of three identical 95% transmission Ni meshes strike a microchannel plate detector (Galileo FTD-2003). The electron trajectories make an angle of 30° with respect to the spectrometer axis. The two outer meshes serve to define the electric field surrounding the foil. Stop pulses

\* Corresponding author.

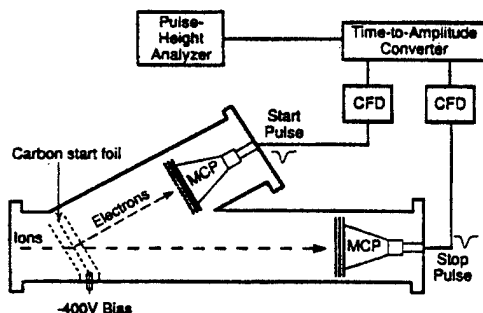


Fig. 1. Schematic of the time-of-flight spectrometer and external electronics consisting of constant fraction discriminators, time-to-amplitude converter and a multichannel analyzer.

are generated when particles impinge directly on the cathode of a second microchannel plate detector approximately 40 cm from the start assembly. A mesh serves to limit the electric field here also. The solid-angle-defining aperture is at the entrance to the spectrometer several cm up-stream of the start foil assembly. The stop detector is biased with its anode at ground potential while the start detector is configured with grounded cathode (or with cathode at about  $-700$  V on older systems). The external electronics are also shown in Fig. 1 although, in the present version of the model, their effects through parameters such as thresholds are not explicitly considered.

The intrinsic (or quantum) efficiency of the spectrometer is defined as the probability that an individual particle entering along the instrument's nominal axis will lead to the generation of a valid event. The factors which determine this efficiency are the secondary electron yield of the start foil, the probability that electrons reach the start detector, the start detector's efficiency for electrons, small angle multiple scattering in the start foil (which causes some particles to miss the stop detector), the efficiency of the stop detector for ions, and finally the collective transmission of the various meshes which are used to control electric fields. External influences such as stray magnetic fields are not considered explicitly.

Measurements of the secondary electron yield as ions exit from thin carbon foils have been reported by Rothard et al. [5]. They report a secondary electron yield per incident ion of  $\gamma_C = \Lambda S_C$ , where  $S_C$  is the electronic stopping power in  $\text{eV}/\text{\AA}$  and  $\Lambda$  is a proportionality constant which has the values  $0.22 \text{ \AA}/\text{eV}$ ,  $0.15 \text{ \AA}/\text{eV}$ , and  $0.11 \text{ \AA}/\text{eV}$ , respectively for protons, He ions and heavy ions. Since secondary electrons are accelerated to a constant energy of about  $400$  eV by the bias on the foil, it is only necessary to know a single number for all ions and energies to properly characterize the probability of generating a start pulse. The probability that a single secondary electron generates a start pulse shall be denoted by  $\lambda$ . Then, assuming that the electrons behave independently, the probability that a start pulse is generated when an ion passes through the start foil complex is  $1 - e^{-\lambda \Lambda S_C}$ .

Fraser has published a study which indicates that the detection efficiency of microchannel plates for few-hundred eV electrons approaches (or may even slightly exceed) the fractional open area of the plates [6]. From the manufacturer's literature, the open area of our plates is about 55%. By rotating the start foil assembly while the spectrometer is operating, we have observed that the size of the electron spot on the microchannel plate is much smaller than the total sensitive area. Thus, electron loss should be small except for the collisions with the mesh which defines the accelerating field. We conclude that a value of 0.5 is a reasonable initial estimate for the parameter  $\lambda$ .

The carbon foils used in our spectrometers are in the range  $2\text{--}3 \mu\text{g}/\text{cm}^2$  or, using the density for carbon of  $2 \text{ g}/\text{cm}^3$  suggested by the manufacturer, about  $10\text{--}15 \text{ nm}$  thick. This is sufficiently thick that a very significant fraction of the particles are scattered by angles larger than the approximately  $2^\circ$  cone angle subtended by the stop detector. In order to quantify the contribution of multiple scattering, Mendenhall and Weller [7] have developed a set of algorithms based on the fast Fourier transform for computing the multiple scattering angular distribution for arbitrary scattering cross sections. The results of these calculations agree to high accuracy with the published tables of Sigmund and Winterbon [8] and with Monte Carlo simulations based on the TRIM algorithm [9] when the same screening functions are used. The procedure described in Ref. [7] has been used to compute the fraction of particles which fall within a  $2^\circ$  cone after passage through a carbon foil. This function, an implicit function of particle species and energy and foil thickness, is denoted simply as  $f$ .

The efficiency of the stop detector for ions has been the most difficult component of this problem to quantify with confidence. Fraser [6] assumed that a microchannel plate produces a pulse if there is at least one secondary electron produced within a microchannel by one of the primary electrons generated by ion impact. The probability that an ion strikes the plate in one of the channels was taken simply as the fractional open area  $A$  of the microchannel plate. Poisson statistics was assumed to govern the emission of secondary electrons both by the primary ions and by the electrons themselves. The use of Poisson statistics is certainly not rigorously correct, but as an approximation it is reasonable. The assumption that the outcome of an avalanche is determined exclusively by the first generation of electrons is not very accurate either if the secondary electron yield of the microchannel is too small. Below, we present expressions based upon Fraser's assumption and a generalization which includes additional generations of multiplication.

We denote the number of secondary electrons generated by ion impact within a channel by  $\gamma$  and assume, as with the carbon foil, that  $\gamma$  is proportional to the electronic stopping power. For computing the stopping power, we assume that the surface of the detector is  $\text{SiO}_2$ , since the



reduced, lead-silicate glass used to make microchannel plates has been observed to have a silica-rich surface layer [10]. (Of course, in some cases ions will impinge directly on the top-surface electrode which is metallic.) The constant of proportionality relating  $\gamma$  and the stopping power is not well known in this case. Rajopadhye et al. and others [11] have published data on secondary electron emission induced by normal-incidence electron impact on Pb glass like that which is used in microchannel plates. However, in practice, particle impacts occur at grazing angles. Moreover, the relative secondary electron yields of protons and electrons under similar conditions have not been extensively studied [12] so that extrapolating the data of Ref. [11] to ions is problematic. Initially,  $\gamma$  was computed using the procedure suggested by Rothard et al. [5] for estimating ion-induced secondary electron yields from a generic metallic surface.

The number of electrons emitted by each electron impact with the walls of a microchannel will be taken to be  $\gamma_s$ . Physical considerations suggest that the value of  $\gamma_s$  must lie in a relatively narrow range. If the average value of  $\gamma_s$  were less than or equal to 1, amplification would not take place. On the other hand, the data of Rajopadhye et al. [11] indicate that the maximum normal incidence yield is approximately 2.5. Thus, even allowing for some variation with the angle of electron impact,  $\gamma_s$  is not expected to be large. The probability that an ion-generated secondary electron fails to initiate an avalanche is  $e^{-\gamma_s}$ . Using Fraser's criterion that the first stage of amplification determines the outcome of a pulse, we obtain an expression for the microchannel plate's intrinsic efficiency for ions:

$$\eta_s = A(1 - e^{-\gamma(1 - e^{-\gamma_s})}). \quad (1)$$

If  $\gamma_s$  is sufficiently large, say greater than 3, as it usually is in discrete dynode electron multipliers, Eq. (1) is a reasonable approximation. However, if  $\gamma_s$  is smaller, then an avalanche can fail at a later stage. The generalization of Eq. (1) which includes the possibility of failure later in the avalanche includes a continued exponent. Using this more general form and representing the transmission of the spectrometer attributable to meshes as  $T$ , the complete expression for the efficiency of the spectrometer is:

$$\eta = ATf(1 - e^{-\lambda \Delta S_c})(1 - e^{-\gamma(1 - e^{-\gamma_s(1 - e^{-\gamma_s(\dots)})})}). \quad (2)$$

Since  $A \approx 0.6$  and there are three 95% transmission meshes in the start assembly as well as one at the stop detector ( $\approx 90\%$ ), a value in the range 0.4–0.5 is a reasonable expectation for the product  $AT$ .

### 3. Discussion

Because of the uncertainty in computing  $\gamma$ , in practice we have written the exponent in the final term of Eq. (2) in the form:

$$\gamma(1 - e^{-\gamma_s(\dots)}) \equiv g \Lambda_n S_{MCP}. \quad (3)$$

Here  $S_{MCP}$  is the electronic stopping power of the ion at the surface of the microchannel plate and  $\Lambda_n$  is a normalized species-dependent factor analogous to  $\Lambda$  above. In the absence of data, the values of  $\Lambda_n$  were taken to be those suggested by Rothard et al. in Eq. (14) of Ref. [5]: 1.0, 0.6, and 0.3 for H, He and heavy ions, respectively. The parameter  $g$  is determined, in principle, both by the electron multiplication term in parenthesis on the left side of Eq. (3) and by the secondary electron yield of the microchannel plate though, in practice, it is adjustable. With the definition given in Eq. (3),  $\eta$  has three other parameters which may also be considered to be adjustable within limits: the product  $AT$ , the foil thickness, which affects  $f$ , and the probability  $\lambda$ . In Ref. [3], we examined the effects of multiple scattering and the start detector response on  $\eta$ . Using the nominal foil thicknesses specified by the manufacturer and assuming a value of 0.3 for  $\lambda$ , we found that it was possible to predict within 10–20% (but with systematic errors) the efficiencies of two similar spectrometers, one used for backscattering and the other for forward recoil studies. The most significant success of that effort was the prediction that the efficiency for detecting hydrogen should peak in the energy range which we examined experimentally. This work led us to the conjecture that it might be possible to characterize a spectrometer approximately by specifying the product  $AT$  alone. The systematic differences between the predicted variation of efficiency with energy and the data were attributed to our decision to assume that the stop detector's response was independent of the particle's energy.

With the inclusion of a model for the stop detector, it was reasonable to search in the space of the above parameters for a best fit to the data. This effort was only marginally successful, however, because the parameters are not completely independent. Indeed, for small  $\lambda$  and  $g$ ,  $\eta$  depends only on the product  $AT\lambda g$ . Increasing foil thickness also has the same general effect on  $\eta$  as decreasing  $\lambda$ . We found that it was not possible to obtain high quality fits for all data using the a priori values of  $\Lambda$  measured by Rothard et al. [5]. However, the adjustments which were necessary were modest, being typically in the 10–20% range, and were consistent with experimental uncertainties in the data and the computation of stopping powers [13]. We also added a  $\Lambda$  value for Li which was determined from the data to be intermediate between those for He and heavy ions. The values which we have used for  $\Lambda$  in the computations below are 0.26, 0.22, 0.14, and 0.10 for H, He, Li, and heavy ions, respectively. The value 0.17 has been used for  $\lambda$ .

The most surprising result from the nonlinear fitting was that foil thicknesses of 3.6  $\mu\text{g}/\text{cm}^2$  and 4  $\mu\text{g}/\text{cm}^2$ , respectively, for the 150° and 42° spectrometers were needed in order to achieve the best agreement with the data. These are about 25% larger than the nominal thicknesses (even allowing for the 30° tilt of the foil) and significantly outside the tolerances specified by the manu-

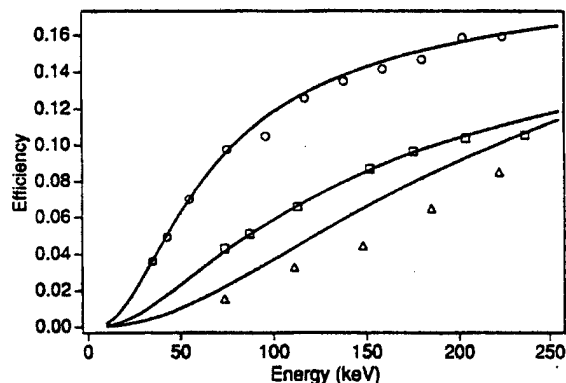


Fig. 2. Comparison of computed and measured efficiencies  $\eta$  of backscattering spectrometer for He (circles), Li (squares) and O (triangles).

facturer. We do not know, at this time, if this is an artifact of the poor orthogonality of the parameters or if the foils are actually unexpectedly thick.

Fig. 2 is a composite showing a comparison between computed values of  $\eta$  (smooth curves) and the measured efficiencies of our backscattering ( $150^\circ$ ) spectrometer for He, Li, and O. Error bars (estimated to be approximately 10% [4]) have been omitted from the graph for clarity. The value of  $AT$  is 0.24. The curves in Fig. 2 were computed with  $g = 0.05 \times 10^{15} / (\text{eV cm}^2)$ . Corrections for the energy loss in the start foil, both to the energy axis itself and to the multiple-scattering factor, have been investigated and, for these ions and energies, found to be negligible on the scale shown. The results of a comparison between the computed and measured efficiencies of our elastic recoil ( $42^\circ$ ) spectrometer for H and C are shown in Fig. 3, where an  $AT$  value of 0.56 was used but all other parameters were held constant.

The difference in normalization between Figs. 2 and 3 is attributable to the differences between the gains of the microchannel plates in the two spectrometers. In practice, valid low amplitude pulses may be below discriminator

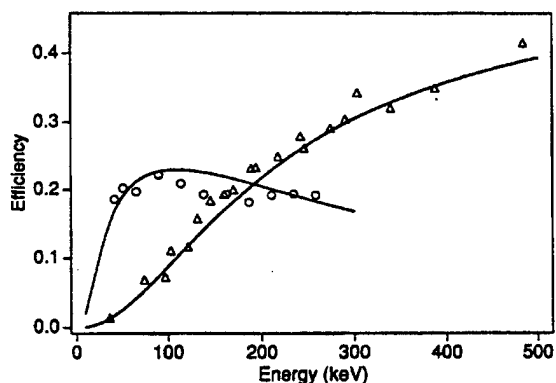


Fig. 3. Comparison of computed and measured efficiencies  $\eta$  of forward recoil spectrometer for H (circles) and C (triangles).

thresholds and therefore lost. This should have the same effect as changing  $\lambda$  and  $g$ . Thus, although the one-parameter approximation used in Figs. 2 and 3 is surprisingly robust, the relatively poor agreement obtained for oxygen in Fig. 2 demonstrates that for highest accuracy it is necessary to consider at least the relative performance of the two microchannel plates. Specifically, there is no reason to expect that values of  $\lambda$  or  $g$  for different systems with different ages and histories are necessarily equal.

#### 4. Conclusion

A model of time-of-flight spectrometer intrinsic efficiency encompassing the effects of secondary electron emission and multiple scattering in the start foil, along with the efficiency of the stop detector for ions has been shown to be successful in representing measured data for ions ranging from approximately 40 keV H to 500 keV O. It should be an especially useful tool for the analysis of medium-energy, time-of-flight spectra of both backscattered and forward-recoiled ions. It affords reasonable accuracy using a priori values for its parameters and, with fitted values of these parameters, appears to be at least as accurate as other computed quantities such as cross sections and stopping powers which are used in the analysis of experiments.

#### Acknowledgements

This work was supported in part by the U.S. Army Research Office under contract DAAL 03-92-G-0037 and by Sandia National Laboratories under contract AH-3292.

#### References

- [1] J.A. Knapp and J.C. Banks, Nucl. Instr. and Meth. B 79 (1993) 457.
- [2] M.H. Mendenhall and R.A. Weller, Appl. Phys. Lett. 57 (1990) 1712.
- [3] R.A. Weller, Nucl. Instr. and Meth. B 79 (1993) 817.
- [4] J.H. Arps and R.A. Weller, Nucl. Instr. and Meth. B 90 (1994) 547.
- [5] H. Rothard, K. Kroneberger, A. Clouvas, E. Veje, P. Lorenzen, N. Keller, J. Kemmler, W. Meckbach and K.O. Groeneveld, Phys. Rev. A 41 (1990) 2521.
- [6] G.W. Fraser, Nucl. Instr. and Meth. 206 (1983) 445.
- [7] M.H. Mendenhall and R.A. Weller, Nucl. Instr. and Meth. B 93 (1994) 5.
- [8] P. Sigmund and K.B. Winterbon, Nucl. Instr. and Meth. 119 (1974) 541, and Nucl. Instr. and Meth. 125 (1975) 491.
- [9] J.P. Biersack and L.G. Haggmark, Nucl. Instr. and Meth. 174 (1980) 257.
- [10] A.M. Then and C.G. Pantano, Non-Cryst. Solids 120 (1990) 178.
- [11] N.R. Rajopadhye, S.V. Bhoraskar and D. Chakravorty, J. Non-Cryst. Solids 105 (1988) 179, and references therein.
- [12] J. Schou, Scanning Microscopy 2 (1988) 607.
- [13] J.F. Ziegler, J.P. Biersack and U. Littmark, The Stopping and Range of Ions in Solids (Pergamon, New York, 1985) p. 202.

## An algorithm for ab initio computation of small-angle multiple scattering angular distributions

Marcus H. Mendenhall and Robert A. Weller \*

*Vanderbilt University, Nashville, TN 37235, USA*

Received 7 January 1994 and in revised form 8 March 1994

Small-angle multiple scattering is a venerable problem in nuclear and particle–solid interaction physics and has received extensive theoretical treatment. In this paper, motivated by the need to establish the efficiency of time-of-flight spectrometers which employ thin foils to generate “start” signals, we revisit this problem. Our objective is to develop an efficient, general computational procedure which is not tied to the current state of computing machinery or specific cross sections, but which takes advantage of significant numerical-algorithmic advances which have occurred since the multiple-scattering problem was originally formulated. By introducing a new approach for dealing with the azimuthal symmetry of the problem, we avoid Hankel transforms which have been used in all previous treatments and, in so doing, make it possible to apply the fast Fourier transform algorithm in one dimension. The resulting computation can be carried out to arbitrary accuracy with sufficiently dense sampling of the cross section and is very fast when compared with numerically computed Hankel transforms. Angular distributions for several scattering potentials and a compound target are compared.

### 1. Introduction

To apply time-of-flight spectrometry to surface analysis using a continuous beam accelerator, you must devise a scheme to determine when a individual scattered ion or neutral particle enters and leaves a drift region with a known length [1]. It is easy to establish when a particle completes the course, since it may be intercepted by any one of a number of styles of particle detectors. However, establishing the time that the particle enters the measured course is another matter, since this determination must be made with minimal perturbation of the particle’s speed and trajectory. The most widely adopted scheme has been to place a thin, self-supporting carbon foil in the particle’s path and to detect bursts of secondary electrons that accompany its passage through the foil. The disadvantage of this technique is that small-angle multiple scattering in the carbon foil can alter the trajectory of the ion sufficiently that it misses the second detector at the end of the drift space and so does not produce a measurable event. Thus, multiple scattering is one of the physical processes which, along with secondary electron emission and the intrinsic responses of the detectors which comprise the spectrometer, determines the overall spectrometer efficiency [2].

The general procedure for computing small angle multiple scattering was developed several decades ago, has been reviewed thoroughly [3], and revisited by several authors subsequently as computing technology and the quality of scattering cross sections has advanced [4–6]. Moreover, the results of multiple-scattering computations continue to be of interest for practical experimental work [7], additional theoretical development [8], and continuing experimental verification [9]. We will confine our attention to the simplification of the general problem in which angles can be assumed to be small in the sense that  $\sin(\theta) \approx \theta$ . Also, we adopt the assumptions, including the neglect of energy loss, binary collisions and a random scattering medium, which have been summarized by Sigmund and Winterbon [6]. In this approximation, the angular distribution of particles as a function of depth of penetration into the solid is described by a transport equation which involves a convolution. This equation is solved, in turn, by integral transforms using the convolution theorem. The desired distribution is recovered by inversion of the integral transform. The cylindrical symmetry of the problem at once suggests the use of Hankel transforms [10] and, so far as our research reveals, this has been the approach which has been used universally in the literature. The results are theoretically appealing, concise and are nicely connected with the large-angle version of the problem through mathematical relationships between special functions [11]. However, Hankel transforms are cumbersome to compute numerically.

\* Corresponding author, tel. +1 615 343 6027, fax +1 615 343 7263, e-mail [weller@vuse.vanderbilt.edu](mailto:weller@vuse.vanderbilt.edu).

This is not the case for Fourier transforms. With the widespread dissemination of the fast Fourier transform (FFT) algorithm in the mid 1960s, it became possible to compute the transform of very large arrays of numbers, even in multiple dimensions, in an acceptable amount of time [12]. Contemporary with this development, and also important for the present application, were the introduction of adaptive quadratures (such as ref. [13]) which, by intelligent selection of sample points, were able to generate high quality numerical integrals very efficiently.

It is possible to attack the multiple scattering problem by brute force using a two-dimensional FFT. However, by using the axial symmetry about the beam direction, the problem can be reduced to a one-dimensional FFT of a set of points each one of which is obtained by numerical integration of a very smooth function. This is the approach taken in this paper. We begin with a brief restatement of the theory which is applicable to our problem, emphasizing the novel approach which we have taken to reduce the dimensionality from two to one. A subsequent section deals with the numerical details of the computation. Finally, we present some sample calculations for the cases of the Rutherford, the Lenz–Jensen [14], and the Ziegler–Biersack–Littmark “universal” [15] scattering cross sections. The algorithms which are presented here are sufficiently simple and general that they can be easily adapted to other cross sections as well as to routine multiple scattering computations in support of experiment and theory.

## 2. Theory

The quantity of interest in the discussion which follows is  $f(z, \theta_x, \theta_y)$ , the probability that a particle which enters a foil along the  $z$  axis will be scattered into an element of solid angle described by  $\theta_x$  and  $\theta_y$  after penetrating a distance  $z$  into the foil. It is possible to describe the direction of the scattered particle by orthogonal displacements  $(\theta_x, \theta_y)$  in a plane because of the small angle approximation. The change in  $f$  which is attributed to penetrating from  $z$  to  $z + dz$  is the sum of the probability that the particle is scattered into the specific solid angle from another direction, less the probability that a particle is already traveling in the appropriate direction and is scattered to any other direction. The total cross section for scattering is denoted by  $\sigma_{\text{tot}}$  while the number density of scattering centers is  $N$ .

$$\begin{aligned} f(z + dz, \theta_x, \theta_y) \\ = f(z, \theta_x, \theta_y) + N dz \int \sigma(\Theta) f(z, \eta_x, \eta_y) d\eta_x d\eta_y \\ - N \sigma_{\text{tot}} f(z, \theta_x, \theta_y) dz, \end{aligned} \quad (1)$$

where  $\Theta = [(\theta_x - \eta_x)^2 + (\theta_y - \eta_y)^2]^{1/2}$  and  $\sigma(\Theta)$  is the laboratory-frame, differential scattering cross section. The Fourier transform of this equation with respect to  $\theta_x$  and  $\theta_y$  is:

$$\begin{aligned} \tilde{f}(z + dz, \omega_x, \omega_y) = \tilde{f}(z, \omega_x, \omega_y) \\ + N dz \tilde{\sigma}(\omega_x, \omega_y) \tilde{f}(z, \omega_x, \omega_y) \\ - N \sigma_{\text{tot}} \tilde{f}(z, \omega_x, \omega_y) dz, \end{aligned} \quad (2)$$

where:

$$\tilde{\sigma}(\omega_x, \omega_y) = \int \int \sigma(\theta_x, \theta_y) e^{-i(\omega_x \theta_x + \omega_y \theta_y)} d\theta_x d\theta_y, \quad (3)$$

and similarly for  $\tilde{f}(z, \omega_x, \omega_y)$ , and where we have invoked the convolution theorem to express the transform of the term representing atoms scattered into the solid angle of interest as the product of the  $\tilde{f}$  and of  $\tilde{\sigma}$ . In the limit of small  $dz$ , this becomes a differential equation for the Fourier transform  $\tilde{f}$

$$\begin{aligned} \frac{\partial \tilde{f}(z, \omega_x, \omega_y)}{\partial z} = N \left( \tilde{\sigma}(\omega_x, \omega_y) \tilde{f}(z, \omega_x, \omega_y) \right. \\ \left. - \sigma_{\text{tot}} \tilde{f}(z, \omega_x, \omega_y) \right). \end{aligned} \quad (4)$$

This is an elementary equation with solution:

$$\tilde{f}(z, \omega_x, \omega_y) = \exp \left[ N \cdot z \left( \tilde{\sigma}(\omega_x, \omega_y) - \sigma_{\text{tot}} \right) \right], \quad (5)$$

where we assume that  $f(0, \theta_x, \theta_y) = \delta(\theta_x) \delta(\theta_y)$  is a two-dimensional Dirac delta function whose transform is, of course, unity throughout the reciprocal space. The angular distribution is obtained from Eq. (5) by the inverse transform:

$$\begin{aligned} f(z, \theta_x, \theta_y) \\ = \frac{1}{(2\pi)^2} \iint \tilde{f}(z, \omega_x, \omega_y) e^{i(\omega_x \theta_x + \omega_y \theta_y)} d\omega_x d\omega_y. \end{aligned} \quad (6)$$

Since the cross section  $\sigma$  is cylindrically symmetrical, previous authors have reduced the two-dimensional Fourier transforms given in Eqs. (3) and (6) to one-dimensional Hankel transforms involving the Bessel function  $J_0$ . It is at this point that our treatment of the problem diverges from previous ones. If a function is cylindrically symmetrical in space, then its Fourier transform is cylindrically symmetrical in reciprocal space. Note that for a cylindrically symmetric function, where  $g(x, y) = g((x^2 + y^2)^{1/2})$ ,  $g(x, 0)$  completely characterizes the function. Similarly,  $\tilde{\sigma}(\omega_x, \omega_y)$  is completely determined by  $\tilde{\sigma}(\omega_x, 0)$  and  $f(z, \theta_x, \theta_y)$  by  $f(z, \theta_x, 0)$ . From the definition of the Fourier transform

$$\tilde{\sigma}(\omega_x, \omega_y) = \iint \sigma(\Theta) e^{-i(\omega_x \theta_x + \omega_y \theta_y)} d\theta_x d\theta_y, \quad (7)$$

we see that for  $\omega_y = 0$ ,

$$\begin{aligned}\bar{\sigma}(\omega_x, 0) &= \iint \sigma(\theta) e^{-i\omega_x \theta_x} d\theta_x d\theta_y \\ &= \int \left( \int \sigma(\theta) d\theta_y \right) e^{-i\omega_x \theta_x} d\theta_x.\end{aligned}\quad (8)$$

Since  $\sigma(\theta) = \sigma(\sqrt{\theta_x^2 + \theta_y^2})$ , one can define a new function

$$s(\theta) = \int \sigma(\sqrt{\theta^2 + \eta^2}) d\eta \quad (9)$$

such that  $\bar{\sigma}(\omega_x, 0) \equiv \bar{s}(\omega)$  is computed by a one-dimensional Fourier transform of  $s(\theta)$ . In the same way, returning to Eq. (5), we can then write for the angular distribution:

$$\begin{aligned}\bar{f}(z, \omega_x, \omega_y) &\equiv \bar{g}\left(z, \sqrt{\omega_x^2 + \omega_y^2}\right) \equiv \bar{g}(z, \omega) \\ &= \exp(N \cdot z(\bar{s}(\omega) - \sigma_{\text{tot}})).\end{aligned}\quad (10)$$

Now, in analogy to Eq. (9), this function can be integrated to allow inversion with a one-dimensional transform. Define  $\tilde{y}$  to be the integral:

$$\tilde{y}(z, \omega) \equiv \int \bar{g}\left(z, \sqrt{\omega^2 + \eta^2}\right) d\eta. \quad (11)$$

The angular distribution of scattered particles follows immediately as the inverse Fourier transform of  $\tilde{y}$ :

$$f(z, \theta) = \frac{1}{(2\pi)^2} \int \tilde{y}(z, \omega) e^{i\theta \cdot \omega} d\omega. \quad (12)$$

Alternatively, it may be desirable in some circumstances to simply generate a rectangular array in reciprocal space using:

$$\bar{f}(z, \omega_x, \omega_y) = \exp\left[N \cdot z\left(\bar{s}\left(\sqrt{\omega_x^2 + \omega_y^2}\right) - \sigma_{\text{tot}}\right)\right] \quad (13)$$

and do a two-dimensional FFT, thus saving the effort expended on the quadratures. The complete solution for  $f(z, \theta)$  consists of computing in order  $s(\theta)$ ,  $\bar{s}(\omega)$ ,  $\bar{g}(z, \omega)$ ,  $\tilde{y}(z, \omega)$ , and finally  $f(z, \theta)$ , or, instead, applying the two-dimensional inverse FFT to Eq. (13). Note that for varying film thicknesses, the form factor  $\bar{s}(\omega)$  does not need to be re-computed.

An important point which needs to be considered in the above calculation concerns the existence of  $\sigma_{\text{tot}}$ , the total scattering cross section. Classically, a potential which extends to infinity, such as those usually used in ion scattering computations, implies a total cross section  $\sigma_{\text{tot}}$  which is also infinite. Consequently, the above equations must be interpreted carefully. Of course, one way to deal with the apparent difficulty would be to simply truncate the interaction at some radius beyond which it is non-physical anyway. It turns out, however, that the divergence is not important, as we shall now demonstrate in two different ways, by

examining first the analytical transforms and then the sampled transforms.

Consider the quantity  $\sigma_{\text{tot}} - \bar{\sigma}(\omega_x, \omega_y)$ . Since  $\sigma_{\text{tot}}$  only occurs in this form, it is sufficient to show that this difference is always finite. For simplicity we shall denote the latter term using vector notation as  $\bar{\sigma}(\omega)$ . Then we can write:

$$\sigma_{\text{tot}} - \bar{\sigma}(\omega) = \int \sigma(|\theta|) \cdot (1 - \exp(-i \cdot \omega \cdot \theta)) d^2\theta. \quad (14)$$

The total cross section diverges because  $\sigma(|\theta|)$  diverges at the origin. However, near  $|\theta| \equiv \theta = 0$ , the complete integrand of Eq. (14) varies as  $\frac{1}{2}\pi\omega^2\sigma(\theta) \cdot \theta^3$ . Thus, the Rutherford cross section, which diverges as  $\theta^{-4}$  for small  $\theta$ , does, indeed, lead to a logarithmically divergent value for  $\sigma_{\text{tot}} - \bar{\sigma}(\omega)$ . However, screened potentials which are used for ion-solid computations are much softer and yield cross sections correspondingly less singular. Since a singularity in  $\sigma$  of order less than 4 is integrable, the quantity  $\sigma_{\text{tot}} - \bar{\sigma}(\omega)$  is finite for all practical cross sections. Now let us examine the case in which we are using a discretely sampled function, which changes the nature of the problem at the origin.

Consider the function  $s(\theta)$  from Eq. (9) which is to be sampled to compute the form factor,  $\bar{s}(\omega)$ . For most potentials,  $s(0)$  will be infinite. However, instead of using  $s(0)$ , one can substitute an adjusted value using, for example,  $s(\Delta\theta/2)$ , where  $\Delta\theta$  is the sampling grid size in  $\theta$ . This amounts to adjusting the single sampled point at the origin by an unknown amount. However, if the sampled function is adjusted at only one point, it amounts to creating a new function  $s'(\theta) = s(\theta) + a\delta(\theta)$  where  $\delta(\theta)$  is the Kronecker  $\delta$  function and  $a$  is a (probably infinite) constant. Since the Fourier transform is linear, and the transform of  $a\delta(\theta)$  is just  $a$ , this adds  $a$  to all components of  $\bar{s}(\omega)$ . However, if  $\sigma_{\text{tot}}$  is computed by summing over the sampled values of  $s(\theta)$ , this also adds  $a$  to  $\sigma_{\text{tot}}$ , so when Eq. (10) is evaluated,  $a$  cancels out exactly. Thus, any reasonable choice for  $s(0)$  makes no difference to the calculation and either setting it to 0 or to the value suggested above will provide the correct answer.

The steps outlined above can be followed relatively directly in order to generate the desired angular distributions as a function of foil thickness or of the dimensionless parameter  $\tau \equiv N \cdot z$ . In the following section we give the details of our implementation.

### 3. Computation

The computation of distributions as outlined above can be implemented very easily by taking advantage of

the extremely smooth nature of the functions involved and of the efficiency with which functions can be evaluated from interpolation tables. First, if  $\sigma(\theta)$  requires significant time to compute (which it typically does), it is convenient to tabulate  $\log(\sigma(e'))$  at uniformly spaced values of  $t$  corresponding to angles ranging from the kinematically allowed maximum angle down to some very small angle, typically  $10^{-7}$  rad. If  $\sigma$  has any tendency towards power law behavior, this tabulated function is extremely smooth, and only about 100 points need to be computed to provide cubic interpolation errors below  $10^{-4}$  in the cross section at all angles.

Now, since  $\sigma(\theta)$  is singular as  $\theta \rightarrow 0$  and the integral in Eq. (9) has the particular form that it does, the computation of  $s(\theta)$  can be greatly simplified by the change of variable  $\eta = \theta \tan(\zeta)$ . The result is that Eq. (9) becomes:

$$s(\theta) = 2\theta \int_0^{\zeta_{\max}} \frac{\sigma \left[ \frac{\theta}{\cos(\zeta)} \right] d\zeta}{\cos^2(\zeta)}, \quad (15)$$

where  $\zeta_{\max} = \arccos(\theta/\theta_{\max})$  and  $\theta_{\max}$  is the maximum value for which the cross section  $\sigma$  is kinematically defined. This transforms the nearly improper integral in which most of the value comes from a very tiny region near the origin into one in which the integration algorithm samples the function primarily where it is large and avoids expending a lot of computing effort integrating the very tiny tails of the integrand near the kinematic limit of  $\theta$ . Using this integral and the tabulated  $\sigma$  value, one can tabulate  $\log(s(e'))$  in exactly the same manner as  $\sigma$ , since  $s$  needs to be evaluated on a fairly fine grid to compute  $\bar{s}(\omega)$ . Again, about 100 points seems to suffice in the tabulation. Then, using the tabulated value, one computes  $s$  at typically 1024 or 2048 points for  $\theta$  ranging out to about 5 times the largest angles of interest. This table can then be Fourier transformed to provide  $\bar{s}(\omega)$  from which  $\bar{g}(z, \omega)$  is calculated for any film thickness.

To compute  $f(z, \theta)$ , we use Eq. (11) and a modified form of the change of variable suggested in Eq. (15),  $\eta = \sqrt{\omega^2 + \omega_{1/2}^2} \cdot \tan(\phi)$ , to obtain the following result:

$$\begin{aligned} \bar{\gamma}(z, \omega) &= 2\sqrt{\omega^2 + \omega_{1/2}^2} \\ &\times \int_0^{\phi_{\max}} \frac{\bar{g} \left[ z, \sqrt{\frac{\omega^2 + \omega_{1/2}^2}{\cos^2(\phi)} - \omega_{1/2}^2} \right] d\phi}{\cos^2(\phi)}, \end{aligned} \quad (16)$$

where  $\phi_{\max} = \arccos((\omega^2 + \omega_{1/2}^2)/(\omega_{\max}^2 + \omega_{1/2}^2))^{1/2}$  above, with the cutoff  $\omega_{\max}$  set to the highest frequency being included in the transform. The parameter  $\omega_{1/2}$  is the estimated half-width of  $\bar{g}$ , as described

below. This modified change of variable correctly accounts for the fact that  $\bar{g}$  is not singular at  $\omega = 0$ , as is  $\sigma(\theta)$  at  $\theta = 0$ , and reduces to the previous one in the limit  $\omega_{1/2} \rightarrow 0$ . When the inverse transform is computed according to Eq. (12), the result is  $f(z, \theta)$ , the scattering density at polar angle  $\theta$  away from the initial beam direction.

To avoid computing many unnecessary values of  $\bar{\gamma}(z, \omega)$  (which is a relatively slow process), it is useful to adaptively determine the range of  $\bar{\gamma}(z, \omega)$  which contains real information. We accomplish this by numerically measuring the half-height point  $\omega_{1/2}$  of  $\bar{g}(z, \omega)$  from Eq. (10). We have empirically determined that  $\bar{\gamma}(z, \omega)$  is typically about twice as wide as  $\bar{g}(z, \omega)$ , so by sampling  $\bar{\gamma}(z, \omega)$  at 20 points, ranging from  $\omega = 0$  to  $\omega_{\max} = 8 \omega_{1/2}$ , we have included frequency components ranging from about 1/5 of the half-width of the actual spectrum to about four half-widths. This sampling includes essentially all the information, since the spectrum decreases quite quickly with increasing frequency. However, if for any particular application, the result is not sufficiently accurate, the sampling density can always be increased. The inverse Fourier transform of the sampled function  $\bar{\gamma}(z, \omega)$  (with zero padding of higher frequency values out to typically 128 points) is then the final scattering distribution for the foil thickness and cross section chosen.

We have implemented the above algorithms in the form of a *Mathematica*<sup>®</sup> [16] package, for the sake of simplicity of use and portability. Although one could surely create a compiled program in, for example, C, which would run much faster than our version, it is probably not worth the effort for most applications. Running *Mathematica*<sup>®</sup> on an Apple Macintosh Quadra 800 (33 MHz 68040 CPU), the time required for the entire process of generating an angular distribution from a cross section is typically about 1 min. However, if the distribution is required for more than one film thickness, it requires of order 10 s starting with an  $\bar{s}(\omega)$  table to compute each new distribution.

#### 4. Results and discussion

In this section we present a comparison of the results of a computation using our algorithm with previous work, a comparison of multiple scattering for three different cross sections and two foil thicknesses, and a computation of the effect on multiple scattering of hydrogen in the scattering foil. The beam species and energy which we have chosen is 270 keV He. This is the most common beam which we use for medium energy backscattering. Fig. 1 shows the angular distribution of He after passing through a 2  $\mu\text{g}/\text{cm}^2$  carbon foil, typical of the thickness that is used in time-of-flight spectrometers. The scattering cross section which has

been used is the approximate Lenz-Jensen cross section given by Sigmund and Winterbon [6]. Also shown in Fig. 1 for comparison is the result of a computation using the Hankel-transform method described in ref. [6]. The graph has been plotted on a log scale to emphasize the range over which the two curves agree. We have deliberately chosen the parameters of our computation to emphasize the disagreement at large angles. The error in the tail of our curve is an intrinsic artifact of the use of the FFT. The periodic boundary conditions which are inherent in this technique cause the distribution function to be over-estimated at the boundary by a factor of two. It is possible to achieve any reasonable accuracy over a specified range of angles by selecting the total range to be large enough. In this case, we specified a region of interest which included approximately five half-widths of the distribution. The result was excellent agreement over nearly four orders of magnitude in the distribution function. This was achieved while saving several orders of magnitude in computer time relative to the Hankel-transform method.

For practical computations needed in the analysis of time-of-flight spectrometers it is not necessary to demand the large dynamic range shown in Fig. 1. Fig. 2 shows the result of the same 270 keV He beam, again on a  $2 \mu\text{g}/\text{cm}^2$  carbon foil, but this time with three different assumptions about the scattering cross section. The lower curve represents the (completely unphysical) result obtained from unshielded Coulomb scattering. The two upper curves are more realistic. They were obtained using screened Coulomb interactions with a Lenz-Jensen screening function [14] for the lower curve and the Ziegler-Biersack-Littmark universal screening function [17] for the upper curve. In each case, the cross sections were computed exactly

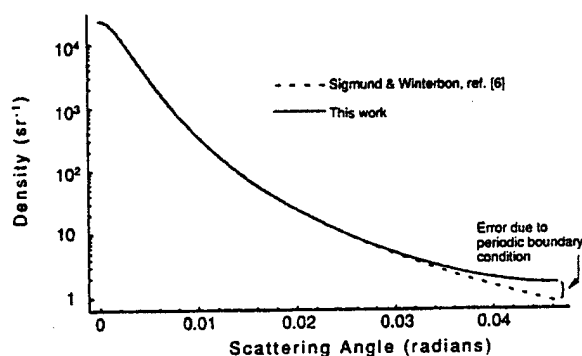


Fig. 1. A comparison of the multiple scattering angular distribution for 270 keV He on  $2 \mu\text{g}/\text{cm}^2$  C foils as computed by the methods of Sigmund and Winterbon [6] and this work. The discrepancy at large angles is the result of our use of periodic boundary conditions and can be reduced by simply extending the angular range of the calculation.

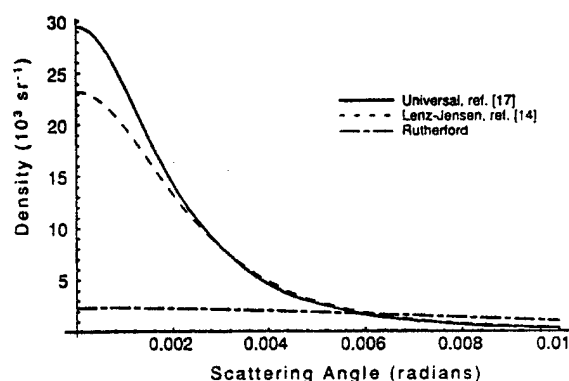


Fig. 2. A comparison of the computed multiple scattering angular distributions for 270 keV He on  $2 \mu\text{g}/\text{cm}^2$  C foils for Rutherford, Lenz-Jensen [14], and universal [17] cross sections.

using an improved version of the algorithms described in ref. [18].

In ref. [18], we concluded that Lenz-Jensen screening is more appropriate for computing scattering cross sections of interest for medium energy backscattering. Our preference for this screening over the more-recently-developed universal screening was based, in part, on the failure of the latter to agree with Hartree-Fock results near the origin. In fact, the universal screening was developed for stopping power where soft collisions dominate. Thus, we might expect that for multiple scattering it is a better representation of nature.

Fig. 3 shows curves identical to Fig. 2 except that the foil thickness is  $100 \mu\text{g}/\text{cm}^2$ . Notice that the difference between the Lenz-Jensen and universal screening functions is diminished for thicker foils.

Fig. 4 shows the effect on the multiple scattering distribution of the addition of hydrogen to the scattering foil. From top to bottom the curves represent multiple scattering by  $10^{18}/\text{cm}^2$  of pure C, CH, and

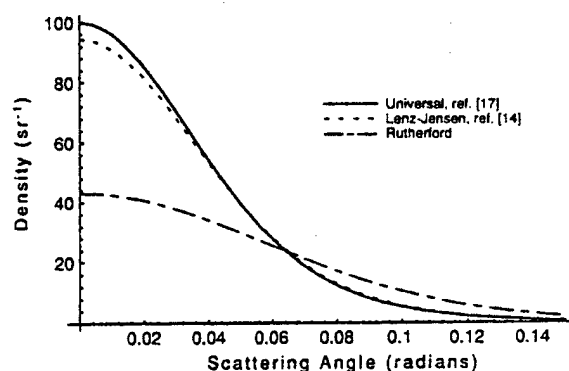


Fig. 3. A comparison of the computed multiple scattering angular distributions for 270 keV He on  $100 \mu\text{g}/\text{cm}^2$  C foils for Rutherford, Lenz-Jensen [14], and universal [17] cross sections.

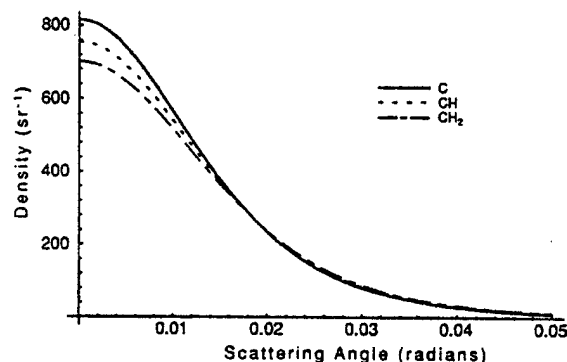


Fig. 4. A comparison of the computed multiple scattering angular distributions for 270 keV He on foils containing  $10^{18}$  carbon atoms/cm<sup>2</sup> in the form C, CH and CH<sub>2</sub>. The cross section was derived from the universal screening function [17].

CH<sub>2</sub>. Again the projectile is He<sup>+</sup>. This figure is particularly significant since it cannot be inferred from the tables of Sigmund and Winterbon [6]. It is perhaps the greatest strength of the new method that multiple scattering can be evaluated in compound targets as easily as in elemental ones. As this figure shows, even a low mass constituent can significantly affect the number of particles which strike a fixed aperture upstream of a scattering foil.

## 5. Conclusion

Routine computations of time-of-flight detector efficiency require fast and accurate evaluation of the multiple scattering produced by ions passing through 1–10  $\mu\text{g}/\text{cm}^2$  foils. By using the axial symmetry of the problem in a novel way, we have constructed algorithms for computing multiple scattering which are independent of any specific choice of cross section, able to handle compound targets, independent of any specific assumptions about computer hardware or software, and fast enough to make ab initio computations practical on currently available desktop computers. These algorithms are sufficiently general that they can provide mathematical precision comfortably exceeding that of the scattering potentials and the small-angle approximation while still rendering angular distributions in reasonable computing time. The results of such computations will form the basis of a mathematical

model of time-of-flight spectrometer efficiency which will be discussed in a forthcoming paper.

## Acknowledgments

This work was supported in part by the U.S. Army Research Office under contract DAAL 03-92-G-0037 and by Sandia National Laboratories under contract AH-3292.

## References

- [1] M.H. Mendenhall and R.A. Weller, Nucl. Instr. and Meth. B 47 (1990) 193.
- [2] J.H. Arps and R.A. Weller, Nucl. Instr. and Meth. B 90 (1994) 547.
- [3] W.T. Scott, Rev. Mod. Phys. 35 (1963) 231.
- [4] J.B. Marion and B.A. Zimmerman, Nucl. Instr. and Meth. 51 (1967) 93.
- [5] L. Meyer, Phys. Status Solidi (b) 44 (1971) 253.
- [6] P. Sigmund and K.B. Winterbon, Nucl. Instr. and Meth. 119 (1974) 541, and Nucl. Instr. and Meth. 125 (1975) 491.
- [7] P. Jaracz and S. Mirowski, Nucl. Instr. and Meth. B 43 (1989) 210.
- [8] P. Bauer, E. Steinbauer and J.P. Biersack, Nucl. Instr. and Meth. B 64 (1992) 711.
- [9] D.J. Schlyer and P.S. Plascjak, Nucl. Instr. and Meth. B 56/57 (1991) 464.
- [10] W. Magnus, F. Oberhettinger and R.P. Soni, Formulas and Theorems for the Special Functions of Mathematical Physics (Springer, New York, 1966) p. 397.
- [11] H.A. Bethe, Phys. Rev. 89 (1953) 1256.
- [12] W.H. Press, B.P. Flannery, S.A. Teukolsky and W.T. Vetterling, Numerical Recipes in C (Cambridge University Press, Cambridge, 1988) p. 407.
- [13] Carl de Boor, in: Mathematical Software, ed. J.R. Rice (Academic Press, New York, 1971) p. 417.
- [14] P. Loftager, F. Besenbacher, O.S. Jensen and V.S. Sorensen, Phys. Rev. A 20 (1979) 1443.
- [15] J.F. Ziegler, J.P. Biersack and U. Littmark, The Stopping and Range of Ions in Solids (Pergamon Press, New York, 1985) p. 202.
- [16] Wolfram Research, Inc., *Mathematica*, version 2.2.1 (Champaign, Illinois, USA, 1993).
- [17] J.F. Ziegler, J.P. Biersack and U. Littmark, op. cit., p. 48.
- [18] M.H. Mendenhall and R.A. Weller, Nucl. Instr. and Meth. B 58 (1991) 11.



## Measurement of time-of-flight spectrometer efficiency for light ions at medium energies

James H. Arps and Robert A. Weller \*

*Dept. of Physics and Astronomy, Vanderbilt University, Box 1807-B Nashville, TN 37235, USA*

Medium energy time-of-flight spectrometry is an effective technique for helium backscattering as well as the elastic recoil detection of hydrogen and other light elements. However, the efficiency of a time-of-flight spectrometer, unlike that of a surface barrier detector, depends strongly on the energy and mass of the detected particle. A thorough understanding of this spectrometer quantum efficiency is necessary for quantitative measurements. We report initial measurements of the quantum efficiency of two similar time-of-flight spectrometers in forward and backscattering geometries for hydrogen, helium, and carbon projectiles over the energy range 50–275 keV. The results are compared with predictions of a model which incorporates multiple scattering and secondary electron emission at the carbon start foil along with an energy-independent microchannel plate response. When these processes are taken into account, the efficiency of a spectrometer as a function of projectile species and energy can be described to within experimental error by a single overall calibration constant.

### 1. Introduction

Carbon-foil-based time-of-flight spectrometry uses timed coincident detection of a projectile and the secondary electrons generated as this projectile passes through a foil placed along its path. Simultaneous acquisition of velocity and energy information is possible, depending on the method used. First applied in nuclear physics to measure recoil velocities of energetic heavy ions, these techniques have found new uses in surface and materials characterization. Employed in conjunction with ion beams with typical atomic numbers from 2 to 20 at energies from 2 to 50 MeV, organic layers [1], oxide layers [2], and materials implanted with low  $Z$  elements [3] have been profiled by the time-of-flight detection of elastic recoils. Our group has applied time-of-flight spectrometry at medium energies to both backscattering and elastic recoil detection [4,5].

In ion beam analyses employing a silicon surface barrier detector, the detector's quantum efficiency, the probability that a single-particle impact will generate a detectable event, is usually considered to be unity for particles with reasonable energies. This is in contrast to time-of-flight detection schemes, where the corre-

sponding probability is often considerably less than one. Thus, to analyze quantitatively a material by time-of-flight spectrometry, it is necessary to understand the variation of the spectrometer's response with respect to the parameters of the particle which enters it. Previous studies have suggested that time-of-flight spectrometer efficiencies for hydrogen [6], oxygen, and silicon [7] are proportional to the electronic stopping powers of these ions. Additional experiments have shown that the efficiency differs substantially as a function of recoil mass [8]. Overall spectrometer efficiency also appears to depend sensitively upon experimental conditions. For example, reported values for hydrogen efficiency over similar energy ranges vary from 2 to 90% [6]. These results suggest that all of the physical processes governing spectrometer response have not been fully elucidated.

In this paper, we report the results of a comparative study of the efficiencies of two time-of-flight spectrometers used for backscattering and forward recoil analyses at medium energies. Efficiencies have been measured for hydrogen, helium, and carbon projectiles in the energy range 50–275 keV. Two processes which clearly contribute to the efficiency of a spectrometer are secondary electron emission and multiple scattering, both of which occur as ions pass through the carbon start foil. The number of secondary electrons controls the probability that a projectile generates a start event, while multiple scattering deflects some

\* Corresponding author, tel. +1 615 343 7225, fax +1 615 343 7263, e-mail [weller@vuse.vanderbilt.edu](mailto:weller@vuse.vanderbilt.edu).

projectiles out of the acceptance angle of the stop detector.

Efficiency curves have been calculated using a simple model based upon secondary electron emission and multiple scattering which assumes, in addition, that the response of the microchannel plate which generates the stop pulse is independent of a projectile's velocity. Reasonable agreement between the data and the model calculations has been obtained in all cases, leading to the conclusion that, in the future, it will be possible to establish experimentally a single number characterizing a spectrometer's quantum efficiency. The variation of the efficiency with projectile species and energy will then be predictable using an appropriately detailed mathematical model based upon the detector's design.

## 2. Experimental

The time-of-flight spectrometer and scattering geometry are shown in Fig. 1. Many of the details of the spectrometer's operation are described elsewhere [9], but parameters which are necessary to understand the efficiency and to construct a theoretical model are identified here. Galileo ElectroOptics, Inc., FTD-2003 microchannel plate assemblies 2.5 cm in diameter are used for the start and stop detectors. The detectors, whose active areas are about 50% of their geometric areas, were operated at a bias of  $-2000$  V. Both the forward recoil system (at  $42^\circ$ ) and the backscattering system (at  $150^\circ$ ) incorporate  $2.5 \pm 0.5 \mu\text{g}/\text{cm}^2$  carbon start foils tilted at  $30^\circ$  with respect to the spectrometer axis for an effective multiple scattering thicknesses of approximately  $3 \mu\text{g}/\text{cm}^2$ . The flight path from the start foil to the stop detector is 37 cm in each case. Under these conditions, the acceptance half angle of

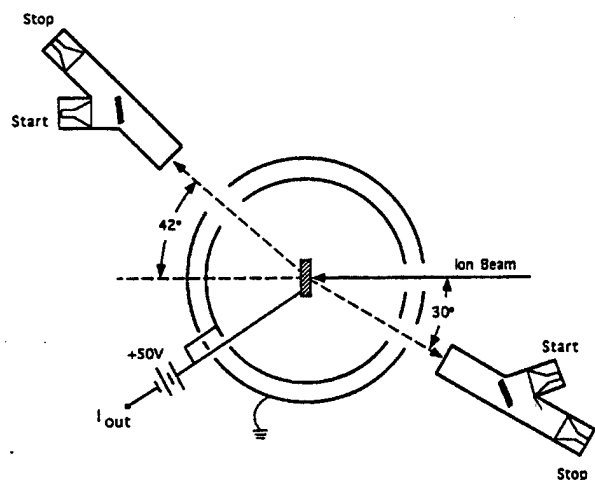


Fig. 1. Schematic of the spectrometer layout, including scattering geometry and biasing of the Faraday enclosure.

the stop detector for multiply scattered ions is approximately  $2^\circ$ . The geometric solid angles subtended by the spectrometers are fixed by entrance apertures at  $1.5 \times 10^{-4}$  and  $7.7 \times 10^{-4}$  sr for the  $42^\circ$  and  $150^\circ$  systems, respectively. Constant fraction discriminators with input sections specially engineered to be compatible with unamplified microchannel plate pulses were used in the spectrometer oriented at  $150^\circ$ . The spectrometer at  $42^\circ$  used conventional constant fraction discriminators which required amplified pulses.

To calibrate the detectors, hydrogen and helium ions with energies from 50 to 275 keV and carbon ions from 100 to 400 keV were backscattered from a silicon sample having a nominal gold coverage of  $(1.0 \pm 0.1) \times 10^{15}$  atoms/cm<sup>2</sup>. Typical doses at each sampled energy were  $1.25 \times 10^{13}$  ions for H and He, and  $6.25 \times 10^{12}$  ions for C. The beam spot size was  $\sim 10$  mm<sup>2</sup>. The sample was reanalyzed after calibration runs by 275 keV He backscattering to check for any sputter removal of Au. As an additional control, 275 keV He backscattering spectra were obtained from a quartz sample lightly coated with colloidal carbon to reduce charging. The heights of the silicon edges in these spectra were compared to verify consistency throughout the experiment.

In the forward scattering experiments, a self-supporting carbon foil was mounted on a stainless steel support with a 6.4 mm diameter hole. A thickness of  $3.6 \pm 0.5 \times 10^{17}$  atoms/cm<sup>2</sup> was derived from both aerial density and energy loss measurements by He backscattering. H and He ions from 50 to 275 keV were forward scattered at  $42^\circ$  using roughly the same doses as the backscattering experiments. Carbon recoils were generated by Ar ions with energies from 125 to 825 keV and doses of  $6.25 \times 10^{11}$  ions at each sampled energy. No measurable change in the foil thickness was observed by He backscattering as a result of the Ar irradiations.

A double-walled, stainless steel Faraday cylinder was used to obtain consistent beam current measurements under the variety of bombardment conditions used in the experiment. Current was summed and integrated from the target and the inner wall of the cylinder, which were electrically connected and biased at +50 V relative to the grounded outer wall. The outer wall shielded the target from stray electrons and ions generated by the ion pumps and vacuum gauge.

## 3. Results and discussion

Fig. 2 shows the spectrometer efficiency data, expressed as the ratio of effective solid angle to the geometric solid angle subtended by the detectors. The effective solid angle was derived for H, He, and C at each energy based on known values for the number of

gold or carbon scattering centers/cm<sup>2</sup>, the Lenz-Jensen scattering or recoil cross section, the number of incident ions, and the measured number of counts in the forward or backscattering peak. The energies at which projectiles entered the detectors were computed using the appropriate kinematic factors with energy loss in the scattering foil taken into account in the forward scattering configuration.

Error estimates equal to  $\pm 10\%$  of measured efficiencies reflect uncertainties in the number of scattering centers/cm<sup>2</sup> and counting statistics. The 42° and 150° spectrometer efficiencies differ by approximately a factor of 2 for each species, as is indicated by the use of differing scales on the left and right axes. We attribute this difference to varying discriminator thresholds and microchannel plate gains in the two systems. The important point to note is that in each case the data are brought into excellent agreement by a

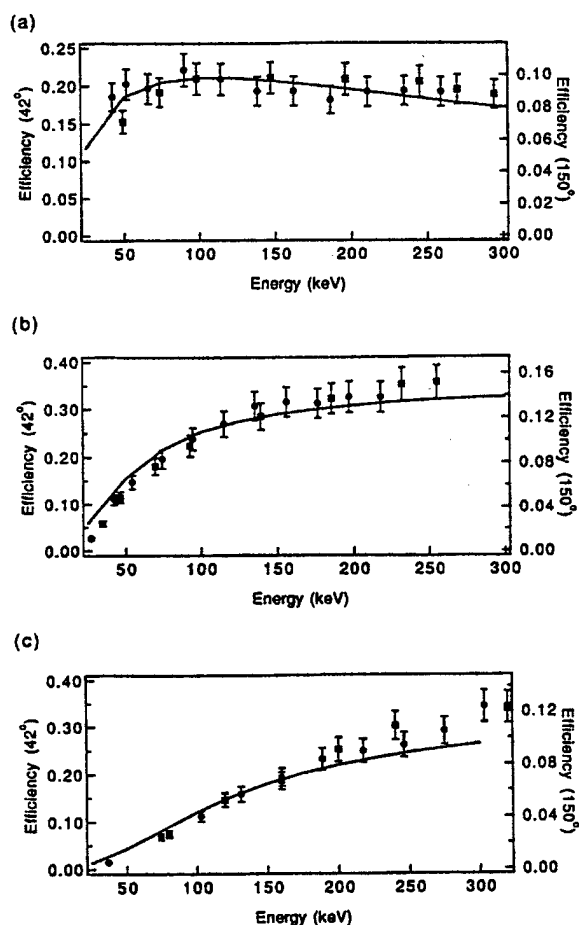


Fig. 2. Data for the 42° (circles) and 150° (squares) spectrometers and normalized theoretical efficiency curves, plotted as a function of energy for (a) hydrogen, (b) helium and (c) carbon.

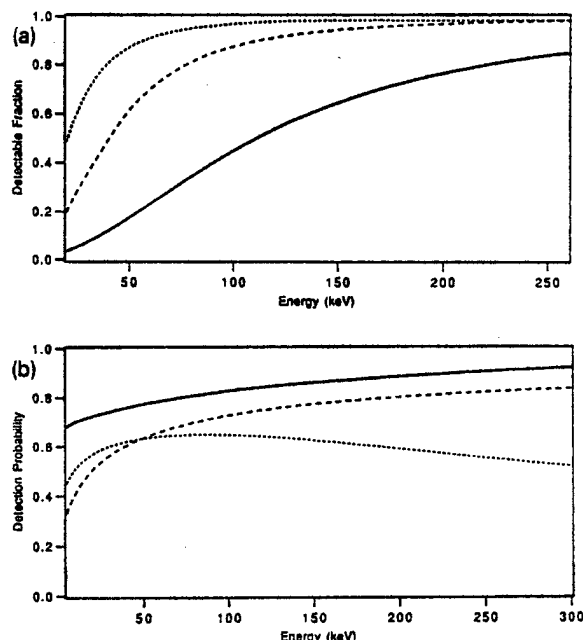


Fig. 3. Theoretical multiple scattering (a) and secondary electron emission (b) contributions to spectrometer efficiency for hydrogen (short dashed), helium (long dashed) and carbon (solid line).

single overall normalization. The solid curves in Figs. 2 are the results of the model calculations described below.

Multiple scattering in the carbon start foil deflects some projectiles enough that they can no longer strike the stop detector. In order to estimate the number of projectiles which are thus lost, we have made ab initio calculations of the multiple scattering distribution functions for H, He and C ions passing through the start foils using the basic equations described in refs. [10,11]. Distribution functions were computed at increments of 25 keV in the energy range corresponding to the measurement using the Lenz-Jensen scattering cross section. These angular distributions were numerically integrated over the solid angle subtended by a 2° cone to give the fraction of multiply scattered ions falling within the acceptance half-angle of the stop detector. The results of the calculation are shown in Fig. 3a as the fraction of ions of each species expected to reach the stop detector as a function of energy.

In his pioneering work on secondary electron emission, Sternglass [12] demonstrated that the yield  $\gamma$  of secondary electrons per incident ion is proportional to the electronic stopping cross section of the ion  $s_e$  in the vicinity of the emitting surface ( $\gamma = \Lambda s_e$ ). Constants of proportionality  $\Lambda$  appropriate to various ions exiting C foils have been reported by Rothard et al. [13]. When the stopping cross section is expressed in units

of  $10^{-15}$  eV cm<sup>2</sup>, the values of  $A$  are 0.25, 0.175, and 0.125 in units of  $10^{15}/(\text{eV cm}^2)$  for H, He, and C, respectively. Since, in principle, only one secondary electron is needed to trigger the start microchannel plate, the probability  $p$  that a pulse is generated by the arrival of  $\gamma$  secondary electrons is  $p = 1 - e^{-\lambda\gamma}$ , where  $\lambda$  is the probability that a single electron will trigger an event. Fig. 3b shows this probability as a function of energy for each species. We have used a conservatively small estimate of  $\lambda = 0.3$  based upon the work of Fraser [14] and the data which he cites. (Larger values of  $\lambda$  cause the curves in Fig. 3b to increase more rapidly.) The stopping cross sections were computed by the methods described in ref. [15].

The solid curves shown in Fig. 2 were computed by taking the product of the multiple scattering function from Fig. 3a and the secondary electron function from Fig. 3b appropriate to each species and computing a normalization for each detector system by a least squares fit to the data. Only those points with energies greater than 50 keV were used since, in this simple model, the response of the stop microchannel plate was ignored. The ratio of the normalization constants for the 42° and 150° spectrometers were used to set the range of the right-hand scales in Fig. 2. For the 42° detector, the normalization constants for H, He and C were respectively:  $0.34 \pm 0.03$ ,  $0.40 \pm 0.03$  and  $0.32 \pm 0.04$ . Similarly, for the 150° detector the values were:  $0.16 \pm 0.04$ ,  $0.17 \pm 0.04$  and  $0.12 \pm 0.04$ . Note that for each spectrometer, there is a reasonable probability that the three constants are, in fact, equal. The probability that  $\chi^2$  would be larger for normally distributed statistical variations is 22% and 63% respectively.

In agreement with the previously cited experiments, our measured detection efficiency for hydrogen is smaller than for He and C. From Fig. 3b, this can be attributed to the secondary electron contribution to efficiency, even though for hydrogen this quantity reaches a maximum in the energy range studied. Note also that for small  $\lambda$  or  $\gamma$ , the efficiency is simply proportional to the stopping cross section. Multiple scattering, on the other hand, tends to dominate the behavior of the carbon efficiency curve, especially at lower energies where broadening of the angular distribution causes significant losses in the number of particles striking the stop detector.

The ability of this simple model to properly and consistently predict the spectrometer response for the various masses and energies is persuasive evidence that multiple scattering and secondary electron emission are the primary physical processes governing spectrometer performance. A more complete theory will necessarily include a mass and energy dependent stop detector response. Let us emphasize again, however, that to within statistical uncertainty, only one normalization factor is needed for each spectrometer in order to

bring the theoretical curves into reasonable agreement with the data for all of the projectile species which were studied.

#### 4. Conclusion

The efficiencies of two similar carbon-foil-based time-of-flight spectrometers have been studied as a function of energy from 50 to 275 keV for H, He, and C at 42° and 150° scattering angles. Within the experimental uncertainties, the efficiency of each detector can be characterized by a single measured number with the variation in efficiency with energy and mass of the analyzed particle being given by a model based upon secondary electron emission and multiple scattering. This result indicates that efficiencies may be estimated for a variety of time-of-flight spectrometer configurations over a wide range of masses and energies by considering parameters such as foil thickness, flight path length, and individual microchannel plate quantum efficiencies. A detailed discussion of the mathematical model of the spectrometer and its range of application, including the effects of variation of parameters such as  $\lambda$  and of additional assumptions about the response of the stop detector, will be the subject of a forthcoming paper.

#### Acknowledgements

This work was supported in part by the U.S. Army Research Office under contract DAAL 03-92-G-0037. We are grateful to J.M. Anthony and J.A. Keenan, Texas Instruments Inc., for their assistance in the design and manufacture of our Faraday cylinder and to Martha Riherd Weller for helpful comments on the manuscript.

#### References

- [1] J. Sokolov, M.H. Rafailovich, R.A.L. Jones and E.J. Kramer, *Appl. Phys. Lett.* 54 (1989) 590.
- [2] H.J. Whitlow, A.B. Andersson and C.S. Petersson, *Nucl. Instr. and Meth. B* 36 (1989) 53.
- [3] R. Groleau, S.C. Gujrathi and J.P. Martin, *Nucl. Instr. and Meth.* 218 (1983) 11.
- [4] M.H. Mendenhall and R.A. Weller, *Nucl. Instr. and Meth. B* 47 (1990) 193.
- [5] J.H. Arps and R.A. Weller, *Nucl. Instr. and Meth. B* 79 (1993) 539.
- [6] S.C. Gujrathi and S. Bultena, *Nucl. Instr. and Meth. B* 64 (1992) 789.
- [7] H.J. Whitlow, G. Possnert and C.S. Petersson, *Nucl. Instr. and Meth. B* 37 (1987) 448.

- [8] E. Arai, H. Funaki, M. Katayama, Y. Oguri and K. Shimizu, *Nucl. Instr. and Meth. B* 64 (1992) 296.
- [9] M.H. Mendenhall and R.A. Weller, *Nucl. Instr. and Meth. B* 40/41 (1989) 1239.
- [10] H.A. Bethe, *Phys. Rev.* 89 (1953) 1256.
- [11] P. Sigmund and K.B. Winterbon, *Nucl. Instr. and Meth.* 119 (1974) 541.
- [12] E.J. Sternglass, *Phys. Rev.* 108 (1957) 1.
- [13] H. Rothard et al., *Phys. Rev. A* 41 (1990) 2521.
- [14] G.W. Fraser, *Nucl. Instr. and Meth.* 206 (1983) 445.
- [15] J.F. Ziegler, J.P. Biersack and U. Littmark, *The Stopping and Range of Ions in Solids* (Pergamon, New York, 1985) p. 202.

## Instrumental effects on time-of-flight spectra \*

Robert A. Weller

*Vanderbilt University, Nashville, Tennessee, USA*

Using two detectors to time individual scattered particles, time-of-flight, medium-energy backscattering has established a new standard for depth resolution by ion backscattering and has been suggested as a means to measure very low levels of contamination on semiconductor surfaces. This paper sets forth a criterion for backscattering sensitivity to trace contaminants based upon the limit imposed by sputtering and analyzes the implications of random coincidence background in time-of-flight spectra for reaching this theoretical limit. The effects of high count rates on spectral shape are discussed as are the effects of the quantum efficiencies of start and stop detectors. An integral equation relating an intrinsic spectrum and the corresponding measured data set is presented along with its formal solution.

### 1. Introduction

The scattering cross section for 200 keV  $^{12}\text{C}^+$  on Fe at  $150^\circ$  is over 700 times larger than the comparable cross section for 2 MeV  $^4\text{He}^+$ . This very large increase in cross section, together with technical advances in the energy spectrometry of backscattered ions in this energy range, has raised the possibility that medium energy backscattering, particularly with heavy ions, may be a superior means of detecting very low levels of trace impurities in semiconductors. Following this reasoning, Knapp and Doyle [1] have developed a technique using surface barrier detectors preceded by range foils which they call HIBS (heavy ion backscattering spectrometry) specifically aimed at very high sensitivity trace element analysis at surfaces, while Mendenhall and Weller [2], following a somewhat more general line, have developed a time-of-flight approach to medium energy backscattering (MEBS) which emphasizes both resolution and sensitivity.

The ultimate sensitivity of both the time-of-flight and range foil techniques is limited by similar physical processes. Two of the most important are multiple scattering, by which ions with energies higher than is kinematically possible from a single collision are reflected from the target, and sputtering, by which all atoms of interest are eventually removed from the target. Brice has recently completed a theoretical investigation of multiple scattering relevant to this application [3]. In this paper, I suggest a criterion for the

limit of sensitivity to trace elements which is imposed by sputtering and present a mathematical model of a time-of-flight spectrometer which may be used to calculate the random coincidence background which, along with sputtering, limits the sensitivity of the time-of-flight approach.

In Chu, Mayer, and Nicolet [4], the standard reference on backscattering spectrometry, the authors do not quantify the limit of sensitivity of backscattering which is imposed by sputtering. However, a more recent text by Feldman and Mayer [5] does consider the issue. These authors assume that the total erosion by the incident beam must be less than the original film thickness for a statistically significant measurement. This is a useful estimate but one which contains a subtle ambiguity which arises because the degree of erosion is not connected more directly with the statistical uncertainty of the measurement. Consider, for example, the meaning of a result with 10% counting statistics (100 counts) when 100% of the target layer has been removed during the measurement. A more consistent estimate of sensitivity can be obtained if the fraction of the trace constituent which is sputtered away during the backscattering measurement is approximately the same as the fractional statistical uncertainty of its measured areal density. In the following section, I will quantify this sensitivity criterion and use it to assess the relative merits of MEBS with ions of several masses.

The principal source of background in a time-of-flight backscattering spectrum is random coincidences between start and stop signals which are produced by different particles. The rate of these random events is clearly related to the rate of true events and this relationship controls the signal-to-background in time-

\* Supported by the U.S. Army Research Office (DAAL 03-92-G-0037). Additional support was provided by a grant from Texas Instruments, Inc.

of-flight spectra. The third section will develop the relationship between an intrinsic time-of-flight spectrum and the random background which accompanies it.

## 2. Sensitivity criterion

Consider a backscattering experiment to measure a surface contaminant in which the physical quantities are defined as follows. Let  $\rho$  be the areal density of the contaminant species,  $\sigma$  the differential scattering cross section,  $\Omega$  the detector solid angle,  $\eta$  the detector quantum efficiency,  $N$  the number of primary ions,  $A$  the cross-sectional area of the incident beam,  $C$  the measured number of backscattered particles,  $B$  the background in the spectral region of the backscatters from all sources,  $P$  the number of sputtered contaminant atoms per primary ion, and  $\epsilon = \Delta\rho/\rho$  the fraction of the contaminant layer that is removed during the measurement. The number of backscatters is:

$$C = N\sigma\rho\Omega\eta. \quad (1)$$

Similarly, the number of sputtered contaminant atoms is:

$$NP = A\Delta\rho = \rho\epsilon A. \quad (2)$$

To these well known relationships we add the condition defined above, that the statistical uncertainty in the measurement be equal to the fraction of the material removed:

$$\epsilon = \frac{\Delta\rho}{\rho} = \frac{\sqrt{C+2B}}{C}. \quad (3)$$

From these, we obtain an expression for the sensitivity of a measurement in terms of the required fractional statistical uncertainty of the result

$$\rho^2 = \frac{1 + \sqrt{1 + 8\epsilon^2 B}}{2\epsilon^3} \frac{P}{A\sigma\Omega\eta}. \quad (4)$$

Of the quantities in this equation,  $P$  is the least well known. In order to estimate  $P$ , let us assume that contaminants are removed randomly in collision cascades which are dominated by the substrate atoms. In this case, one might expect that the yield of the contaminant is just the yield of the substrate reduced by the proportion of contaminant atoms in the total pool from which sputtered atoms are drawn:

$$P \approx Y_s \frac{\rho}{\rho_s}, \quad (5)$$

where  $\rho_s$  ( $\gg \rho$ ) is the areal density of a layer of the substrate from which sputtered atoms originate; that is, a region about three atomic layers thick. With this added assumption, we arrive at the final expression for

Table 1

Detectable level  $\rho$  of Au on Si with various 100 keV beams in the absence of background. Also shown are  $\sigma_{LJ}$ , the Lenz-Jensen cross section for scattering from Au at  $150^\circ$ , and  $Y_s$ , the sputtering yield of the Si substrate.  $N$  is the number of incident ions required for the measurement. These values are based upon assumptions that  $\rho_s = 4 \times 10^{15} \text{ cm}^{-2}$ ,  $A = 0.03 \text{ cm}^2$ ,  $\Omega\eta = 10^{-4} \text{ sr}$ , and  $\epsilon = 0.3$ .

Beam	$\sigma_{LJ}$ [ $10^{-22} \text{ cm}^2$ ]	$Y_s$	$\rho$ [ $10^9 \text{ cm}^{-2}$ ]	$N$ [ $10^{15} \text{ cm}^{-2}$ ]
$^{20}\text{Ne}$	344	0.40	36	0.09
$^{16}\text{O}$	255	0.23	28	0.15
$^{12}\text{C}$	169	0.11	20	0.32
$^{11}\text{B}$	128	0.075	18	0.48
$^4\text{He}$	28	0.0046	5.1	7.8
$^1\text{H}$	8	0.00024	0.9	150

the minimum density layer given a number  $B$  of background counts and a required precision  $\epsilon$  of the result:

$$\rho = \frac{1 + \sqrt{1 + 8\epsilon^2 B}}{2\epsilon^3} \frac{Y_s}{\rho_s A \sigma \Omega \eta}. \quad (6)$$

Casual intuition suggests that the increase of scattering cross section with increasing atomic number of the projectile would favor heavy ions for highest sensitivity. This conjecture is tested in table 1 which gives the level at which Au can be detected on Si with several different ions. Table 1 assumes that  $\epsilon = 30\%$  (that is a non-zero result with a confidence level of three standard deviations), that  $B = 0$ , and that the beam energy is 100 keV. Notice that the greatest sensitivity (smallest  $\rho$ ) is obtained for the lightest projectile even though the cross section is lowest in this case. The reason for this rather surprising result is that sputtering is the dominant effect. Greatest sensitivity is obtained by using light ions but at a cost of longer (often much longer) run times. Heavy ions are preferred only when constraints are placed on the allowed duration of the measurement. One would, therefore, expect that it would be desirable to use as large a beam current as possible, in order to perform the measurement in the least time. Unfortunately, as the following section shows, with time-of-flight detection it is not possible to compensate in this way, because using large beam currents drives up the background,  $B$ .

## 3. TOF background

Eq. (6) shows the effect of background on the best attainable sensitivity for trace element analysis. In a time-of-flight spectrometer such as is described in ref. [2], most background events occur when a start pulse and stop pulse are initiated by different particles. In

this section, I present an integral equation which describes the distortion of time-of-flight spectra which results from these random coincidences in the spectrometer. Let us assume that the true rate of particles entering the spectrometer is  $\lambda$ , that the normalized intrinsic distribution of flight times  $t$  is  $f(t)$ , and that the efficiencies of the start and stop detectors as a function of flight time are  $\eta_1(t)$  and  $\eta_2(t)$ . We assume further that the rate of random start and stop pulses caused, for example, by electronic noise, cosmic rays, etc. can be neglected. Define the mean efficiencies of the detectors as:

$$\eta_1 = \int \eta_1(t) f(t) dt \quad \text{and} \quad \eta_2 = \int \eta_2(t) f(t) dt. \quad (7)$$

With these definitions, it is possible to express the mathematical form of the probability,  $P(t)$ , that an ion entering the time-of-flight spectrometer generates an event with flight time  $t$ , in terms of the intrinsic distribution  $f(t)$  and the true event rate  $\lambda$ . The expression is:

$$P(t) = p e^{-\eta_2 \lambda t} \left[ \eta_1(t) \eta_2(t) f(t) + \eta_1 \eta_2 \lambda - \eta_2 \lambda \int_0^t \eta_1(t') \eta_2(t') f(t') dt' \right]. \quad (8)$$

Here  $p$  is the probability that the system is not busy with a previous pulse at the time that a start pulse arrives. This expression is derived by considering all possible variations for an event. For example, the first term in the brackets corresponds to the composition of probabilities in the following sequence: 1) the particle entering the spectrometer has flight time  $t$ ,  $f(t) dt$ ; 2) the spectrometer is not busy,  $p$ ; 3) the start detector is triggered,  $\eta_1(t)$ ; 4) no random stop occurs during the interval  $(0, t)$ ,  $e^{-\eta_2 \lambda t}$ ; and finally; 5) the stop detector is triggered,  $\eta_2(t)$ .

The principal predictions of eq. (8) are that there is a component of additive random background proportional to  $\lambda$  and that a multiplicative exponential damping factor  $e^{-\lambda_2 t}$  ( $\lambda_2 \equiv \eta_2 \lambda$ ) tends to attenuate the spectrum at long arrival times. In measured time-of-flight backscattering spectra, such as fig. 1, this attenuation is ordinarily negligible in the portion of the spectrum that has features of interest and so can be ignored. It is the rate dependent background which defeats the use of increased beam current to shorten measurement times. Fortunately, the principal constituent of the additive background, at least for the common case of analyzing heavy constituents on a lighter substrate, is  $\eta_1 \eta_2 \lambda$ , a constant that can be determined easily by examining regions of the spectrum which do not contain kinematically allowable backscattering events. Thus, background subtraction in time-of-flight spectra is straightforward in contrast to

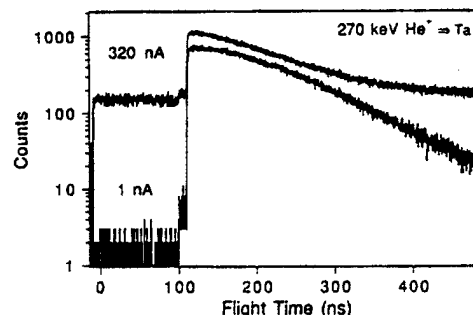


Fig. 1. Time-of-flight spectra for  $^4\text{He}^+$  backscattering at  $150^\circ$  from a solid Ta target with the same total charge delivered by beam currents of 1 and 320 nA. The event rates were  $\eta_1 \lambda = 7500 \text{ s}^{-1}$  and  $740 \text{ ks}^{-1}$  respectively and  $\eta_2 \lambda = 1000 \text{ s}^{-1}$  and  $320 \text{ ks}^{-1}$  respectively. Several factors, including the uncertainty of the current integration for the 1 nA spectrum and an electronic time-out at 500 ns, complicate the quantitative comparison of these data with eq. (8). However, the trend toward higher relative background at the high event rate is clear as is the essential flatness of the background in the kinematically inaccessible region of the spectrum. The small step in the level of the background near the Ta edge is an artifact of the external electronics which has now been eliminated.

subtraction of pulse pile-up which is experienced in energy spectra measured with surface barrier detectors. However, as eq. (6) clearly shows, even theoretically well understood background exacts a toll in diminished sensitivity.

Two additional points need to be made with reference to eq. (8). First, although the background increases approximately linearly at low event rates, this is true only so long as  $p$  is near unity. At very high rates, the effect of this factor, which is discussed further below, must also be considered. Finally, even at low counting rates, it is necessary to measure the total system efficiency  $\eta(t) \equiv \eta_1(t) \eta_2(t)$ , which is, of course, dependent on the ion being analyzed, in order to recover  $f(t)$  from a measured spectrum. This is a minor inconvenience of time-of-flight spectrometry when compared with the near unit quantum efficiency of energy spectrometry using surface barrier detectors.

Eq. (8) can be converted to a differential equation and so can be formally inverted to obtain the best achievable approximation,  $\eta_1(t) \eta_2(t) f(t)$ , to the true distribution,  $f(t)$ , from the measured distribution  $P(t)$ . The result is of theoretical interest but is not very useful for practical data analysis, since in a real experiment one does not ordinarily sample the distribution for a large enough range of  $t$  values. The formal inversion of eq. (8) is:

$$\eta_1(t) \eta_2(t) f(t) = p^{-1} e^{\eta_2 \lambda t} \int_0^t [\eta_2 \lambda P(t') + P'(t')] dt', \quad (9)$$



where  $P'$  denotes the derivative,  $P(t)$  and  $\eta_2\lambda$  are known from experiment, and it is assumed that  $\eta_1(t)\eta_2(t)f(t) = 0$  when  $t = 0$ . Using the simple assumption that the detector's mean dead time  $\tau$  is the mean duration of observed events, one obtains for  $\tau$ :

$$\tau = \frac{\int_0^\infty tP(t) dt}{\int_0^\infty P(t) dt} \quad (10)$$

and, consequently, for the live time factor,  $p$ :

$$p = \frac{1}{1 + \eta_1\lambda\tau}. \quad (11)$$

This equation is, of course, only valid when  $\lambda_1 \equiv \eta_1\lambda$  is not too large. The random coincidence background sets a lower limit on the sensitivity of time-of-flight measurements but, as eq. (8) shows, this background depends upon the rate of events in the stop detector. If a significant portion of the total counts in a spectrum is generated by uninteresting, low-energy particles such as backscatters from the substrate, then the signal-to-noise performance of a spectrometer can be enhanced by placing a range foil like that used by Knapp and Doyle [1] just before the stop detector. In this location, the foil introduces negligible loss of timing resolution for the particles which pass through it, and pin holes in the foil only cause an increase in the uniform background, not localized distortions in the spectrum.

#### 4. Conclusion

Here are the principal conclusions of this paper. 1) When total measurement time is unlimited, maximum sensitivity for detecting heavy contaminants on a light substrate is obtained with light ions such as H or He rather than heavier ions such as C or Ne. 2) When run time (or total number  $N$  of incident ions) is limited, eqs. (2), (3) and (5) together imply that heavier ions are required, but from eq. (6) one then finds that less overall sensitivity can be achieved. 3) Measured time-

of-flight spectra contain a flight-time-dependent efficiency factor which is independent of count rate and an approximately uniform rate dependent background. Thus, greatest sensitivity is obtained with low beam currents so long as the actual rate of detected events is a few times larger than the true electronic background. 4) An effective strategy for reducing background with minimal loss of timing resolution, and therefore increasing sensitivity to heavy trace contaminants, is to tailor the response  $\eta_2(t)$  of the stop detector to reduce the rate of uninteresting backscatters from the substrate. One obvious way to do this is to place a foil in front of the stop detector which is thick enough to eliminate most particles backscattered from the substrate but thin enough to pass those which are scattered from the species of interest.

As of this writing, the only reliable method to obtain the quantum efficiency  $\eta(t) = \eta_1(t)\eta_2(t)$  of a time-of-flight spectrometer is to measure it. It is clear that one factor strongly affecting  $\eta_1(t)$  is the secondary electron emission of the 2–3  $\mu\text{g}/\text{cm}^2$  carbon foil which generates the electrons which trigger the start detector. Similarly, multiple scattering in this foil is very important in determining  $\eta_2(t)$  since particles deflected from the axial trajectory of the spectrometer will not be detected. The degree to which the flight-time-dependent functions  $\eta_1(t)$  and  $\eta_2(t)$  can be predicted from first principles is presently unknown, but is the subject of active research.

#### References

- [1] J.A. Knapp and B.L. Doyle, Nucl. Instr. and Meth. B45 (1990) 143.
- [2] M.H. Mendenhall and R.A. Weller, Nucl. Instr. and Meth. B59/60 (1991) 120.
- [3] D.K. Brice, Nucl. Instr. and Meth. B69 (1992) 349.
- [4] W.-K. Chu, J.W. Mayer and M.-A. Nicolet, Backscattering Spectrometry (Academic Press, New York, 1978).
- [5] L.C. Feldman and J.W. Mayer, Fundamentals of Surface and Thin Film Analysis (North-Holland, New York, 1986) p. 54.

## Medium energy elastic recoil analysis of surface hydrogen

James H. Arps and Robert A. Weller

*Vanderbilt University, Nashville, Tennessee, USA*

We describe a technique for the detection of light mass constituents at or near the surface of a material using two microchannel detectors to time the individual recoils. Sensitivity to hydrogen is demonstrated by probing samples of Kapton, hydrated titanium, and wafer grade silicon with 270 keV helium, neon, and argon ions. Because the detector is sensitive to particle velocity rather than energy, recoil atoms and scattered ions are easily distinguished. Processes which affect the system's sensitivity to hydrogen are identified and a value for the hydrogen detection efficiency is established. The method may realize a number of advantages over conventional elastic recoil detection, including the elimination of the absorber foil, heightened sensitivity, and improved depth resolution.

### 1. Introduction

The greatest strength of surface analysis by ion backscattering is that the fundamental interaction cross section describing the probability of collision between the ions of the beam and the atoms of the sample is calculable from first principles. If, in addition, the species of interest is present in a thin layer at or near the surface and has an atomic mass greater than that of the bulk of the sample, then the resulting spectra are especially easy to interpret. Conversely, if the species of interest has an atomic mass lighter than the substrate upon which it rests, then backscattering spectra are difficult to interpret and the quality of the resulting data is lower. This is particularly true of hydrogen, which is invisible in backscattering spectra.

Hydrogen is present to a greater or lesser degree on almost all surfaces. Its presence in significant quantities in a material may be useful, as in the case of silicon [1] or, as in the case of titanium [2], may significantly degrade the material's performance. In either case, detecting and quantifying hydrogen, especially in small quantities, is a continuing challenge. It is, of course, invisible to electron spectroscopies, and, while it is readily observable by secondary ion mass spectrometry, these observations are virtually impossible to quantify.

The most reliable quantitative techniques for measuring surface hydrogen make use of energetic ion beams. The most highly developed is nuclear resonant reaction analysis in which a beam of particles such as  $^{15}\text{N}$  causes the specimen to emit  $\gamma$  radiation in proportion to the hydrogen concentration by, in this case, the nuclear reaction  $^{15}\text{N}(p, \alpha\gamma)^{12}\text{C}$  [3]. Narrow resonances

in the reaction are used to obtain information not only about the quantity of hydrogen present, but also its depth distribution. An alternative technique, known as elastic recoil detection (ERD), is more direct. An energetic beam is directed onto the surface to be analyzed at an oblique angle so that low angle forward recoils as well as scattered beam ions can be detected. In this way target constituents with low atomic masses are visible even when they reside on substrates with much larger atomic mass. Much of the original development of ERD used silicon surface barrier detectors for the energy spectrometry of recoiling atoms [4]. In order to effectively profile hydrogen, it was necessary to use them in conjunction with range foils to remove the scattered ions and heavy recoils. Thomas et al. [5] first observed that the correct parameter to use to differentiate particles in the forward geometry is not energy (which surface barrier detectors measure) but rather time, since lighter forward recoils move faster (up to nearly twice the speed of the incident projectiles). Using technology in common use for heavy ion nuclear spectroscopy, he showed that time-of-flight detection could produce superior depth resolution and discrimination of species when used with beam energies ranging up to a few tens of MeV.

Our group has previously demonstrated that backscattering spectrometry using time-of-flight detection and beams with energies in the range 200–300 keV is a valuable complement to conventional Rutherford backscattering (RBS) [6]. The extension of the medium energy time-of-flight technique to forward scattering is natural because a number of advantages of using lower energy beams, such as less total deposited energy and a smaller accelerator, also obviously apply

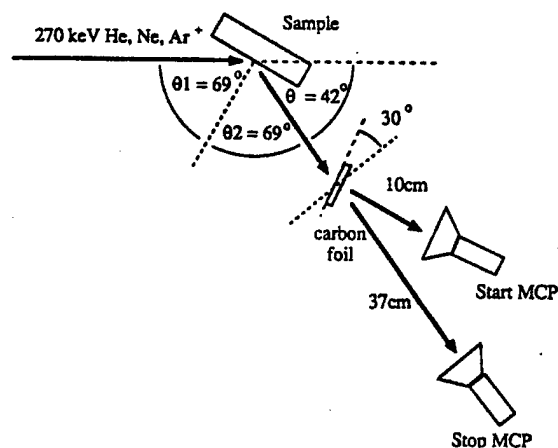


Fig. 1. Schematic of scattering geometry and detector layout.

to this case. Others, such as enhanced sensitivity and depth resolution, must be verified experimentally.

In this paper, we report preliminary measurements of hydrogen and other low mass surface species using time-of-flight medium energy elastic recoil detection. Samples of clean and hydrated titanium, etched and oxidized device-grade silicon, and Kapton have been studied. Beams of 270 keV He<sup>+</sup>, Ne<sup>+</sup>, and Ar<sup>+</sup> ions were used to study the effects of probe species on the sensitivity of the system to hydrogen. Near surface concentrations of hydrogen and oxygen have been estimated and the relative depth distributions of hydrogen in these materials are compared.

## 2. Experiment

The scattering and detection geometry is shown in fig. 1. Beams of singly charged He, Ne, and Ar ions were focused on the target in spots approximately 3 mm in diameter. Beam currents were typically in the 1–2 nA range with a total deposited charge of approximately 200 nC. The sample was oriented so that the scattering angle was 42° and incident and scattered angles,  $\theta_1$  and  $\theta_2$ , were 69° with respect to the target normal. Both the detector and the analysis chamber

were maintained at a base pressure of  $\sim 1 \times 10^{-8}$  Torr.

The time-of-flight detector used for these measurements is similar to the one discussed in an earlier paper [7]. A recoil or scattered atom (charged or neutral) passes through a rotateable  $3 \mu\text{g}/\text{cm}^2$  carbon foil which is ordinarily tilted at 30° with respect to the particle's trajectory, and traverses a 36.4 cm long flight path before encountering the stop detector. The stop pulse is produced when the atom strikes a microchannel plate (Galileo ElectroOptics FTD-2003). The secondary electrons generated in the foil are accelerated to 800 eV and detected by a second microchannel plate assembly. The microchannel plate pulses are amplified and time markers are generated by constant fraction discriminators. The time markers are used to generate a time-proportional analog pulse using a time-to-amplitude converter. A multichannel analyzer converts and histograms the pulses into 2048 channel spectra. The measured timing resolution of the elastic recoil TOF system is approximately 1.5 ns. The detector solid angle, defined by a small aperture in front of the detector, was  $1.5 \times 10^{-4}$  sr.

The detection efficiency for hydrogen was investigated by bombarding an  $8.5 \mu\text{g}/\text{cm}^2$  carbon foil with protons with energies from 50 to 270 keV. The foil was oriented normal to the beam and scattered H was measured at  $\theta = 42^\circ$  with respect to the beam. The transmitted beam was collected by a Faraday cup and the resulting current was used, along with a correction for charge neutralization in the foil, to establish the total number of incident ions. Preliminary measurements of the efficiencies for helium, carbon, and oxygen have also been studied similarly.

Samples were chosen to contain hydrogen in a range of concentrations both on the surface and in the bulk. A Kapton ( $\text{C}_{22}\text{H}_{10}\text{N}_2\text{O}_4$ ,  $\rho = 1.42 \text{ g}/\text{cm}^3$ ) sample was cut to size from a 35  $\mu\text{m}$  thick sheet made commercially by DuPont. Hydrated titanium was prepared from a 0.127 mm thick, 99.98% titanium foil in an electrolysis cell assembled using the titanium as the cathode and high purity graphite as the anode. The electrodes were immersed in a 0.05M solution of hy-

Table 1

Comparison of probe beams and respective parameters which affect the measurement of hydrogen in silicon. The columns from left to right indicate (1) probe beam species, (2) recoil hydrogen cross section, (3) surface recoil H flight time in the detector, (4) surface scattered beam flight time, (5) surface recoil Si flight time, (6) resolveable surface contaminants, and (7) Si normal incidence sputtering yield

Ion	$\sigma_{\text{H}}(42^\circ)$ [ $10^{-23} \text{ cm}^2$ ]	$\Delta t_{\text{H}}$ [ns]	$\Delta t_{\text{ion}}$ [ns]	$\Delta t_{\text{Si}}$ [ns]	Resolveable species	$Y_{\text{Si}}$
$^4\text{He}^+$	1.73	92.1	112.2	599.5	H, D	0.022
$^{20}\text{Ne}^+$	694	171.5	287.9	384.8	H, D, C	0.19
$^{40}\text{Ar}^+$	6750	239.5	641.0	385.5	H, D, C, O, F	0.84

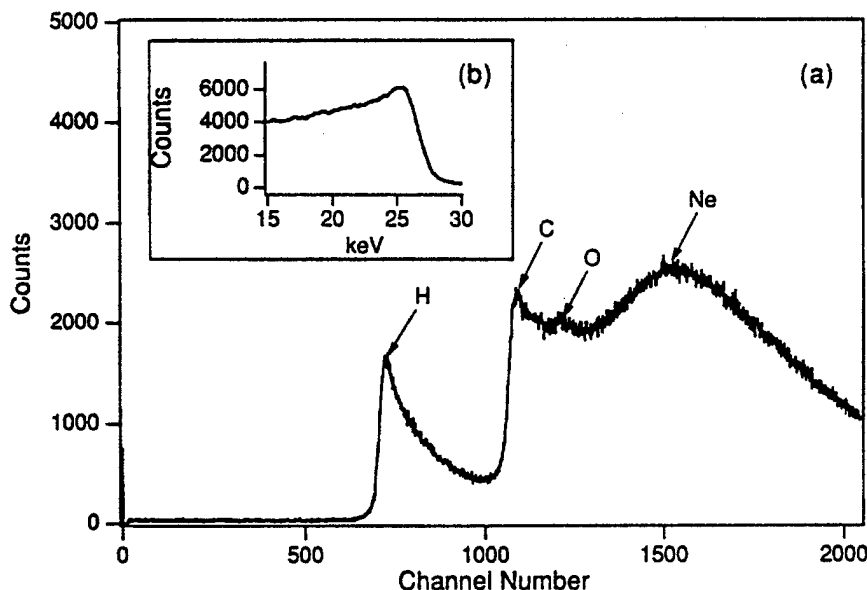


Fig. 2. (a) TOF spectra for 270 keV  $\text{Ne}^+$  on the polymer Kapton. A total charge of  $1.25 \times 10^{13}$  ions was deposited during the analysis. (b) Transformed energy spectrum for recoil hydrogen in Kapton.

drochloric acid in deionized water for 3 h while a current of 100 mA at 30 V was passed between them. Two silicon samples were cut from a pristine, 6-in., device-quality wafer cleaved along the [100] surface. One sample was dipped in reagent grade hydrofluoric acid (49%) for 1 min and rinsed in deionized water for 2 min with the intent of removing the surface oxide.

### 3. Results and discussion

For quantitative work it is essential to know the quantum efficiency of the time-of-flight detector. We define this simply as the probability that an ion entering the detector will generate an observable event. The efficiency was determined for protons scattered from carbon based on known values for the cross section, the number of scattering centers/ $\text{cm}^2$  and the number of incident ions. For protons the result was an efficiency of  $30 \pm 5\%$  over a wide energy range. The value is comparable with other reported results [8]. Because the energy loss for protons in the carbon start foil is nearly a maximum over our range of interest, the efficiency of secondary electron emission is high. However, this is offset by multiple scattering in the start foil. A significant increase in the count rate at the stop detector was observed during a sample irradiation when the start foil was rotated out of the particle's flight path. Calculations using an independent implementation of the TRIM algorithm [9] suggest that at least

half of the recoil protons in the range 25–50 keV will be scattered out of the  $2^\circ$  acceptance half-angle of our stop microchannel plate. Multiple scattering of an incident beam of Ne or Ar is even greater by comparison. This can be used to advantage because it limits the count rate from scattered beam ions which provide little useful information yet contribute to the background.

A comparison of the effects of the probe beam on some crucial parameters of the spectrum of hydrogen in silicon are shown in table 1. Hydrogen recoil cross sections, calculated using the Lenz-Jensen potential, favor Ne and Ar for optimal sensitivity. It should be noted that the recoil cross section using 270 keV  $^{20}\text{Ne}^+$  is 5 orders of magnitude larger than 4 MeV  $^4\text{He}^+$  and  $\sim 1000$  times larger than 30 MeV  $\text{Cl}^+$ , a typical probe beam used in conventional ERD. However, at medium energies, sputtering of the surface is a greater concern. Sputter yields from silicon calculated using the empirical formula of Matsunami et al. [10] clearly indicate that the deposited charge should be minimized when the heavier probe ions are used.

The flight time of an atom in the detector can be calculated using

$$\Delta t = \sqrt{\frac{mL^2}{2\left(E - x \frac{dE}{dx}\right)}} - t_0, \quad (1)$$

where  $m$  is the mass of the particle,  $L$  is the flight

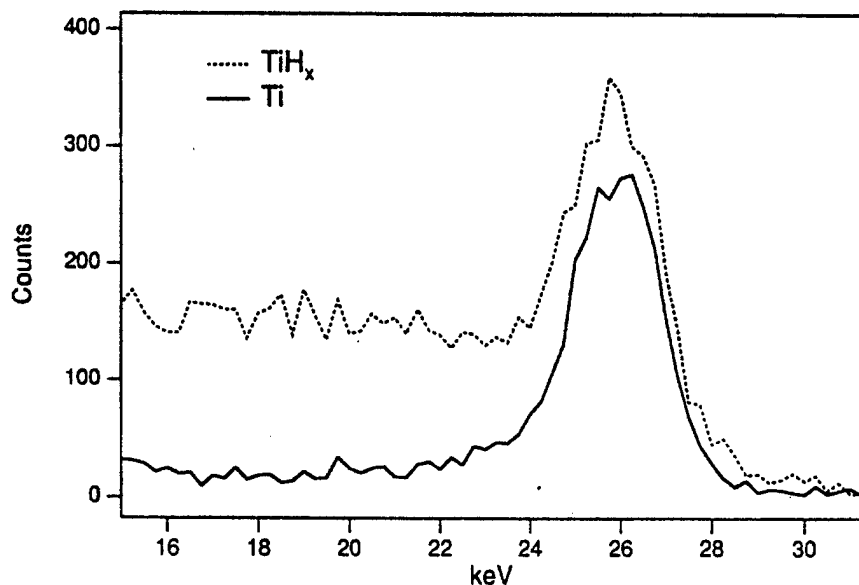


Fig. 3. Hydrogen recoil energy spectra for pure and hydrated titanium, for a deposited charge of  $1.25 \times 10^{12}$  ions.

path,  $x$  is the foil thickness, and  $dE/dx$  is the stopping power of the atom at an energy  $E$  in carbon. The electron flight time is contained in  $t_0$ . In general, the difference in flight times between recoil hydrogen and the scattered beam will increase with increasing probe

mass, while the time difference between hydrogen and other recoils from the host material will decrease. This must be considered when trying to maximize the analyzable depth for hydrogen in a material. For our system, a Ne probe beam seems to be the best compro-

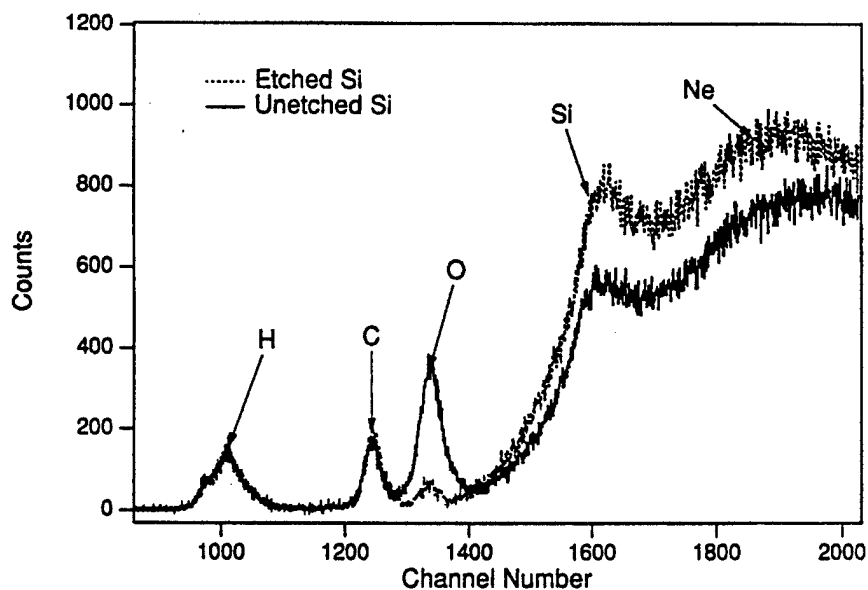


Fig. 4. TOF spectra for 270 keV  $\text{Ar}^+$  on etched and unetched silicon; total charge of  $1.25 \times 10^{12}$  ions.

mise for the sensitive profiling of near surface hydrogen in materials.

Fig. 2a shows a time-of-flight spectrum for 270 keV Ne<sup>+</sup> on Kapton. The deposited charge was increased for this analysis to increase the visibility of the oxygen feature and improve the signal to background. Recoil carbon, oxygen and scattered neon are observed in addition to a substantial hydrogen feature. The hydrogen region is transformed from time into energy and displayed in fig. 2b. The atomic concentration of hydrogen near the surface may be calculated using relations derived from ref. [11]:

$$C_H = N_H \frac{\epsilon(E_0) \cos \theta_1}{\Delta E} \times 100\%, \quad (2)$$

where

$$N_H = \frac{Y}{\sigma_r Q \Omega \eta} \quad (3)$$

gives the concentration in atoms/cm<sup>2</sup>.  $Y$  is the yield over the energy range  $\Delta E$ .  $\sigma_r$  is the recoil cross section,  $Q$  is the number of incident ions,  $\Omega$  is the solid angle,  $\eta$  is the detector efficiency, and

$$\epsilon(E_0) = \frac{1}{\cos \theta_1} K' S(E_0)_{Ne} + \frac{1}{\cos \theta_2} S(K'E_0)_H, \quad (4)$$

with  $K'$  the recoil kinematic factor and  $S(E)$  the stopping cross section in eV/10<sup>15</sup> atoms/cm<sup>2</sup>. With  $\theta_1 = \theta_2$ , the angular dependence in eqs. (2) and (4) cancels. We estimate the hydrogen atomic concentration to be  $31 \pm 5\%$ , in reasonable agreement with a prediction of 26% based on stoichiometry. The analyzable depth for Kapton using neon is approximately 100 nm.

The recoil hydrogen energy spectra for pure and hydrated titanium are overlaid in fig 3. Both samples show a hydrogen enrichment at the surface probably due to hydrocarbon adsorption. The measured hydrogen coverage for the pure sample was  $6 \times 10^{15}$  cm<sup>-2</sup> at the surface. Our measurements yield a result of  $18 \pm 4\%$  for the bulk atomic hydrogen concentration in hydrated titanium. The estimate is complicated by the fact that the hydrogen concentration enters into the computation of the stopping cross section in eq. (4). Moreover, depletion of hydrogen near the surface of the hydrated sample was observed after only  $6.25 \times 10^{12}$  ions were deposited. However, this is still roughly 5 times the charge deposited during a typical analysis.

As noted in table 1, a 270 keV argon beam is capable of simultaneously resolving hydrogen, carbon, and oxygen surface contaminants on silicon. Fig. 4 shows the time of flight spectra for etched and unetched silicon using such a probe. As expected, reduction in the native oxide caused by the etch is very

apparent while little variation was observed in the hydrogen and carbon features attributable to organic contaminants which are not affected by the treatment. Based on our experience in helium backscattering from silicon, the scattering yield from the substrate is strongly influenced by channeling and blocking. We therefore attribute the variation in size of the recoil Si and scattered Ar features to the random orientation of the samples. The thickness of the native oxide layer was determined to be 15 Å, based upon an estimate of the detector efficiency for oxygen of roughly 25% and a density of 2.5 g/cm<sup>3</sup> of SiO<sub>2</sub>. After etching, only  $\sim 1 \times 10^{15}$  cm<sup>-2</sup> of oxygen were found to remain. A third silicon sample, etched in HF but not rinsed, had a detectable fluorine residue estimated to be  $\sim 1 \times 10^{14}$  cm<sup>-2</sup>.

The fluorine coverage of the etched Si sample probably approaches the limit of sensitivity to heavier contaminants currently possible with our apparatus. Because of the recoil cross section and detector response, we estimate the minimum detectable level of hydrogen to be lower. Let us define a minimally detectable feature as one whose integrated yield is three times the standard error. Then the analysis of the sample of pure titanium, with an integrated region of 80 channels for hydrogen and a background of 6 counts/channel nearby, would establish a minimum detectable coverage of  $3 \times 10^{13}$  H atoms/cm<sup>2</sup> near the surface. The lowest limit for hydrogen surface sensitivity we have found reported in the literature for conventional ERD is  $1 \times 10^{12}$  H atoms/cm<sup>2</sup> [12]. The result was based on the detection of a single recoil H atom. Using our sensitivity criteria this limit would be increased by at least an order of magnitude, and is comparable with our reported value.

#### 4. Conclusion

We have demonstrated the feasibility of elastic recoil detection of light elements in materials using 270 keV ions of several species in conjunction with time-of-flight spectroscopy. The quantum efficiency for hydrogen detection of the present detector configuration is approximately 30% and is relatively independent of energy in the range studied. Using this efficiency, it has been possible to obtain reasonable agreement between the measured and theoretical concentration of hydrogen in Kapton. Extrapolating from the measurement of hydrogen in titanium, we estimate that the minimum detectable areal density of surface hydrogen is about  $3 \times 10^{13}$  cm<sup>-2</sup> with the current experimental geometry. Experiments currently under way are designed to study the depth resolution of the technique including the degree to which surface and bulk hydrogen can be resolved.

### Acknowledgements

This work was supported in part by the U.S. Army Research Office and by a grant from Texas Instruments, Inc.

### References

- [1] D.B. Fenner, D.K. Biegelsen and R.D. Bringans, *J. Appl. Phys.* 66 (1989) 419.
- [2] R.J. Brewer, J.K. Gimzewski and S. Veprek, *J. Nucl. Mater.* 103 (1982) 465.
- [3] W.A. Lanford, H.P. Trautvetter, J.F. Ziegler and J. Keller, *Appl. Phys. Lett.* 28 (1976) 566.
- [4] B.L. Doyle and P.S. Peercy, *Appl. Phys. Lett.* 34 (1979) 811.
- [5] J.P. Thomas, M. Fallavier and A. Ziani, *Nucl. Instr. and Meth.* B15 (1986) 443.
- [6] M.H. Mendenhall and R.A. Weller, *Nucl. Instr. and Meth.* B47 (1990) 193.
- [7] M.H. Mendenhall and R.A. Weller, *Nucl. Instr. and Meth.* B40/41 (1989) 1239.
- [8] S.C. Gujrathi and S. Bultena, *Nucl. Instr. and Meth.* B64 (1992) 789.
- [9] J.P. Biersack and L.G. Haggmark, *Nucl. Instr. and Meth.* 174 (1980) 257.
- [10] N. Matsunami et al., *Atom Data Nucl. Data Tables* 31 (1984) 1.
- [11] W.K. Chu, J.W. Mayer and M.A. Nicloet, *Backscattering Spectrometry* (Academic Press, New York, 1978) chaps. 3 and 4.
- [12] H. Nagai, S. Hayashi, M. Aratani, T. Nozaki, M. Yanokura, I. Kohno, O. Kuboi and Y. Yatsurugi, *Nucl. Instr. and Meth.* B28 (1987) 59.

# High-resolution medium-energy backscattering spectrometry

Marcus H. Mendenhall and Robert A. Weller

*Vanderbilt University, Nashville, Tennessee 37235, USA*

We describe a new form of backscattering spectrometry using medium-energy ions and time-of-flight detection that is particularly useful in characterizing surfaces and thin films. The technique uses incident ions with energies from a few tens of keV up to about 500 keV. It combines the advantages of conventional Rutherford backscattering, including insensitivity to the scattered ion's charge, with increased surface sensitivity, increased depth resolution and reduced target damage. Several ions have been used successfully for analyses, with  $\text{He}^+$  and  $\text{Li}^+$  at 270 keV and  $\text{C}^{2+}$  at 500 keV being particularly useful because of the range of cross sections and the resolution for depth profiling that they offer. Measurements of heavy constituents on low-mass substrates have been demonstrated at the  $2 \times 10^{12}/\text{cm}^2$  level and depth resolutions of less than 4 nm are routinely achievable. In this article we review the current status of the technique with particular emphasis on its use in applications which are complementary to conventional MeV Rutherford backscattering.

## 1. Introduction

For nearly two decades Rutherford backscattering spectrometry (RBS) has been the most versatile tool for the analysis of thin films [1]. Unlike alternative techniques, it is quantitative because the fundamental interaction cross section is well known, and it may be used to measure the concentration of various components of a sample as a function of depth without overtly destroying the sample. These strengths have made Rutherford backscattering the analytical tool of choice for the study of semiconductor device structures and for a variety of surface related physical processes. Nevertheless, the fundamental technology for performing backscattering has changed little since the technique came into widespread use.

The key step in backscattering spectrometry is the energy analysis of the backscattered particles. Although some early experiments explored other technologies, the silicon surface barrier detector quite quickly became established as the transducer of choice for this measurement. Surface barrier detectors are inexpensive, rugged, insensitive to the charge state of the particle, approximately linear in energy, and have unit quantum efficiency for ions such as  $\text{He}^+$ . This formidable combination of assets is encumbered by only a few minor liabilities, the most significant of which is the energy resolution which can be obtained. For He ions, the resolution of a surface barrier detector is typically in the range of 12–20 keV. This resolution, along with the requirement that spectral features of interest be resolved, establishes a practical lower limit of about 1 MeV for the incident ion beam energy. Thus, an accel-

erator of significant size has been required to implement backscattering spectrometry.

In two previous publications we have described a new time-of-flight detection scheme which makes it practical to do backscattering analyses with ion beams having energies in the range 100–500 keV [2,3]. We call the new technique medium-energy backscattering spectrometry (MEBS). The time-of-flight detector shares many of the advantages of surface barrier detectors but has significantly improved resolution. This article describes recent improvements to the detector and to our accelerator which have resulted in significant improvements in resolution and sensitivity. As a demonstration of system performance, we present the results of three measurements, trace element analysis on an aluminum surface, the thickness of the  $\text{SiO}_2$  layer at the surface of a  $\text{TiSi}_2$  film, and the selective depletion of fluorine from an ion beam irradiated  $\text{CaF}_2$  thin film.

## 2. Experimental procedure

The time-of-flight detector used in these experiments is shown schematically in fig. 1. It was used in place of a surface barrier detector in an otherwise conventional backscattering configuration. The energy of the ion beam was typically 270 keV and the scattering angle  $150^\circ$ . The effective solid angle for detection is about  $10^{-4}$  sr. All measurements were performed in a bakeable ultrahigh vacuum chamber. The relative quantum efficiency of the detector as a function of energy has been measured by analyzing a thin Au film on Si for various beam energies in the range 50–270 keV. The



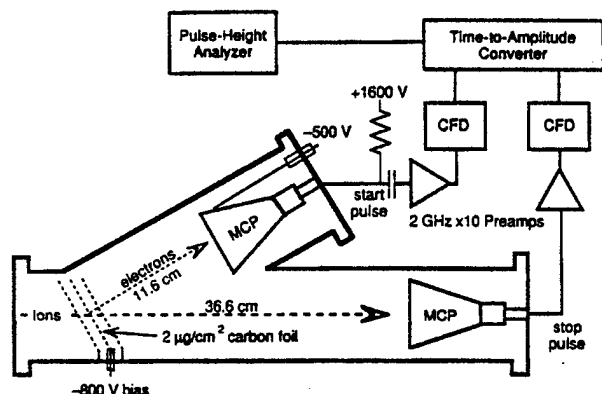


Fig. 1. Schematic of the time-of-flight spectrometer showing approximate flight distances, biases, and external electronics.

time-of-flight spectra presented here have been rebinned into energy spectra with random coincidence background subtracted before rebinning.

The two principal limitations to the energy resolution of the time-of-flight detector were identified in ref. [2] as the stability of the primary ion beam energy and an effect arising from charge exchange in the carbon foil shown in fig. 1. Notice that a particle which gains or loses electrons in passing through the start foil will gain or lose energy in increments of the foil bias. Acting as a miniature tandem accelerator, this foil dispersed isolated peaks in backscattering spectra into at least three components with a total separation of twice the foil bias. This phenomenon limited the effective energy resolution of the detector to about 6 keV because a 3 keV bias on the start foil was required. In the present configuration, the microchannel plate detector has been biased with its cathode at -500 V and its anode at +1600 V so that the start foil bias may be reduced to -800 V. This has reduced the contribution of peak splitting to total peak width to about 1600 eV. This resolution, while not as good as that of the best electrostatic analyzer (typical observed resolution about 1 keV as shown, e.g., in fig. 9 of ref. [4]) is such that, for heavy ions, we believe the inelasticity in the collision process, which has been estimated at 2% of the kinetic energy [5], dominates the observed width at most energies. Also, the time-of-flight system's somewhat lower resolution is offset by an enormously increased throughput, since it does not require tuning to each energy to be detected.

The other limitation to system performance was the instability of the accelerating voltage. This has been eliminated by installing a new 300 kV high-voltage supply on the accelerator. The new supply has < 10 V of ripple at full power. As a result of these modifications, the effective energy resolution for backscattering analysis has been reduced to as low as 1800 eV for  $\text{Li}^+$  at 270 keV as determined by the edge width of thick Be

target yield curves. The typical width of isolated peaks is 3–5 keV using this beam.

### 3. Results and discussion

Fig. 2 shows a 270 keV  $\text{Li}^+$  backscattering spectrum of an aluminum foil with several trace constituents on its surface. The inset shows the region of the spectrum from 100 to 250 keV expanded vertically. The improvement in resolution when compared with previous spectra [2] is substantial. The width of the aluminum thick target edge is 3.2 keV which is comparable to the width (2.5 keV) of the surface oxygen peak. The widths of the heavy element peaks shown in the inset are typically 5 keV. Overall, the mass resolution demonstrated in fig. 2 is comparable to that which can be obtained with conventional MeV  $\text{He}^+$  backscattering. As an example, note that the energy separation of Br and Ag peaks in a 2 MeV  $\text{He}^+$  backscattering spectrum is 82 keV or about 4–5 times the FWHM of an isolated peak. This compares with a separation of 3–4 FWHM for the data in fig. 2. The areal density of gold derived from the data shown is  $3 \times 10^{13} \text{ cm}^{-2}$ .

The most dramatic effect of the enhanced energy resolution which is obtained by time-of-flight detection is an improvement in the depth resolution of backscattering spectra. The stopping power of ions in the 200–300 keV range is not significantly different from that of 1–3 MeV ions. Thus, an improvement in the detector's energy resolution translates directly into an improvement in depth resolution. In order to demonstrate this, we have revisited a well studied problem which is relevant to semiconductors.

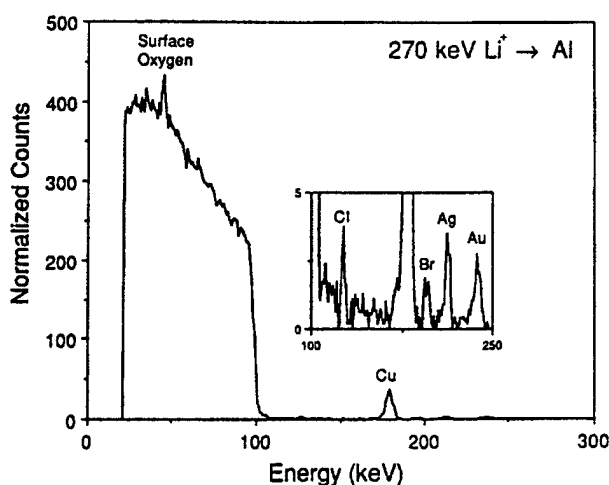


Fig. 2. 270 keV  $\text{Li}^+$  backscattering spectrum showing trace elements on an aluminum surface. The total beam charge was approximately 60  $\mu\text{C}$ . The original time-of-flight data have been rebinned into an energy spectrum.

It has been known for many years that, when certain silicides oxidize, the net effect is that an  $\text{SiO}_2$  layer appears at the surface above the silicide [6]. The presence of this insulating layer over what is nominally a conductor has important implications for semiconductor devices. Previously, in order to investigate this layer and to measure its thickness and uniformity, it has been necessary to use a combination of Auger electron spectroscopy and sputtering to produce depth profiles. In ref. [6], the authors note that, even under the most favorable conditions of analysis, the presence of the  $\text{SiO}_2$  is not directly observable by backscattering. Results of Auger depth profiling revealed that the  $\text{SiO}_2$  layer on a PtSi film was  $< 5$  nm thick. In a more recent study of the formation of a  $\text{TiSi}_2$  film, a similar Auger depth profile has also been measured [7]. These authors did not estimate the  $\text{SiO}_2$  layer thickness. However, an examination of their data suggests that it is less than 10 nm.

In fig. 3 we show two superposed MEBS spectra of a titanium metal foil and of a titanium silicide film about 80 nm thick. Both spectra were obtained by 270 keV  $\text{Li}^+$  scattering at  $150^\circ$ . Notice the substantial shift in the position of the edge of the titanium peak, the slight discontinuity in slope of the Si edge and the oxygen peak which sits on a large background of Si counts. Both the high-energy Si edge and the oxygen peak are at precisely the energies expected for scattering at the surface of the material. The Ti, on the other hand, is shifted to lower energy by approximately 2 keV. The conclusion from these observations is that silicon and oxygen are present at the target surface but that titanium is not. Furthermore, since titanium is completely absent from the surface, the  $\text{SiO}_2$  film can be assumed to be unbroken and approximately uniform in thickness. Using a value of  $150 \text{ eV}/10^{15} \text{ molecules/cm}^2$  for the

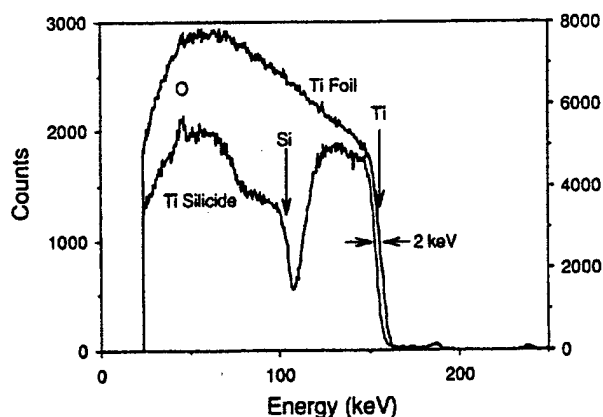


Fig. 3. 270 keV  $\text{Li}^+$  backscattering spectra showing a  $\text{TiSi}_2$  thin film and a Ti metal foil. The displacement of the Ti edges is a result of approximately 3.5 nm of  $\text{SiO}_2$  covering the silicide. These analyses were each performed with  $30 \mu\text{C}$  of  $\text{Li}^+$ .

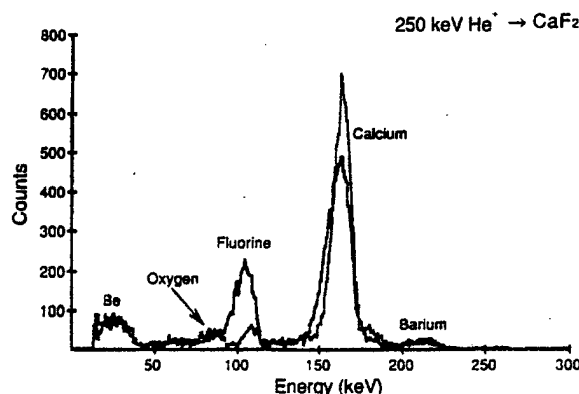


Fig. 4. 250 keV  $\text{He}^+$  backscattering spectrum showing a 17 nm  $\text{CaF}_2$  film before (black line) and after (grey line) irradiation with  $2 \times 10^{17} \text{ He}^+$  ions/ $\text{cm}^2$ . Note the preferential loss of F.

stopping power of the 270 keV  $\text{Li}^+$  in  $\text{SiO}_2$  and  $2.2 \text{ g/cm}^3$  for the density, we conclude that the thickness of the  $\text{SiO}_2$  layer is about 3.5 nm. It should be emphasized that by fitting the Ti edge with an appropriate function it is possible to detect with confidence shifts in its position of as little as 500 eV. This corresponds to a thickness of  $\text{SiO}_2$  of less than 1 nm.

Another application for which the improved depth resolution of MEBS has been valuable is the study of radiation effects in thin films.  $\text{CaF}_2$  has attracted significant interest recently because it may be grown epitaxially on Si and, therefore, is a candidate as an insulator in numerous semiconductor applications [8]. Fig. 4 from ref. [9] shows the result of an experiment testing the effects of energetic  $\text{He}^+$  irradiation on room temperature  $\text{CaF}_2$  thin films.  $\text{CaF}_2$  films about 17 nm thick were subjected to 270 keV  $\text{He}^+$  irradiation for fluences up to  $2 \times 10^{17} \text{ He}^+/\text{cm}^2$  and were periodically analyzed by MEBS using the same beam. The spectra shown in fig. 4 were taken before and after irradiation. The remarkable conclusion is that F atoms were systematically depleted without loss of Ca. The rate of F

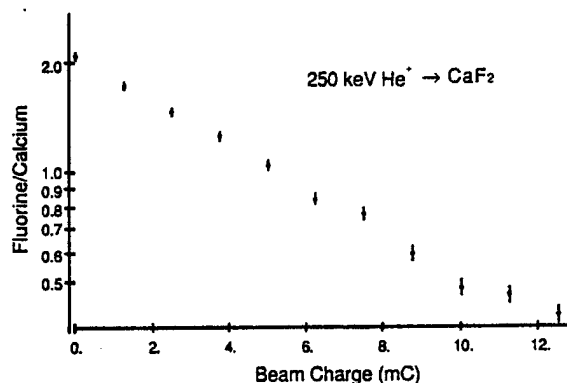


Fig. 5. Evolution of the fluorine to calcium ratio in the thin film of fig. 4 as a function of total beam charge.

loss is shown in fig. 5 which displays the mean fluorine-to-calcium ratio in the foil as a function of total deposited charge. The preferential depletion of fluorine proceeds to near completion implying significant mobility of fluorine in the material. The initial rate of loss of fluorine was about 0.7 F atoms/He<sup>+</sup>. Notice, finally, the calcium peak in the spectrum of fig. 4. The removal of fluorine from the lattice has resulted in a surprising increase in the height of this peak; however, the peak is also noticeably narrower. As a result, the total number of counts remains unchanged. This reduction in peak width, which is approximately 2.5 keV, is further evidence of the unique depth resolution that medium-energy backscattering provides.

#### 4. Conclusion

High-resolution medium-energy backscattering spectrometry is a powerful complement to conventional MeV Rutherford backscattering and is especially useful for the study of processes in the first few tens of nanometers of a material. Using 270 keV Li<sup>+</sup> ions, MEBS is competitive with conventional  $\alpha$  backscattering both in sensitivity and mass resolution. It offers a depth resolution of less than 1 nm and does not require a large particle accelerator. Current work suggests that an additional factor of 2 in effective energy resolution may be achieved using the detector configuration of fig. 1. An additional factor of 5 enhancement in sensitivity is also expected by improving known shortcomings. These improvements will even further increase the number of problems which may be attacked by backscattering techniques.

#### Acknowledgements

Portions of this work were performed under contract number DE-AC05-84OR21400, subcontract number 19X-SF583V, with the Optics MODIL at Oak Ridge National Laboratory, Martin Marietta Energy Systems. We wish especially to thank Charles M. Egert of the Optics MODIL for his interest and J.M. Anthony, Texas Instruments, Inc. for providing the titanium silicide sample. Additional support was provided by the National Aeronautics and Space Administration under contract NAG8-156.

#### References

- [1] W.-K. Chu, J.W. Mayer and M.-A. Nicolet, *Backscattering Spectrometry* (Academic Press, New York, 1979).
- [2] M.H. Mendenhall and R.A. Weller, *Nucl. Instr. and Meth.* B40/41 (1989) 1239.
- [3] M.H. Mendenhall and R.A. Weller, *Nucl. Instr. and Meth.* B47 (1990) 193.
- [4] W.C. Turkenburg, W. Soszka, F.W. Saris, H.H. Kersten and B.G. Colenbrander, *Nucl. Instr. and Meth.* 132 (1976) 587.
- [5] H.H. Andersen, F. Besenbacher, P. Loftager and W. Moller, *Phys. Rev.* A21 (1980) 1891.
- [6] R.J. Blattner, C.A. Evans Jr., S.S. Lau, J.W. Mayer and B.M. Ullrich, *J. Electrochem. Soc.* 122 (1975) 1733.
- [7] R. Pantel, D. Nicolas and J.P. Ponpon, *J. Appl. Phys.* 62 (1987) 4319.
- [8] L.J. Schowalter and R.W. Fathauer, *CRC Crit. Rev. Solid State and Mater. Sci.* 15 (1989) 367.
- [9] M.H. Mendenhall and R.A. Weller, *Nucl. Instr. and Meth.* B51 (1990) 400.

## Algorithms for the rapid computation of classical cross sections for screened Coulomb collisions

Marcus H. Mendenhall and Robert A. Weller  
*Vanderbilt University Nashville, TN 37235, USA*

Received 27 August 1990 and in revised form 3 December 1990

The development of medium energy backscattering with ions whose energies are as low as 50 keV and whose masses range up to that of  $^{12}\text{C}^+$  has generated the need for accurate and efficient mathematical methods for the computation of classical cross sections for screened Coulomb collisions. This paper presents a procedure for the computation which preserves most of the accuracy of more elaborate numerical solutions and is fast enough for all but the most time consuming Monte Carlo calculations. Comparisons are made between this approach and previous computations and approximations, and between the computed scattering cross sections for several screening functions.

### 1. Introduction

It is often necessary in the routine practice of particle–solid interaction physics to compute the classical scattering integral or the cross section for scattering by a screened Coulomb potential. The two most conspicuous examples are the reduction of backscattering spectra [1] and the use of Monte Carlo simulation programs such as TRIM [2]. In backscattering spectrometry, the effects of screening, are frequently ignored. However, for precise measurements, this is not possible [3]. In order to correct for screening the authors of [3] and other groups [4,5] have chosen to obtain approximate expressions for the cross section, or more precisely for the correction to the Rutherford cross section, as a function of energy. These formulae have the distinct virtues of being easily computable and quite accurate for weakly screened collisions, but they are inappropriate, in general, for strongly screened collisions.

In the past, strongly screened collisions have been most commonly encountered in the theories of the stopping power and simulations of the range of ions in matter. However, it has been recently demonstrated that, by the use of time-of-flight detection, high quality backscattering spectra may be obtained using ions with energies from a few tens to a few hundreds of keV where screening may be significant [6]. For the proper interpretation of these spectra, the relevant cross sections must be computed. Although the basic principles of these computations are well known, there is little guidance in the literature on computing them effi-

ciently. As a result, a number of approximations have been suggested [7–9].

In this paper we revisit the problem of computing the classical scattering integral given an arbitrary screening function. The surprising conclusion which we have reached is that it is possible to obtain a solution which is independent of the precise form of the screening function, which may be computed almost as efficiently as the common approximations, and which is often substantially more accurate.

### 2. The scattering integral

The essential elements of the problem which we consider are summarized in most textbooks on mechanics [10] and have been described by many previous authors [11–13]. They are repeated here in order to establish the notation which we shall use. The interaction potential is assumed to take the form:

$$V(r) = \frac{Z_1 Z_2 e^2}{r} \phi\left(\frac{r}{a}\right). \quad (1)$$

Here  $Z_1$  and  $Z_2$  are the charges of the incident and target ions,  $r$  is their separation,  $e$  is the electron's charge, and  $\phi$  is the screening function. The parameter  $a$  is the screening length. Except as noted, we will work in the center of mass system where the energy of the projectile will be  $E_c$ , the classical impact parameter will be  $b$ , and the scattering angle will be  $\theta_c$ . Following the conventional approach we will use dimensionless energy

and length variables  $\epsilon$  and  $x$  defined so that  $r = ax$  and:

$$\epsilon = \frac{E_c}{Z_1 Z_2 e^2 / a}. \quad (2)$$

The dimensionless variable corresponding to  $b$  will be  $\beta = b/a$ . With the further definition of the function  $f(x)$ :

$$f(x) = \left(1 - \frac{\phi(x)}{x\epsilon} - \left(\frac{\beta}{x}\right)^2\right)^{-1/2} \quad (3)$$

the scattering integral becomes:

$$\theta_c = \pi - 2\beta \int_{x_0}^{\infty} f(z) dz/z^2 \quad (4)$$

where  $x_0 = r_0/a$  and  $r_0$  is the distance of closest approach.  $x_0$  is given by the solution of the transcendental equation:

$$\begin{aligned} [f(x_0)]^{-1} &= 0 \quad \text{or equivalently} \\ x_0 - \frac{\phi(x_0)}{\epsilon} - \frac{\beta^2}{x_0} &= 0. \end{aligned} \quad (5)$$

With these definitions, the (dimensionless) differential cross section is given by:

$$\left(\frac{d\sigma}{d\Omega}\right)_c = \frac{\beta}{\sin(\theta_c)} \left|\frac{d\theta_c}{d\beta}\right|^{-1}. \quad (6)$$

Of course, there is no general analytical expression for the integral (4). The computation is complicated because the integral is improper (since the integrand is singular at  $x_0$  and the upper limit is infinite) and because one does not ordinarily know either the impact parameter  $\beta$  or the distance of closest approach  $x_0$  but rather must compute them for the observed scattering angle. The standard mathematical maneuver for dealing with both an integrable singularity and an improper limit is to change variables. Both irregularities can be handled simultaneously by properly choosing a new variable to replace  $x$ . Robinson has suggested  $z$  defined by  $x = x_0/(1 - z^2)$  [12]. A similar expression was also used by Latta and Scanlon [13]. The choice of the new variable is important for an efficient quadrature. It also affects the region in  $\epsilon$  and  $\beta$  space where one obtains the least variation with  $z$  of the resulting integrand. We have chosen to let

$$x = \frac{x_0}{\cos(\pi z/2)}. \quad (7)$$

This produces an integrand which is always unity at  $z = 1$  and which is nearly independent of  $z$  for  $\epsilon$  near 1. The resulting form for the scattering integral is:

$$\theta_c = \pi \left(1 - \frac{\beta \alpha(\epsilon, \beta)}{x_0}\right). \quad (8)$$

Here the function  $\alpha(\epsilon, \beta)$  is given by:

$$\alpha(\epsilon, \beta) = \int_0^1 \sin(\pi z/2) f\left(\frac{x_0}{\cos(\pi z/2)}\right) dz. \quad (9)$$

The computation of the scattering integral may be seen from (8) to be a matter of computing  $\alpha$ . In turn, for computing the cross section one needs  $d\alpha/d\beta$  since:

$$\left|\frac{d\theta_c}{d\beta}\right| = \pi \left[ \left( \frac{x_0 - \beta dx_0/d\beta}{x_0^2} \right) \alpha + \left( \frac{\beta}{x_0} \right) \frac{d\alpha}{d\beta} \right]. \quad (10)$$

The expression for  $d\alpha/d\beta$  may be obtained by differentiating (9). Special care must be exercised since the expression depends on  $\beta$  both explicitly through the function  $f$  and implicitly through the dependence of  $x_0$  on  $\beta$ . The result is:

$$\frac{d\alpha}{d\beta} = \int_0^1 \sin(\pi z/2) \frac{df(x(z))}{d\beta} dz, \quad (11)$$

where the derivative of  $f$  is given by:

$$\begin{aligned} \frac{df(x)}{d\beta} &= x^{-2} \left(1 - \frac{\phi(x)}{x\epsilon} - \frac{\beta^2}{x^2}\right)^{-3/2} \left\{ \beta + \left(\frac{dx}{d\beta}\right) \right. \\ &\quad \times \left[ \left( \frac{x\phi'(x) - \phi(x)}{2\epsilon} \right) - \frac{\beta^2}{x} \right] \left. \right\} \end{aligned} \quad (12)$$

with  $x$  is given in terms of  $z$  by (7) and

$$\frac{dx(z)}{d\beta} = \left( \frac{1}{\cos(\pi z/2)} \right) \frac{dx_0}{d\beta}. \quad (13)$$

The derivative of  $x_0$  follows from eq. (5) and has the explicit form:

$$\frac{dx_0}{d\beta} = \frac{2\beta}{x_0} \left(1 - \frac{\phi'(x_0)}{\epsilon} + \frac{\beta^2}{x_0^2}\right)^{-1}. \quad (14)$$

Taken together the above equations constitute a complete prescription for the computation of the scattering angle and cross section given the screening function, the reduced energy, and the impact parameter. The key steps in the computation are the solution of (5) for  $x_0$ , the computation of  $\alpha(\epsilon, \beta)$ , and the inversion of eq. (8) to obtain  $\beta$  as a function of  $\epsilon$  and the center of mass scattering angle  $\theta_c$ .

### 3. Computation of $x_0$ , $\alpha$ , and $\beta$

The dimensionless distance of closest approach  $x_0$  is the solution of eq. (5). Since, it is usually not possible to obtain an analytic expression for  $x_0$  in terms of  $\epsilon$  and  $\beta$ , a numerical solution is indicated. Robinson [12] and most subsequent authors have solved for  $x_0$  using Newton's method. This technique, which requires a single initial guess, exhibits quadratic convergence, so that the number of significant digits doubles with each iteration [14]. However, it also requires that both the screening

function and its derivative be evaluated at each stage of the iteration. The secant method, which requires two initial starting values instead of one [15], converges more slowly (as  $\delta^{1.6}$ ) but only requires one evaluation of the screening function at each stage. We have compared three techniques for the solution of this problem, one using Newton's method, one using the secant method and one using a combination of the two. We have found that, for a given convergence criterion, using one Newton's method step to refine the initial guess followed by secant method iterations is about 10% faster on average than using Newton's method exclusively. Clearly, however, both techniques depend for rapid convergence upon the quality of the initial guess (or guesses) for  $x_0$ .

In the FORTRAN implementation of the TRIM algorithm presented in ref. [16], the authors used an empirical method for obtaining the initial guess for  $x_0$  which is often very accurate for soft collisions, but not very good for the high-angle collisions encountered in ion backscattering. We have chosen a different approach. If  $\epsilon$  is large, then a good first guess of  $x_0$  is the exact value for unscreened collisions which is given by the solution of (5) with  $\phi(x) = 1$ , or:

$$x_0 = \frac{1}{2\epsilon} + \left[ \left( \frac{1}{2\epsilon} \right)^2 + \beta^2 \right]^{1/2}. \quad (15)$$

An expression to use for small  $\epsilon$  (say  $\epsilon < 5$ ) may be obtained by observing that, if  $\phi(x) = kx^{-3}$ , where  $k$  is a constant, then eq. (5) can be solved with the result:

$$x_0^2 = \frac{\beta^2}{2} + \left( \frac{\beta^4}{4} + \frac{k}{\epsilon} \right)^{1/2}. \quad (16)$$

Notice that if  $\beta = 0$ , the distance of closest approach is  $(k/\epsilon)^{1/4}$ . Defining  $\rho$  to be the distance of closest approach for head on collisions, one can write:

$$x_0^2 = \frac{\beta^2}{2} + \left( \frac{\beta^4}{4} + \rho^4 \right)^{1/2}. \quad (17)$$

Now clearly  $\rho$  is only a function of  $\epsilon$ , so eq. (17) may be viewed as a method of extrapolating from  $\rho$  for a head-on collision to an estimate of the corresponding value for a collision with reduced impact parameter  $\beta$ . We have obtained an empirical expression for  $\rho(\epsilon)$  using the Universal potential [7]. However, this expression is adequate for making the initial guess of  $x_0$  for all the potentials that we have examined. This is given by the following expression where  $y = \ln(\epsilon)$ :

$$\ln(\rho^4) = -(3.517 \times 10^{-4}y^4 + 1.401 \times 10^{-2}y^3 + 2.393 \times 10^{-1}y^2 + 2.734y + 2.220). \quad (18)$$

Although originally constructed for the range  $10^{-6} < \epsilon < 1$ , this expression is acceptable for  $\epsilon$  values up to 5. For  $\epsilon < 5$ , the algorithm for the computation of  $x_0$  as a function of  $\epsilon$  and  $\beta$  consists of computing  $\rho$  using eq. (18), obtaining an initial guess for  $x_0$  by eq. (17),

refining this estimate by one Newton's method iteration, and continuing to iterate using the secant method until the desired precision is reached. For  $\epsilon > 5$ , eq. (15) is used to obtain an initial estimate for  $x_0$  directly. Alternatively, one can use Newton's method exclusively with little loss of speed. It is significant for the work below that this procedure is especially fast for  $\beta \ll 1$ .

Most previous computations of the cross section or the scattering integral have involved Gaussian quadratures of rather high order. For example, Robinson's tables [12] are constructed using 96 point Gauss-Mehler and 100 point Gauss-Legendre quadratures. Such precision is certainly an appropriate precaution when preparing tables for reference, but it is hardly convenient for routine computation. As Robinson's work shows, however, lower order quadratures are often very accurate. For the computation of  $\alpha$ , we have chosen to use the Lobatto quadrature [17]. This is a variation of Gaussian quadrature in which the integrand is sampled at the two end point as well as at points within the range of integration. This procedure is well suited to the present problem since the integrand of eq. (9) is always 1 at  $z = 1$ . It is straight forward to compute the limiting value at  $z = 0$  also. The resulting expression, which is defined to be  $\lambda_0$ , is:

$$\begin{aligned} \lambda_0 &\equiv \lim_{z \rightarrow 0} \sin(\pi z/2) f\left(\frac{x_0}{\cos(\pi z/2)}\right) \\ &= \left( \frac{1}{2} + \frac{\beta^2}{2x_0^2} - \frac{\phi'(x_0)}{2\epsilon} \right)^{-1/2}. \end{aligned} \quad (19)$$

For routine computations, adequate accuracy is obtained by using the fourth order Lobatto quadrature which requires this limit and only two additional evaluations of the function at intermediate points. Thus, we have:

$$\begin{aligned} \cos(\pi z_1/2) &= 0.9072248, & \sin(\pi z_1/2) &= 0.4206461, \\ \cos(\pi z_2/2) &= 0.4206461, & \sin(\pi z_2/2) &= 0.9072248. \end{aligned} \quad (20)$$

From which it follows that:

$$\begin{aligned} \alpha &= \frac{1}{12} \left\{ 1 + \lambda_0 + 5 \left[ 0.4206 f\left(\frac{x_0}{0.9072}\right) \right. \right. \\ &\quad \left. \left. + 0.9072 f\left(\frac{x_0}{0.4206}\right) \right] \right\}. \end{aligned} \quad (21)$$

This expression along with equations (19), (3) and (8) are the solution for  $\theta_c$  given  $\epsilon$  and  $\beta$ . A comparison of the results for the Molière screening function using this fourth order quadrature, a tenth order Lobatto quadrature and Robinson's tables is given below. We observe, with reference to eq. (8), that for small  $\theta_c$  a loss of precision results from the subtraction of two terms with values near 1. For applications such as the TRIM algorithm, where  $\theta_c$  is being obtained as a function of  $\epsilon$

and  $\beta$ , it is better to compute a quantity such as  $\sin(\theta_c/2)$  since:

$$\sin(\theta_c/2) = \cos(\pi\beta\alpha/2x_0). \quad (22)$$

The last numerical algorithm which is needed for computing the scattering integral is a procedure for inverting eq. (8) to give  $\beta$  as a function of  $\theta_c$  and  $\epsilon$ . Since (8) is also a transcendental equation, it is important to find good initial guesses for a root. An upper limit to  $\beta$  is always given by the unscreened value:

$$\beta_R = [2\epsilon \tan(\theta_c/2)]^{-1}. \quad (23)$$

However, for small  $\epsilon$  or large  $\beta$  this estimate is much too large. Another estimate is suggested by examining the numerical values of  $\alpha(\epsilon, \beta)$ . It is a remarkable fact that  $\alpha$  never differs from unity by more than about 30% for all physically reasonable pairs of  $\epsilon$  and  $\beta$ . Thus, a surprisingly good estimate of  $\beta$  may be made by setting  $\alpha = 1$  in eq. (8). One thus obtains:

$$\beta \approx \left( \frac{\pi - \theta_c}{\pi} \right) x_0 \equiv \gamma x_0, \quad (24)$$

which is the defining relation for  $\gamma$ . By substituting this value for  $\beta$  in eq. (5) one obtains a scaling law which says that a good estimate for  $\beta$  is  $\gamma$  times the distance of closest approach corresponding to energy  $(1 - \gamma^2)\epsilon$  and impact parameter 0. This is quite convenient numerically since the algorithm for  $x_0$  is particularly fast and accurate for head-on collisions. By extending this idea and using the extrema of  $\alpha$  values, it is possible to place limits on the value of  $\beta$ . Thus, we arrive at an algorithm for inverting eq. (8). Let  $x_\beta$  be the distance of closest approach corresponding to energy  $(1 - \gamma^2)\epsilon$  and impact  $\beta = 0$  and let  $\beta_0 = \gamma x_\beta$ . Then:

$$\begin{aligned} \epsilon \geq 1 & \quad 0.70\beta_0 < \beta < (2\epsilon \tan(\theta_c/2))^{-1}, \\ \epsilon < 1 & \quad 0.90\beta_0 < \beta < 1.4\beta_0. \end{aligned} \quad (25)$$

We bracket the root using the relations (25) and apply the secant method iteratively (using eq. (8)) until the desired convergence is obtained. Note that the numerical values used in (25) are, again, specifically for the Universal potential but are adequate for other potentials as well.

#### 4. Computation of the cross section

As indicated in eq. (6), the cross section is obtained by differentiating  $\theta_c$  with respect to  $\beta$ . Robinson [12] chose to do this numerically using a central difference method. Certainly, numerical differentiation is appropriate for this problem. However, in general, it is unstable. For most computations we prefer the integral procedure outlined in eqs. (10)–(14). For maximum accuracy and speed, one would normally choose an adaptive quadrature such as the one given in ref. [18]

rather than the fixed-point methods which have been used previously. Note, however, that since the integrand of eq. (9) is constant at the upper limit, the integrand of (11) vanishes there. Based upon examination of several specific instances of the integrand, we speculated that a relatively low order Lobatto quadrature might also be appropriate for this case and this speculation was confirmed by numerous comparisons between the two methods. There is, in fact, a danger in using an adaptive quadrature. Although the algorithm discussed in ref. [18] was deemed satisfactory in all cases, a much simpler adaptive quadrature [19] which is normally quite robust, found a nonexistent singularity near  $z = 0$  when computing cross sections. This artifact of round-off error served as a sobering reminder of the pitfalls which may be encountered in a "routine" computation using "standard numerical procedures". We have found that, when performing the integral (11) using expression (12), significant round-off may be experienced for small  $z$  values even when using double precision arithmetic. Greater overall accuracy will ordinarily be obtained by using fewer point and the following limiting expression which is needed for the Lobatto quadrature:

$$\lim_{z \rightarrow 0} \sin\left(\frac{\pi z}{2}\right) \frac{df}{d\beta} = \left( \frac{g^{-1/2}}{2} \right) \left( \frac{dx_0}{d\beta} \right) \left[ \left( \frac{\beta}{x_0^2} \right) \left( \frac{dx_0}{d\beta} \right) - \frac{1}{x_0} + \frac{\phi''(x_0)}{2g\epsilon} \right], \quad (26)$$

where:

$$g = \frac{1}{2} + \frac{\beta^2}{2x_0^2} - \frac{\phi'(x_0)}{2\epsilon}. \quad (27)$$

Because of the greater variation of the integrand in eq. (11), our standard routine for the cross section uses a sixth order Lobatto quadrature.

For computations on a hand-held calculator, a simpler approach to computing cross sections has been found to be quite accurate. This involves the use of inverse quadratic interpolation to obtain both  $\beta$  (for a given  $\theta_c$ ) and its derivative [20]. The parameter  $\alpha$  is computed using 4-point Lobatto integration as described above, but the integrand is evaluated explicitly at a point near  $z = 0$  to estimate its value at the origin, rather than being computed exactly from eq. (19) which requires the derivative of the potential. In this procedure, one simply examines successive values of  $\theta(\beta)$  until the actual value of  $\theta$  is bracketed and then inverse interpolates to obtain the value of  $\beta$  corresponding to this angle. The derivative is obtained as a by-product of the calculation. Since for most backscattering calculations  $\beta$  is not less than 70% of the value computed assuming a Rutherford collision [from eq. (23)], this procedure, starting with  $\beta = \beta_R$  and stepping downwards in 10% steps usually takes only 2 or 3 steps to bracket the correct value of  $\beta$ . With the bracketing

values and a central point, inverse quadratic interpolation simultaneously yields a very good value of both  $\beta$  and  $d\theta/d\beta$ . To save code space (at the expense of a little speed), the calculator version uses the Rutherford value for an initial guess for  $x_0$  rather than using eq. (18) and uses the built in root finder of the HP-28S calculator to refine this value. What this approach may lack in elegance, it more than makes up in simplicity and speed. The calculator implementation provides cross sections which agree with the more elaborate calculations to about 0.1%. The computation takes about 5–10 seconds for  $\epsilon > 0.01$  and  $\theta_c > 90^\circ$ . Thus, for most cases of practical interest, an extremely abbreviated algorithm, requiring only the screening function and no analytic derivatives, can provide accuracy which exceeds that of any available potential. Even on a larger computer, for collisions with  $\epsilon > 0.01$  and back angles, this implementation is a useful alternative to the full computation described above.

## 5. Numerical results

In order to test the accuracy of the above procedures we have duplicated Robinson's calculations [12] for the Molière screening function which is given by:

$$\phi_m(x) = 0.35 \exp(-0.3x) + 0.55 \exp(-1.2x) + 0.10 \exp(-6x). \quad (28)$$

The results of these computations are shown in fig. 1 and table 1. Table 1 contains a selection of representative values of  $x_0$ ,  $\theta_c$  and corresponding cross sections with the order of quadrature shown in the column headings. Note that, following Robinson's convention, we have tabulated  $4\pi$  times the differential cross section. In all cases, the distances of closest approach are equal to Robinson's tabulated values to the precisions shown in the table. The values of  $\theta_c$  and the cross sections obtained with tenth order quadratures agree with Robinson's values to a few parts in  $10^6$ . Fig. 1a is a contour map showing the error in the value of  $\theta_c$  which is incurred by using the fourth order Lobatto quadrature (eqs. (21), (19), (3), and (8)) in place of the more precise procedure. Fig. 1b shows a similar plot for the cross section. In the case of the scattering angle, Robinson's values are considered to be definitive. It is difficult to judge the precision of the cross section values since Robinson did not give details of his numerical differentiation. However, the point is irrelevant since all values agree to a precision which exceeds the quality of the screening function and of the description of the collision in those terms.

One of the most extensive discussions of the screening correction to the Rutherford cross section is that which given in ref. [4] by Andersen and coworkers. They show experimental data which establish the validity of the screening correction which they propose. While this correction, following the spirit of ref. [3], is a

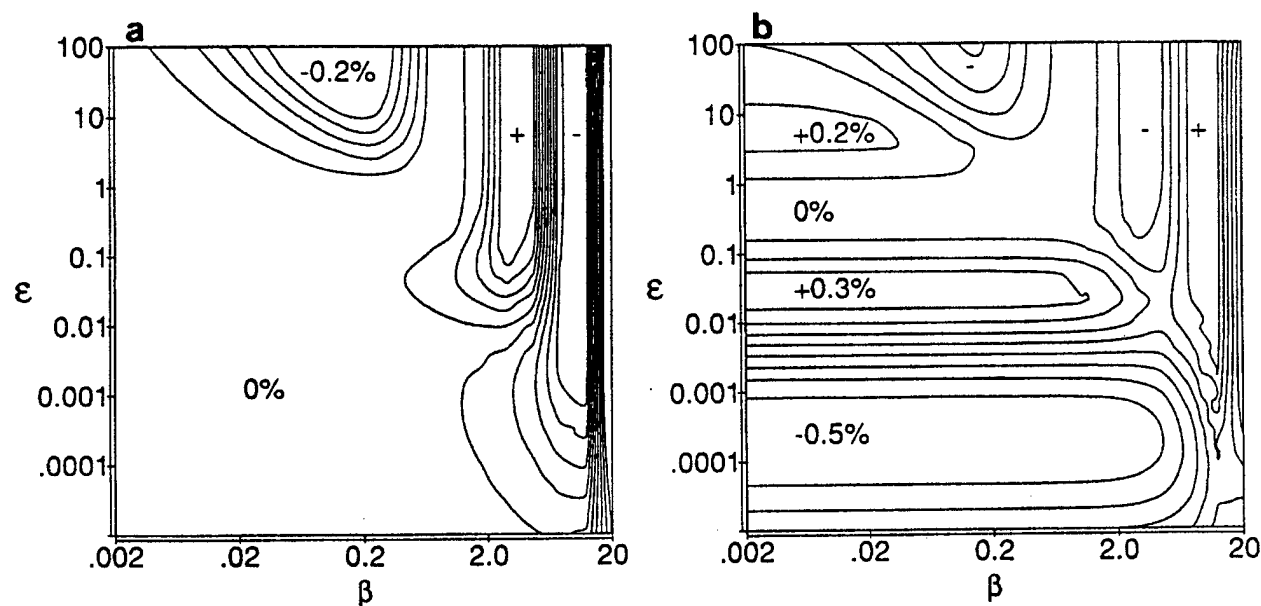


Fig. 1. Contour plots of the relative errors in a)  $\theta_c$  and b)  $(d\sigma/d\Omega)$  which are incurred by using the lower order quadratures for the scattering problem with Molière screening function. The contour interval in a) is 0.04% and in b) is 0.1%. These figures indicate that for most practical purposes the simple solutions suffice.



Table 1

Representative numerical values of distances of closest approach  $x_0$  in reduced units, scattering angles  $\theta_c$  in degrees, and cross sections  $4\pi(d\sigma/d\Omega)$  in reduced units for various values of  $\epsilon$  and  $\beta$  for the Molière screening function. The order of the quadratures used for the computation are given in the column headings.

$\epsilon$	$\beta$	$x_0$	$\theta_c$ (4th)	$\theta_c$ (10th)	$4\pi\left(\frac{d\sigma}{d\Omega}\right)$ (6th)	$4\pi\left(\frac{d\sigma}{d\Omega}\right)$ (10th)
1.0 E-03	5.0 E-01	11.4162361	173.61373	173.62814	253.50019	254.64592
1.0 E-03	2.0 E+01	20.3896494	6.92354	6.89720	60737.081	60954.151
1.0 E-01	2.0 E-01	2.2097357	163.91113	163.90159	6.5146334	6.5070475
1.0 E-01	8.0 E+00	8.1532189	4.73609	4.74710	40733.430	40650.216
1.0 E+01	2.5 E-02	0.0952773	123.53774	123.58530	0.011260996	0.011276772
1.0 E+01	1.0 E+00	1.0211878	3.42319	3.42275	2387.1452	2386.9955

correction to the cross section, it nevertheless uses the slope of the Lenz-Jensen screening function at origin as an input parameter. In order to verify that our computations agree with Andersen's data, we have computed the cross section for a collision using the Lenz-Jensen screening function and the Lindhard screening radius and show this computation along with Andersen's approximate expression in fig. 2. This comparison serves both to confirm that our computation agrees with experiment in the high energy region and to quantify the deviation of Andersen's approximation in the low energy region. The form used for the Lenz-Jensen screen-

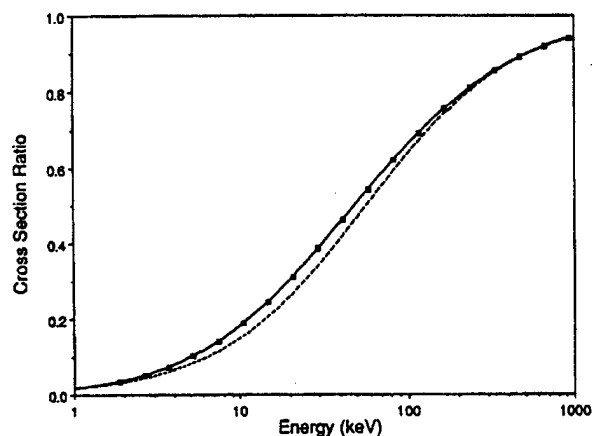


Fig. 2. The differential cross sections for  ${}^7\text{Li}^+$  scattering from  ${}^{209}\text{Bi}$  at laboratory angle of  $150^\circ$  and energies in the range 1 keV to 1 MeV. The results are expressed as a fraction of the unscreened Rutherford value. The solid line is the result of the computation described in this paper applied to the Lenz-Jensen potential with Lindhard screening radius. The dashed line is the angle independent approximation obtained from eq. (14) of ref. [4]. The data points indicated were computed on a Hewlett-Packard 28S calculator using the abbreviated procedure described in the text.

ing function is given by Gombas [21] and also by Loftager and collaborators [22]. It is

$$\phi_{\text{LJ}}(x) = \exp(-y)(1 + y + 0.3344y^2 + 0.0485y^3 + 2.647 \times 10^{-3}y^4),$$

$$\text{where } y = 3.108x^{1/2}. \quad (29)$$

The slope of this function at the origin is  $-1.599$  and is nearly equal to the corresponding slope of the Thomas-Fermi screening function which is  $-1.588$ . Both functions have weakly divergent second derivatives.

It is interesting that the Universal screening function has a slope of only  $-1.188$  and finite second derivative at origin. To test the effects of these differences, we have calculated the cross section for a typical collision using the Universal potential with Biersack's screening radius [7]. The results are shown in fig. 3 along with the equivalent results using Lenz-Jensen and Molière screening and the Lindhard screening radius. The relatively large differences in cross sections at high energies are consistent with the significant differences in the slopes and curvatures at origin and are not compensated for by differences in the screening radii.

O'Connor and Biersack have undertaken an extensive review of interatomic potentials in which they conclude that the Universal potential agrees best with experimental data [23] and should be selected for general use. However, the scheme which they use for determining quality of fit does not properly account for the observation that very near origin the statistical atoms are quite accurate when compared with self-consistent field calculations [24]. In light of the data of refs. [4] and [22], and the results displayed in fig. 3, it seems most appropriate to recommend the use of the Lenz-Jensen potential over the Universal potential for back-scattering computations. For highest reliability one should, of course, use screening functions derived from self-consistent field calculations. For simulations of

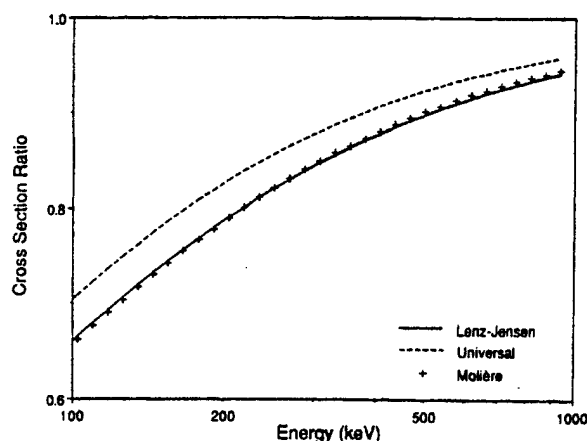


Fig. 3. The differential cross section for  ${}^7\text{Li}^+$  scattering from  ${}^{209}\text{Bi}$  at laboratory angle of  $150^\circ$  for the Lenz-Jensen potential (solid line), Molière potential (symbols), and Universal potential of ref. [7] (dashed line). The results are expressed as fractions of the corresponding values for unscreened Rutherford collisions. The lack of consistency is a result of the poor performance of the Universal screening function near  $x = 0$ .

heavy ion bombardment at typical ion implantation energies, the Universal potential appears to be completely satisfactory [7]. We observe that a screening function with proper slope and curvature at and near the origin combined with the excellent behavior of the Universal potential for larger radii would be a useful addition to the literature.

## 6. Conclusion

A set of algorithms is presented which may be used for accurately and efficiently computing classical scattering integrals and cross sections for screened Coulomb collisions. The algorithms are generic and will work with arbitrary screening functions. The simplicity and speed of the algorithms are such that they may be implemented and used conveniently on virtually any computing device including programmable scientific calculators. When compared with previously available approximations, they offer greater accuracy at the expense of a modest penalty in speed. While somewhat slower than the so called "magic formula" approximation employed in TRIM [2] or the series expansion of ref. [9], the present methods are nevertheless fast enough for use in a Monte Carlo simulation if highest accuracy for high energy collisions is desired. A comparison of the cross sections obtained for the Lenz-Jensen, Molière, and Universal potential suggests that the Lenz-Jensen is most appropriate for high energy collisions.

## Acknowledgements

Portions of this work were performed under contract number DE-AC05-84OR21400, subcontract number 19X-SF583V, with the Optics MODIL at Oak Ridge National Laboratory, Martin Marietta Energy Systems. We wish especially to thank Charles M. Egert for his interest.

## References

- [1] W.-K. Chu, J.W. Mayer and M.-A. Nicolet, Backscattering Spectrometry (Academic Press, New York, 1979) p. 26.
- [2] J.P. Biersack and L.G. Haggmark, Nucl. Instr. and Meth. 174 (1980) 257.
- [3] J. L'Ecuyer, J.A. Davies and N. Matsunami, Nucl. Instr. and Meth. 160 (1979) 337.
- [4] H.H. Andersen, F. Besenbacher, P. Loftager and W. Moller, Phys. Rev. A21 (1980) 1891.
- [5] E. Huttel, W. Arnold, H. Baumgart, and G. Clausnitzer, Nucl. Instr. and Meth. B12 (1985) 193.
- [6] M.H. Mendenhall and R.A. Weller, Nucl. Instr. and Meth. B47 (1990) 193.
- [7] J.P. Biersack, Nucl. Instr. and Meth. B27 (1987) 21.
- [8] J.P. Biersack, W. Kruger and R.L. Stuller, Radiat. Effects Lett. 85 (1985) 193.
- [9] J.P. Blanchard, N.M. Ghoniem, and S.P. Chou, J. Appl. Phys. 61 (1987) 3120.
- [10] J.B. Marion and S.T. Thornton, Classical Dynamics of Particles and Systems, 3rd ed. (Harcourt Brace Jovanovich, New York, 1988) p. 332.
- [11] E. Everhart, G. Stone, and R.J. Carbone, Phys. Rev. 99 (1955) 1287.
- [12] M.T. Robinson, Oak Ridge National Laboratory Publication ORNL-4556 (1970) (unpublished). (Available from the United States National Technical Information Service, Springfield, Virginia.)
- [13] B.M. Latta and P.J. Scanlon, Phys. Rev. A10 (1974) 1638.
- [14] W.H. Press, B.P. Flannery, S.A. Teukolsky and W.T. Vetterling, Numerical Recipes in C (Cambridge University Press, Cambridge, 1988) p. 272.
- [15] W.H. Press et al., op. cit., p. 263.
- [16] J.F. Ziegler, J.P. Biersack and U. Littmark, The Stopping and Range of Ions in Solids (Pergamon, New York, 1985) p. 241.
- [17] M. Abramowitz and I. Stegun (eds.) Handbook of Mathematical Functions (Dover, New York, 1965) p. 888.
- [18] C. de Boor, Mathematical Software, ed. J.R. Rice (Academic Press, New York, 1971) p. 417.
- [19] R.A. Weller, unpublished.
- [20] W.H. Press et al., op. cit., p. 267.
- [21] P. Gombas, Die Statistische Theorie des Atoms und Ihre Anwendungen (Springer Verlag, Wien, 1949) p. 73.
- [22] P. Loftager, F. Besenbacher, O.S. Jensen, and V.S. Sørensen, Phys. Rev. A20 (1979) 1443.
- [23] D.J. O'Connor and J.P. Biersack, Nucl. Instr. and Meth. B15 (1986) 14.
- [24] N.H. Sabelli, M. Kantor, R. Benedek, and T.M. Gilbert, J. Chem. Phys. 68 (1978) 2767.

# Destruction of a $\text{MgF}_2$ optical coating by 250 keV $\alpha$ particle irradiation

Marcus H. Mendenhall and Robert A. Weller  
*Vanderbilt University, Nashville, Tennessee 37235*

(Received 11 May 1990; accepted for publication 1 August 1990)

Magnesium fluoride coatings  $\sim 170$  Å thick have been evaporated onto mirror-quality Be substrates in ultrahigh vacuum and subsequently subjected to 250 keV  $\alpha$  particle irradiation at room temperature. Analysis of the irradiated area by medium energy backscattering spectrometry revealed that the irradiation selectively removed fluorine with an initial yield of 2.2 fluorine atoms per incident  $\alpha$  particle. A visible degradation in reflectivity, which became progressively more extensive with increasing dose, was observed after an  $\alpha$  particle fluence of  $10^{16}$   $\text{cm}^{-2}$ . After a total irradiation of  $4 \times 10^{17}$   $\text{cm}^{-2}$  less than 20% of the fluorine in the film remained, effectively reducing it to metallic magnesium. The effect of this change on the reflectivity of the surface was catastrophic.

Magnesium fluoride is a common optical coating material. It is used because it is robust, easily evaporated, and has high transmission well into the ultraviolet portion of the spectrum. Perhaps the most conspicuous use of the material is as the final coating of the surface of the primary mirror of NASA's Hubble Space Telescope. This mirror is made of an ultralow expansion titanium silicate glass with a reflective surface of aluminum. The final coating on the surface is  $\text{MgF}_2$ . The purpose of this coating is to inhibit the formation of an oxide layer on the aluminum which would limit the usefulness of the telescope in the ultraviolet portion of the spectrum. The  $\text{MgF}_2$  is, in effect, a transparent blanket that shields the aluminum surface from oxygen in the atmosphere, protecting it from oxidation before the telescope is launched into earth orbit.

The primary mirror of the space telescope is located deep within the instrument and is, therefore, relatively well shielded from the space environment. However, the scale of the Space Telescope project serves to underscore the importance of understanding the long term behavior of materials in a radiation environment. Although there is a significant body of literature dealing with desorption and other radiation damage processes in single-crystal alkaline earth fluorides,<sup>1</sup> previous work using ion irradiation and thin-film targets appears to be quite limited.<sup>2</sup>

The purpose of this work was to determine the effects of energetic  $\alpha$  particle bombardment on thin evaporated  $\text{MgF}_2$  films in the thickness range commonly used for coating optical elements. The analytical tool used to determine film thicknesses and compositions was medium energy backscattering spectrometry.<sup>3</sup> This technique is a form of backscattering spectrometry which uses a medium energy primary beam and time-of-flight detection of the scattered particles to achieve results similar to conventional Rutherford backscattering with MeV ions. In order to obtain data of the highest quality, an electrically conducting substrate of low atomic mass was essential. The low atomic mass minimized backscattering from the substrate while the high electrical conductivity minimized electric fields in the sample produced by beam-induced charge displacement. To meet these requirements, we chose to use as a model system fused silica with an evaporated Be film thicker than the  $\alpha$  particle range. The native oxide surface of this film

was coated with an evaporated  $\text{MgF}_2$  layer in an ultrahigh vacuum chamber (base pressure  $2 \times 10^{-10}$  Torr) at room temperature. The film was determined by subsequent backscattering analysis to be 170 Å thick assuming a typical density for  $\text{MgF}_2$  of 3.1  $\text{g}/\text{cm}^3$ . The irradiation of the sample took place in an ultrahigh vacuum scattering chamber (base pressure  $3 \times 10^{-10}$  Torr) in the 300 kV Accelerator Laboratory at Vanderbilt. Figure 1 shows the sample as it appeared in the vacuum chamber before the irradiation.

The experiment consisted of alternating sequences of irradiation by 250 keV  $\alpha$  particles and evaluation by medium energy backscattering spectrometry also using 250 keV  $\alpha$  particles. During irradiation, the  $\alpha$  particle beam was rastered to produce a uniform beam spot of  $\sim 0.2$   $\text{cm}^2$ . The current delivered onto the target during each such irradiation was about 1.5  $\mu\text{A}$  for an integrated dose of 1.25 mC or equivalently a fluence of about  $4 \times 10^{16}$   $\text{cm}^{-2}$ . During measurements, the current was about 200 nA and an additional 50.0  $\mu\text{C}$  was deposited in an area of about 0.07  $\text{cm}^2$ . This gave an additional fluence in the measurement region of about  $4 \times 10^{15}$   $\text{cm}^{-2}$ . Alternating periods of irradiation and measurement were continued until the total fluence of  $\alpha$  particles in the measurement region was  $4 \times 10^{17}$   $\text{cm}^{-2}$ .

The results of the experiment are presented in Figs. 2-4. Figure 2 shows the ratio of fluorine to magnesium in the film as a function of irradiated dose. The initial rate of removal of fluorine was 2.2 F atoms/ $\alpha$  particle. This diminished in proportion to the quantity of fluorine remaining in the film. The magnesium content of the film remained constant throughout the last six cycles of irradiation to within the experimental uncertainty. An initial loss of magnesium is discussed below. Figure 3 shows a time-of-flight backscattering spectrum of the film after the full erosion dose was delivered. Notice peaks corresponding to Mg, F, and the native oxide on the Be surface. The small step feature near 270 ns results from scattering in the Be layer which is thicker than the present measurement can resolve. This spectrum shows the nature of the data leading to Fig. 2 and verifies that the irradiation did not result in the deposition of contaminants such as carbon. The optical effect of the removal of the fluorine is shown in Fig. 4, which is an image of the target taken after

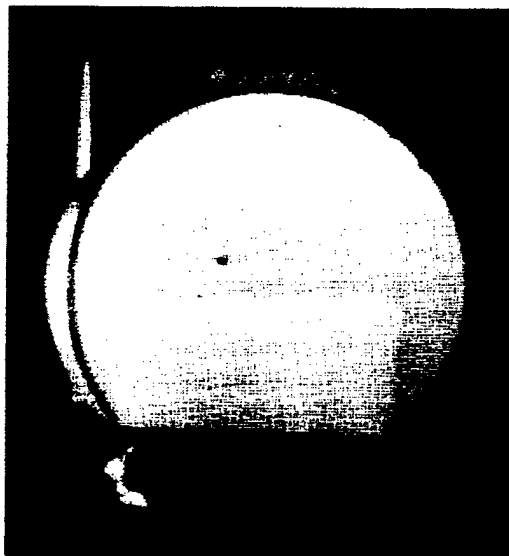


FIG. 1. Be mirror, 2.5 cm in diameter, with  $\text{MgF}_2$  coating. The rectangular area at the bottom of the mirror was masked to serve as a control.

the second irradiation (fluence =  $9 \times 10^{16} \text{ cm}^{-2}$ ). The irradiated area is the dark square on the mirror disk. The damage to the film is unmistakable here even though the fluorine removal is only about 25%.

There are two remarkable aspects to these data. The first is the size of the initial yield of fluorine (2.2 atoms/ $\alpha$  particle) in comparison with the negligible yield of Mg. Alone, this large difference in sputtering (or desorption) yields would quickly lead to a highly enriched Mg layer and a much reduced yield of F. However, in this case, there is evidently a large and probably beam-induced mobility of F atoms that replenishes the surface. The mobility is sufficient that the concentration of F remains constant (to the extent that we can determine) throughout the film and, as a result, F diminishes uniformly throughout the full 170 Å thickness as the irradiation progresses.

A significant variation of behavior under irradiation was also observed as a function of beam flux. At high

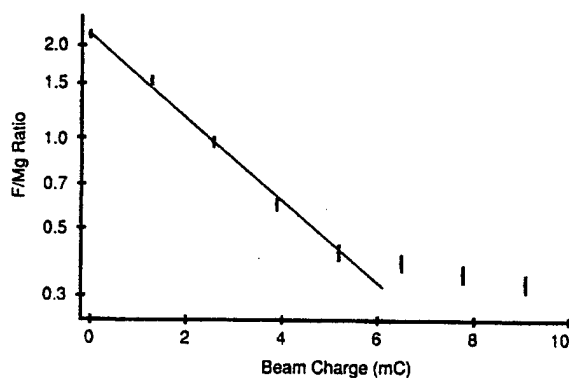


FIG. 2. Semilogarithmic plot of the ratio of F to Mg as a function of irradiation deposited beam charge. The small initial deviation from 2.0 is attributed to uncertainty in the calibration of the detector and is not considered to be significant. The change in slope near 6 mC may be real or may be the result of edge effects.

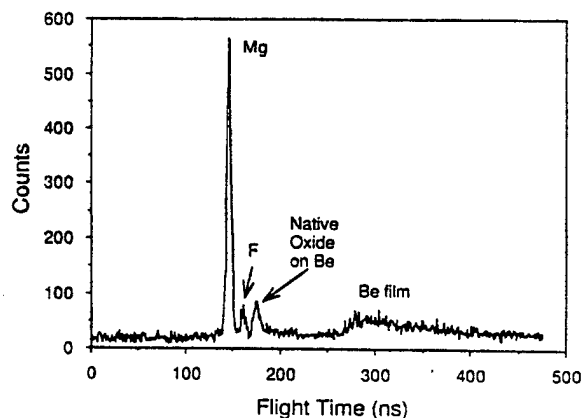


FIG. 3. Time-of-flight medium energy backscattering spectrum of the  $\text{MgF}_2$  film after completion of the erosion. Note that the fluorine peak is well resolved from the native oxide on the Be. The irradiation clearly did not leave any contaminants such as C.

fluxes, where the deposited beam energy was sufficient to produce target heating, the magnesium was found to be removed from the target surface also, in a process reminiscent of the depletion of magnesium from spinel by high voltage electron microscope irradiations which has been observed by Shaibani *et al.*<sup>4</sup> The small white dot visible to the left of the primary spot in Fig. 4 is an area from which all of the film was stripped by the use of an intense focused beam spot. This effect is presumed to be responsible for the loss, mentioned above, of about 25% of the Mg in the film in the first two irradiation cycles. During these cycles some difficulty was experienced in producing a sufficiently low intensity  $\text{He}^+$  beam. It is interesting that this did not significantly affect the trend toward F loss as shown in Fig. 2.

We have observed and previously reported a similar behavior for  $\alpha$  particle erosion of a  $\text{CaF}_2$  film.<sup>5</sup> In that case

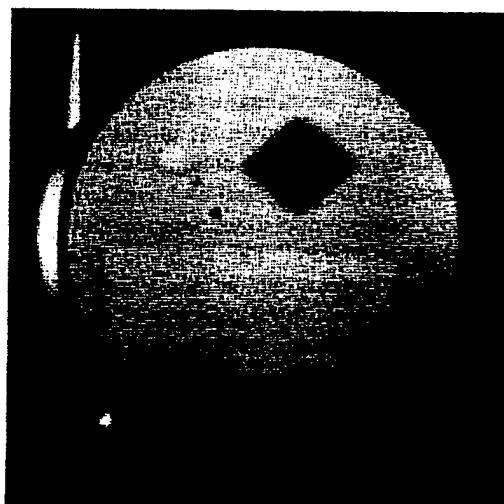


FIG. 4. Be mirror, 2.5 cm in diameter, after a dose of  $9 \times 10^{16} \alpha$  particles/ $\text{cm}^2$ . The beam spot is the large dark area. A smaller light spot to the left is an area from which all of the  $\text{MgF}_2$  film was removed by a separate irradiation which also produced local heating.

we speculated that the similarity in crystal structure of Ca metal (fcc structure, lattice constant = 5.582 Å) and CaF<sub>2</sub> (fluorite structure, lattice constant = 5.462 Å) might facilitate room-temperature, beam-induced F migration even in a polycrystalline evaporated film. The data reported here do not support this hypothesis. The structure of metallic Mg (hcp) and MgF<sub>2</sub> (tetragonal) are quite different in contrast to the similarity of Ca and CaF<sub>2</sub>. It is possible that in both cases the fluorine mobility is an artifact produced, for example, by migration along grain boundaries. However, crystalline CaF<sub>2</sub> is known to be an ionic conductor at elevated temperatures.<sup>6</sup> More probably, ion beam enhanced mobility of fluorine is not strongly dependent upon the structure of the material but rather is quite large in both materials. The persistence of this diffusion with decreasing F (and, therefore, increasing film conductivity) argues persuasively that its origin is not solid state electrolysis initiated by beam-induced charge separation.<sup>4</sup>

To summarize, a MgF<sub>2</sub> thin film subjected to 250 keV  $\alpha$  particle irradiation was observed to experience a selective removal of F that ultimately led to a nearly complete reduction to a metallic layer. This was accompanied by a large change in reflectance which was observable by eye after an  $\alpha$  particle fluence of about  $10^{16}$  cm<sup>-2</sup>. The initial yield of F was 2.2 atoms/ $\alpha$  particle and this diminished approximately in proportion to the amount of F remaining in the film. The film also fluoresced visibly during the initial stages of the irradiation. We offer these final observations. The use of MgF<sub>2</sub> for an optical coating should be avoided when the element will be exposed to  $\alpha$  particle (and probably also proton) irradiation in a vacuum envi-

ronment. Second, in a thick sample the loss of fluorine at the surface can be masked by the high mobility and the large volume of fluorine available. Therefore, data on irradiation effects obtained by the study of bulk MgF<sub>2</sub> cannot be easily extrapolated to predict the behavior of thin films. Third, the character of the erosion of the sample is strongly temperature dependent since Mg is vaporized at elevated temperatures. Finally, in experiments designed to simulate the effects of radiation in space,<sup>7</sup> it is essential to work in an ultrahigh vacuum environment where surface effects may be properly studied.

The authors wish to thank Charles M. Egert, Optics MODIL, Oak Ridge National Laboratory, for supplying the evaporated Be surfaces and Martha Riherd Weller for critical comments on the manuscript. The financial support of Deans V. J. Voegeli and E. A. Parrish is greatly appreciated.

<sup>1</sup>See, for example, Katsumi Tanimura and Noriaki Itoh, Nucl. Instrum. Methods B 46, 207 (1990); R. T. Williams and E. Joseph Friebele, in *CRC Handbook of Laser Science and Technology V III*, edited by Marvin J. Weber (CRC, Boca Raton, 1986), p. 299.

<sup>2</sup>G. C. Farlow and L. A. Boatner, Nucl. Instrum. Methods B 46, 422 (1990).

<sup>3</sup>Marcus H. Mendenhall and Robert A. Weller, Nucl. Instrum. Methods B 47, 193 (1990).

<sup>4</sup>S. J. Shaibani, S. N. Buckley, and M. L. Jenkins, Radiat. Eff. 99, 485 (1986).

<sup>5</sup>Marcus H. Mendenhall and Robert A. Weller, Nucl. Instrum. Methods (to be published, 1990).

<sup>6</sup>J. Oberschmidt and D. Lazarus, Phys. Rev. B 21, 5823 (1980).

<sup>7</sup>J. Becher, R. L. Kernell, and C. S. Reft, J. Phys. Chem. Solids 44, 759 (1983).

## PERFORMANCE OF A TIME-OF-FLIGHT SPECTROMETER FOR THIN FILM ANALYSIS BY MEDIUM ENERGY ION SCATTERING

Marcus H. MENDENHALL and Robert A. WELLER

*Vanderbilt University, Box 1687 Station B, Nashville, Tennessee 37235, USA*

Received 20 July 1989 and in revised form 18 October 1989

In this paper we describe the performance of a recently developed time-of-flight detector for surface analysis by medium energy ion scattering (MEIS). Using ions in the 100–500 keV energy range, this detector is capable of providing sensitivity and depth resolution exceeding that of conventional MeV Rutherford backscattering spectrometry (RBS) performed with a surface barrier detector. For the detector design on which we report here, the timing resolution is between 140 and 200 ps and the effective solid angle is about  $3 \times 10^{-5}$  sr. In future designs the effective solid angle should be easily increased by a factor of four by eliminating known losses. In the studies reported here, the energy resolution is limited by the intrinsic resolution of the ion beam used to make the measurements. This paper reports measurements of the detector efficiency as a function of energy for  $\alpha$  particles and provides examples of the detector performance analyzing thin films by  $\alpha$  backscattering,  $C^{2+}$  backscattering, and (forward) elastic recoil detection.

### 1. Introduction

In most cases the lower limit of projectile energy used for surface analysis by Rutherford backscattering (RBS) is not dictated by physical considerations but, rather, by the energy resolution of Si surface barrier detectors. Thus, in common practice, energies in the 1–3 MeV range have come to be preferred [1]. In fact, for some measurements there are compelling reasons to use lower energies. A comparison of  $\alpha$  particle backscattering at 2 MeV and 200 keV in Al reveals that the cross section in the latter case is approximately two orders of magnitude larger and that the stopping power is comparable. The former leads to greater sensitivity for a given beam fluence while the latter, combined with the much better energy resolution of our detector compared to that of a Si surface barrier detector, provides improved depth resolution.

In the past, the principal obstacle to the use of projectiles in the 100–500 keV energy range has been the difficulty, or perhaps more accurately, the inconvenience of measuring their energy after backscattering. The silicon surface barrier detector is so easy to use and provides measurements of such high quality that it is used almost exclusively today in routine analyses. However, for  $\alpha$  particles the best resolution of these detectors at room temperature is about 10 keV. As a result, it is necessary to use an incident beam with sufficient energy to guarantee at least this much separation between spectral features of interest. This precludes the general use of surface barrier detectors below about 500 keV.

Electrostatic analyzers are not subject to this restriction and can be made to have very high resolving power. However they have disadvantages when used for routine thin film analyses. Most significantly, they can only detect ions. This complicates the analyses of spectra especially at low energies. In addition, they are single channel devices. That is, they can examine only one energy at a time. To measure a complete spectrum it is necessary to successively sweep the region of interest. This makes electrostatic analyzers much less efficient than surface barrier detectors. Finally, electrostatic analyzers are large, relatively expensive and much less convenient to use than surface barrier detectors. As a result, they have found their principal application in surface structure studies where their disadvantages are less important [2].

In a previous publication [3] we presented designs and theoretical analyses of two time-of-flight detectors for use in backscattering analyses using particles in the 50–500 keV range. These detectors retain most of the advantages of surface barrier detectors while circumventing the disadvantages of electrostatic analyzers. In particular, they analyze all energies simultaneously, instead of requiring tuning from one energy to another. Moreover, to first order, they measure the energies of both ions and neutrals with equal efficiency. Thus, as with conventional RBS using surface barrier detectors, a knowledge of the scattering cross section is sufficient for the quantitative evaluation of thin films. For the sake of brevity, we shall refer to the technique of thin film analysis by time-of-flight medium energy ion scattering by the acronym ToF MEIS.

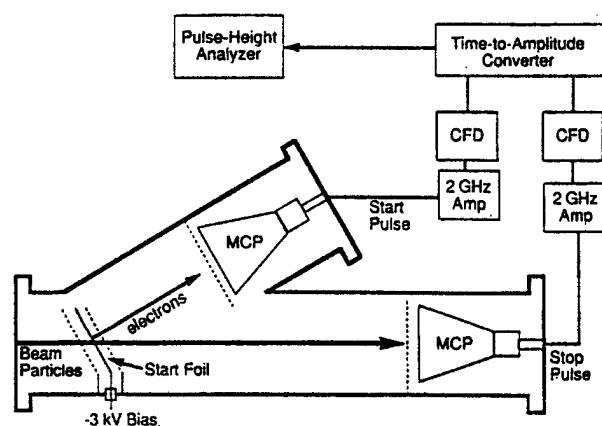


Fig. 1. A schematic of the time-of-flight spectrometer. Scattered particles enter from the left along the long axis of the detector. The distance from the carbon foil to the start detector is 11.6 cm and to the stop detector is 36.6 cm. The electron and ion trajectories make an angle of  $30^\circ$ .

The general design of the detector is described in ref. [3]. In this work, we describe some of the details of the actual implementation of this design. The detector, which is shown in fig. 1, consists of two microchannel-plate (MCP) assemblies and a negatively biased carbon foil mounted between two grounded grids. A particle incident on the detector passes through the carbon foil (called the start foil) and emits secondary electrons which generate a pulse (called the start pulse) in the off-axis channel plate. After exiting the foil, the particle itself travels axially through the length of the detector and initiates a second pulse (called the stop pulse) in the axially mounted channel plate. The interval between these pulses is measured electronically and yields the velocity of the detected particle.

This paper describes the construction and measured performance of the detector and gives an initial evaluation of its performance as a thin film analyzer. The detector is generally very well behaved and, using a mono-energetic  $\alpha$  particle source ( $^{210}\text{Po}$ ), performs as predicted. The resolution of the ToF MEIS technique is found to be limited by the energy spread of our accelerator beam.

The detector has an efficiency of about 3% (which might be viewed as the effective  $d\Omega/\text{geometric } d\Omega$ ) for 100 keV He. The measured efficiency is a smooth function of energy that is, very roughly, proportional to  $\sqrt{E}$  for He. An interesting effect which was not considered in ref. [3] is charge exchange in the start foil of the detector. This effect has been observed experimentally and is found to complicate somewhat the interpretation of spectra.

## 2. General structure of ToF spectra

Readers familiar with RBS energy spectra may find the ToF spectra unfamiliar and difficult to interpret. The differences result from the transformation from flight time to particle energy, and the effect of the Jacobian of the transformation on the shape of the background and the height of peaks.

In a ToF detector, one measures directly the amount of time required for a particle to pass from one reference position to another. Since the energy of a particle is  $E = mv^2/2$ , and the velocity computed from a flight time  $t$  is  $v = L/t$  where  $L$  is the flight path, one arrives at  $E = mL^2/2t^2$ . In practice, this energy must be corrected for the energy loss in the start foil to get the actual energy of the backscattered particle. However, this correction is small and nearly constant, so it does not significantly affect the discussion which follows. (For a complete discussion see ref. [3].)

To analytically transform a spectrum from the time domain

$$dN(t) = N_i(t) dt, \quad (1)$$

to the energy domain

$$dN(E) = N_E(E) dE = N_i(E(t)) \left| \frac{dt}{dE} \right| dE, \quad (2)$$

one replots the time-domain spectrum as a function of energy and multiplies it by the Jacobian of the time-energy transformation,

$$\left| \frac{dt}{dE} \right| = \frac{t^3}{mL^2} = \frac{L\sqrt{m}}{E^{3/2}}. \quad (3)$$

This transformation makes peaks at high energy (short time) in the ToF spectrum appear much smaller in the energy spectrum because of the  $t^3$  factor. Thus, peaks in time-of-flight spectra corresponding to heavy elements that are clearly visible when the spectrum is plotted on a linear vertical scale may become invisible when the spectrum is transformed to an energy spectrum unless it is plotted on a logarithmic vertical scale.

This effect is demonstrated in figs. 2, 3a and 3b. Fig. 2 is an unmodified time-of-flight backscattering spectrum taken using our detector and plotted on a linear scale. Note the height of the heavy element peaks. In fig. 3a, the spectrum has been rebinned into an energy spectrum and plotted on a linear scale. Here the same peaks are barely visible. Fig. 3b shows the energy spectrum plotted on a logarithmic vertical scale; now the peaks are again distinct. This dynamic range compression is a convenient intrinsic feature of time-of-flight spectra when displayed directly. It is for this reason that all spectra presented in this paper are so displayed.

A time-of-flight spectrum has a background due to random coincidences from ions and also probably from beam induced X-rays. This background is observed to

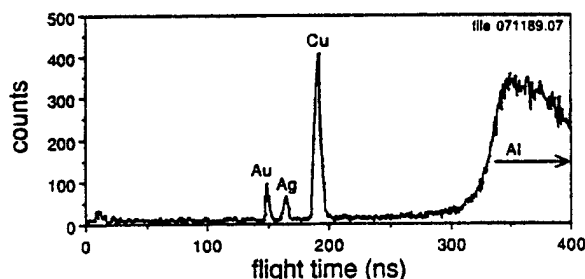


Fig. 2. A typical time-of-flight backscattering spectrum. This spectrum was produced by scattering 450 keV  $C^{2+}$  ions from an Al foil with thin sputter deposited layers of Cu, Ag and Al. The areal densities of Cu, Ag, and Au are respectively,  $2.7 \times 10^{15}/\text{cm}^2$ ,  $1.0 \times 10^{14}/\text{cm}^2$  and  $3 \times 10^{13}/\text{cm}^2$ . This spectrum was accumulated in  $10^{-3}$  s with about 10 nA of beam.

be flat in the time domain (unlike the pile-up in an energy spectrum produced using a surface-barrier detector) and, in a typical spectrum (for example, fig. 9) which has 1000 counts/s of real events, the random coincidence background is about 20 counts/s. This flat background in the time spectrum is ideal for heavy element analysis since in the energy domain, the background is proportional to  $E^{-3/2}$  and, therefore, is decreasing smoothly and steeply at high backscattered energy, where heavy element peaks are found. The simple shape of this background makes it much easier to subtract than the pile-up background from a Si detector, which has a quite complicated shape.

Ordinarily, for backscattering spectroscopy, where all the analyzed ions are of the same species, the effect of the transformation from the time to the energy domain is largely cosmetic. This is not true for spectra

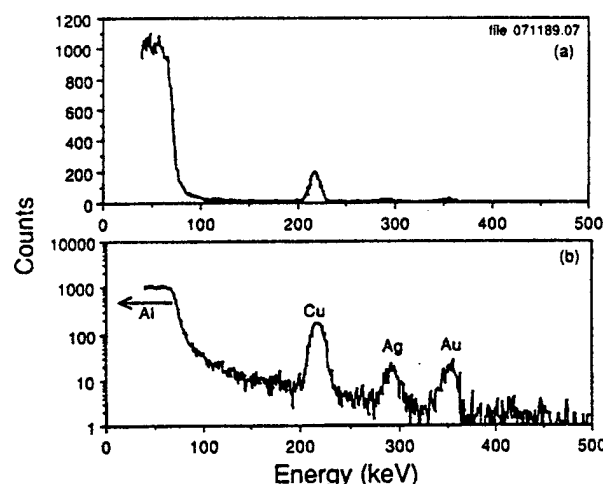


Fig. 3. The energy backscattering spectrum corresponding to the data of fig. 2 plotted (a) on a linear vertical scale and (b) on a logarithmic vertical scale. The effect of the Jacobian of the transformation from the time-of-flight to the energy domain is to obscure the high mass overlayers.

that may contain features that arise from different atomic species. An important example of this principle is the analysis of light ions by elastic recoil detection. In this spectroscopy (which is used primarily to detect light species in a heavy target) the incident ion beam causes target atoms to be forward scattered into a detector. The energy of these forward scattered particles is measured and, by considering the cross section and kinematics of the collision, the type and number of light atoms in the target is determined. If the beam species is heavier than the target species of interest, then the energy of the forward recoil is less than that of the beam ions while its velocity is greater. If an energy dispersive detector (such as a surface barrier detector) is used for the analysis, then the spectral feature associated with the light target species may be in a region that contains a large background from scattered beam ions. In a time dispersive detector, the corresponding spectral feature will be unaffected by background since the light target atom moves faster than ions of the incident beam and, therefore, much faster than any scattered ions [4]. This effect can produce dramatic improvements in the sensitivity for detecting species such as hydrogen. An example of this is given below.

### 3. Detector design and construction

The detector uses a  $1 \mu\text{g}/\text{cm}^2$  carbon foil (Arizona Carbon Foil Co.) mounted on a 90% transmission 70 line/in. nickel mesh (Buckbee-Mears Co.) as its start foil. Mounting the foil on the mesh makes it quite rugged; we have had no problems with damage to the foil during routine handling or during venting of the system, but have experienced foil failures twice at the time of this writing. These are characterized by high levels of electron emission from the start foil assembly which occur in the absence of an ion signal. The start foil holder is fabricated from commercially available general purpose ion optical components (B-series eV parts from Kimball Physics, Inc.). The nickel meshes for the start foil and for the ground planes are attached to the stainless steel mounting plates using Torr-Seal resin (Varian). The carbon foil is mounted on a plate which has a circular opening 0.5 in. (1.27 cm) in diameter. The ground plane meshes (also 90% 70 line/in. Ni) are mounted on plates with 0.625 in. (1.59 cm) circular apertures.

The start-foil assembly is tilted at  $30^\circ$  to the axis of the detector, is 11.6 cm from the start microchannel plate, and is 36.6 cm from the stop MCP. The distance from the center of our vacuum chamber to the start foil is 30.5 cm. We use a  $-3$  kV bias on the start foil; this value is not critical.

The microchannel plate assemblies, which include integral  $50 \Omega$  impedance matched anode structures



(Galileo Electro-Optics Corp. part FTD-2003), are run in grounded-anode mode with a 22 M $\Omega$  anode resistor and a total bias voltage of  $-2.1$  kV (including the drop across the anode resistor). In front of each assembly is another 90% transmission mesh that establishes a ground plane parallel to the biased cathode. The pulses from these detectors are amplified by 2 GHz pulse amplifiers (Phillips Scientific 6954B-10) and then passed to fast constant fraction discriminators (Phillips 6915) with 600 ps shaping cables and a 50 mV threshold. The time to amplitude conversion is performed by an Ortec 566 time to amplitude converter, and the events are histogrammed in a conventional multichannel pulse height analyzer (Canberra Series 40).

The detector is housed in a custom made enclosure with 4.5 in. OD Conflat flanges for the ports and 3 in. tubing (larger than the usual 2.5 in. tubing used with 4.5 in. Conflat flanges). The entrance aperture for the detector is formed by mounting the detector onto the vacuum chamber using a solid copper gasket with a 12.5 mm diameter hole drilled in the center.

#### 4. Measured detector characteristics

##### 4.1. Experimental setup

For these measurements the detector was used in three configurations. Initially, for intrinsic timing resolution measurements it was used in a stand-alone configuration with a radioactive  $\alpha$  particle source. For accelerator based backscattering measurements, the ion beam was perpendicularly incident upon the target, with the detector mounted at  $150^\circ$  with respect to the beam. For the forward recoil experiment, the detector was mounted at an angle of  $42^\circ$  with respect to the beam. In the accelerator experiments, the target was not enclosed in a Faraday cage, thus the accuracy of the current integration was limited. The pressure in the scattering chamber during accelerator runs was typically below  $10^{-8}$  Torr ( $1.3 \times 10^{-6}$  Pa).

##### 4.2. Energy and time resolution

To measure the intrinsic timing resolution of the detector, one needs a source of particles with very narrow velocity spread. We chose a thin, commercially manufactured  $^{210}\text{Po}$   $\alpha$  source (Isotope Products Laboratories). This source was removed from its (non-vacuum compatible) holder and installed in the vacuum system with our detector. The source produces essentially monoenergetic 5.3044 MeV  $\alpha$  particles. Although the count rate in our detector from this source was very low ( $3 \times 10^{-2}$  counts/s), it was sufficient for the detector calibration. We collected a spectrum for  $2.4 \times 10^5$  seconds (2.8 days) of live time and accumulated 7260

counts in the peak. The integrated background in the 50 ns coincidence window of the detector was  $8 \times 10^{-4}$  counts/s corresponding to  $3 \times 10^{-6}$  counts/s in the region of the peak. The spectrum from that run is shown in fig. 4. Because of the low count rate of the source we have not studied the complex shape of the peak, but the FWHM of the peak (excluding the shoulder) is about 200 ps, and if a FWHM is deduced from the width of the leading edge the resolution is 140 ps. Thus, although the resolution depends on how it is calculated, the worst case of 200 ps compares well with the theoretical prediction of 150 ps.

For data taken with our 300 kV accelerator, the apparent resolution of the detector is much worse than that measured using the  $\alpha$  source. We have determined that the origin of this discrepancy is instability in the 300 kV power supply that establishes the accelerating voltage. The voltage ripple on this supply has been measured using a capacitive pickup and found to be approximately sinusoidal with amplitude of about 1 kV peak-to-peak at a terminal voltage of 200 kV. This level of ripple is sufficient to explain most of our apparent loss of resolution. An additional factor appears to be long term drift in the voltage of the 300 kV supply. This is less easily quantified but appears to be comparable in magnitude to the ripple and affects spectra on a time scale of a few minutes. A new high voltage power supply with superior stability and ripple specifications is being procured to eliminate this problem.

Another phenomenon which contributes to the loss of resolution when using ions from the accelerator is the splitting of peaks which results from charge exchange in the carbon start foil. If an ion enters the foil in a given charge state and leaves in a different state, it will gain or lose energy in multiples of the 3 kV bias on the C foil. This will produce side lobes at an energy separation of 3 keV on spectral features that would otherwise be

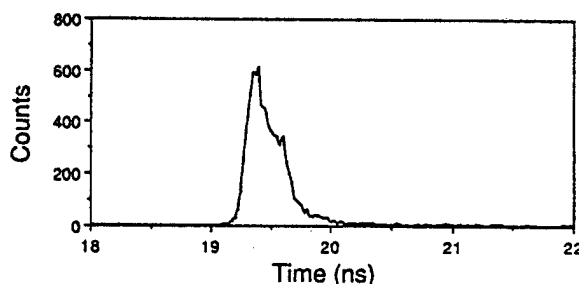


Fig. 4. The time-of-flight spectrum for 5.3044 MeV  $^{210}\text{Po}$   $\alpha$  particles. This spectrum was used to determine the intrinsic timing resolution of the detector. The peak appears to be a composite of at least two components but the low activity of the source precluded our investigating the structure in detail. The timing obtained just above the shoulder (at 0.6 of peak height) is 200 ps. The resolution as determined from the leading edge of the pulse is 140 ps.

isolated peaks [5]. In most cases which we have observed, these side peaks correspond to  $\Delta q = \pm 1$  and are somewhat smaller than the central ( $\Delta q = 0$ ) peak (see the oxygen and carbon peaks of fig. 6). The intrinsic resolution of the detector is sufficiently small (perhaps less than 500 eV for all flight times shown in fig. 6) that, if the ion beam energy did not have the instability discussed above, the splitting would be extremely well resolved at all energies. For the spectra shown, the splitting can only be resolved for scattering from low mass species such as C, O and Si where the 3 keV is a large fraction of the total backscattered energy. When combined with the instability of the accelerator beam, this charge exchange splitting results in an apparent 6 keV resolution for many of our spectra.

The detector, in its present configuration, has a geometric solid angle of about  $1 \times 10^{-3}$  sr, or about ten times larger than we had discussed in our earlier paper. With this large solid angle, the ultimate resolution of the system is limited by the kinematic shift in energy with scattering angle. With a stable ion beam, it will be necessary to reduce this solid angle to about  $2 \times 10^{-4}$  sr to achieve a resolution which is not degraded by kinematics.

#### 4.3. Efficiency

To measure the efficiency of the detector for  $\alpha$  particles, we have compared thick target  $\alpha$  particle backscattering spectra with computed spectra for several combinations of target species and initial beam energy. The ratio of measured to computed yield is taken as the detector efficiency.

For He at most energies on an arbitrary light substrate, multiple scattering is not significant, and a thick target spectrum can be synthesized directly based upon a single scattering approximation. For these cases we have synthesized spectra according to the following procedure. We assume that the incident beam direction is normal to the target surface, and that the scattering cross section  $d\sigma(E', \Psi)/d\Omega$  and the particle range  $R(E)$  are known as a function of energy. The laboratory scattering angle  $\Psi$  is assumed to be fixed as are the incident beam energy  $E_0$  and incident projectile and target atomic numbers and masses. To synthesize a spectrum, one considers a set of final detected energies  $E_f$  and solves the transcendental equation

$$R(E_0) - R(E') = |\cos(\Psi)| [R(\kappa E') - R(E_f)], \quad (4)$$

to get the energy  $E'(E_f)$  at which the corresponding scattering occurs. The factor  $\kappa$  is the well known kinematic factor which expresses the fraction of its kinetic energy that a particle retains in collision. The number of

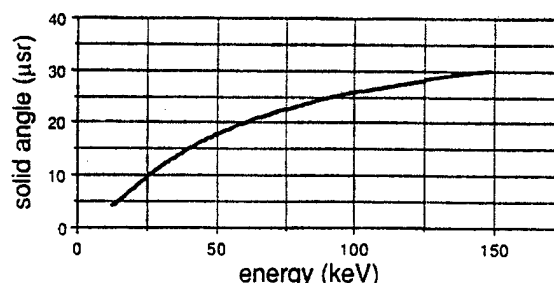


Fig. 5. The measured efficiency of the detector shown in fig. 1 for  $\alpha$  particles in the energy range from 25 keV to 150 keV. The data are presented as an effective, energy-dependent solid angle for the detector. The geometric solid angle subtended by the detector is approximately 1 msr.

backscattered particles per unit energy per sr per incident particle is then computed as:

$$\frac{d^2 N(\Omega)}{d\Omega dE_f} = \sigma(E') \frac{dR(E'(E_f))}{dE_f}. \quad (5)$$

The cross section  $\sigma(E')$  is computed by numerically differentiating the scattering integral from the "Magic Formula" used in the TRIM code [6]. By performing this procedure sequentially for each  $E_f$ , a spectrum is generated.

For  $\alpha$  particles incident on heavier substrates multiple scattering in the target must be considered and a more elaborate procedure must be used to generate reference spectra. For the case of 44 keV  $\alpha$  particles incident on a Au target, the thick target spectrum was computed using an in-house implementation of TRIM using the Ziegler-Biersack-Littmark universal potential [7].

Fig. 5 shows the measured detector efficiency for  $\alpha$  particles as a function of energy. For convenience, the efficiency is expressed as an effective solid angle subtended by the detector. Thick targets of Be, Al and Au were used as were various incident beam energies ranging from 44 keV on Au to 254 keV on Al. The calculated efficiencies in all cases agreed within about 10%. (These measurements had only one free parameter, an absolute scale, which was used to scale each curve for the uncertainty in beam current integration.) The resulting efficiency (fig. 5) is independent of the target used and is a smooth function of the  $\alpha$  particle energy. This efficiency has been used to correct spectra in order to make accurate quantitative measurements of thin films as discussed in the next section.

#### 5. Thin film analysis

In this section, we present spectra which highlight particular features of the time-of-flight spectrometer and demonstrate its application to the analysis of

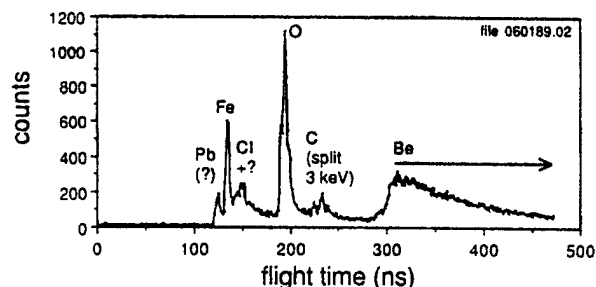


Fig. 6. A time-of-flight spectrum obtained by scattering 185 keV  $\alpha$  particles from a commercially manufactured Be foil. The O forming the native oxide on the surface is the most distinct feature of the spectrum. Also present, however, are several features associated with contaminants on the foil. Note especially the complex structure of the C feature and, less obviously, the similar shape of the O peak. This structure is caused by charge exchange in the start foil (fig. 1) which produces energy shifts in multiples of 3 keV for particles which enter and leave the start foil in different charge states. The detector is capable of fully resolving these artifacts when used with a sufficiently stable accelerator beam.

surfaces and thin films. These spectra were taken from various samples, some of which were made expressly for detector calibration and some of which were of previously unknown or only partially known composition.

### 5.1. Helium backscattering

Fig. 6 shows an  $\alpha$  particle backscattering spectrum obtained by bombardment of a commercially prepared 0.25 mm Be foil whose method of manufacture and treatment prior to delivery were unknown. The stated purity of the foil was 99.5% for metal contaminants and 99% for total impurities. The sample was washed with a freon TF spray before analysis but was otherwise untreated. The Be substrate is identified as the edge at the right of the figure. The most prominent feature of the spectrum is the large oxygen peak associated with the native oxide on the surface. Also visible, however, is a significant carbon contamination. The presence of this carbon both before (not shown) and after freon degreasing indicates that it is not part of a loosely adhering surface film of oil. Clearly visible are three heavy element peaks with masses near those of Cl, Fe, and Pb. A significant background arising from the bulk contaminants is clearly present. Because of the charge exchange phenomenon discussed above, low mass peaks such as the carbon peak have a complicated structure. Note that in this spectrum higher masses are to the left since scattering from them leads to shorter flight times. Conventional RBS spectra measured with energy dispersive detectors have high mass features to the right.

The spectrum from the second sample of practical interest is shown in fig. 7. This is the result of  $\alpha$  backscattering from a device-grade Si wafer which has

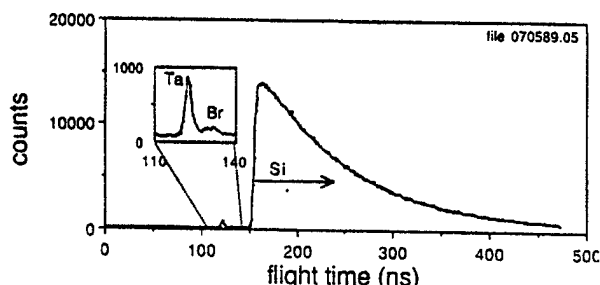


Fig. 7. A time-of-flight spectrum of 185 keV  $\alpha$  particles scattered from a Si wafer with a very thin sputter-deposited layer of Ta. The inset contains an expanded view of the high mass region of the spectrum. Note the second peak to the right of the Ta peak. This feature is caused by a small amount (about  $1.2 \times 10^{14}/\text{cm}^2$ ) of Br which was deposited in the cleaning process. The Ta layer contains only about  $1.1 \times 10^{14}$  atoms/ $\text{cm}^2$  but is larger because of a larger scattering cross section.

been etched in HF/ $\text{HNO}_3$  and then rinsed in a Br/methanol solution. (This is a commonly used cleaning procedure for Si wafers.) This wafer was then coated with about  $1.1 \times 10^{14}/\text{cm}^2$  of Ta by sputtering a Ta target with Ar. It is important to note that the Ta is clearly visible, even though the layer is much thinner than would commonly be used in device fabrication. Further, the residual Br from the Br/methanol wash is quite evident, and is calculated to be present at a level of  $1.2 \times 10^{14}/\text{cm}^2$ .

### 5.2. Elastic recoil detection

In fig. 8 we show an elastic recoil detection (ERD) spectrum obtained by 185 keV  $\text{He}^+$  ions normally incident on a  $5 \mu\text{g}/\text{cm}^2$  carbon foil supported on a Ni mesh. The detector is positioned at an angle of  $42^\circ$

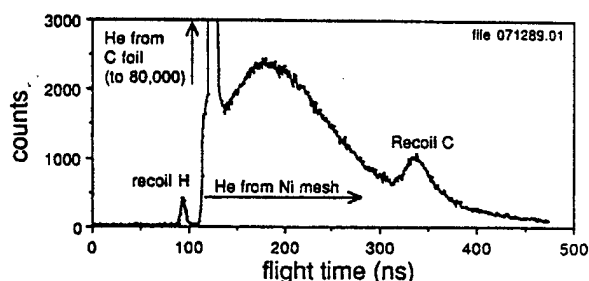


Fig. 8. An elastic recoil spectrum produced by 185 keV  $\alpha$  particles incident on a  $5 \mu\text{g}/\text{cm}^2$  C foil mounted on a Ni mesh. This spectrum was accumulated in 500 s with about 35 nA of beam. The dominant feature of the spectrum, the elastic scattering of the  $\alpha$  particles from C atoms, has been truncated for clarity. The most significant feature of the spectrum is the peak identified with elastically scattered H which is present as a contaminant in the sample. This peak corresponds to a surface layer of about  $10^{15}/\text{cm}^2$ .

with respect to the incident beam. This spectrum was obtained in 500 s with a beam current of about 35 nA. The most prominent feature of the spectrum is the large peak corresponding to  $\alpha$  particles elastically scattered from C. (This peak sits atop a large background resulting from  $\alpha$  scattering in the Ni mesh.) However, the most significant feature is the small hydrogen peak. As discussed above, this feature is in a region of the spectrum that is almost completely without background. Using an energy dispersive detector, this peak would be much more difficult to distinguish because it would be in a region of high background caused by scattered beam ions. Techniques such as the use of a thick stopping foil to range out the beam ions have been employed but they inherently produce a loss of resolution [8,9]. The hydrogen feature in fig. 8 is calculated to correspond to approximately  $1 \times 10^{15}$  H atoms/cm<sup>2</sup>. We estimate on the basis of these data that, with a comparable number of incident ions, we would be able to measure hydrogen in this foil at a concentration of about 0.02 at.% (200 ppm) with 10% statistical error. This sensitivity exceeds that of ref. [10] when the same criteria for sensitivity are used. Longer run times or heavier incident ions (Li, C) will yield yet more sensitivity.

### 5.3. Heavy ion backscattering

For the detection and identification of heavy element overlayers on materials, it is beneficial to scatter an ion which is heavier than He because a larger kinematic shift in energy will occur. This larger energy dispersion facilitates the discrimination of heavy species whose masses are too close together to be differentiated by  $\alpha$  backscattering. In addition, if the incident particle is more massive than the substrate, single event backscattering from the substrate is kinematically forbidden. This can improve the sensitivity for the detection of overlayers significantly. Recently, a few groups have begun to use time-of-flight techniques for (MeV) heavy ion Rutherford backscattering (HIRBS) [11,12]. However, this work has typically been carried out with projectiles whose initial energies are several MeV. Although excellent mass resolution and sensitivity have been demonstrated in HIRBS analyses, beams of such high energy typically deposit a large amount of energy in the target and are, thus, quite damaging. In addition, such applications of HIRBS are limited to those laboratories which have larger accelerators.

Although our detector was not originally conceived for heavy ion work, calculations (ref. [3]) in the design phase of this project indicated that the detector's performance for heavy ions with velocities corresponding to at least 50–100 keV/u should be excellent. It was less certain from theoretical considerations whether or not meaningful ToF MEIS thin film analyses with heavy

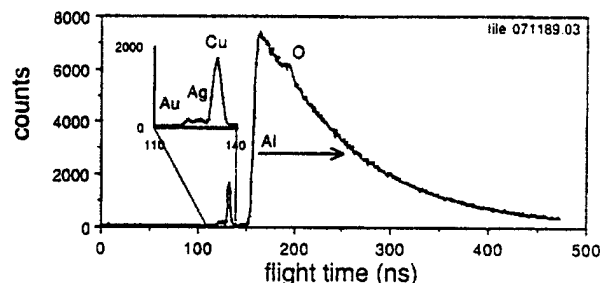


Fig. 9. A time-of-flight spectrum of  $\alpha$  particles scattered from the same Al target used for fig. 2. An expanded view of the high mass region of the spectrum is shown in the inset. A comparison of figs. 2 and 9 clearly demonstrates the advantage of using heavy ions for backscattering when improved high-mass resolution is important. Note, however, that the presence of O is not revealed in the C spectrum of fig. 2 because the resulting backscattered energy is too low to measure.

ions would be possible. Data obtained thus far confirm that heavy ion ToF MEIS is not only possible but is a useful complement to light ion MEIS.

Because of the present instability and upper limit of our beam energy and additional limitations imposed by our ion source, we have not yet tested the detector under optimum conditions for heavy ions (such as might be obtained using 500 keV  $\text{Li}^{2+}$  or 1 MeV  $\text{C}^{2+}$ ) and have, therefore, not yet attempted to measure its efficiency for these species. Nonetheless, the performance observed for, for example, 450 keV  $\text{C}^{2+}$  is quite respectable. In figs. 9 and 2, we show a comparison of spectra obtained from the same sample using 185 keV  $\text{He}^+$  and 450 keV  $\text{C}^{2+}$  backscattering. This sample is an aluminum foil which was used as a catcher foil in a sputtering experiment and has roughly  $3 \times 10^{13}/\text{cm}^2$  Au,  $1.0 \times 10^{14}/\text{cm}^2$  Ag and  $2.7 \times 10^{15}/\text{cm}^2$  Cu on its surface. Note that in the He scattering spectrum, the Au and Ag peaks are poorly resolved (although if our ion beam energy were stable, these peaks would be well resolved). By using C, all of the species are completely resolved although the background (presumably from low energy recoils) is higher. We believe that with a stable C beam at 300 keV we will be able to resolve the isotopes of Cu. With a beam of around 1.4 MeV C, the isotopes of Ag should be fully separated [3].

### 5.4. Sensitivity

The issue of sensitivity in thin film analysis by backscattering is complicated, because it involves detector efficiency, detector resolution, various forms of background and the sputtering rate of the substrate by the ion beam. The time-of-flight detector discussed here has essentially no intrinsic background in the absence of the accelerator beam. The spread in beam energy which degrades mass resolution also degrades ultimate sensi-

tivity since peaks are spread out over a greater region of the background. Even with our present energy resolution, however, it is possible to make very sensitive measurements of sparse overlayers. The Al foil shown in fig. 9 has only about  $3 \times 10^{13}/\text{cm}^2$  of Au on its surface, yet the resulting signal is 3 times the background. In a second example (fig. 6), we note that in 20 minutes of  $\alpha$  backscattering we have detected  $2.5 \times 10^{13}/\text{cm}^2$  of a contaminant which is thought to be Pb and have done so with a statistical error of 6%. In this case, the resulting spectral feature was a factor of 30 above the background (note that this is peak height/background, not signal/noise; there are 1100 counts in the whole peak and only 72 counts of background so signal to noise is dominated by the  $\sqrt{N}$  statistics of the peak itself). We expect the sensitivity for submonolayer films to improve by at least a factor of five when we install the high-stability power supply on our accelerator. This implies, for a counting rate twice background, a sensitivity of about  $3 \times 10^{11}/\text{cm}^2$  for heavy elements on a light substrate using a 200 keV He beam. Using other targets and longer run times we have achieved sensitivities of  $3 \times 10^{12}/\text{cm}^2$  with the present apparatus. Based upon these results, we believe that the ultimate sensitivity of ToF MEIS using  $\alpha$  particles with the present detector will be about  $3 \times 10^{11}/\text{cm}^2$ . As fig. 2 suggests, the sensitivity may be much better using heavy ions, as is the case with heavy ion Rutherford backscattering [13].

We note, finally, that the Rutherford scattering cross section decreases more rapidly with increasing beam energy ( $E^{-2}$ ) than does the sputtering yield (roughly  $E^{-1}$ ). In the energy range where we are working, the cross sections calculated as described above are within about 20% of the Rutherford values. For example, using the equations of Matsunami, et al. [14] the sputtering yield for carbon on silicon is found to be 0.03 at 400 keV and 0.002 at 10 MeV. Thus, at the higher energy, the sputtering yield has fallen a factor of 15 while the cross section has fallen a factor of roughly 600. As a result, MEIS is preferred over conventional MeV RBS for maximum sensitivity.

### 5.5. Depth resolution

Depth resolution in thin film analysis by backscattering is determined approximately by the energy resolution of the particle detector divided by the stopping power of the ion in the sample [1]. ToF MEIS excels in depth resolution because of the excellent timing (energy) resolution of the detector and because the stopping power of the ion in the sample at keV and MeV energies is comparable. In order to demonstrate the depth resolution of ToF MEIS we have created a target with vertical structure.

Fig. 10 shows a spectrum obtained from a sample of

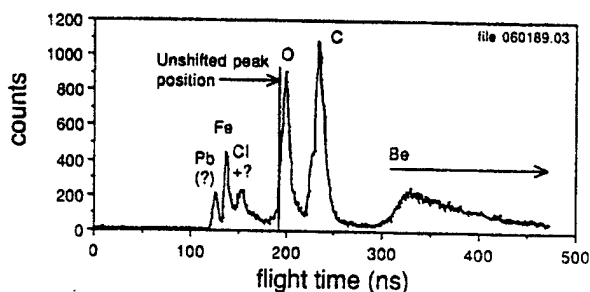


Fig. 10. A time-of-flight spectrum of  $\alpha$  particles backscattered from a Be foil sample with a  $1.8 \mu\text{g}/\text{cm}^2$  C overlayer. The presence of the C covering the native oxide produces a clearly visible shift in the position of the O peak which is only about 3.6 keV. Energy shifts of 500 eV in the centroid of peaks are detectable and with improved accelerator beam stability, shifts of 100 eV should be observable.

the same Be foil used in fig. 6 that has been covered with a carbon foil whose nominal thickness is  $1 \mu\text{g}/\text{cm}^2$  (about 40 Å). Note that in fig. 10 the oxygen peak is significantly shifted to lower energy (longer flight time) because the oxygen is physically below the carbon foil. With a knowledge of the rate of energy loss of He in carbon one can infer from this shift that the carbon thickness is  $1.8 \mu\text{g}/\text{cm}^2$ , in reasonable agreement with the nominal thickness. An independent measure of the carbon thickness may, of course, be made using the total number of counts in the carbon peak and the cross section for He scattering. The two results are consistent within errors. Notice that the 3.6 keV energy shift of the oxygen peak is easily resolved (even by eye) in this spectrum. Since the resolution of Si surface barrier detectors used in conventional MeV RBS is typically 15 keV, this shift would be very difficult to detect with conventional backscattering. We estimate (conservatively) that with a stable ion beam ToF MEIS will be able to resolve structural differences corresponding to about  $10^{16}$  atoms/ $\text{cm}^2$  using a normally incident ion beam. Care must be taken in analyzing complex targets by ToF MEIS since masses may be misidentified if they are present as buried layers even a few ångströms below the surface.

### 6. Summary

Time-of-flight medium energy ion scattering has been shown to be a powerful new technique for surface and thin films analyses both in backscattering and forward recoil configurations. It provides information comparable to that provided by RBS but, in principle, surpasses RBS in sensitivity and depth resolution. The time-of-flight spectrometer is simple, reliable and almost as easy to use as a Si surface barrier detector. It has been demonstrated to work well with protons, He and heavy

ions such as C, N and O. It excels at elastic recoil detection, because light recoils are detected at short flight times where the detector shows very low background.

Work described in this paper was funded primarily through the College of Arts and Science, the School of Engineering, the University Research Council and the Natural Sciences Council of Vanderbilt University. The authors wish particularly to thank D.A. Bromley, Director of the A.W. Wright Nuclear Structure Laboratory at Yale University, for his assistance in establishing the laboratory in which this work was performed. Also, we would like to thank Martha Rihard Weller for providing some of the calibration samples used in this work, and Martha Weller and Alan Barnes for thoughtful comments on the manuscript.

## References

- [1] W.-K. Chu, J.W. Mayer and M.-A. Nicolet, Backscattering Spectrometry (Academic Press, New York, 1979).
- [2] R.G. Smeenk, R.M. Tromp, H.H. Kersten, A.J.H. Boerboom and F.W. Saris, Nucl. Instr. and Meth. 195 (1982) 581.
- [3] M.H. Mendenhall and R.A. Weller, Nucl. Instr. and Meth. B40/41 (1989) 1239.
- [4] J.P. Thomas, M. Fallavier and A. Ziani, Nucl. Instr. and Meth. B15 (1986) 443.
- [5] W.N. Lennard, H.R. Andrews, M. Freeman, I.V. Mitchell, D. Phillips, D.A.S. Walker and D. Ward, Nucl. Instr. and Meth. 203 (1982) 565.
- [6] J.P. Biersack and L.G. Haggmark, Nucl. Instr. and Meth. 174 (1980) 2567.
- [7] J.F. Ziegler, J.P. Biersack and U. Littmark, The Stopping and Range of Ions in Solids (Pergamon, New York, 1985).
- [8] B.L. Doyle and P.S. Peercy, Appl. Phys. Lett. 34 (1979) 811.
- [9] B.L. Doyle and D.K. Brice, Nucl. Instr. and Meth. B35 (1988) 301.
- [10] H. Nagai, S. Hayashi, M. Aratani, T. Nozaki, M. Yanokura, I. Kohno, O. Kuboi and Y. Yatsurugi, Nucl. Instr. and Meth. B28 (1987) 59.
- [11] A. Chevarier, N. Chevarier and S. Chiodelli, Nucl. Instr. and Meth. 189 (1981) 525.
- [12] M.R. Weller, M.H. Mendenhall, P.C. Haubert, M. Döbeli and T.A. Tombrello, Proc. of the Workshop on High Energy and Heavy Ion Beams in Materials Analysis, Albuquerque, New Mexico, June 14-17 1989, Materials Research Society, in press.
- [13] M.H. Mendenhall, Nucl. Instr. and Meth. B10/11 (1985) 596.
- [14] N. Matsunami et al. At. Data Nucl. Data Tables 31 (1984) 1-80.

## A TIME-OF-FLIGHT SPECTROMETER FOR MEDIUM ENERGY ION SCATTERING

Marcus H. MENDENHALL<sup>1)</sup> and Robert A. WELLER<sup>2)</sup>

<sup>1)</sup> Department of Physics and Astronomy and <sup>2)</sup> Department of Materials Science and Engineering,  
Center for Atomic and Molecular Physics at Surfaces, P.O. Box 1807 B, Vanderbilt University, Nashville, TN 37235, USA

We are developing a new time-of-flight particle energy spectrometer for use in the 10–200 keV/u range. This spectrometer is designed as a detector for medium energy ion scattering (MEIS) surface analysis. MEIS, when applied to the charged component of scattered particles, has been demonstrated to be a useful complement to Rutherford backscattering analysis (RBS) and low energy ion scattering (LEIS) in the elemental and structural analysis of surfaces and thin films. However, despite its demonstrated advantages, it has never come into widespread use because of the difficulty of energy analyzing uncharged particles in the relevant energy range of 10–250 keV. Our detector will be equally sensitive to both scattered ions and neutrals and calculations indicate that it will enable MEIS to rival conventional RBS in precision, speed and ease of use and to surpass it in sensitivity, surface specificity and depth resolution.

### 1. Introduction

The four most widely used tools for determining the composition of a surface are Auger electron spectroscopy (AES), secondary ion mass spectrometry (SIMS), low energy ion scattering (LEIS), also called ion scattering spectrometry (ISS), and Rutherford backscattering analysis (RBS). In each of these techniques, a probe beam of particles is directed onto the surface to be investigated. The interaction of one of these primary particles with the atoms of the material causes either the emission of a particle or the reflection of the primary particle. The analysis of this secondary particle's properties gives information about the surface.

Of the techniques noted, RBS most directly provides reliable quantitative information about the composition of the surface under study [1,2]. This is because in RBS the fundamental interaction is the Coulomb interaction between the nucleus of the primary ion and that of the surface atom with which it collides. This makes RBS much less sensitive to the chemical environment of the surface than the other techniques, all of which depend upon atomic phenomena for their effectiveness.

The literature on medium energy ion scattering (MEIS) through the mid 1970s has been reviewed by Buck [3]. A significant motivating factor for much early MEIS work was the need to understand neutralization in scattering in order to interpret the results of data obtained with electrostatic analyzers. A significant advance in developing a spectroscopy uniting the advantages of RBS and LEIS has been made by Saris's group at the FOM Institute for Atomic and Molecular Physics in the Netherlands [4] following earlier work by van Wijngaarden et al. [5] and Feuerstein et al. [6]. The intrinsic lower limit of primary beam energies for which

RBS retains its quantitative accuracy is determined by the deviation of the true cross section from the Rutherford value. For an incident beam of protons this limit is around 30 keV. However, the effective limit is set by the resolution of the detector used. The only detectors which are common today are solid state Si surface barrier detectors. These devices are simple, accurate and inexpensive, but even the best have  $\alpha$  particle energy resolutions of about 10 keV. This relatively high value sets a lower limit on the energy beam of several hundred keV. The Dutch group avoids this difficulty by using a large electrostatic spectrometer which can analyze scattered ions when the incident projectile is typically 50–200 keV [7].

In this paper a new detector is described which, as preliminary calculations indicate, will lead to reliable ion scattering analyses using proton beams with energies as low as 20–40 keV. It is based upon a time-of-flight technique which was developed for use in nuclear physics [8,9] and which more recently has been applied in heavy ion RBS [10–15]. In our detector, the start pulse is produced by a microchannel plate detecting the secondary electrons from a 1  $\mu\text{g}/\text{cm}^2$  carbon foil, and the stop pulse is produced by the impact of the backscattered particle on another microchannel plate.

The time-of-flight technique will be superior to the current procedure using electrostatic analyzers in two very important respects. First, the time-of-flight method will be sensitive to both scattered neutrals and ions whereas the electrostatic analysis detects only ions. This becomes increasingly important as the energy of the beam is decreased. Second, the time-of-flight technique is inherently capable of analyzing the flight time of each particle that enters the sensitive solid angle and will be much faster (or, equivalently, less invasive) than single

channel detectors such as electric and magnetic sectors. When compared with conventional RBS, it is also expected to be more surface specific (since the range of the primary ions in the target is shorter and the stopping power higher), and to have a depth resolution of perhaps a little as 0.6 nm [5]. In addition, using 50 keV protons it will be about 400 times more sensitive than conventional RBS with 2 MeV He<sup>+</sup> because of the larger cross section at lower energies.

## 2. Spectrometer design

A schematic diagram of the prototype of the Mark I spectrometer is shown in fig. 1a. This prototype is currently being constructed at Vanderbilt. Ions which have been scattered from the target surface in the direction of the detector pass through the first of two grids held at ground potential and then through a 1 µg/cm<sup>2</sup> self-supporting carbon foil which is at a potential of -1 to -5 kV. As the backscattered ion exits the foil it causes the emission of secondary electrons which are accelerated by the electric field between the foil and the second grid. The electrons subsequently strike the microchannel plate detector and generate a start pulse. Meanwhile, the backscattered ion continues past the second grid to be stopped by collision with a second microchannel plate which generates a stop pulse. The time interval between the start and stop pulses is measured by a time to digital converter and a time-of-flight spectrum is accumulated by the data acquisition computer. Our spectrometer will have a 50 cm ion flight path and a 15 cm electron flight path. The electrons will be accelerated to a transport energy of 3 keV. Because of the short flight distance of the electrons, no electrostatic focussing will be needed to assure that they strike the microchannel plate detector. We are using Galileo FTD-2003 microchannel plates (a chevron plate designed for saturated pulse operation) with their special 50 Ω anode designed for fast timing applications. The data acquisition will be performed by an Apple Macintosh II computer driving a CAMAC crate through an IEEE-488 bus.

Fig. 1b shows the design for the Mark II detector which we will test when we have completed construction of the Mark I version. The Mark II design will dispense with off-axis electron detection, which is used in the Mark I to allow the electron detector to be close enough to the foil so that it subtends a large enough angle to permit collection of all of the emitted electrons. Instead, the electrons will be transported over the same path as the heavy particles, and will be confined by a weak electrostatic lens. This design will substantially simplify the spectrometer, but does require careful design of the electron optics. The lens used must be as weak as possible so that it does not significantly affect

the trajectories of the heavy particles, since not all of the particles will be charged and any electric fields could destroy the insensitivity of our system to charge state. In the design of our system, the electrons being transported will have energies no greater than 5 keV, and the heavy particles will have energies typically in excess of 50 keV; thus, a lens sufficiently strong to confine the electrons should not strongly influence the higher energy heavy particles.

For most particle scattering spectroscopies, three important figures of merit are the energy resolution of the detector, the solid angle of the detector, and the scattering cross section. For the MEIS technique, the scattering cross section  $\sigma$  is quite large compared with the cross sections typically encountered in MeV He scattering. What a new detection scheme must provide is a large solid angle and good energy resolution. For typical MeV particle scattering systems, an energy resolution of about 1% (15 keV at 1.5 MeV) is considered very good, and solid angles of around  $10^{-3}$  sr are typical. Our detector should, without difficulty, be capable of subtending a solid-angle  $d\Omega$  of order  $10^{-4}$  and  $\sigma d\Omega$  (hence total sensitivity) exceeding substantially that of MeV He scattering. The remaining parameter to be addressed is, then, the resolution.

The resolution of the system we are building will be affected by a number of variables: the acceleration time of the secondary electrons; the flight time of the secondary electrons; the intrinsic timing resolution of the electron detector; the energy loss of the particle traversing the carbon foil; the intrinsic timing resolution of the ion detector; and the intrinsic timing resolution of the pulse amplifiers, discriminators and time-to-digital converter. The apparent flight time  $t_f$  of a particle in the system is

$$t_f = \frac{L}{\sqrt{2(E_0 - \Delta E)/m_1}} - t_e,$$

where  $t_e$  is the electron flight time.  $E_0$  is the scattered particle kinetic energy,  $\Delta E$  is the energy lost by the particle in the carbon foil,  $m_1$  is the scattered ion mass (assumed exact), and  $L$  is the flight distance:

$$E_0 = \frac{m_1 L^2}{2(t_f + t_e)^2} + \Delta E.$$

Thus, the fractional energy resolution is

$$\left\{ \frac{\delta E_0}{E_0} \right\}^2 = 4 \left\{ \frac{\delta L}{L} \right\}^2 + \frac{4}{(t_f + t_e)^2} \{ (\delta t_f)^2 + (\delta t_e)^2 \} + \left\{ \frac{\delta \Delta E}{E} \right\}^2,$$

where  $\delta \Delta E$  is the rms energy straggling in the foil,  $\delta t_f$  is the rms uncertainty in the stop pulse time,  $\delta t_e$  is the rms uncertainty in the start pulse time, and  $\delta L$  is the



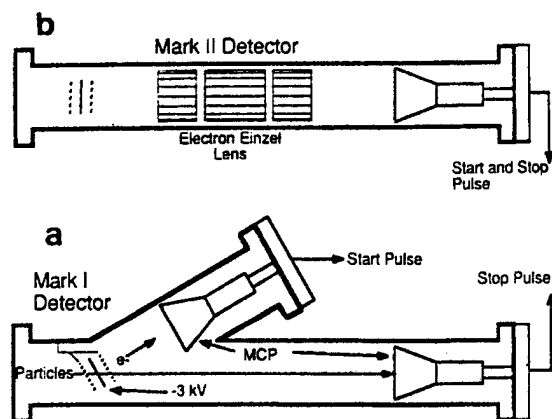


Fig. 1. Schematic of time-of-flight detector design, showing (a) the Mark I prototype design and (b) the Mark II design.

rms uncertainty in the flight path length. For the Mark I spectrometer, the uncertainty in flight path is dominated by the difference in flight path due to the angle  $\theta$  between the start foil and the stop detector. A simple integration yields an rms value  $\delta L = (r/2) \sin \theta$  where  $r$  is the radius of the start foil aperture. In the Mark II model, the foil is parallel to the detector, so the only uncertainty is due to real flight path differences, which are insignificant.

We calculate, based on simple kinematics for the electrons and on the specified timing resolution of our electronics, that the system will have a timing resolution  $\delta t_e$  for the start pulse of about 150 ps. When this is combined with the uncertainty due to straggling in the foil, we get energy resolutions  $E/\Delta E$  which range from around 200 to around 400, depending on the species scattered. Thus, the technique has a resolution greatly exceeding that available with Si surface barrier detectors, which have maximum resolutions of about  $E/\Delta E = 100$  for 2 MeV helium ions and much lower resolutions at lower energies and with heavier ions.

The resolution of a scattered particle detector affects its ability to measure a number of different properties of a surface. First, it will affect the depth resolution attainable, although this resolution is often limited by factors other than the detector. Second, it will affect the mass resolution, i.e. the ability of the system to distinguish the masses of the species on the surface from which the particle was scattered. The energy lost by a particle in a single binary collision is

$$\Delta E = E_i \frac{4m_1 m_2}{(m_1 + m_2)^2} \sin^2(\theta/2),$$

where  $m_1$  is the mass of the scattered particle,  $m_2$  is the mass of the target particle, and  $\theta$  is the center-of-mass scattering angle. When  $m_2 \gg m_1$ ,  $\Delta E$  is small so one finds that for a given energy resolution, mass resolution decreases with increasing mass. Thus, a figure of merit

for mass resolution is the highest mass at which  $\Delta m = 1$  can be distinguished. Referring back to the above formula, one can convert a given mass resolution into an energy resolution. This can then be related through velocity to the intrinsic timing resolution of the spectrometer and the energy spread of the scattered particles produced by their passage through the foil in the detector. In the discussion and computations below, we predict the resolution of the spectrometer, both as  $E/\Delta E$  and as the mass at which  $\Delta m = 1$  is just resolved.

The timing uncertainty in the acceleration and transport of the secondary electrons depend on their initial distribution, the acceleration voltage, the distance over which the acceleration occurs, and the length of the drift region between the acceleration grid and the electron detector. As all of the distances in the problem are made smaller and the voltages larger, the timing uncertainty due to the initial energy distribution of secondary electrons from the start foil decreases; however, mechanical and electrical considerations limit the ultimate size and voltage that can be achieved. The actual timing calculations are done using the trivial kinematic formulas from classical physics, which are exact for this calculation.

The time required for an electron to travel from the start foil to the end of the acceleration region is computed by solving the quadratic

$$\begin{aligned} d &= \frac{at^2}{2} + v_0 t = \frac{q_e E}{2m_e} t^2 + \sqrt{2T_0/m_e} t \\ &= \frac{q_e V_0}{2m_e d} t^2 + \sqrt{2T_0/m_e} t, \end{aligned}$$

where  $d$  is the distance from the foil to the accelerating grid,  $V_0$  is the acceleration voltage,  $T_0$  is the initial kinetic energy of the electrons and  $m_e$  and  $q_e$  are the electron mass and charge, respectively. This can be more conveniently recast in natural units with  $q_e = 1$ ,  $m_e = 511 \text{ keV}/c^2$ , and  $T_0$  expressed in eV to yield

$$\frac{V_0 c^2}{2(m_e c^2) d} t^2 + \sqrt{\frac{2T_0}{m_e c^2}} ct - d = 0.$$

Let the solution of this equation, obtained by the quadratic formula, be designated  $t_1$ . The drift time between the accelerating grid and the detector can be computed from the total kinetic energy of the electron. The energy after acceleration will be  $T = T_0 + V_0$  (in eV) and the drift speed will be

$$v_d = c \sqrt{\frac{2(T_0 + V_0)}{m_e c^2}}$$

and the flight time,  $t_2$ , will be  $t_2 = l/v_d$ , where  $l$  is the distance between the grid and the detector. Then,  $t = t_1 + t_2$  is the total electron flight time and  $t(T_0 = 0) - t(T_0 = \text{max secondary energy})$  is our estimate of the timing

Table 1

Predicted resolution and sensitivity of the detector for various beam species:  $m$  = mass of the scattered particle,  $z$  = charge of scattered particle,  $E$  (keV) = energy of scattered particle,  $E/\Delta E$  = resolution of detector,  $m_1$  = the highest target nuclide mass for which  $\Delta m = 1$  should be resolvable,  $E_B$  = the incoming beam energy required to produce a scattered particle of energy  $E$  (keV) from a target nucleus of mass  $m_1$ ,  $\sigma(\text{Au})$  = the cross section, in  $\text{\AA}^2$ , for scattering a particle of energy  $E_B$  from an Au nucleus at  $135^\circ$ ; provided for comparison. These cross sections are computed from the ZBL universal potential [16] to include corrections for non-Rutherford scattering.

$m$	$z$	$E$ (keV)	$E/\Delta E$	$m_1$	$E_B$	$\sigma$ ( $10^{-8} \text{\AA}^2$ )
1	1	25	230	28	28	9663
1	1	50	290	32	56	2942
1	1	100	301	32	111	806
1	1	200	253	29	225	206
2	1	50	338	48	58	2754
2	1	100	400	52	114	768
2	1	200	351	49	230	197
4	2	300	370	71	364	311
6	3	300	328	82	385	606
10	5	1000	322	105	1386	135
12	6	1000	312	114	1435	180
16	8	1000	265	122	1569	262
28	14	3000	283	167	5350	69
35	17	4000	281	187	7643	49

spread attributable to the secondary electron energy distribution. The more conventional technique of expanding a Taylor series to get  $\delta t/\delta T_0$  does not work well here since  $\delta t_1/\delta T_0$  is infinite at  $T_0 = 0$ .

If we assume an initial energy spread of 20 eV for the secondary electrons, an acceleration distance of 1 cm, an acceleration voltage of 2 kV, and a drift path of 20 cm, the total timing uncertainty is 110 ps. The actual electron flight time, including acceleration, is 8.3 ns. The assumption of a 20 eV secondary electron energy spread is probably conservative; it is likely to be smaller. In table 1, we use a 150 ps total timing resolution  $\delta t_e$ .

The precision in measuring the scattered particle's flight time is also limited by the uncertainty in the energy loss of the particle in the foil used to generate the start pulse. This uncertainty contains two terms, one due to the intrinsic variation in energy loss known as straggling, the other due to variations in the foil thickness. For the foils we are using ( $1 \mu\text{g}/\text{cm}^2$  of carbon), we estimate for 50 keV deuterons a total energy loss of about 590 eV, with a variation due to straggling about 132 eV. The uncertainty due to variations in the thickness of the foil can be estimated at 5% of the total energy loss, based upon the manufacturer's guarantee of uniformity of the foils. Adding the two uncertainties in quadrature yields a final estimate for the resolution for the detector. As can be seen in table 1, the resolution  $E/\Delta E$  can approach 400, and is above 300 for many

beams. If this resolution is achieved, it will be unprecedented for charge-state-independent detection of particles in this energy range and will allow extremely high quality backscattering spectra to be collected. Some features of this table are important to highlight. First, note the cross section for 100 keV deuterons on gold is  $7.6 \times 10^{-6} \text{\AA}^2$ ; for comparison, the cross section for 2 MeV He is  $6.8 \times 10^{-8} \text{\AA}^2$ , a factor of 100 smaller. Another important feature is the very high value for the unit mass separation limit,  $m_1$ , that can be realized using heavy ions. For a Li beam at 300 keV (which will be routinely available with our accelerator), we predict a unit mass separation at masses as high as 80 u. This is extremely difficult, if not impossible, to do using conventional RBS or even heavy-ion RBS at the normal energies used with Si surface barrier detectors.

### 3. Conclusion

Time-of-flight medium energy ion scattering promises to be a technique capable of providing unprecedented sensitivity and resolution for surface analysis. It will provide detailed structural information in conjunction with channeling and blocking techniques. Because of the large scattering cross-section, lower total beam fluences will be required and surface damage induced by the analyzing beam will be minimized. In addition, it will provide better resolution and simpler operation than pulsed-beam time-of-flight measurements, since it is very difficult to perform pulsed-beam worked with resolution much better than 1 ns.

Support for this project has been provided by the School of Engineering, the College of Arts and Science, and the University Research Council at Vanderbilt University.

### References

- [1] H.-J. Grossmann and L.C. Feldman, Materials Analysis with High Energy Ion Beams Part I: Rutherford Backscattering, Mater. Res. Soc. Bull. XII (6) (1987) p. 26.
- [2] W.-K. Chu, James W. Mayer and M.-A. Nicolet, Backscattering Spectrometry (Academic Press, New York, 1978) chap. 2.
- [3] T.M. Buck, in: Inelastic Ion-Surface Collisions, eds. N.H. Tolk, J.C. Tully, W. Heiland and C.W. White (Academic Press, New York, 1977) p. 47.
- [4] W.C. Turkenburg, H.H. Kersten, B.G. Colenbrander, A.P. de Jongh and F.W. Saris, Nucl. Instr. and Meth. 138 (1976) 271.
- [5] A. van Wijngaarden, B. Miremedi and W.E. Baylis, Can. J. Phys. 49 (1971) 2440.
- [6] A. Feuerstein, H. Grahmann, S. Kalbitzer and H. Oetzmann, in: Ion Beam Surface Layer Analysis, eds. O.

- Meyer, G. Linder, and F. Kappeler (Plenum, New York, 1976) p. 471.
- [7] R.G. Smeenk, R.M. Tromp, H.H. Kersten, A.J.H. Boerboom and F.W. Saris, *Nucl. Instr. and Meth.* 195 (1982) 581.
- [8] G. Gabor, W. Schimmerling, D. Greiner, F. Bieser and P. Lindstrom, *Nucl. Instr. and Meth.* 130 (1975) 65.
- [9] J.D. Bowmann and R.H. Heffner, *Nucl. Instr. and Meth.* 148 (1978) 503.
- [10] A. Chevaier, N. Chevarier and S. Chiodelli, *Nucl. Instr. and Meth.* 189 (1981) 525.
- [11] A. Chevarier and N. Chevarier, *Nucl. Instr. and Meth.* 218 (1983) 1.
- [12] J.P. Thomas, M. Fallavier, D. Ramdane, N. Chevarier and A. Chevarier, *Nucl. Instr. and Meth.* 218 (1983) 125.
- [13] A. Chevarier, N. Chevarier, M. Stern, D. Lamouche, P. Clechet, J.R. Martin and P. Person, *Nucl. Instr. and Meth.* B13 (1986) 207.
- [14] P. Person, A. Chevarier, N. Chevarier, P. Clechet, D. Lamouche, J.R. Martin and M. Stern, *Nucl. Instr. and Meth.* B15 (1986) 425.
- [15] J.P. Thomas, M. Fallavier and A. Ziani, *Nucl. Instr. and Meth.* B15 (1986) 443.
- [16] J.F. Ziegler, J.P. Biersack and U. Littmark, *The Stopping and Ranges of Ions in Solids* (Pergamon, New York, 1985) chap. 2.